Compact microwave microfluidic sensors and applicator

Ali Amin Abduljabar

A thesis submitted to Cardiff University
for the degree of Doctor of Philosophy

March 2016

Declaration

This work has not previously been accepted in substance for any degree and is not concurrently submitted in candidature for any degree.

Signed…….. (candidate) Date……

Statement 1

This thesis is being submitted in part fulfilment of the requirements for the degree of PhD.

Signed…….. (candidate) Date……

Statement 2

This thesis is the result of my own independent work/investigation, except where otherwise stated. Other sources are acknowledged by explicit references.

Signed…….. (candidate) Date……

Statement 3

I hereby give consent for my thesis, if accepted, to be available for photocopying and for inter-library loan, and for the title and summary to be made available to outside organisations.

Signed…….. (candidate) Date……

ACKNOWLEDGEMENTS

This PhD project would not be possible without the assistance of many people. I wish to express my gratitude to them all for their contributions.

First of all, I would like to express my deepest gratitude to my supervisors Prof. Adrian Porch and Prof. David Barrow. Their wide knowledge, deep academical insights, support, guidance and encouragement have given me the strength and confidence necessary to complete this work. There are no words to express my thanks towards both of them.

I would also like to thank Dr. Jonathan Lees, Dr. Chris Yang, Dr. Jack Naylon, Dr. Heungjae Choi, Dr. Hassan Hirshy, Dr. Jerome Cuenca, and Mr. Nicholas Clark for their valuable assistance and advice during my study.

Many thanks to the technicians in the electrical/electronic workshop, mechanical workshop, and IT group in the School of Engineering for their help and cooperation.

I am grateful to my parents and family for their love and support throughout this long endeavour.

Above all I thank the Almighty God for showering his infinite bounties and grace upon me, which has helped me to successfully complete my research work.

ABSTRACT

There is a need in the industrial, chemical, biological, and medical applications for sensors capable for providing on line real-time non-destructive and non-chemical measurements methods of liquid properties. There are huge advantages that microwave-based microfluidic sensing techniques offer over conventional methods due to the strong interaction of microwave electromagnetic fields with the molecules of polar liquids, so their properties can be revealed. Furthermore, in recent years there has been growing interest in utilizing microwaves in microfluidic heating owing to the efficient, selective, and volumetric properties of the resultant heating, which is also easily controlled.

The research work presented here encapsulates:

(1) The design and realization of novel microwave microfluidic microstrip sensors which can be used to characterize accurately liquid permittivities. This resonator is both compact and planar, making it suitable for a lab-on-a-chip approach. Moreover, the sensor has been developed to measure properties of multi-phase liquids where the sensor is a variant of the split ring resonator realized in a microstrip implementation.

(2) A microwave microstrip sensor incorporating a split ring resonator for microsphere detection and dielectric characterization within a microfluidic channel.

(3) A new dual mode microwave microfluidic microstrip sensor which has the ability to measure the liquid permittivity with temperature variations. Two quarter ring resonators were designed and fabricated. The first resonator is a microfluidic sensor whose resonant frequency and quality factor depend on the liquid sample. The second is used as a reference to adjust for any changes in temperature.

(4) A microwave microfluidic applicator with electronically-controlled heating, which has been proposed, designed, and realized. The concept is based on feeding the resonator with two synchronized inputs that have a variable phase shift between them.

Table of contents

CHAPTER 1 – INTRODUCTION AND THESIS OVERVIEW

The assessment of the dielectric properties of materials are of interest to scientists in various disciplines: physicists, chemists, engineers, biologists [1]. The interest varies from one discipline to another. For example in electrical engineering, the aspect is to identify the capacitance (i.e. stored energy) and energy loss of the materials as a function of frequency and temperature. In chemistry, the knowledge of dielectric properties leads the chemist to deduce molecular properties and interactions between molecules, and even monitor the progress of chemical reactions. Biologists can diagnose or identify living cells or biological tissues by measuring the dielectric properties of them.

The common approach to measure the dielectric properties of solid, liquid, and gaseous materials is to quantify their interaction with the fields (in this thesis, specifically, the electric field) of an applied electromagnetic wave [2]. This provides a contactless measurement of electrical properties such as permittivity and conductivity [3]. The use of the microwave (few GHz) to millimetre (10's GHz) electromagnetic wave bands to explore material properties needs the understanding of materials' dielectric and conducting properties [2]. For liquids, which are the focus of this thesis, there is a wide spectrum of information such as relaxation processes and orientational polarization of the molecules, all of which contribute to the liquid's complex dielectric function and its variation with frequency and temperature.

Microwave approaches (e.g. in the frequency range from about 1 to 10 GHz) offer smart means of liquid characterization. The polar nature of the liquids makes their molecules interact with the electric field of electromagnetic waves at microwave frequencies. Therefore, technically it should be promising to design and realize microwave sensors which utilize this interaction for liquid characterization.

1.1 Microwave microfluidic and micro-particles sensing

Among the microfluidic sensing platforms that are widely used in industry, and in medicine in particular, microfluidic sensing methods are noteworthy as diagnostic systems become miniaturised. The use of microwave techniques in microfluidic sensing is highly versatile and provides the ability of continuous measurements of the liquid properties, also as a function of the temperature. The principle of sensing is the fundamental interaction of microwaves with materials involved in microfluidics [4]. Microwave microfluidic sensing for pure liquids, or a mix of solid/liquid phases (e.g. microparticles in a microfluidic flow), is based on two approaches [2]: resonant and non-resonant methods. In resonant methods, cavities or dielectric resonators are used in which the change in resonant frequency and bandwidth due to the perturbation of the resonator's energy owing to the presence of a sample is exploited to measure the dielectric properties of liquids or micro-particles. Resonant microwave measurements provide extremely precise and sensitive characterization of a liquid's complex permittivity at specific frequencies and as a function of temperature. The second approach of microwave microfluidic sensing uses broadband transmission line methods. They lack the sensitivity of the resonant method, but offer a continuous spectrum for measurement, so allowing dielectric spectroscopy of the material under test.

1.2 Microwave microfluidic heating

Some materials such as liquids have the ability to convert the electromagnetic energy into heat. Such dielectric heating (driven by the electric field) at microwave frequencies is more efficient than conventional conductive heating, and is also volumetric and spontaneous in nature, so is very attractive in chemistry applications and material processing [5]. In polar liquids at microwave frequencies, heat is generated due to the frictional forces between the liquid molecules [6]. This efficient method of heating has

been adopted in many applications. Rapid, selective, and uniform heating of fluid volumes, ranging from few microliters to as low as few nanolitres, is vital for a wide range of microfluidic applications [7], such as DNA amplification by polymerase chain reaction (PCR) and organic/inorganic chemical synthesis [8]. The use of microwave heating in microfluidic systems provides many advantages: the ability of direct delivery (and focusing) of the energy to the sample with minimal transfer to the other parts of the microfluidic system, non-contact delivery of energy, and the very high heating rate (especially for low volume samples as met in microfluidics) which can decrease the reaction time compared to conventional techniques.

1.3. Context

The accurate dielectric measurement of liquids is still challenging in many applications. Although many types of microwave microfluidic sensors have been presented, there are several problems that are needed to be solved. This project addresses some of these problems in microwave microfluidic sensor design. The problems addressed can be summarized as: accuracy, size, cost, simplicity, real time measurements, single micro-particle characterization, dependence on temperature and heating efficiency.

The proposed sensors in this work are suitable to characterize liquid and micro-particles for industrial, chemical, and biological applications, also taking into account the temperature dependence of the liquid permittivity. Part of this work concerns the design of efficient microwave applicator for microfluidic application.

1.4. Aims and objectives

1.4.1. Aims

The aims of this project were to develop a new microwave microfluidic sensor, microwave micro-particles sensor and microwave microfluidic applicator based on microwave resonators that could be used for measurement and diagnostics for generic (bio)chemical, medical, and industrial real-time applications.

1.4.2. Objectives

- Investigate and develop robust sensing approaches for liquids and micro-particles in a microfluidic system taking in account the cost, size, and measurement accuracy.

- Maximize the sensor sensitivity by optimising the sensor design, geometries and materials.
- Investigate and develop methods for on-line, label-free, real-time liquid and micro-particle characterizations.
- Improve the interaction between the microfluidic and microwave systems to maximize the sensitivity.
- Characterize liquid and micro-particles in microfluidic channels using microwave technology.
- Characterise the dielectric properties of multi-phase liquid flow with time.
- Provide for temperature correction in temperature dependent liquids by adding a reference resonator to detect small changes in temperature.
- Develop microwave microfluidic heating using a multi-feed microwave resonator.
- Propose future developments for the microfluidic sensing and heating applications.

1.5. Original contributions

There are five main novel aspects to this work, which are briefly described in subsections 1.5.1 to 1.5.5 below.

1.5.1. Microstrip microfluidic sensor

Firstly, a new type of microwave microfluidic sensor was developed to detect and determine the dielectric properties of common liquids. The technique is based on perturbation theory, in which the resonant frequency and quality factor of the microwave resonator depend on the dielectric properties of the material placed in the resonator. A microstrip split-ring resonator with two gaps is adopted for the design of the sensors (i.e., a double split-ring resonator, or DSRR) as shown in Figure 1.1. This resonator is both compact and planar, making it suitable for a lab-on-a-chip approach, with a resonant frequency of around 4 GHz. Several types of solvents have been tested with two types of capillaries to verify sensor performance.

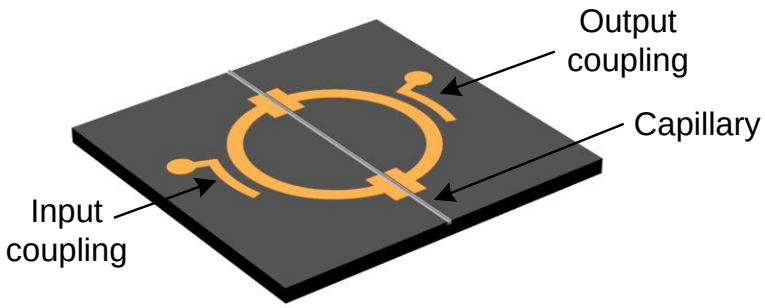

Figure 1.1: Schematic of DSRR microfluidic sensor.

1.5.2. Microwave microfluidic sensor for segmented flow

Secondly, the new type of double split ring resonator was applied to measure the length, volume, speed and dielectric properties of different liquids in a segmented microfluidic flow. Measurements of the changes of the resonant frequency and quality factor are performed when a segment enters the sensing region, in this case the gap regions. Two different geometries of resonators were used for the sensors, each with two gaps to accommodate a planar microfluidic channel as illustrated in Figure 1.2. The segments consisted of mineral oil and water.

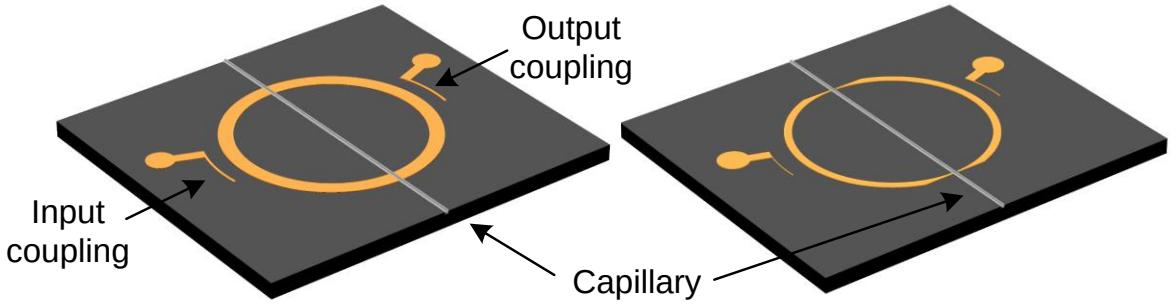

Figure 1.2: Schematic of DSRR microfluidic segmented flow sensors.

1.5.3. Microsphere detection resonator

Thirdly, a microwave microstrip sensor incorporating a split ring resonator (SRR) was developed for microsphere detection and dielectric characterization within a microfluidic channel. Three SRRs of approximately equal gap dimensions, but with different radii to give different resonant frequencies of 2.5, 5.0 and 7.5 GHz (thus altering their sensitivity) were designed and fabricated as illustrated in Figure 1.3. To validate the SRR sensors, two

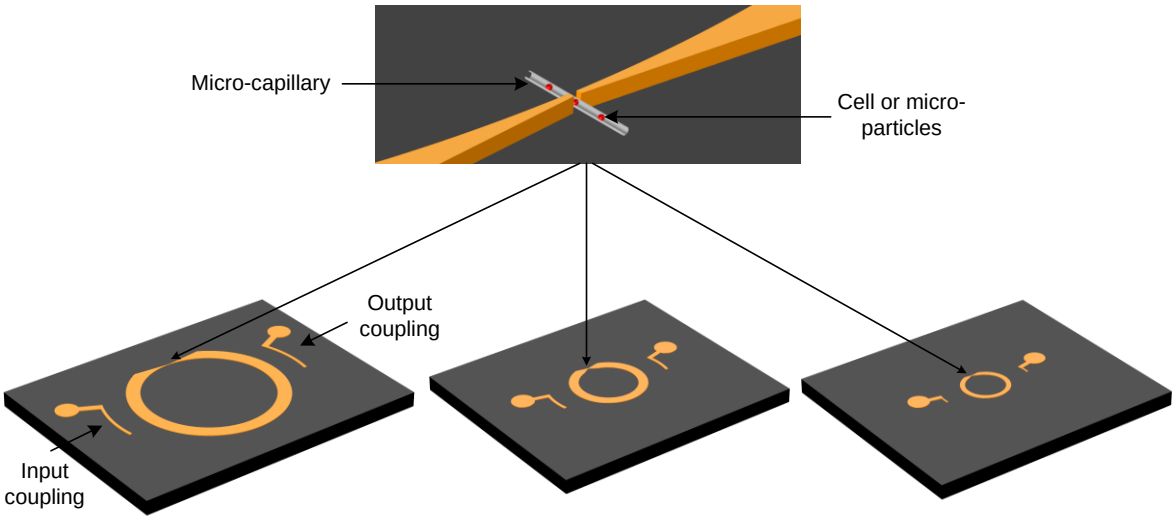

Figure 1.3: Schematic of three sizes of microstrip split ring resonator for cells or micro-particles detection.

sizes of polystyrene microspheres were tested, of diameters 15 and 25 μm. Measurements of changes in resonant frequency and insertion loss of the odd SRR mode were related to the dielectric contrast provided by the microspheres and their host solvent, here water. The even SRR mode was used investigated to provide temperature compensation in a completely novel way, owing to its decreased sensitivity to the presence of the sample.

1.5.4. Dual mode microwave microfluidic sensor

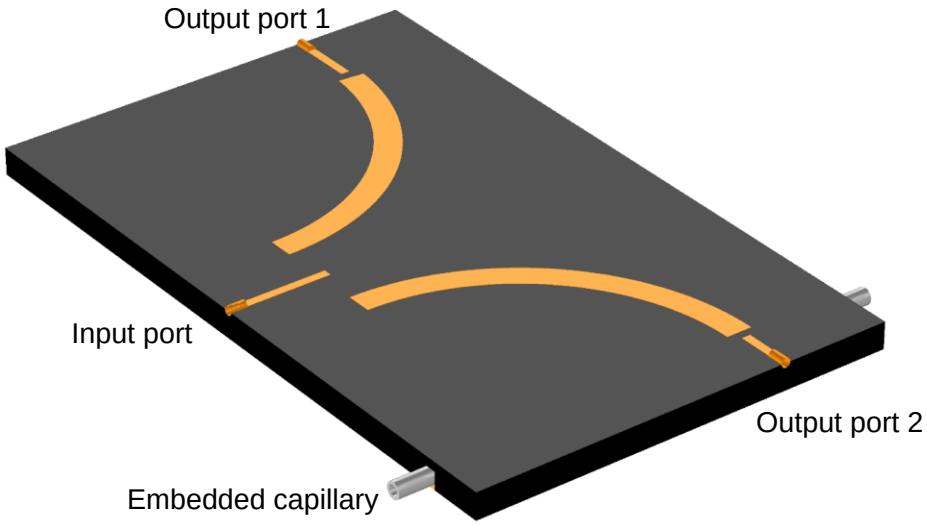

Figure 1.4: Schematic of the dual mode microstrip sensor with two resonators.

Fourthly, a new dual mode microwave microfluidic microstrip sensor was designed, built and tested, which has the ability to measure the liquid permittivity and compensate for temperature variations. It involves the simultaneous excitation of two quarter ring resonators. The first of these is a microfluidic sensor where its resonant frequency and quality factor depend on the liquid sample as shown in Figure 1.4. The second one is used as a reference to adjust for changes in the ambient temperature. To validate this sensor, two liquids (water and chloroform) have been tested with range of temperature from 23 to 35 ºC.

1.5.5. Adaptive coupling technique

Fifthly, an electronically adaptive coupling technique was proposed and demonstrated for a microwave microstrip resonator to improve the efficiency of liquid heating in a microfluidic system. The concept is based on feeding the resonator with two synchronized inputs that have a variable phase shift between them. A Wilkinson power divider and phase shifter were designed and fabricated for this purpose as shown in Figure 1.5.

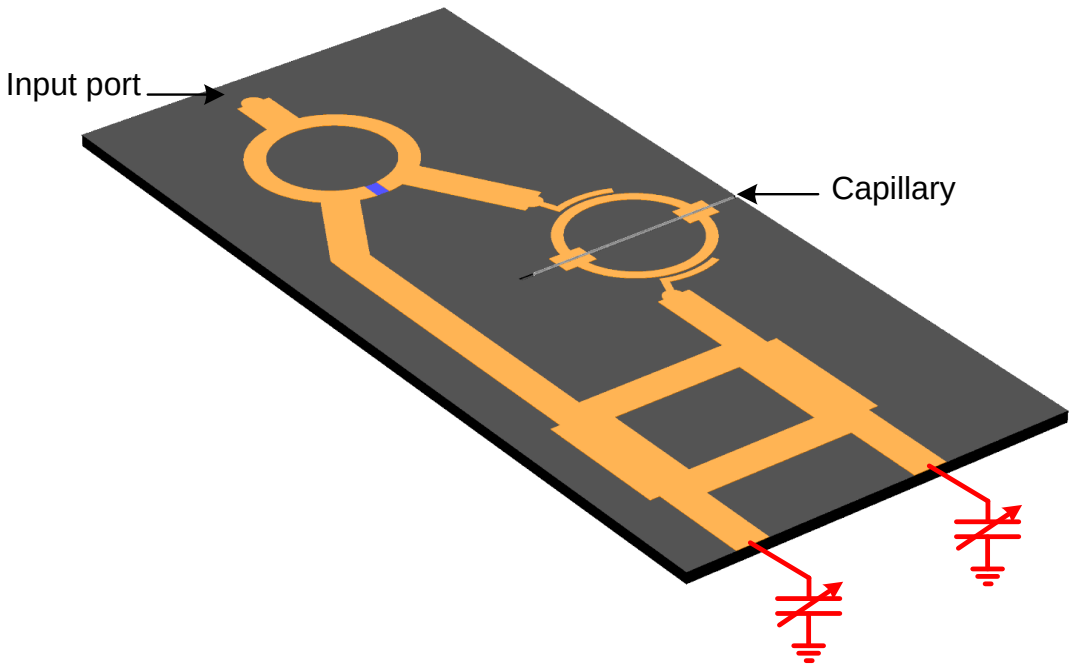

Figure 1.5: Schematic of adaptive coupling microfluidic applicator.

1.6. Thesis overview

Chapter 2 attempts to give the reader a basic understanding of the microwave microfluidic sensing techniques via a comprehensive literature review. The review includes microwave liquid sensing, cells and micro particles detection, and microwave heating of liquids.

Chapter 3 describes the theories behind all of the works in this thesis. The theories include the dielectric properties of polar liquids, microstrip structures, perturbation theory, and microwave heating.

Chapter 4 presents a new resonant microstrip technique which has been realized and tested to measure the dielectric permittivity of liquids. The method is based on resonator perturbation theory in which the resonant frequency and the bandwidth change as a result of adding a liquid sample in a microfluidic circuit. A planar double split ring resonator is adopted and designed to reduce the size and weight of the sensor. Moreover, Chapter 4 presents a new method to measure length, speed, volume and permittivity of liquids in a microfluidic system with segmented flow. A double split-ring microwave resonator is used as the resonant sensor element. Two models were designed and fabricated to study the effect of the gap on the sensor performance.

Chapter 5 describes a new type of microwave sensor for micro-particles detection where three models of microwave sensor based on a microstrip split ring resonator were developed and tested for the dielectric measurement, size measurement and counting of microspheres.

Chapter 6 describes a new type of microwave microfluidic microstrip sensor in which the change in the temperature can be detect to obtain more accurate results of the measured complex permittivity of the liquid.

Chapter 7 proposes a novel adaptive coupling method that provides the ability to change (and, in principle, control) the coupling of a microwave resonator electronically. This approach can be exploited in microfluidic heating applications, where the heating rate can be optimized without changing the source power.

Chapter 8 draws together all of the general conclusions of the techniques and data presented in Chapters 4-7, together with some suggestions for future work.

1.7. Publications

The following articles have been prepared/published throughout the course of this work, which includes four full IEEE-MTT papers in print (one further IEEE-MTT paper under review), and two IMS publications accepted for oral presentation and published in the proceedings.

1.7.1. Journal publications

A. A. Abduljabar, A. Porch, and D. Barrow, "Dual mode microwave microfluidic sensor for temperature variant liquid characterization," *Submitted to IEEE Transactions on Microwave Theory and Techniques*, under review.

A. A. Abduljabar, X. Yang, D. Barrow, and A. Porch, "Modelling and measurements of the microwave dielectric properties of microspheres," *IEEE Transactions on Microwave Theory and Techniques*, vol. 63, no. 12, pp. 4492 - 4500, December. 2015.

A. A. Abduljabar, H. Choi, D. A. Barrow, and A. Porch, "Adaptive coupling of resonators for efficient microwave heating of microfluidic systems," *IEEE Transactions on Microwave Theory and Techniques*, vol. 63, no. 11, pp. 3681 - 3690, November. 2015.

A. A. Abduljabar, D. J. Rowe, A. Porch, and D. A. Barrow, "Novel microwave microfluidic sensor using a microstrip split-ring resonator," *IEEE Transactions on Microwave Theory and Techniques*, vol. 62, no. 3, pp. 679-688, March 2014.

D. J. Rowe, S. al-Malki, **A. A. Abduljabar**, A. Porch, D. A. Barrow, and C. J. Allender, "Improved split-ring resonator for microfluidic sensing," *IEEE Transactions on Microwave Theory and Techniques*, vol. 62, no. 3, pp. 689-699, March 2014.

1.7.2. Conference publications

A. A. Abduljabar*, X. Yang, D. A. Barrow, and A. Porch, "Microstrip split ring resonator for microsphere detection and characterization," in *IEEE MTT-S Int. Microw. Symp. Dig. (IMS)*, Phoenix, AZ, 2015, pp. 1-4. *[* presenter, oral]*

A. A. Abduljabar*, A. Porch, and D. A. Barrow, "Real-time measurements of size, speed, and dielectric property of liquid segments using a microwave microfluidic sensor," in *IEEE MTT-S Int. Microw. Symp. Dig. (IMS)*, Tampa, FL, 2014, pp. 1-4. *[* presenter, oral]*

CHAPTER 2 – LITERATURE REVIEW

2.1. Review of microwave microfluidic sensing and heating techniques

This chapter presents a literature review of the techniques that have been used in microwave sensing and heating of liquids in microfluidic systems, linked to the material presented in this thesis. Section 2.2 of this chapter provides a review of the microwave sensing of liquids in microfluidic systems where many approaches have been proposed to characterize liquids using different types of microwave resonators and circuits. In Section 2.3, a review of techniques that have been used to measure multi-phase liquids properties are presented. Section 2.4 reviews the recent applications of microwave sensing to micro particles and cell detection. The final section of this chapter addresses the microwave approaches for liquid heating.

2.2. Microwave microfluidic sensing

Microwave microfluidic sensors are very attractive for a wide range of applications. One class of these sensors uses microwave resonant circuits to determine the dielectric properties of liquids contained within micro-capillaries. Such sensors (which involve the direct interaction of the liquid with the electromagnetic fields) have many advantages, such as the ability to miniaturize the device, the minimal invasiveness of the technique, the simplicity of operation, the fact that there is no chemical reaction (and so long “shelf life”), and that any changes of dielectric properties of the liquids can be measured instantaneously. All of these have intensified the research efforts to develop and improve microfluidic microwave sensor performance, in particular for medical and industrial applications [9]-[12]. Microwave microfluidic sensors can be categorized to three groups: the first group of sensors are based on broadband measurements in which

wide band microwave circuits are used, usually incorporating non-resonant microwave transmission lines; the second group of sensors utilize microwave resonator circuits where the resonant frequency and quality factor are measured to characterize the liquids at certain ("spot") frequencies at the specific resonant frequencies of the circuits; the third type of microwave microfluidic sensors are designed using microwave filter techniques, and are closely linked to the resonant sensor in that the change in the centre frequency and bandwidth of the filter vary with liquid sample, but operate in a restricted frequency range defined by the bandwidth of the filter.

2.2.1. Broadband measurements techniques

A review has been conducted in this section of the most and recent works of microwave microfluidic sensing using broadband measurements. Microwave broadband sensing can be classified into several groups according to the type of microwave transmission line or circuit that has been used for liquid sensing or measuring.

A- Coplanar waveguide model

High-frequency coplanar waveguide (CPW) transmission lines have been used for the broadband microwave measurement liquids in [13] and [14]. CPW structures have been adopted in [14] to fabricate a microwave microfluidic sensor for the rapid and quantitative determination of the complex permittivity of nanoliter fluid volumes over the continuous frequency range from 45 MHz to 40 GHz, as shown in Figure 2.1. A transmission-line model was developed to obtain the distributed circuit parameters of the fluid-loaded transmission line segment from the response of the overall test structure. Finite-element analysis of the transmission line cross section was used to calculate the complex permittivity of fluid from the distributed capacitance and conductance per unit length of the fluid-loaded transmission line segment.

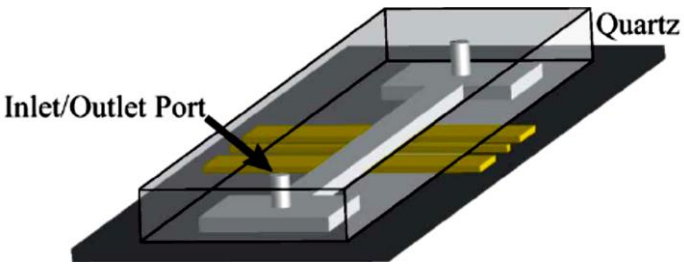

Figure 2.1: Schematic of the integration of a microfluidic channel with a patterned coplanar waveguide device [14].

Other broadband coplanar waveguide transmission lines were developed in [15] to extract the permittivity of the fluids in a microfluidic microelectronic platform up to 40 GHz. Broadband measurements from 100 MHz to 40 GHz were conducted to validate the performance of the sensor to measure the permittivity of the polystyrene beads in an aqueous liquid. In [16] an integrated capacitor with a microfluidic channel were designed to measure the broadband electrical properties (from 40 MHz to 40 GHz) of alcohols and biological liquids. It was found that mixtures of 10% and 20% of ethanol in water changed the capacitance at 13 GHz to 30 fF and 60 fF, respectively. Another microfluidic sensor based on an interdigitated capacitor (IDC) with a microfluidic channel to confine liquids (for nanolitre volumes) was developed in [17], as illustrated in figure 2.2. Wide band measurements were taken from 40 MHz to 40 GHz.

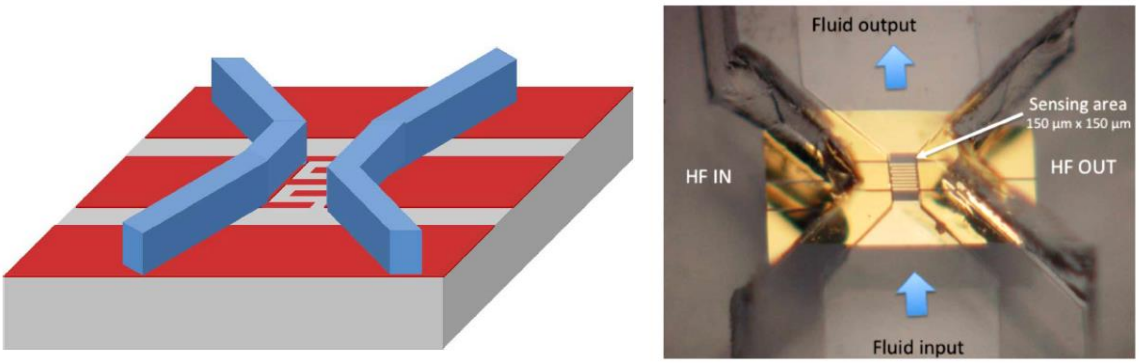

Figure 2.2: (a) Schematic of an interdigitated capacitor (IDC) presented in [17] for broadband dielectric characterisation to 40 GHz. (b) Photograph of the fabricated microfluidic IDC [17].

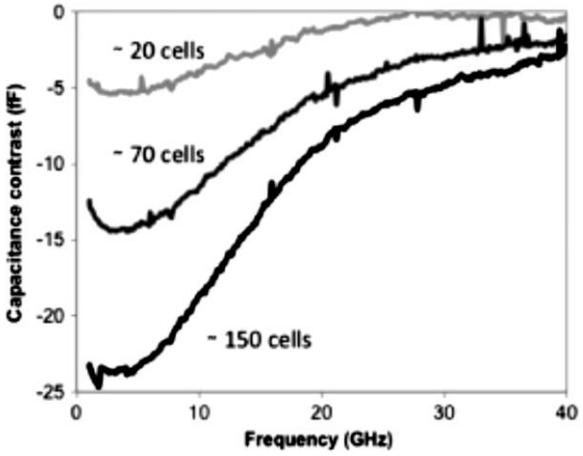

Figure 2.3: Contrast spectra of the capacitance for different concentations of living RL lymphoma cells, measured relative to their biological culture medium. [17].

The sensor was used to characterize, identify, and quantify alcohols and biological aqueous solutions in terms of capacitance and conductance contrasts with respect to pure de-ionized water. The value of the capacitance contrast of the IDC varies from 110 fF to 7 fF at 11 GHz when the concentration of ethanol in water was decreased from 20% down to 1%, respectively. Moreover, this sensor was tested in a biological application involving cell detection, where a contrast of 5 fF at 3 GHz relative to the reference bio-medium was measured for less than 20 living cells, as shown in figure 2.3.

In [18] a borosilicate glass chip was integrated with a microfluidic duct with a coplanar waveguide to build microwave biosensor to monitor the properties of lipid bilayer formation. Broadband measurements of the transmission coefficient were taken from 50 MHz to 13.5 GHz, which illustrate the change in the attenuation with formation of the dioleoylphosphocholine (DOPC) bilayer. An integrated microfluidic microelectronic measurement platform was designed in [19] to extract accurate results of the dielectric properties of the liquids and biological samples. Measurements of the S-parameters were taken up to 40 GHz to extract the capacitance and conductance of the liquid per unit length, leading to the final aim of finding the relative permittivity. The sensor was tested by using de-ionized water and methanol. A broadband liquid permittivity measurement from 1 GHz to 35 GHz was presented in [20]. The sensor design is based on quasi-lumped structures using coplanar waveguide transmission lines in which the sensor was verified by using saline solution, water and ethanol:water mixtures.

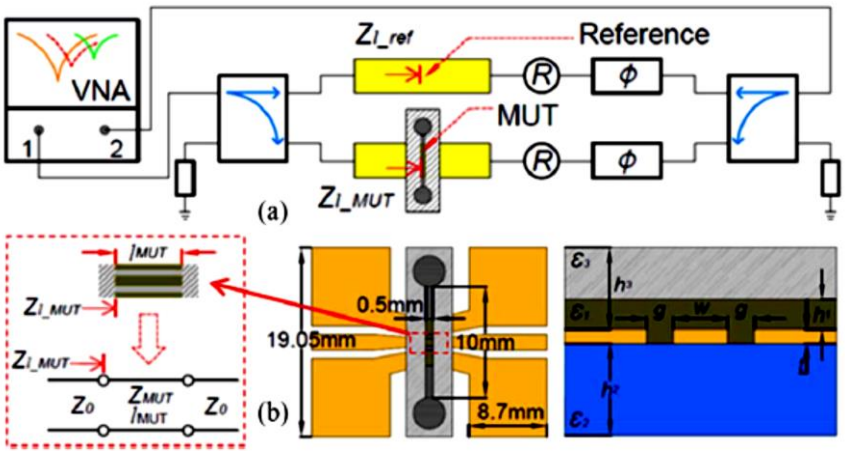

Figure 2.4: (a) A schematic of the RF sensor described in [21]. (b) The top and cross section view of the sensing zone.

Finally, in [21], [22], a tunable microwave microfluidic sensor based on micron scale coplanar waveguides was presented, as shown in figure 2.4, to measure the dielectric properties of aqueous solutions. Two quadrature hybrids are utilized to achieve destructive interference that eliminates the probing signals at both measurement ports. As a result, the presence of the material-under-test (MUT), via its dielectric properties, were quantified at different frequencies. The relative permittivity of propanol:water solutions were measured from 4 GHz to 12 GHz. To calibrate the sensor, de-ionized water and methanol:water solution were used.

B- Microstrip model

In [23] a microstrip line with a 50 µm gap capacitor at the centre of the line was designed to build a microfluidic sensor. The microfluidic channel was fabricated on the top of the gap region where the liquid can influence the capacitance of this gap region. Broadband measurements of the voltage transmission coefficient, S_{21}, were taken from 14 MHz to 4 GHz, where the sensor was validated by several liquid such as ethanol, ethylene glycol, and ethyl acetate.

C- Waveguide model

Broadband measurements from 20 to 110 GHz were shown in [24] for the complex permittivity of the biological and organic liquids. A proposed sensor in this system was designed by using a two port waveguide structure. The sensor was validated by measuring the complex permittivity of dioxane, methanol, and blood. WR90 and WR62 waveguides were used in [25] to measure the complex frequency of the liquids at X (8-12 GHz) and Ku (12-18 GHz) bands. These systems were verified by several liquids such as methanol, propyl alcohol, ethyl alcohol, chlorobenzene, dioxane, cyclohexane and binary mixtures.

D- Capacitor model

In [26] a novel, three-dimensional parallel-plate, capacitive sensing structure was proposed to measure the relative permittivity of ethanol and ethanol glycol in the frequency range of 14 MHz to 6.5 GHz, with rms errors between 3.5% to 5.6% in the complex relative permittivity values.

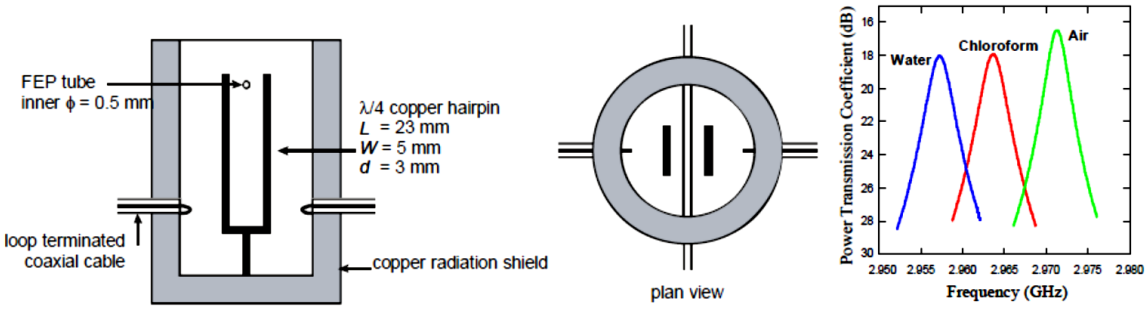

Figure 2.5: Schematic of a 3 GHz copper hairpin resonator. The phase-separated liquid sample flows through the tubing, which is positioned at the region of maximum electric field at the open end of the resonator. The measured resonance responses of the device with the capillary filled with water, chloroform and air are illustrated [29].

2.2.2. Resonance measurement techniques

Many types of microfluidic sensors based on microwave resonators have been fabricated, which are highly sensitive to the presence and dielectric properties of the liquid. These sensors can be categorized regarding to the type of the microwave resonator that is used in the design of the microfluidic sensor.

A- Hairpin resonator sensor

A hairpin resonator was used in [27]-[29] to design a microfluidic sensor for in-situ compositional analysis of an acetonitrile-toluene solvent mixture within a PEEK micro-capillary. The same hairpin resonator was also used to monitor the compositional output of a multiphase-flow liquid phase separator, as shown in figure 2.5. Cavity perturbation theory was employed to analyse the measured results (the change in the resonant frequency and bandwidth) to extract the values of the dielectric properties of the mixtures.

B- Cavity resonator sensor

A cylindrical cavity resonator operating in its TM_{010} mode was developed in [30] to measure the complex permittivity of the liquids with high accuracy. The liquid sample is inserted into a dielectric tube which passes through holes in the cavity walls. Two types of liquids, ethanol and milk, were tested using this sensor to measure the complex permittivity as function of the percentage of ethanol in water, and fat percentage in the milk. Another cylindrical resonator was designed in [31] to provide online measurements of the concentration of binary liquid mixtures. The resonator was set up

at a resonant frequency of 1.61 GHz to take the measurements using a quasi TM_{010} mode. Several mixtures, such as water:methanol and magnesium sulphate solution, were used to verify the performance of this sensor. In [32], a 3 GHz TM_{010} cylindrical cavity was developed, together with numerical procedures for solving a complex characteristic equation, to extract the complex permittivity of lossy liquids. This device was validated by using sodium chloride and gelatine solutions in water. The method proposed in this work was also suggested for measuring permittivity at different temperatures of the liquids. A rectangular waveguide cavity operating in the TE_{101} mode with a resonant frequency of 1.91 GHz was developed in [33] to measure the concentration of solutes in water. The sensor capability was verified by using water:sodium chloride and water:sucrose solutions, where the shift in the resonant frequency and change in the attenuation of the transmission coefficient are the most important measurements for extracting permittivities of these mixtures.

Cylindrical sapphire dielectric resonators (SDRs) were presented in [34] for in-situ analysis of solvent composition within a machined microfluidic channel, as shown in figure 2.6. The microwave electric field of the SDR is aligned parallel to the circular microfluidic channel, thus resulting in the highest possible sample polarization, in order to maximize the sensitivity of the senor to extract very accurate value of the liquid permittivity. The sensor works at 22.7 GHz and was used to assess the concentration of acetonitrile in toluene. The resonant frequency decreases and the bandwidth increases

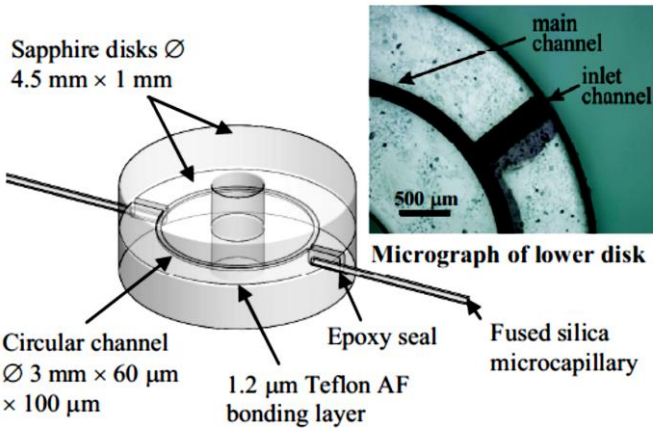

Figure 2.6: Configuration of the miniaturized sapphire dielectric resonator (SDR) with laser-ablated micro-channels of [34]. The inset shows a micrograph of the fabricated lower sapphire disk.

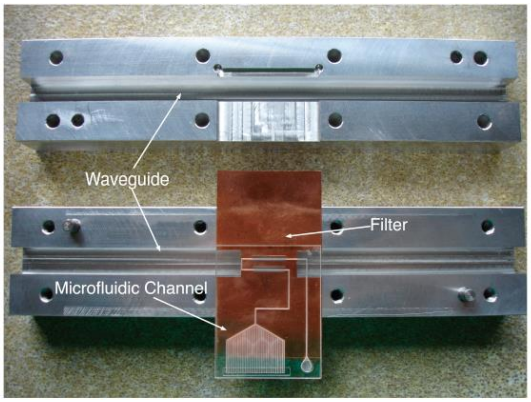

Figure 2.7: X-band waveguide halved along the E-plane, with an insert for a filter and microfluidic channel [36].

when the concentration of acetonitrile rises because of increased polarization. A sapphire cylinder and a quartz plate with a 400 nl cavity was designed in [35] to measure the complex permittivity of liquids. This microwave resonator works at 10 GHz and high quality factor (1.1×10^5) owing to the very low loss tangent of sapphire, even at room temperature. Several liquids were tested using this sensor such as ethanol, methanol, propanol, glycerine, and oil. Moreover, the sensor was used to measure aqueous solution of glucose with sensitivity of 0.1 between the measured and calculated (i.e. Debye model) results due to the weight concentration and temperature dependence.

Finally, a waveguide resonator was proposed in [36] to build a label-free chemical/biochemical sensing device, as shown in figure 2.7. An integrated microfluidic channel was inserted inside the waveguide resonator. The voltage transmission coefficient S_{21} was measured for a Phosphate Buffer Solution (PBS). PBS is an isotonic salt solution used to dilute blood, whilst maintaining cellular osmotic integrity and a constant test sample pH. Measurements of PBS were compared to those of the empty channel. The difference in the resonant frequency between two cases (empty and PBS filled channel) is 62.5 MHz where the resonant frequency when the channel was empty was 9.837 GHz.

C- Split ring resonator sensor

A split ring resonator was modified in [28], [37] to build a highly sensitive microfluidic sensor that was able to measure a very small (0.1%) volume fraction of Acetonitrile in toluene, in an active volume of around 50 nl.

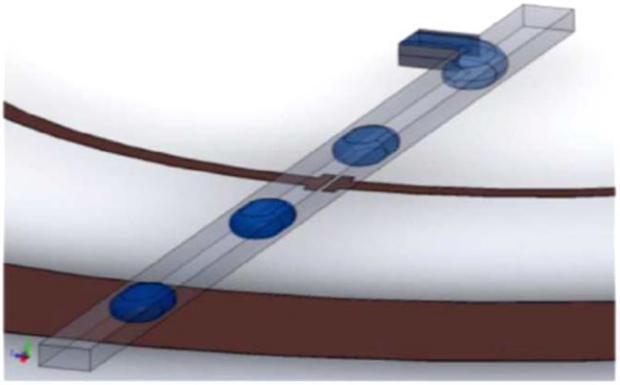

Figure 2.8: An illustration of the alignment of the microchannel with the resonator for the microfluidic sensor described in [38].

A cost-effective, scalable microwave system that can be integrated with microfluidic devices enabling remote, simultaneous sensing and heating of individual nanoliter-sized droplets generated in micro-channels is proposed in [38], as shown in Figure 2.8. To examine the sensor performance, the reflection coefficient of the sensor was measured on changing the different fluids in the microfluidic channel. The shift in the resonant frequency for silicon oil, FC-40, and water was 18.5 MHz, 12.5 MHz, and 174.5 MHz, respectively. In addition, the sensor was tested by using various dairy fluids. This sensor was also proposed to detect droplets of water.

D- Microstrip resonator sensor

A sensitive radio frequency, microfluidic sensor to measure minute changes in the dielectric properties of liquids was presented in [39]. The sensor was designed using an on-chip Wilkinson power divider, a rat-race hybrid, microstrip lines, and film chip resistors. Mixtures of methanol: water and ethanol:water with different molar fractions were used to verify the sensor performance.

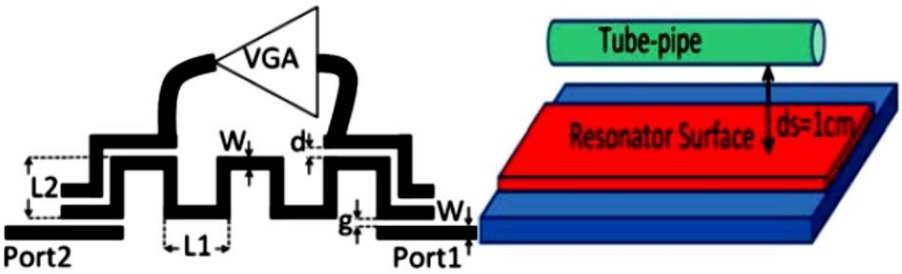

Figure 2.9: An active resonator sensor and and its conceptual schematic [40].

Moreover, an active feedback loop has been introduced in [40] within a passive ring resonator in the design microfluidic sensor to generate negative resistance and compensate for the resonator's loss in, as shown in figure 2.9. This active resonator can increase the quality factor from 240 to 200000 in air. The performance of this sensor was verified by using methanol, ethanol and acetone. The results obtained by using active resonator are far superior than those attained using the passive version of the resonator, in terms of the sensitivity of the measurement. A new type of microwave microfluidic sensor was demonstrated in [41] for crude oil in water, as shown in figure 2.10. A shift of 500MHz in resonant frequency was measured for a 50% (vol.) water in anhydrous crude oil sample, and a 50MHz shift for a 5% (vol.) water concentration. The sensor was fabricated using a low cost, direct write fabrication method.

A square ring microstrip resonator was presented in [42] to characterize the dielectric permittivity of solvents at multiple frequencies. The sensor was tested by solvents at three resonant frequencies of the ring resonator (1 GHz, 2 GHz, and 3GHz). Another resonator was proposed in this work in which an open loop resonator was designed to measure glucose:water solutions of various concentrations at 1 GHz. A planar half-wavelength ($\lambda/2$) microstrip line resonator at 2 GHz was proposed in [43] to design a sensitive microfluidic sensor for liquid permittivity measurement. The microfluidic channel is placed on the top of the resonator to obtain the required interaction the electric field and the liquid. The improvement of the microwave microfluidic sensor sensitivity was achieved in [44] by developing the cancellation level and using stronger coupling to transmission lines, and used to characterize methanol:water mixtures.

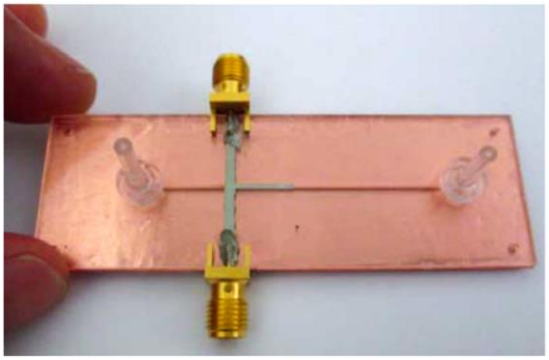

Figure 2.10: Fabricated T-resonator-based, disposable crude oil in water sensor [41].

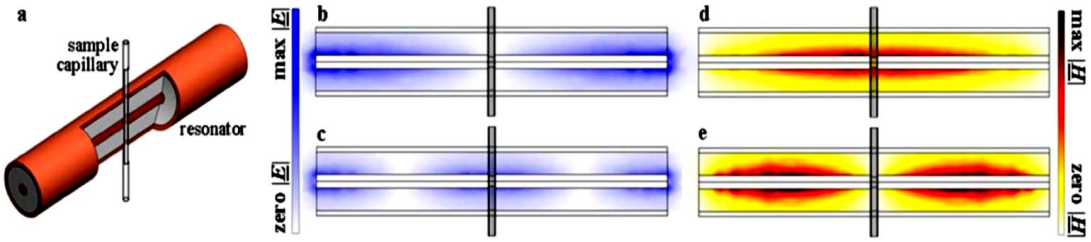

Figure 2.11: Device construction and field distributions of a coaxial resonator for dielectric measurement of liquids. (a) Cutaway view of the resonator (excluding the coupling structure) perturbed with a sample-filled quartz capillary. (b), (c) Cross-sectional colour maps of electric field magnitude for the first and second TEM modes of the device, respectively. (d), (e) Equivalent colour maps of magnetic field magnitude. It can be seen that the sample perturbs zero electric field (b) and maximum magnetic field (d) for the first TEM mode, and maximum electric field (c) and zero magnetic field (e) for the second TEM mode [46].

E- Coaxial resonator sensor

A micro-milled polytetrafluoroethylene (PTFE) microfluidic chip with an embedded, open-circuited, half-wavelength gigahertz coaxial resonator was presented in [45]–[51], which was used for analysing the chemical composition of single- and multi-phase solvent flows. This coaxial method is multi-mode, so combines the sensitivity of resonator methods whilst being broadband (albeit at spot frequencies) to open up the measurement of a partial dielectric spectrum. In [52] a microwave-frequency coaxial resonator was chosen to design the sensor shown in figure 2.11. This sensor was proposed to quantify simultaneously the electric and magnetic properties of liquids for biological, chemical, and pharmaceutical applications. A capillary is passed through the centre of the resonator so the sample occupies either a position of maximum electric field (zero magnetic field) or maximum magnetic field (zero electric field), depending on whether an odd or even TEM mode is excited. The sensor performance was verified by characterizing a serial dilution of saline solution.

F- Coplanar resonator sensor

A planar resonator was adopted to design a microwave microfluidic sensor in [53], as shown in figure 2.12. A microfluidic channel was fabricated on the top of the resonator to obtain the required interaction between the electric field and the liquid. This enables a

predictable relationship between response of the resonator (resonant frequency and associated insertion loss) and the complex permittivity of the fluid (real and imaginary parts) to be developed. The sensor was tested by using de-ionized water:ethanol mixtures with ethanol concentrations ranging from 0% to 20%, which were passed through the microfluidic channel. The measured results are shown in figure 2.13, where an increased concentration of ethanol in water increases both the resonant frequency and attenuation. This work was proposed as a sensor for liquid characterization applications for biology and chemistry.

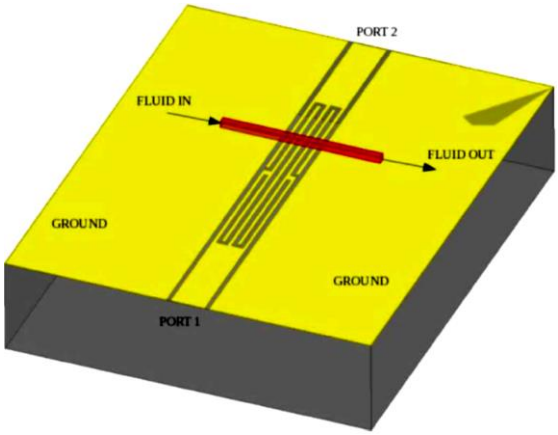

Figure 2.12: Schematic view of an RF coplanar resonator with a microfluidic channel placed on top [53].

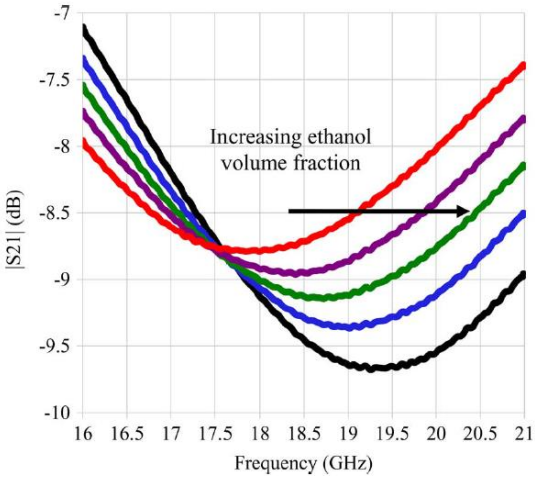

Figure 2.13: Voltage reflection coefficient $|S_{21}|$ of a microwave sensor for the five ethanol:DI water mixtures at volume fractions f_v of: 1/5; 1/7; 1/10; 1/20 ; 0 (pure water)[53].

G- Metamaterial resonator sensor

Metamaterial microwave techniques have been introduced to build microfluidic sensors. A metasurface based on metallic electric-field coupled resonators at 3.6 GHz was fabricated in [54] to sense and track the change in the flow of fluid in industrial, biomedical, and chemical reactions. Measurements of S-parameter were taken from 2.6 GHz to 3.95 GHz, where the sensor was tested by DI water. In [55] a new microwave microfluidic sensor was presented using a metamaterial-inspired structure, as illustrated in figure 2.14. They used a microstrip coupled, complementary split-ring resonator (CSRR), where the microfluidic channel is run along the sides of the CSRR where there is a strong electric field. The resonant frequency and attenuation of the CSRR change as the dielectric properties of the liquid inside the channel changes. An empirical relation was developed to extract the dielectric properties of the liquid sample. This sensor was introduced to be compatible with lab-on-a-chip applications. The sensor was validated by testing a mixture of water:ethanol. As the water volume fraction was varied from 0% to 100%, with the step size of 20%, the corresponding shift in the resonant frequency was around 400 MHz.

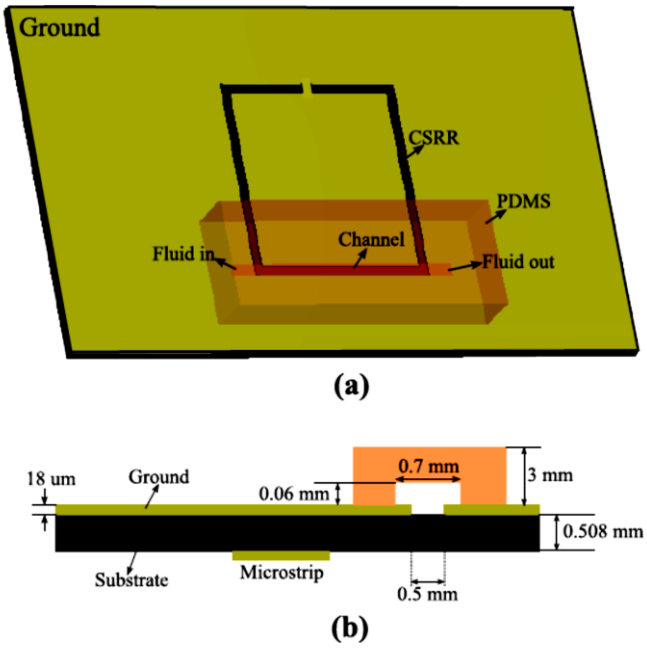

Figure 2.14: Schematic diagram of the microstrip coupled, complementary split ring resonator (CSRR) with the polydimethylsiloxane (PDMS) microfluidic channel (from [55]). (a) Top view of the structure (b) Side view with dimensions.

A single split-ring resonator was developed in [56] to fabricate metamaterial structure resonator at 2 GHz for microfluidic sensing in which the complex permittivity of the liquid affects the resonant frequency and the bandwidth. Mixture of ethanol-water and methanol-water were adopted to verify the sensing performance of the sensor.

2.2.3. Filter measurement techniques

Microwave filters have also been chosen in the design of microfluidic dielectric sensors [57]-[59]. An example is for the measurement of the concentration of salt in water [58]. A micro-machined stop-band filter with a microfluidic channel is employed to identify the properties of the fluid that passes beneath the filter circuit. A spiral resonator using coupled microstrip lines was fabricated for liquid sensing through a microfluidic channel in [59], as shown in figure 2.15. The insertion of chemical liquids in the microfluidic channel caused changes the resonant frequency and the insertion loss. A mixture of water:methanol was used to verify the performance of the sensor where the resonant frequency shifts from 2.15 GHz to 2.0 GHz, with change in dielectric constant from 25 (pure methanol) to 75 (pure water).

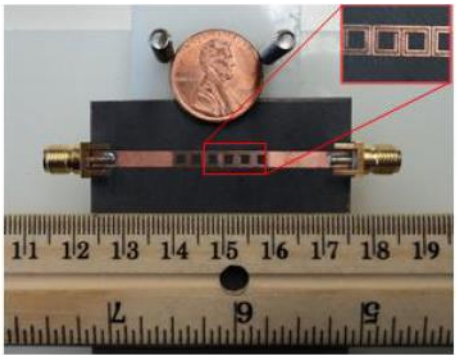

Figure 2.15: Fabricated metamaterial microstrip transmission line based on a double spiral structure [59].

2.3. Multi-phase liquids measurements using non-microwave techniques

In recent years, the measurement of the volume, length, speed and dielectric properties of the segments in microfluidic systems with high precision has become a major challenge. Many techniques have been developed to monitor and measure droplets of liquids noninvasively due to the increasing demands of this application in medical and chemical applications. The two most common means of droplet detection are optical and electrical sensing [60].

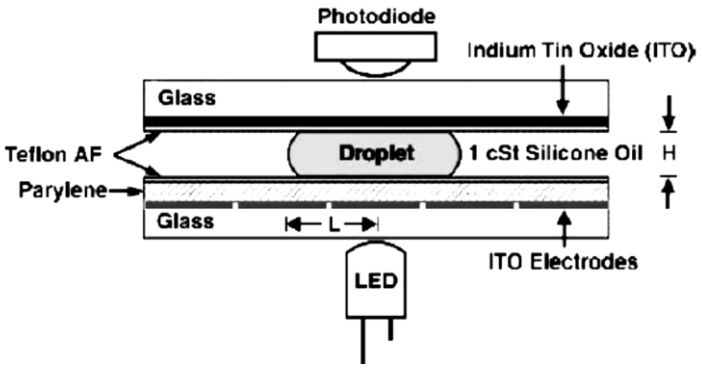

Figure 2.16: Vertical cross-section of the electrowetting chip along with the optical detection instrumentation [61].

2.3.1. Optical sensors

In optical sensing, an optical (i.e. non-microwave) microfluidic lab-on-a-chip platform for in vitro measurement of glucose for clinical diagnostic applications was presented in [61], as shown in Figure 2.16. A colour change is detected using an absorbance measurement system consisting of a light emitting diode and a photodiode. A hybrid polymeric microfluidic device with optical detection for droplet-based systems was reported in [62], in which the detected signal at the photo diode can be used for evaluating droplet size, droplet shape, and droplet formation frequency. An integrated microfluidic flow sensor with ultra-wide dynamic range, suitable for high throughput applications such as flow cytometry and particle sorting/counting, was demonstrated in [63] using fibre-optic sensor alignment, guided by preformed microfluidic channels. A parallel microdroplets technology was described in [64], which uses an inverted optical microscope and a charge-coupled device (CCD) camera to collect images and analyse them, for compartmentalization and simultaneous monitoring of different reactions in parallel strings of microdroplets generated in microsystems. An automated microfluidic system that screens the speeds of individual droplets at high precision and without human intervention was demonstrated in [65].

2.3.2. Electrical sensors

On the other hand, several ways of using electrical sensing have been proposed for measuring dimensions and properties of droplets in microfluidic systems. A microactuator for rapid manipulation of discrete microdroplets was presented in [66], as illustrated in Figure 2.17. Two sets of opposing planar electrodes fabricated on glass were used to study the transport of droplets. A micromachined chip, based on the micro

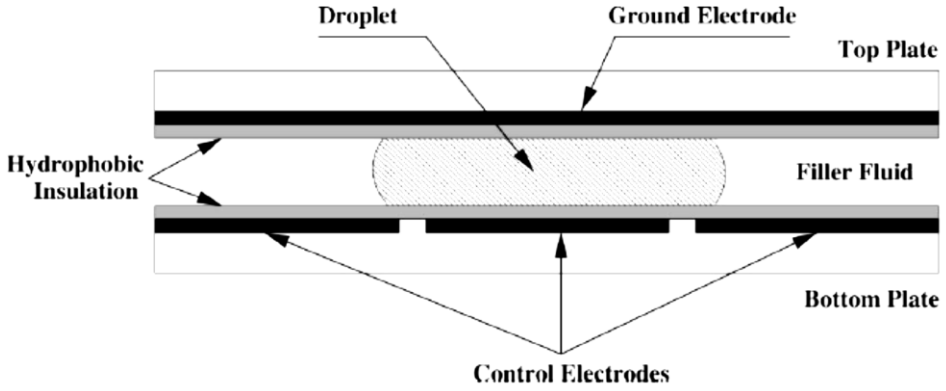

Figure 2.17: Schematic cross-section of the electrowetting microactuator [66].

Coulter particle counter (mCPC) principle, aimed at diagnostic applications for cell counting and separation in haematology, oncology or toxicology is described in [67], which can already be used for counting, sizing and population studies. A miniaturized coplanar capacitive sensor is presented in [68], whose electrode arrays can also be a function as resistive microheaters for thermocapillary actuation of liquid films and droplets. The method in [69] exploits the built-in capacitance of an electro-wetting device to meter the droplet volume and control the dispensing process. The electrode methods utilize changes in electrical conductivity, when the air/liquid interface of the droplet passes over a pair of electrodes, and were described in [70] using analogue and digital techniques. The design and implementation of capacitive detection and control of microfluidic droplets in microfluidic devices were reported in [71], in which the capacitive detection of microfluidic droplets based on the dielectric constant contrast between the droplets and the carrying fluid was adopted.

A charge-based capacitance measurement method was used in [72] for lab-on-chip applications using a CMOS-based capacitive sensor. A fast voltage modulation, capacitance sensing, and discrete-time PID feedback controller are integrated on the operating electronic board in [73] to improve the precision of volume measurement of the droplets. A 4×4 multiplexed arrays of resistive and capacitive sensors was shown in [74] to monitor the passage of discrete liquid plugs through a microfluidic network. Detection of the presence, size and speed of microdroplets in microfluidic devices is presented in [60] using commercially available capacitive sensors, which make the droplet based microfluidic systems both scalable and inexpensive. A new approach for splitting sample volumes precisely was demonstrated in [75] by gradually ramping down voltage, in place of abruptly switching off electrodes.

2.4. Microwave detection of cells and micro-particles

Much research has been undertaken in the use of microwave methods for the realization of rapid, reliable, accurate and non-invasive bio-sensors. Recent use of microwave methods for detecting the dielectric properties of human cells has yielded compelling results. A review of the biological cell dielectric properties was presented in [76], which includes the concepts of the biological dielectric properties, the dielectric properties of the cell components, how to create the electrical properties models of the biological cells, and the techniques and their implementations. An electromagnetic model to describe the biological cell was proposed in [77] in which the cell was defined in terms of its size, capacitance of the cell layers and conductivity of the cytoplasm. The electric field inside the microfluidic channel was determined by using 3D finite element model for several cell parameters (i.e. dielectric properties, size and position in the channel). A circuit model of the biological cell was proposed in [78]. Each cell part was modelled as a one-port element consisting of three elements: a resistor, a capacitor, and a series connection of a resistance and a capacitance. A nanosecond measurement was conducted on the biological cell to obtain the transfer function of the model. The use of microwave signals was illustrated in [79]. Microwave dielectric spectroscopy has been identified as a promising method to study the membrane permeabilization of cells induced by chemo-treatment, and its consequences for the cells [80]. Cells or micro-particles microwave detection and identification can be divided into two approaches; broadband and resonance measurements (i.e. similar to the microwave microfluidic techniques).

2.4.1. Broadband measurements techniques

A coplanar structure has been used in most of the broadband microwave measurements of cells or micro-particles. Coplanar waveguides with finite ground planes were designed in [81] to measure the complex permittivity of living cells (e.g. human embryonic kidney cells) where the broad band measurements were taken from 1 to 32 GHz. Another microwave coplanar waveguide (CPW) transmission line was proposed in [82], as shown in Figure 2.18, to measure the dielectric properties of cancer cells (HepatomaG2, HepG2). Wide band measurements (1-40 GHz) were taken to prove the performance of this sensor, which was proposed for applicationh in postoperative cancer diagnosis. The relationship between the attenuation and the cell density was found to be 0.12×10^{-3} dB/μm for 20 cells/μL, 0.58×10^{-3} dB/μm for 200 cells/μL, 0.81×10^{-3} dB/μm

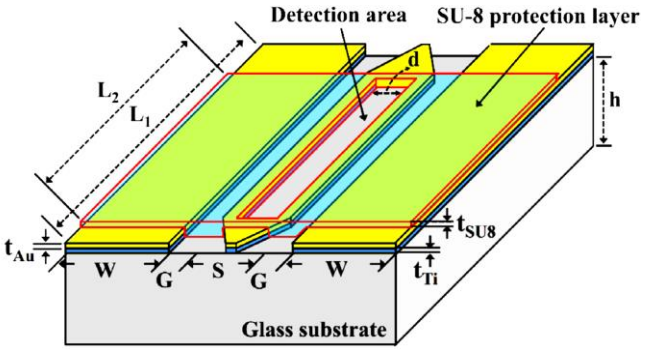

Figure 2.18: 3D illustration of the coplanar waveguide sensor for measurement of human cells [82].

for 1000 cells/μL, and 1.26×10^{-3} dB/μm for 2000 cells/μL at 40GHz. This attenuation occurs due to the polarization and dielectric loss of the cells.

A coplanar waveguide was used in [83] to design a broadband sensor for biological cell detection. This sensor was proposed to detect both live and dead cells, tested by using Jurkat cells. The experimental results revealed that the resistance of the live cells was lower that the dead ones, while the capacitance of the live cells was higher. The dielectric properties of tumorous Blymphoma cells was identified in [84] by broadband microwave measurements up to 40 GHz, where this approach also provided the ability to detect living cells without their deterioration. A coplanar waveguide structure was used in this work to build the sensor, where the microfluidic channel was fabricated on the top of the sensing area. The dielectric property of a single cell has also been investigated by using a microwave biosensor in [85], [86], incorporating a capacitive sensing zone for trapped cells within microfluidic channel, as illustrated in Figure 2.19. Two types of tests were conducted, involving single and two beads. In the former case

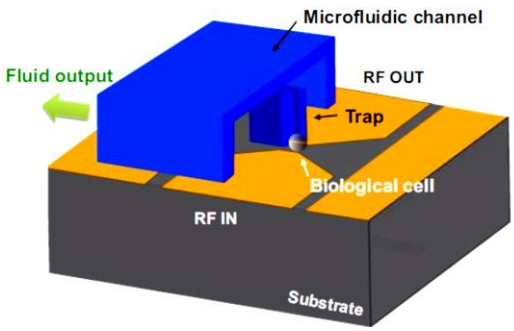

Figure 2.19: Schematic of the microwave-based biosensor for living and single cell analysis. [85].

the contrast in the capacitor was 1.2 fF at 5 GHz, while in the latter the contrast was 2.1 fF at 5 GHz. This sensor was also verified by using a living B lymphoma cell, where the measurement was taken from 40 MHz up to 40 GHz for the capacitive and conductive changes of the material in the gap. In this case the contrast in capacitance was 0.53 fF at 5 GHz, with the maximum value observed across the full wideband response. The cultivation stadium of a yeast culture was monitored to detect permittivity changes. In [87], [88], broadband microwave measurements and sensing of single Jurkat and HEK cells were used to overcome electrode polarization, with ac dielectrophoresis used to precisely place cells between narrowly spaced electrodes, and relatively wide microfluidic channels incorporated to prevent cell clogging, as shown in Figure 2.20.

A miniaturized microwave based biosensor was fabricated in [89], [90] for the characterization of living and dead cells via their dielectric properties. These biosensors were based on coplanar interdigitated capacitors featuring a dielectric sensing area of

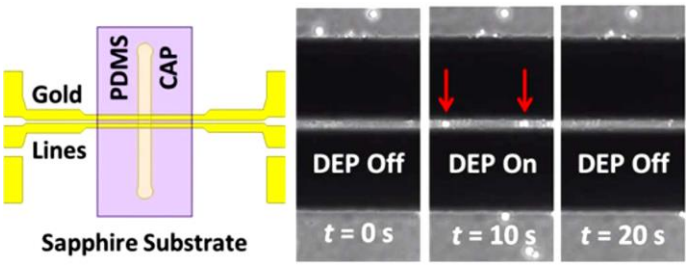

Figure 2.20: Schematic of a coplanar transmission line, which is narrowed down in the middle and intersected by a microfluidic channel at a right angle and two live cells trapped between the coplanar lines 10 s after a dielectrophoresis (DEP) signal was applied [88].

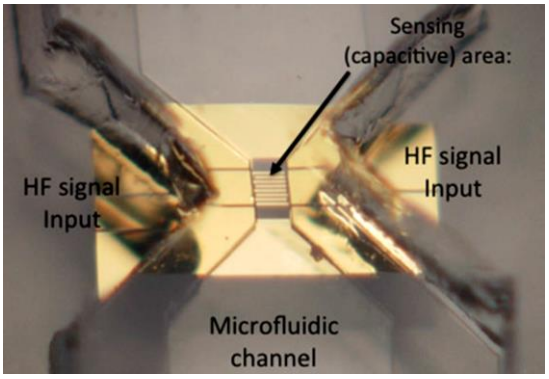

Figure 2.21: Microphotograph of the fabricated IDC structure of [89].

150×150 μm^2, as shown in figure 2.21. The contrast in the capacitance of the sensing area was 4 % between the cells suspension and their pure medium when measured at 20 GHz, and 12 % at 40 GHz. Furthermore, this sensor was proposed to detect living and dead cells, where a 5 % in capacitive contrast was measured at 30 GHz between these two cases. This sensor was developed by adding an oscillator, two detectors (composed of 4-quadrant Gilbert-cell multipliers), and DC processing circuitry. These added components were used to increase the sensitivity of the sensor toward the simplicity of on-chip microwave signal processing at 30 GHz.

Finally, coplanar waveguide devices were developed in [91] to measure the dielectric of the biological samples over the frequency range from 40 Hz to 26.5 GHz. This sensor was designed to measure the properties of haemoglobin solutions and suspensions of *E. coli* bacteria at microwave frequencies.

2.4.2. Resonance measurements techniques

A- Microstrip resonator sensor

An RF biosensor was designed in [92] for characterisation of biomolecules. The device is based on a planar split ring resonator with resonant frequency around 10 GHz. To verify this sensor, several biological samples were tested such as anti-prostate specific antigen, as a result of which the shift in the resonant frequency was 30±2 MHz. A new type of biosensor based on a two pole microstrip filter, using the inter–resonator's planar coupling capacitor as an ultrasensitive bio-sensing element, has been developed to investigate the electrical parameters of human cells [93]. The design idea of this sensor is to employ the change in the filter coupling caused by some of the biological cells located on the capacitor of the filter to extract cell properties. U87 glial cells were adopted to validate the sensor capability. Successful measurements with three U87 cells within the capacitor gaps were achieved, where a 35 MHz frequency shift and 1.5 dB attenuation at the centre frequency (12.75 GHz) of the filter frequency response was measured. Another sensor which is dedicated for one cell detection was presented in the same work, where a shift in the frequency of 13 MHz was measured.

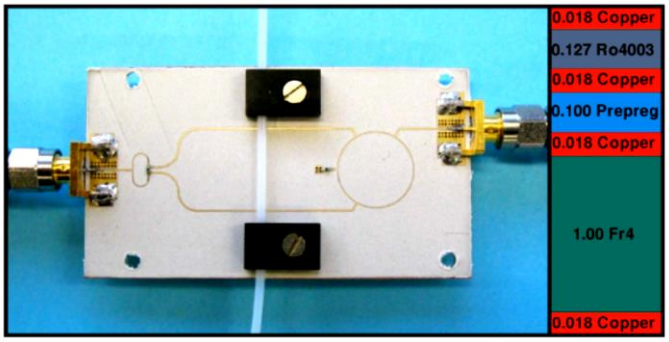

Figure 2.22: Experimental setup and layer stack of a microwave sensor for cell cultivation [94], all dimensions in mm.

A passive microwave sensor based on microstrip lines for characterizing cell cultivation in aqueous compartments is presented in [94] and is shown in Figure 2.22. The sensor was validated by measuring yeast cultivation where a 20 dB difference in transmission at 7.44 GHz was achieved after 20 hours of cultivation. An impedance spectroscopy analysis at microwave frequencies was used to characterize the biological cells properties in [95]. A classical planar microwave filter approach was chosen to design the biosensor, in which the dielectric properties of the biological cells influence the coupling area of the filter. This device was verified by several types of biological cells, such as biological cancerous stem cells to detect the contrast between them.

B- Cavity resonator

In [96] the permittivity of Chinese hamster ovary cells was identified by comparing with the host medium at 3.1 GHz. A near-field folded cavity resonator was adopted in this sensor.

C- Coplanar resonator

An original label free bio-sensing approach for cellular study based on micro-technologies at RF frequencies has also been proposed [97]. This bio-detection method presents advantages in that it is label free and of sub-millimetric size, allowing operation at the cell scale and with a limited number of cells. A coplanar, bandstop RLC resonator structure made with a meandered inductor coupled to an inter-digital capacitor was developed in [97], as shown in Figure 2.23. The sensor was tested by two different human cell types: keratinocytes HaCaT cells (skin cells) and glial-cells derived tumor glioblastoma (nervous system astrocyte cells).

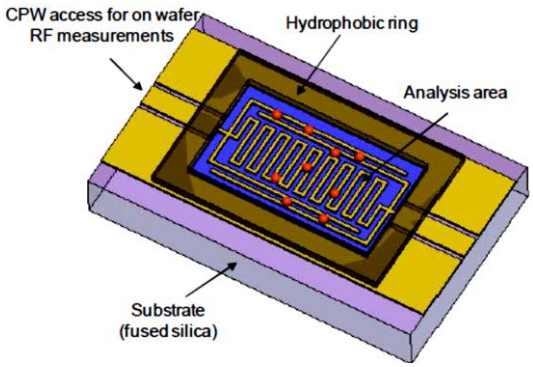

Figure 2.23: Design view of the proposed micro biosensor for cell characterization. [97].

A planar resonator at 16 GHz was chosen to build the biosensor in [98] to determine and identify the dielectric properties of human cells. A shift of 370 MHz was measured when the sensor is loaded by the glial-cells. A tuneable, resonant microwave biosensor that allowed measurement of the dielectric permittivity of microscale particles over a range of frequencies is presented in [99]. The sensor was validated with 20 μm diameter polystyrene beads to measure the dielectric permittivity. Moreover, the sensor was tested by using glioblastoma cells where a significant shift in the resonant frequency was detected. A method to measure the permittivity of single latex particles and yeast cells at microwave frequencies is presented in [100], [101], respectively. In [100], single particles with diameters between 1 and 5 μm in water are characterized using the sensor shown in Figure 2.24. In this design, in addition to the material-under-test (MUT) channel, a reference channel was introduced which was filled with water.

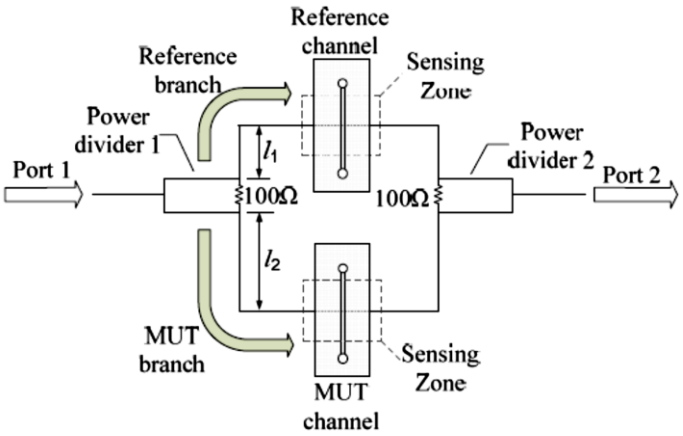

Figure 2.24: A schematic of the proposed microwave sensor in [100], which incorporates coplanar waveguides.

An electrical approach for single-cell analysis, wherein a 1.6 GHz microwave interferometer detects the capacitance changes produced by single cells flowing past a coplanar interdigitated electrode pair, is demonstrated in [102]. A polystyrene sphere with a diameter of 5.7 µm was used to calibrate the measurements. The change in the capacitance is 10 aF and 50 aF due to the presence of yeast cells and the polystyrene sphere, respectively. Moreover, the sensor changes are detected in less than 80 ms. The dielectric permittivity of the individual cells was measured in [103] using the changes in frequency of a microwave microfluidic biosensor. A passive LC resonator with interdigitated capacitor was developed to design the microwave resonator of the sensor in the range from 5 GHz to 14 GHz. Noticeable differences in the electromagnetic signatures were obtained between different aggressiveness levels of the cancer cells. Cancer cells were identified in [104] by using a biosensor based on RF resonators. The resonators are bandstop and operate between 5 and 14 GHz. It was noticed that the increase of cell malignancy led to an increase in the permittivity, which then decreased the resonant frequency.

2.5. Microwave liquid heating

Precision microfluidic heating control is required in many applications, such as for polymerase chain reactions (PCR) [105], analysis of complex biological sample solutions [106], denaturizing dynamics of fluorescent proteins at the millisecond time scale [107], and the spatially localised heating of micro-channel environments [108]. Microwave heating techniques have been adopted and developed for many industrial, domestic and medical applications. A growing number of studies have focused on microfluidic heating systems, which is the subject of the work reported here. The microwave liquid applicators can be reviewed according to the microwave circuit that is used to heat the liquid.

2.5.1. Microwave transmission line applicator

A- Microstrip transmission line applicator

A microstrip transmission line was designed in [109] for heating applications of parallel DNA amplification platforms. The microfluidic channel was drilled through the substrate between the transmission line and the ground. It required 400 mW of microwave power to increase the temperature to 72ºC at 6 GHz, where a fibre optic

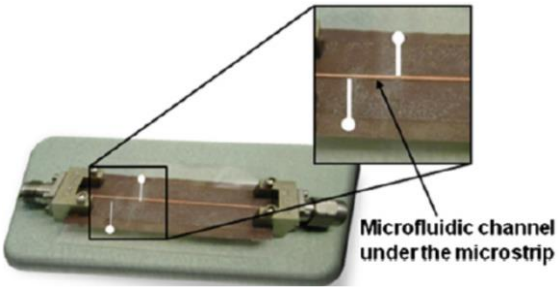

Figure 2.25: A picture of the integrated microfluidic device for generating microwave-induced temperature gradients [110].

temperature sensor was adopted to measure the temperature. In [110], an on-chip microwave generation of spatial temperature gradients was described within a polymeric microfluidic device that was coupled to an integrated, microstrip transmission line, as illustrated in Figure 2.25. The method of measuring the temperature of the fluid is by observing the temperature-dependent fluorescence intensity of a dye solution in the microfluidic channel.

B- Coplanar transmission line applicator

The performance of a planar microwave transmission line, integrated with a microfluidic channel to heat fluids with relevant buffer salt concentrations, was characterized and modelled over a wide range of frequencies [111]. The liquid was heated by the electric field component of the electromagnetic field, which is confined between the signal and ground lines, as illustrated in Figure 2.26. The heating performance of this system was measured by *S*-parameters and optical fluorescence-based temperature. The temperature rises were 0.88ºC mW^{-1} at 12 GHz, and 0.95ºC mW^{-1} at 15 GHz. In addition, a microwave power absorption model was proposed in this work to describe the distribution of the power through the applicator.

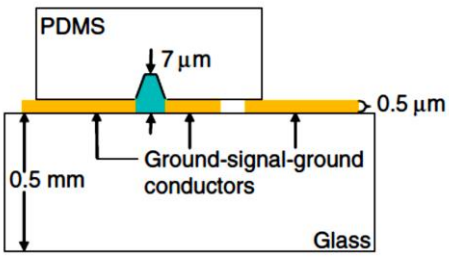

Figure 2.26: Schematic of a cross-section of a coplanar waveguide (CPW) transmission line integrated with PDMS microchannel [111].

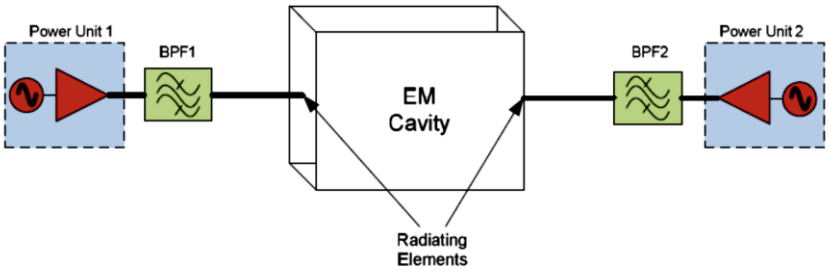

Figure 2.27: System diagram for improved feed isolation [112].

2.5.2. Microwave resonator applicator

A- Microwave Cavity resonator applicator

Much research has been undertaken to improve the heating performance when using microwave resonators as the applicator device in both large- and small-scale, fluidic heating systems. In litre-sized liquid heating, for instance, improved electromagnetic heating of a load was demonstrated by increasing the isolation (or decoupling) factor between two electromagnetic feed elements [112], as shown in Figure 2.27. Multiple feeds were used in the system to increase the delivered power to the load. Two band pass filters were used to increase the isolation between the two sources. The refinement of heavy fractions of petroleum by using microwave methods was discussed in [113]. It was discovered that the dielectric loss of the heavy petroleum is very small but enough to heat by microwave techniques, and the development of the microwave actuator system for cracking of heavy oil was discussed in this work.

A microwave heating system presented in [114] had a response time which was orders of magnitude faster than that of current commercial systems. This system was presented to implement polymerase chain reaction in a microfluidic device. A copper microwave cavity that operates at 8 GHz was chosen in this work to heat the microfluidic device. The delivered power to the cavity was up to 10 W, where the temperature of the sample was measured by using junction thermocouple which connected to the PCR chamber. Moreover, a 2.45 GHz microwave cavity resonator was presented in [115] with the novel dual function of both sensitive dielectric characterisation and directed, volumetric heating of fluids in a microfluidic chip. A microwave waveguide structure was chosen in this work. The approach which was used in this system to monitor the temperature was by using permittivity information. This approach provides the ability to observe the temperature without the need of conventional temperature sensors.

B- Split ring resonator applicator

A cost-effective, scalable microwave system was demonstrated in [38] that can be integrated with microfluidic devices, thus enabling remote, simultaneous sensing and heating of individual nanoliter-sized droplets generated in micro-channels. A small microwave ring resonator was developed in this work which works below 3 GHz. A capacitive gap with a T shape was fabricated, which was employed for sensing and heating of the liquid. A loop was adapted to excite the resonator. A microscopy fluorescence thermometry technique was adopted in this work to measure the temperature of the liquid inside the capillary. The heating was done when the droplets flow through the gap region, where 367 mm long droplets needed 5.6 ms to be heated up to 42ºC when the input power was 27 dBm.

2.5.3. Microwave irradiation applicator

In [116]-[118] the microwave irradiation was used to provide the required energy for micro-reactor applications. Single and multi-capillary reactors were design to excite liquids for synthesis processing. Finally, in [119] a new wireless heating approach was presented for microfluidic systems. This heater was designed for sterilization of *Escherichia coli* and for healthcare applications, where the temperature could be raised to 93ºC by using 0.49 W of microwave power.

2.5.4. Microwave capacitor applicator

An integrated, microwave microfluidic heater that locally (and rapidly) increased the temperature of water drops in oil was demonstrated in [120], as shown in Figure 2.28. This system works at 3 GHz, where the source and amplifier are commercially available. The temperature dependent fluorescence intensity of cadmium selenide nanocrystals suspended in the water drops was tracked to measure the temperature of the drops. The required time to heat the sample in this microfluidic device by 30ºC was 15 ms.

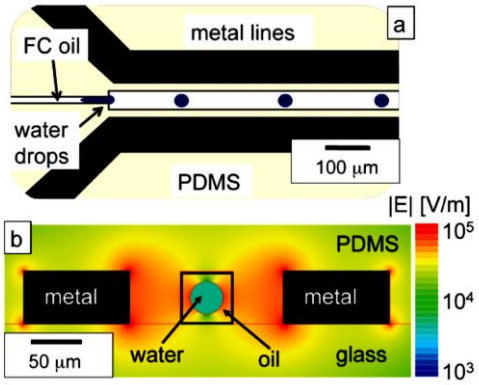

Figure 2.28: (a) A schematic of the microwave heater. The black lines represent the metal lines which are connected to the microwave source, the center fluid channel carries drops of water immersed in fluorocarbon (FC) oil, (b) a cross section of the microwave heater with a quasi-static electric field simulation superimposed is shown, with the electric field plotted on a log scale [120].

2.5.5 Other microwave applicators

Another detection system was based on a microwave coupled transmission line resonator integrated into an interferometer [121], designed for the detection of biomaterials in a variety of suspending fluids. This sensor was used to characterize polystyrene microspheres, living cells baker's yeast, and Chinese hamster ovary cells. A microwave heater at 20 GHz was designed in [122] for nanoliter scale liquids in a microfluidic system. The temperature was measured by reflection coefficient of the heater, as the water permittivity is dependent on the temperature. The performance of this heater was measured in which the rise of the temperature was found to be 30ºC per second.

CHAPTER 3 – THEORETICAL ASPECTS OF MICROWAVE LIQUID SENSING AND HEATING

This chapter briefly demonstrates the theoretical basis of relative permittivity of the liquids and how it is used to quantify a materials interaction with electromagnetic field, the microwave heating of liquids, microstrip resonators, and cavity perturbation theory.

3.1. Dielectric properties of liquids

In the 1830s, Faraday was the first observer of the dielectric properties of materials due to the capacity change of an empty capacitor. He defined its *specific inductive capacity*, which later became known as a material's relative permittivity and is symbolized ε [123]. The physical origin of e is the presence of polarisation charges, which become induced on the dielectric's surfaces which are oriented with their planes perpendicular to the electric field, as shown in figure 3.1.

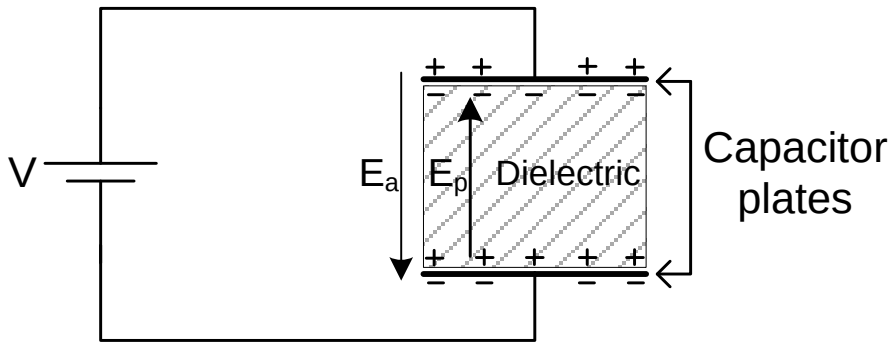

Figure 3.1: Dielectric material between the plates of capacitor.

The surface charge density on the capacitor plate can be given as:

$$\sigma_s = \varepsilon_o \varepsilon_r \frac{V}{d} \quad 3.1$$

where ε_o is the permittivity of free space ≈8.85 × 10^{-12} F/m, ε_r is the relative permittivity of the material, *d* is the distance between the two plates (assumed parallel). This behaviour arises since dielectric materials possess relatively few free charge carriers [124], which are mostly bound and cannot contribute to conduction. In contrast, by applying an external electric field, the charge carriers (electrons) are still bound with atoms but their cloud distorts. This reaction of a material to the applied electric field is called electronic polarization, whereby there is a physical shift δ of the centre of electronic charge. It the charge on the atom (or molecule) is q then the dipole moment p is:

$$p = q\delta \quad 3.2$$

Electronic polarization occurs in all materials and gives rise to low values of e (as found, for example, in most plastics). There are two main other types of polarization relevant to this thesis. These are **molecular polarization** in the bonds between atoms of material when a field is applied, and **orientational polarization** when the molecules of a liquid (or gas) have a permanent electric dipole moment (e.g. in water) and leads to large values of ε since an electric field causes the dipole moments to align.

The dipole moment per unit volume is expressed as $\bar{P}$, and for a linear and isotropic material can be defined as a function of the internal electric field intensity $\bar{E}$ within the dielectric as:

$$\bar{P} = \varepsilon_o \chi_e \bar{E} = \varepsilon_o (\varepsilon_r - 1)\bar{E} \quad 3.3$$

where χ_e is the electric susceptibility of the material. Furthermore, the electric flux density $\bar{D}$ can be defined as:

$$\bar{D} = \varepsilon_o \varepsilon_r \bar{E} = \varepsilon_o (1 + \chi_e)\bar{E} = \varepsilon_o \bar{E} + \bar{P} \quad 3.4$$

Ampère's law is used to describe the currents in material, also including the displacement current term, for ac fields at some frequency ω, via:

$$\nabla \times \bar{H} = \bar{J} + j\omega\bar{D} \quad 3.5$$

where *H* is the magnetic field intensity and *J* is the conduction current density which is given by:

$$\bar{J} = \sigma\bar{E} \quad 3.6$$

and σ is the conductivity of material. Equation 3.5 can be rewritten as:

$$\nabla \times \bar{H} = \sigma\bar{E} + j\omega\varepsilon_o\varepsilon_r\bar{E} = j\omega\left(\varepsilon_o\varepsilon_r - j\frac{\sigma}{\omega}\right)\bar{E} \quad 3.7$$

From Equation 3.7, the new expression of permittivity is:

$$\varepsilon = \varepsilon_o\varepsilon_r - j\frac{\sigma}{\omega} = \varepsilon_1 - j\varepsilon_2 \quad 3.8$$

ε is now called complex dielectric constant which consists of real and imaginary parts. In liquid material, the values of the real and imaginary parts of ε are related to the response of the electric dipoles of molecules to the applied alternative electric field. Liquids can be classified into two kinds: polar and non-polar liquids. In a polar liquid the molecules have permanent electric dipoles. The dipoles in a polar liquid can rotate physically to try to align themselves with the applied field, thus producing orientational or rotational polarization. This response of diploes due to the alternative electric field is called dielectric relaxation, and this specifically determines the values of real and imaginary parts of ε. The polarization of polar liquids tries to be in phase with applied sinusoidal electric field. However, on increasing the frequency of the applied field the polarization starts to lag the field and therefore there is a phase shift between the dipoles and the electric field. This phenomenon can be described by a relaxation time τ_t, which is the characteristic time over which alignment occurs when the field is suddenly applied [125].

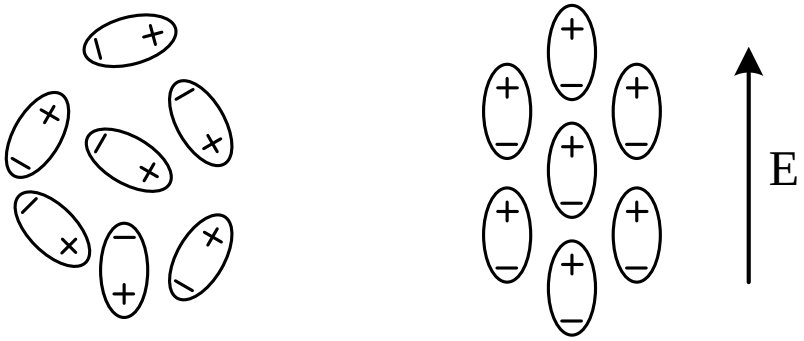

(a) (b)

Figure 3.2: The difference in dipoles' orientation within a polar liquid, with and without electric field. a- Dipoles are randomly orientated when there is no electric field. a- Dipoles become orientated parallel with the electric field, over a characteristic time known as the relaxation time τ_t.

The simplest relaxation model to describe the response of the polarization of the polar liquid with the frequency is the *Debye Relaxation* as in [125]-[127] which can be defined as:

$$\varepsilon(f) = \varepsilon_\infty + \frac{\varepsilon_s - \varepsilon_\infty}{1 + j2\pi f\tau} \qquad 3.9$$

where ε_s is the static permittivity (i.e. the value of $\varepsilon(f)$ at DC) and ε_∞ is the high frequency permittivity (i.e. the value of $\varepsilon(f)$ at infinite frequency).

The dielectric relaxation response of a polar liquid as a function of frequency, modelled using Debye theory, is shown in figure 3.2 and can be broken down into three regimes, as in [125]:

1- Low frequency response ($\omega\tau_t << 1$), where the dipoles can easily rotate and be the phase with applied electric field. This polarization gives the maximum value of the real part of the permittivity ε_1, where the imaginary part ε_2 is low and a there is a small amount power loss (in the form of heat).

2- Frequencies around the relaxation frequency ($\omega\tau_t \approx 1$), where the dipoles struggle to keep in the phase with electric field and there is significant relaxation. This decreases ε_1 and ε_2 is a maximum, giving maximum power loss.

3- High frequency response ($\omega\tau_t >> 1$), where the polarisation is 90º out of phase with the electric field. Both ε_1 and ε_2 are small.

The Debye parameters of several liquids [128] and [129] are given in table 3.1. Typical permittivity responses of several liquids are illustrated in figure 3.3 according to Equation 3.9 and parameters in table 3.1.

Table 3.1: Deybe relaxation model parameters of several liquids at 25 ºC.

Liquid	ε_s	ε_∞	τ *(ps)*
Hexane	1.89	1.89	5.8
Chloroform	4.7	2.5	7.96
Ethanol	24.3	4.2	163
Methanol	32.5	5.6	51.5
Water	78.36	5.16	8.27

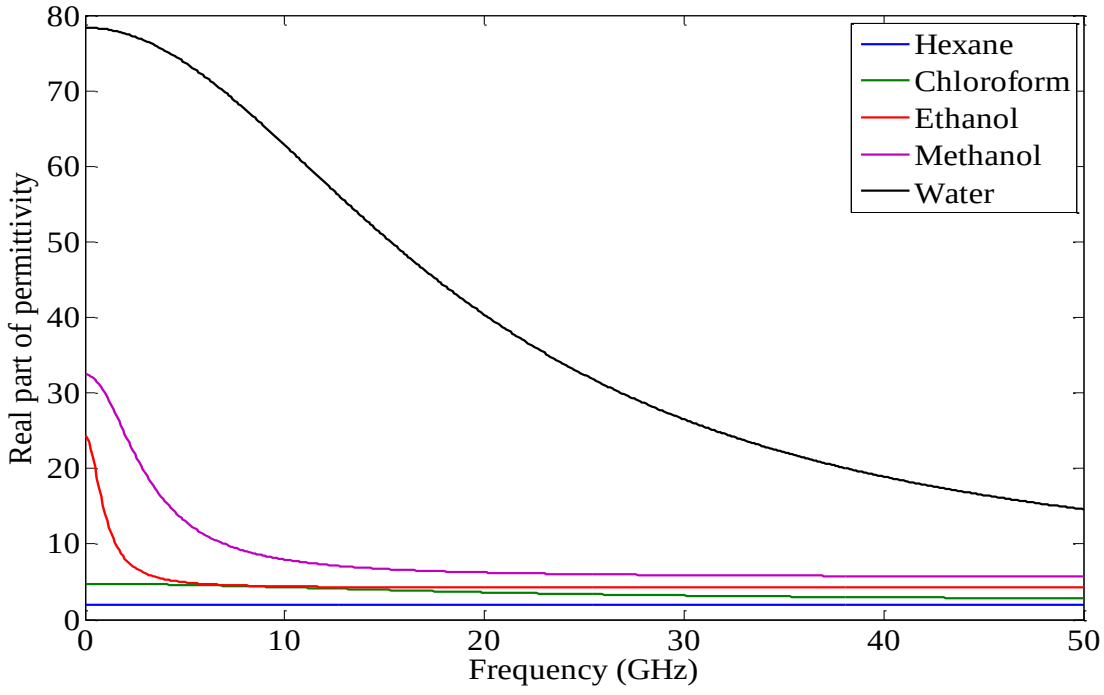

(a)

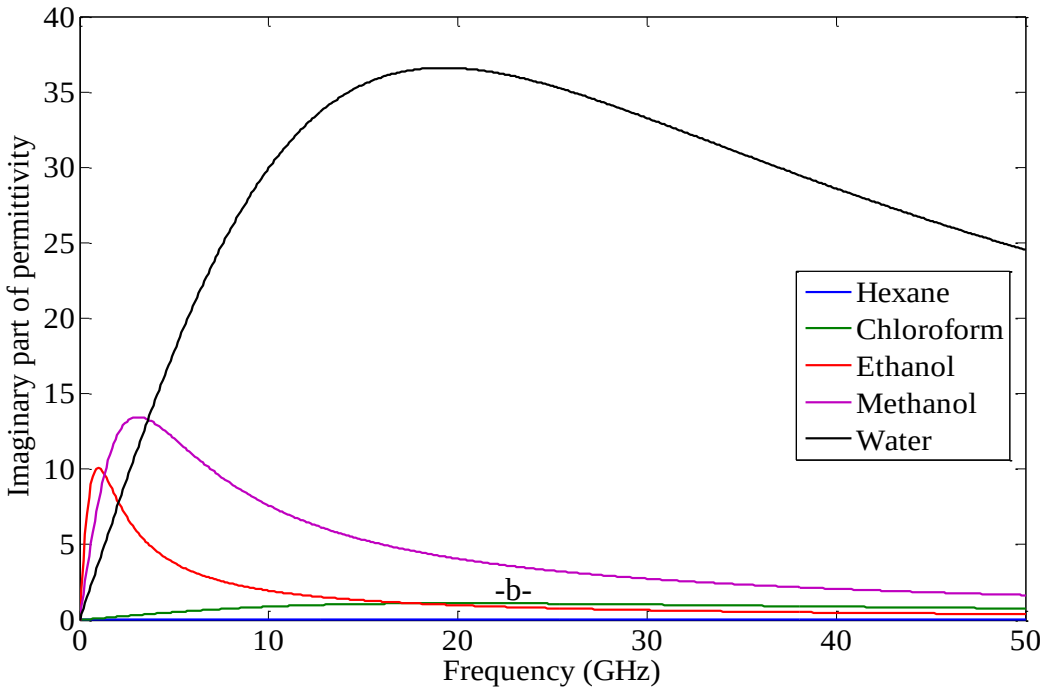

(b)

Figure 3.3: Debye relaxation of several solvents (hexane, chloroform, ethanol, methanol, and water) according to table 3.1 and equation 3.9. a- The real part of the permittivity ε_1, b- Imaginary part of the permittivity ε_2.

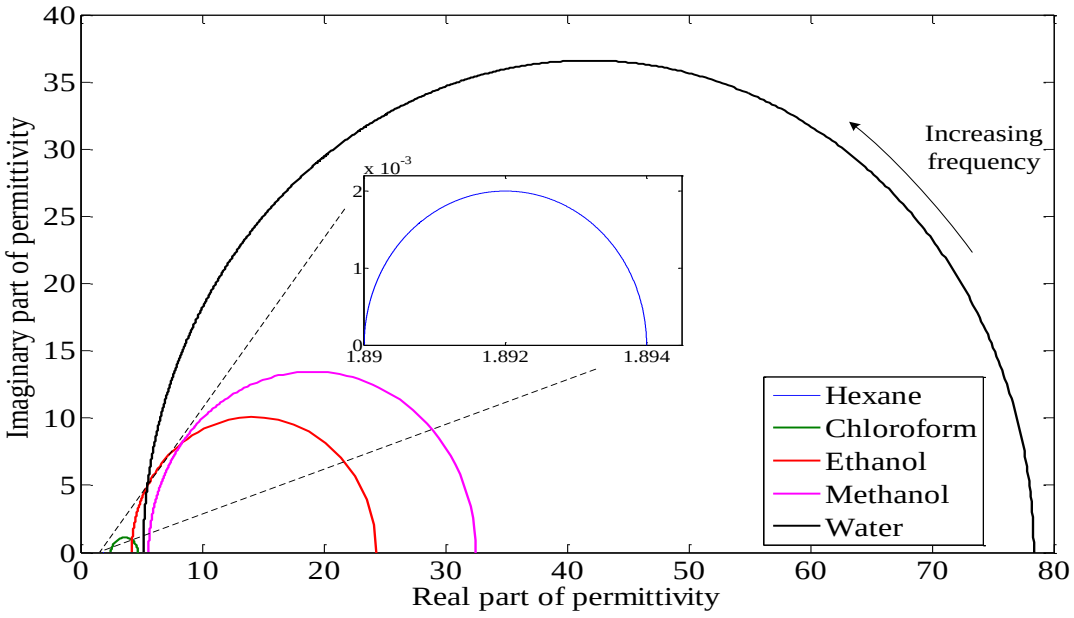

Figure 3.4: A Cole-Cole plot of ε_2 and ε_1 using of the data of the solvents in figure 3.3.

The complex permittivity of the polar liquids varies significantly with temperature due to the influence of heat on orientational polarization. Water has been adopted to provide an insight into the molecular properties with temperature and frequency as water plays a dominant role in many fields of scientific and industrial applications [130]-[135]. An increase of temperature decreases the strength and extent of the hydrogen bonding in water ([136] and [137]). This, in turn, causes the frictional forces between water molecules to reduce, meaning that the rotation of the water molecules becomes easier (i.e. τ_t decreases). Furthermore, the values of ε_s and ε_∞ both decrease.

Therefore, the variation of complex permittivity of the polar liquid with temperature and frequency can be defined as [138], [139]

$$\varepsilon(f,T) = \varepsilon_\infty(T) + \frac{\varepsilon_s(T)-\varepsilon_\infty(T)}{1+j2\pi f\tau(T)} \quad 3.10$$

and

$$\varepsilon(f,T) = \varepsilon_1(f,T) - j\varepsilon_2(f,T) \quad 3.11$$

where T is the temperature. The values of the Debye relaxation parameters for water at different temperature are shown in Table 3.2. The plots of both the real and imaginary parts of the relative permittivity as a function of frequency are illustrated in Figure 3.5, obtained by using Equation 3.10 and the data in Table 3.2. Moreover, the change in the complex permittivity of water with temperature at 2.45 GHz is shown in Figure 3.6.

Table 3.2: Debye relaxation model parameters for water at various temperatures [130].

T °C	$\varepsilon_s \pm \Delta\varepsilon_s$	$\varepsilon_\infty \pm \Delta\varepsilon_\infty$	$\tau \pm \Delta\tau$ (*ps*)
0	87.91±0.2	5.7±0.2	17.67±0.1
5	85.83±0.2	5.7±0.2	14.91±0.1
10	83.92±0.2	5.5±0.2	12.68±0.1
15	82.05±0.2	6.0±0.5	10.83±0.2
20	80.21±0.2	5.6±0.2	9.36±0.05
25	78.36±0.05	5.2±0.1	8.27±0.02
30	76.56±0.2	5.2±0.4	7.28±0.05
35	74.87±0.2	5.1±0.3	6.50±0.05
40	73.18±0.2	3.9±0.3	5.82±0.05
50	69.89±0.2	4.0±0.3	4.75±0.05
60	66.70±0.2	4.2±0.3	4.01±0.05

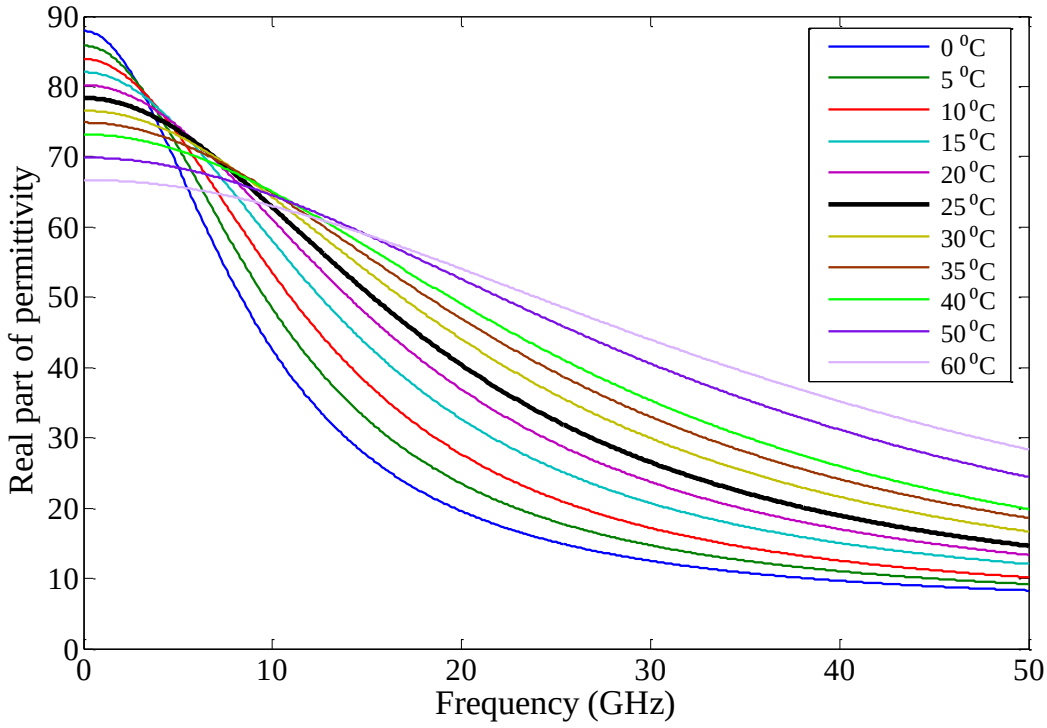

(a)

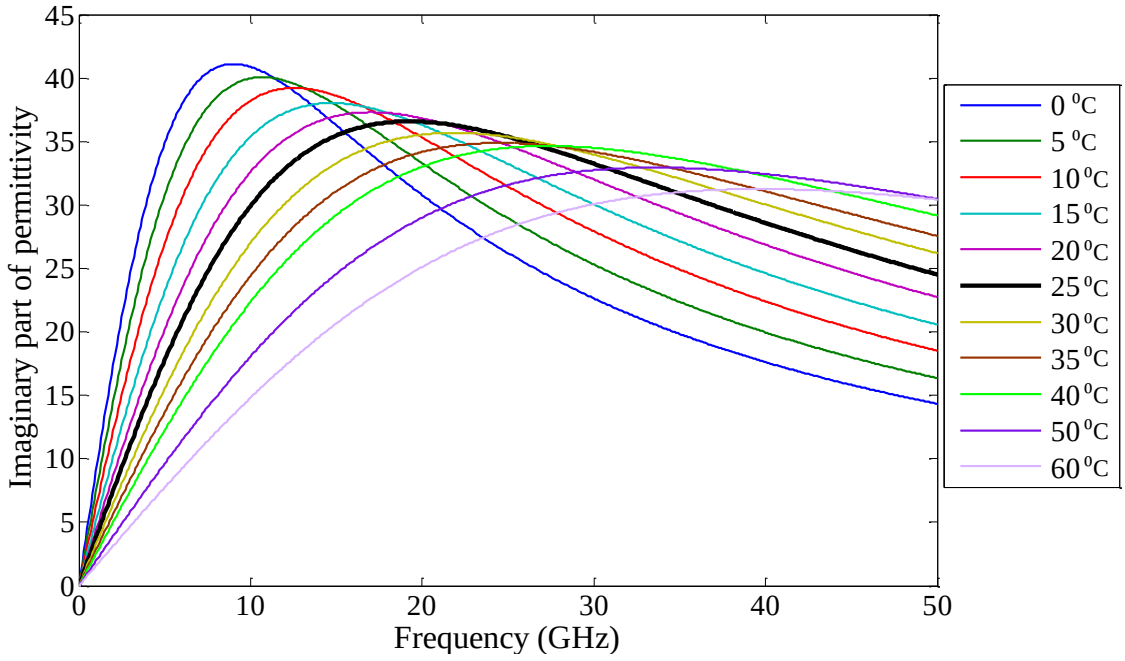

(b)

Figure 3.5: The complex relative permittivity of water as a function of frequency, with variation of the temperature from 0°C to 60°C and frequencies from DC up to 50 GHz. a- Real part, b- Imaginary part.

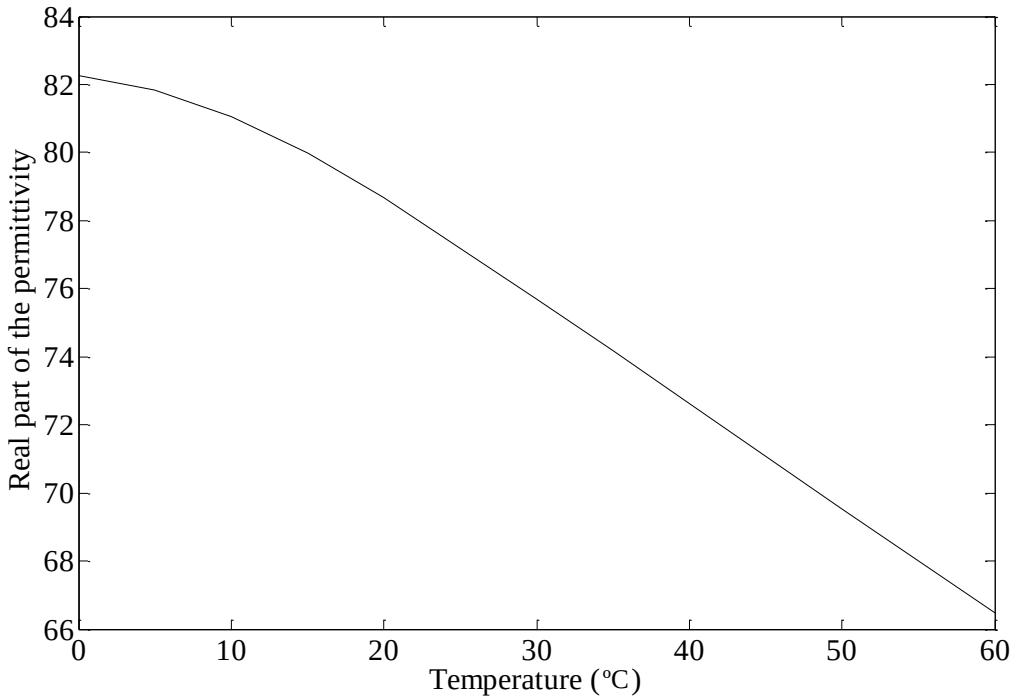

(a)

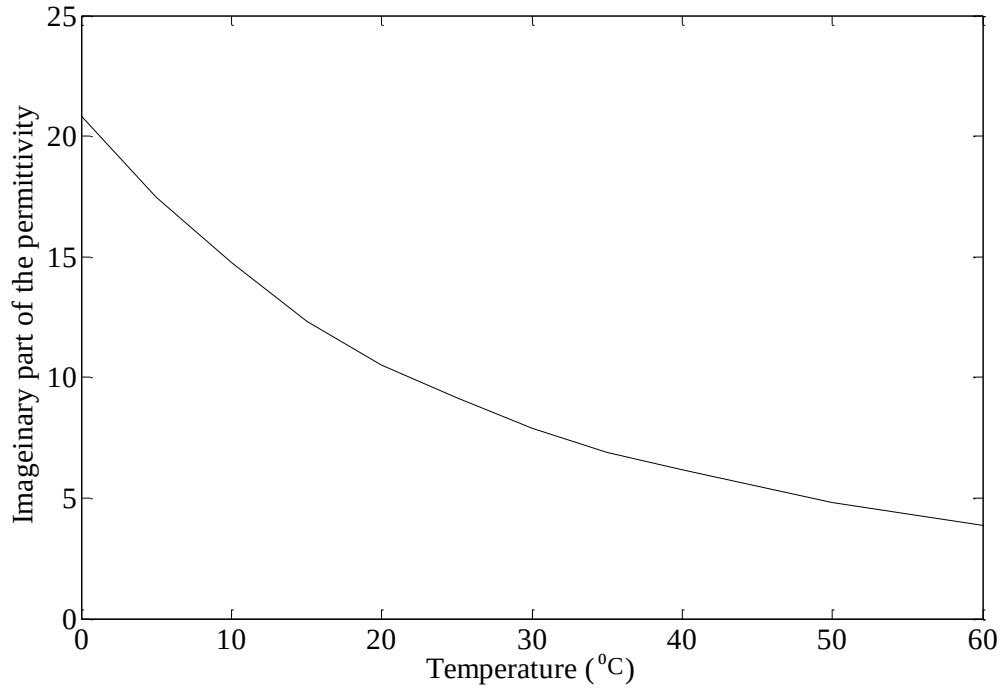

(b)

Figure 3.6: The complex relative permittivity of water as a function of temperature at 2.45 GHz. a- Real part, b- Imaginary part.

3.2. Perturbation theory

A number of references have illustrated the theory of perturbation of resonators or cavities [140]-[142]. The perturbation can be due to several causes, namely:

1- Small change in cavity resonator shape or volume.
2- Small change in cavity resonator material, such as the insertion of a small piece of dielectric or metallic material.

These factors will introduce small changes in the resonant frequency and quality factor of the cavity resonator, which can be employed to determine the complex permittivity of the small material sample in the case of material perturbation. The exact equation of the material perturbation can be found starting from Maxwell's time dependent equations:

$$\nabla \times \bar{E}_o = -j\omega_o \mu \bar{H}_o \quad 3.12$$

$$\nabla \times \bar{H}_o = j\omega_o \varepsilon \bar{E}_o \quad 3.13$$

$$\nabla \times \bar{E} = -j\omega(\mu + \Delta\mu)\bar{H} \quad 3.14$$

$$\nabla \times \bar{H} = j\omega(\varepsilon + \Delta\varepsilon)\bar{E} \quad 3.15$$

where $\bar{E}_o$, $\bar{H}_o$, and ω_o are electric field, magnetic field and resonant frequency, respectively, within the cavity before introducing the material sample. $\bar{E}$, $\bar{H}$, and ω are the corresponding values after introducing the material. From these [140], the final expression of the change in the resonant frequency due to the material perturbation is:

$$\frac{\omega - \omega_o}{\omega} = \frac{-\int_{V_o}(\Delta\varepsilon\bar{E}\cdot\bar{E}_o^* + \Delta\mu\bar{H}\cdot\bar{H}_o^*)dv}{\int_{V_o}(\varepsilon\bar{E}\cdot\bar{E}_o^* + \mu\bar{H}\cdot\bar{H}_o^*)dv} \quad 3.16$$

Also, the change of the quality factor can be found using:

$$\Delta Q = Q_o - Q = \frac{\omega_o \cdot U_{tot_o}}{P_o} - \frac{\omega \cdot U_{tot}}{P} \quad 3.17$$

where Q_o, U_{tot_o}, and P_o are the quality factor, total stored electromagnetic energy, and dissipated power, respectively, in the resonator before introducing the sample; Q U_{tot}, and P are the corresponding values after the sample has been introduced. However, in general, it is difficult to know $\bar{E}$ and $\bar{H}$, therefore, Equations 3.16 and 3.17 can be approximated depending on the structure of the cavity to give acceptable results. In the

following chapters these equations have been approximated and modified depending on the type of the resonator and the results have been supported with the simulated results to extract the value of the complex permittivity of the liquid sample.

3.2.1. Cavity perturbation by liquid sample

The properties of cavity resonators are often intentionally modified (i.e. perturbed) by the introduction of small material samples [140]. For dielectric samples placed in a region of high electric field this leads to a reduction in resonant frequency (associated with the polarization of the material) and a reduction in the *Q* factor (associated with the dielectric loss of the material). Together, these can be used to measure the complex relative permittivity of the sample. Figure 3.7 shows schematically the changes in resonant frequency and 3 dB bandwidth when a sample is introduced into the resonator, in our case a liquid which passes through a micro-capillary.

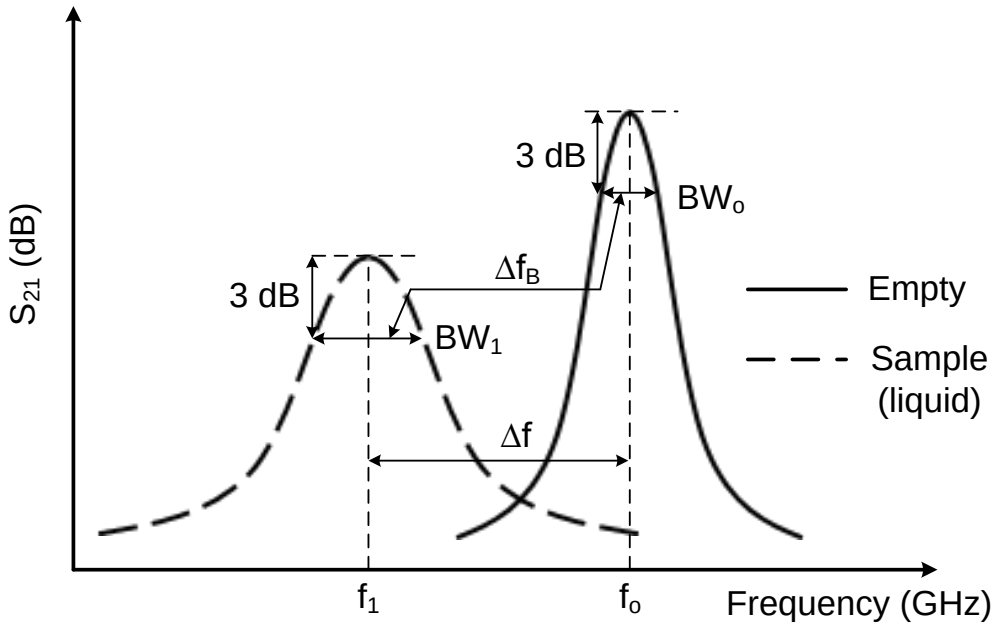

Figure 3.7. A typical response of power transmission of a cavity or resonator with and without sample (in this case a liquid).

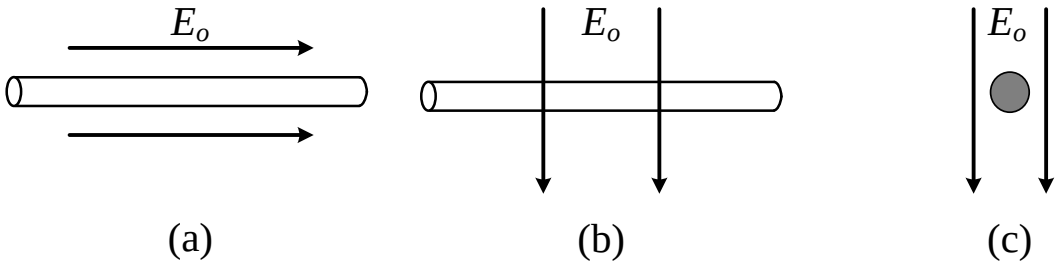

Figure 3.8: a- The applied electric field is parallel to the tube, b- The applied electric field is perpendicular to the tube, and c- the applied electric field to a sphere.

3.3. Sample shape effect on the internal electric field

We have three cases of the relationship between the applied electric field and the sample shape, of relevant to this thesis, as shown in Figure 3.8. In all three the magnitude of the internal electric field due to the applied filed E_o can be given in [143] as

$$E = \frac{E_o}{1+N(\varepsilon_r-1)} \tag{3.18}$$

where N is the dimensionless quantity called as the depolarization factor, which depends on the sample shape and the direction of the applied electric field. The depolarization factor in the case of the electric applied field is parallel to the tube is approximately equal to zero [143], therefore, the internal field will be

$$E \approx E_o \tag{3.19}$$

The second case is when the applied electric field is perpendicular to the tube as shown in Figure 3.8 (b), where $N \approx 1/2$ and the internal electric field is approximately written as

$$E \approx \frac{2E_o}{1+\varepsilon_r} \tag{3.20}$$

The final case is when the electric field is perpendicularly applied to sphere as shown in Figure 3.8 (c). In this case $N \approx 1/3$ and the approximated internal field is given in [143] as

$$E \approx \frac{3E_o}{2+\varepsilon_r} \tag{3.21}$$

3.4. Solution of the cavity perturbation equations

In this section, two cases of perturbation are presented and derived. The first case is when the liquid filled capillary is inserted in the two gaps of the Double Split Ring Resonator (DSRR) and the second case the perturbation of the Split Ring Resonator (SRR) when the micro-sphere passes through its gap inside liquid filled capillary.

3.4.1. DSRR with liquid filled capillary

In our sensor design, we use a microstrip resonant circuit consisting of a double split ring resonator, as shown in Figure 3.9. The capillary is fixed inside the gap regions; hence the capacitance of the gap regions is affected by the liquid, which in turn results in a perturbation of the resonator.

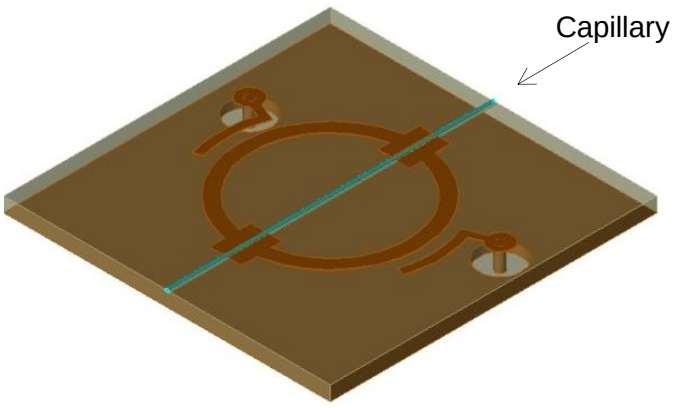

Figure 3.9. A schematic of the sensor which consists of a double split-ring microstrip resonator DSRR and a capillary.

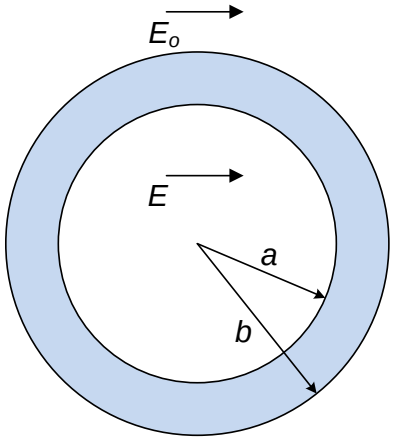

Figure 3.10. A cross section of the liquid-filled capillary in uniform electric field.

Figure 3.10 illustrates the cross section of a cylindrical capillary filled by a liquid sample in uniform applied electric field. Here, *a* and *b* are the inner and outer radii of the capillary, respectively. When the electric field is perpendicular to the axis of the capillary the relationship between the electric field intensity *E* within the liquid and the applied electric field E_0 is [28],

$$E = \frac{4\varepsilon_{rT}E_0}{(\varepsilon_{rT}+1)(\varepsilon_{rT}+\varepsilon_{rL})+(\varepsilon_{rT}-1)(\varepsilon_{rT}-\varepsilon_{rL})a^2/b^2} \quad 3.22$$

The resulting dipole moment for a liquid column of length *l* is

$$p \approx 2\pi\varepsilon_0 b^2 l \left(\frac{(\varepsilon_{rT}-1)(\varepsilon_{rT}+\varepsilon_{rL})+(\varepsilon_{rT}+1)(\varepsilon_{rT}-\varepsilon_{rL})a^2/b^2}{(\varepsilon_{rT}+1)(\varepsilon_{rT}+\varepsilon_{rL})+(\varepsilon_{rT}-1)(\varepsilon_{rT}-\varepsilon_{rL})a^2/b^2}\right) E_0 \quad 3.23$$

where ε_{rT} and ε_{rL} are the relative permittivity of the capillary (tube) and the liquid , respectively. The simplest equivalent circuit approximation of the resonator consists of parallel *L* and *C* components. The capacitor is formed from three parallel components: one due to charge storage on the gap regions (which are perturbed by the liquid), another due to charge storage on the circumference on the ring, and finally the capacitance to ground. The resonant frequency of the circuit is $f_r = 1/2\pi\sqrt{LC}$, and so any change in resonant frequency Δf_r due to a material perturbation is then

$$\frac{\Delta f_r}{f_r} = -\frac{1}{2}\frac{\Delta U}{U_{tot}} \quad 3.24$$

where ΔU is the change in energy of the resonator and U_{tot} is the total time averaged stored electromagnetic energy in the resonator. If a liquid sample is placed at the position of largest electric field magnitude E_0 and gains a dipole moment p, then

$$\Delta U = \frac{1}{2}Re(pE_0^*) \quad 3.25$$

The extraction of $\Delta f_r/f_r$ and $\Delta f_B/f_r$ as functions of complex relative permittivity of the liquid sample is detailed in appendix I, where Δf_B is the change in resonant bandwidth. Finally, $\Delta f_r/f_r$ and $\Delta f_B/f_r$ can be presented as:

$$\Delta f_r/f_r \cong f_1(\varepsilon_{rL}) \quad 3.26$$

$$\Delta f_B/f_r \cong f_2(\varepsilon_{rL}) \quad 3.27$$

where f_1 and f_2 are functions of ε_{rL} as shown in Equations 3 and 6 in appendix I. These two equations give approximate values of $\Delta f_r/f_r$ and $\Delta f_B/f_r$. The approximation comes from the fact that the electric field is not uniform around the tube and is also a function of the permittivity of the liquid. Equations 3.26 and 3.27 can be used to obtain approximate values of the complex relative permittivity of the liquid.

3.4.2. SRR with micro-sphere

Next a simple and approximate theory is developed to account for the change of electric dipole moment of the capillary within the gap when a microsphere is present. This allows us to calculate the resonator perturbation using first order perturbation theory [140], [28].

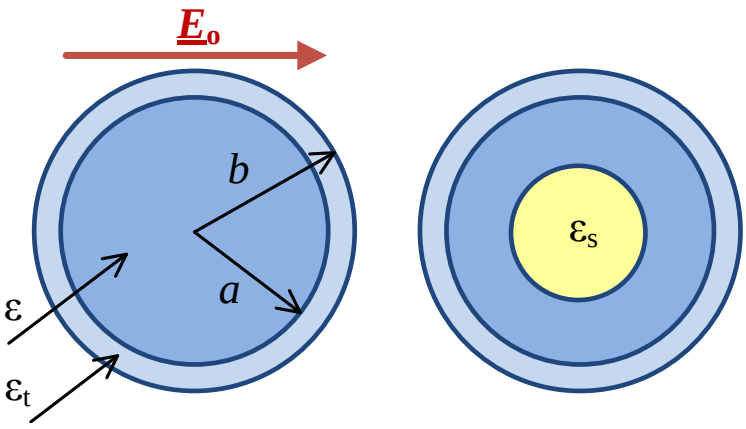

Figure 3.11: Cross section of the capillary filled by liquid, (a) without a microsphere, and (b) with a microsphere. The dimensions and relative permittivities of all regions are shown.

Consider first a liquid of complex relative permittivity ε completely filling a low loss tube (for example, glass, as in the experiments here). Referring to Figure 3.11(a), we define ε_t as the (real) permittivity of the tube, and b and a to be its outer and inner radii, respectively. The complex electric dipole moment p induced for a length ℓ of a filled

tube can be calculated analytically based on the direct solution of Laplace's equation for a quasi-static electric field as given in Equation 3.23 The perturbations measured experimentally in Chapter six are due to the presence of polystyrene microspheres within the gap region. Referring to Figure 3.11(b), we next analyse quantitatively how the presence of a small spherical particle, assumed to be homogeneous and of relative permittivity ε_s, modifies the electric dipole moment of a water filled tube and so leads to perturbations of the resonator parameters. If the sphere occupies a volume fraction β of the liquid within the tube (with $\beta << 1$), the complex permittivity of the liquid in the tube can be considered to have changed from ε to an effective value ε_{eff}. This is estimated from simple effective medium theory to be:

$$\varepsilon_{eff} \approx \varepsilon\left(1+\frac{3\beta(\varepsilon_s-\varepsilon)}{\varepsilon_s+2\varepsilon}\right) \qquad 3.28$$

where the derivation of Equation 3.28 is illustrated in appendix II. The resulting perturbation in electric dipole moment is then the difference

$$\Delta p \approx p(\varepsilon_{eff})-p(\varepsilon) \qquad 3.29$$

First order cavity perturbation theory states that a small change in electric dipole moment Δp due, for example, to a change in ε will result in changes (i.e. perturbations) in both the resonant frequency f and unloaded quality factor Q, given by the approximate formulae:

$$\Delta f = f_1 - f_0 \approx -f_0 \,\mathrm{Re}\left(\frac{\Delta p\, E_0^*}{4U}\right) \qquad 3.30$$

$$\Delta\left(\frac{1}{Q}\right) = \frac{1}{Q_1}-\frac{1}{Q_0} \approx -\mathrm{Im}\left(\frac{\Delta p\, E_0^*}{2U}\right) \qquad 3.31$$

Here the subscripts "1" and "0" denote the perturbed and unperturbed states of the resonator, respectively. The quantity U is the time averaged stored energy of the resonator in its unperturbed state, defined by

$$U = \frac{1}{2}\varepsilon_0 \oint_V E^2 dV \equiv \frac{1}{2}\varepsilon_0 E_0^2 \, V_m, \quad V_m = \oint_V \frac{E^2}{E_0^2} dV \tag{3.32}$$

where E_0 is the unperturbed electric field magnitude at the position of the tube and V_m is the mode volume of the resonator. This latter term quantifies the concentration enhancement of electric energy density at the position of the tube relative to the average electric energy density elsewhere in the resonator. Miniaturising the resonator by, for example, reducing the gap width or the ring radius, results in a decreased value of V_m and hence also a decreased value of U, thus causing larger changes in resonator parameters for a given perturbation Δp (i.e. enhanced sensitivity to the cause of the perturbation), which we will return to in more detail below. To gain a better physical understanding of how the presence of a microsphere affects the SRR, for the moment we ignore the presence of the glass tube (assumed to be very thin walled) and develop an approximate formula for Δp in the limit when the permittivity of the host liquid ε is much greater than that of the microsphere ε_s. This will indeed be the case when water ($\varepsilon \approx 78 - j12$ at 2.45 GHz) and polystyrene ($\varepsilon_s \approx 2.0$) are considered, respectively. Then, Equations 3.23, 3.28-3.31 reduce to the very simple results, where the derivation of Equation 3.33 is shown in Appendix III:

$$\Delta p \approx -\frac{6\pi \ell a^2 \beta}{\varepsilon} \varepsilon_0 E_0 \tag{3.33}$$

$$\frac{\Delta f}{f_0} \approx +\frac{3\beta V_t}{V_m} \mathrm{Re}\left(\frac{1}{\varepsilon}\right) \tag{3.34}$$

$$\Delta\left(\frac{1}{Q}\right) \approx +\frac{6\beta V_t}{V_m} \mathrm{Im}\left(\frac{1}{\varepsilon}\right) \tag{3.35}$$

where $V_t = \pi \ell a^2$ is the physical volume of the sample within the gap region. From this we see that on introducing a polystyrene microsphere into the gap region, the resonant frequency increases, but that the Q factor decreases (i.e. the microwave loss increases). This is illustrated further in Figure 3.12, where we consider the effects of the presence of a microsphere on the voltage transmission coefficient S_{21} in the frequency domain, with perturbation calculated using both Equation 3.23, 3.28, 3.29 and the simplified formula 3.33.

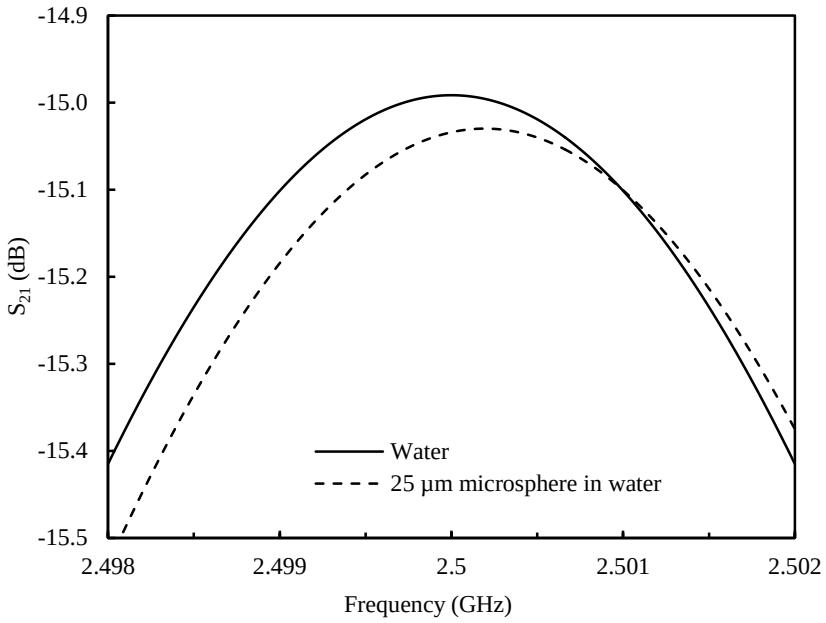

Figure 3.12: The calculated transmission spectrum of the SRR with (dotted) and without (solid) a plastic microsphere in the gap region. Both resonant frequency and microwave loss increase with the presence of the sphere. In this calculation, the SRR is assumed to have a Q factor of 200 and a resonant frequency of 2.5 GHz when unperturbed by the microsphere. The microsphere is assumed to occupy a volume fraction of 0.1 of the gap volume, and the ratio of tube volume to mode volume is 0.02. The microsphere permittivity is assumed to be 2 and the water permittivity 78 – j12. In this limit when $\varepsilon >> \varepsilon_s$*, the simplified analysis using Equation 3.33 for* Δp *gives almost identical results to the more rigorous analysis using Equations 3.23, 3.28, 3.29.*

This can be understood by referring to Figure 3.13, where we plot the electric field intensity E^2 in the space in an around a sphere placed in a uniform electric field when (a) the sphere's permittivity is much less than that of its host liquid (as is the case here), and (b) when the sphere's permittivity is much greater than that of its host (as would be the case for a metal sphere). In (a), we note that the intensity is enhanced within the host liquid adjacent to the equatorial regions of the sphere, whilst in (b) it is enhanced adjacent to the polar regions. In both cases, this intensity enhancement increases the overall dielectric loss. However, in (b) there is an increase in electrical potential energy owing to the strong polarisation of the sphere, so the resonant frequency would decrease. In (a), since the sphere is of a low permittivity material, its polarisation is small and overall the electric potential energy is reduced, resulting in an increased resonant frequency.

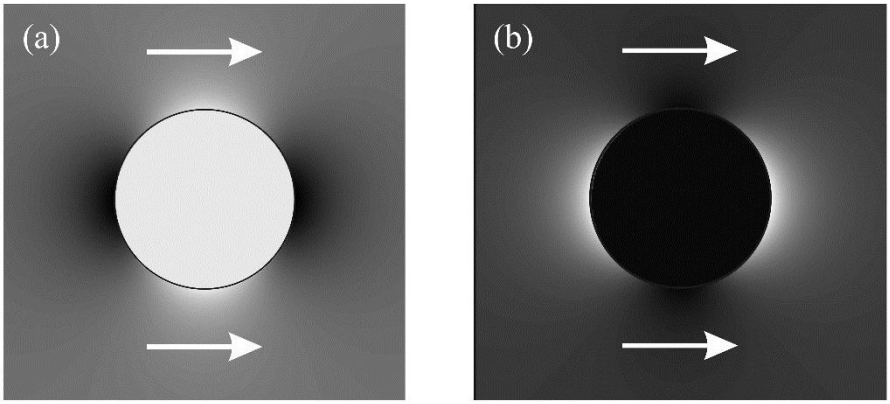

Figure 3.13: The calculated electric field intensity E^2 around a sphere when (a) its permittivity is much less than that of its host liquid, and (b) much greater than that of its host (the arrows show the direction of the applied field). The enhancement of E^2 in the host in both cases gives rise to increased losses but in (a) the overall electric potential energy is reduced, giving rise to an increased resonant frequency.

3.5. Microwave heating

Many dielectric materials can be successfully heated by using microwave electromagnetic energy. This essential technique of "microwave heating" has variety applications in industrial, scientific, and medical fields. The microwave heating method differs depending on the material properties such as shape, size, dielectric constant, and the nature of the microwave equipment used [144]. The mechanism of heating liquid materials is the dipolar loss in which the dipole moments attempt to align themselves with electric field. As discussed in the previous section, the viscosity of the liquid causes energy to be dissipated as heat into the liquid [145]. This gives microwave heating many advantages over conventional heating, which can be summarized in three fundamental points:

1- Preferential heating capability where the electromagnetic energy can be delivered to the sample in microfluidic system without heating other parts of the system.
2- Non-contact heating in which the sample can be heated and cooled faster than the other traditional heating methods.
3- The heating is volumetric, rather than from the surface inwards.

We will choose water as an exemplar polar liquid to explain the mechanism of microwave heating. The water molecule consists of an electronegative oxygen atom and

two (electropositive) hydrogen atoms. The 105° bond angle causes the water molecule to have a strong, permanent electric dipole moment. This results in water molecules rotating when an electric field is applied. Intermolecular forces result from hydrogen bonds formed by the oxygen atom of one water molecule with the hydrogen atoms of neighbouring molecules [7]. When a sinusoidal electric field is applied to water, the water dipoles rotate at the same frequency as the applied electric field. Friction results from this rotation to generate heat, wherever the electric field is applied. The extent of loss (or heating) is quantified by the imaginary part of the relative permittivity ε_2, which is often called the dielectric loss factor. This parameter is function of frequency and temperature, as described in section 3.1. A displacement current is generated due to the response of the dipoles to the applied electric field according to Maxwell-Ampère law.
The volumetric power dissipation within the sample can be written as the volume integral of the work per unit volume *EJ*, giving for a polar liquid:

$$P_{av} = \frac{1}{2}\omega\varepsilon_o\varepsilon_2 \int (E^* \cdot E) dV \qquad 3.36$$

For water the frequency band of heating is from 0.5 GHz up to 50 GHz. It is most efficient at around 20 GHz. A frequency of 2.45 GHz is used for microwave ovens so that there is a sufficiently large ε_2 but the frequency is still own enough to allow sufficient penetration of the microwave electric field into the foodstuff (at least a few cm). Above 50 GHz the molecular dipoles cannot orient with the applied electric field and no heating occurs.

3.6. Microstrip resonator

3.6.1. Microstrip structure

The microstrip line is one of the most popular types of planar transmission lines [140]. It can be fabricated by either by electro-deposition or by rolling and can be easily miniaturized and integrated with both passive and active microwave components. Microstrip structures consist of three parts: metal strip, dielectric, and ground plane, as shown in Figure 3.14. The fields of microstrip line are quasi-TEM if the dielectric thickness is very thin ($h \ll \lambda$). Then the phase velocity and propagation constant can be written as:

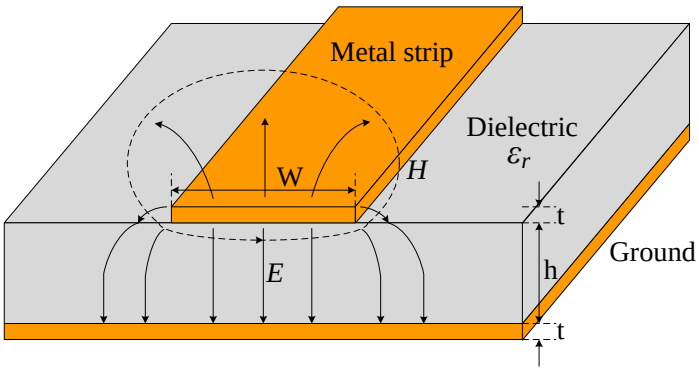

Figure 3.14: Microstrip transmission line, showing electric (solid) and magnetic field lines (dotted).

$$v_p = \frac{c}{\sqrt{\varepsilon_e}} \tag{3.37}$$

$$\beta = k_o\sqrt{\varepsilon_e} \tag{3.38}$$

where ε_e is the effective dielectric constant of the microstrip line, as some of the electric fields is in the space outside of the dielectric region. No analytic form of effective dielectric constant exists, but a useful approximation when the substrate thickness *h* is much smaller than the line width *W* is [140]:

$$\varepsilon_e \approx \frac{\varepsilon_r+1}{2} + \frac{\varepsilon_r-1}{2} \cdot \frac{1}{\sqrt{1+12h/W}} \tag{3.39}$$

From this it is clear that the effective dielectric constant is a weighted average of the air and microstrip dielectric regions, dependent on the cross sectional geometry. The characteristic impedance of the microstrip line can also be estimated given the following equation if the dimensions are known [140]:

$$Z_o = \begin{cases} \frac{60}{\sqrt{\varepsilon_e}} \ln\left(\frac{8h}{W} + \frac{W}{4d}\right) & for\ W/d \leq 1 \\ \frac{120\pi}{\sqrt{\varepsilon_e}[W/d + 1.393 + 0.667\ln(W/d + 1.444)]} & for\ W/d \geq 1. \end{cases} \tag{3.40}$$

3.6.2. Coupling between microstrip lines

Coupled microstrip line is used to deliver the energy to the microstrip resonator. The configuration of a pair of coupled microstrip lines is shown in Figure 3.15. There are two quasi -TEM modes, which are the even and odd modes. In the even mode, the two

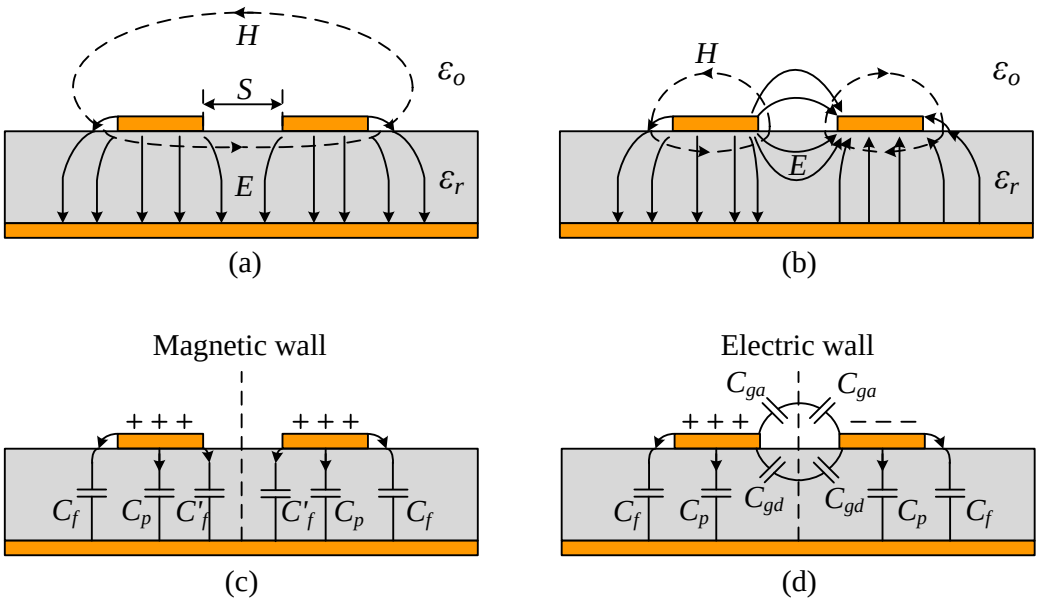

Figure 3.15: Configuration of a pair of coupled microstrip lines. (a) Field distributions of even mode. (b) Field distribution of odd mode. (c) Capacitance of even mode. (d) Capacitance of even mode.

microstrip lines carry parallel currents, forming a magnetic wall between them. Conversely, the odd mode occurs when the current of the first microstrip line is in opposite direction of the second microstrip, forming an electric wall between them, as shown in Figure 3.15. Referring to this figure, the total even mode capacitance C_e can be written as:

$$C_e = C_p + C_f + C'_f \tag{3.41}$$

where C_p is the parallel plate capacitor between the microstrip line and the parallel part of the ground, C_f is the fringe capacitance , and C'_f the fringe capacitance of the coupling side, as shown in Figure 3.15. Similarly, the odd mode capacitance C_o can be written as:

$$C_o = C_p + C_f + C_{gd} + C_{ga} \tag{3.42}$$

where C_{gd} and C_{ga} are the capacitances between the two microstrip lines (in the gap) across the dielectric and air, respectively.

3.6.3. Microstrip resonators

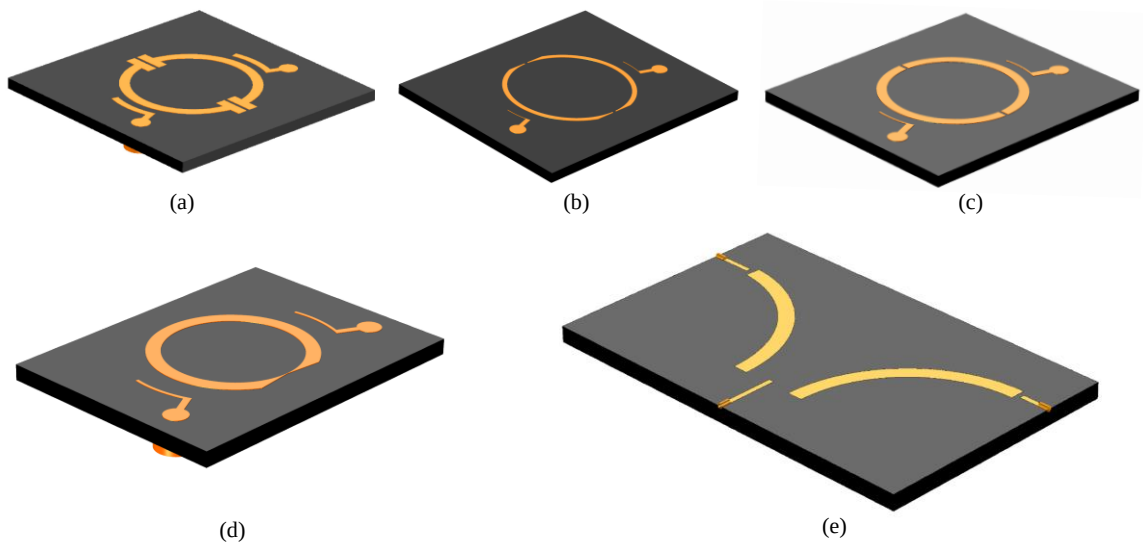

Figure 3.16: Several types of microstrip resonator that were designed in next chapters are shown. (a), (b), and (c) Double split ring resonator DSRR. (d) Split ring resonator SRR. (d) Dual mode resonator DMR.

Several types of microstrip resonators were design and realization in this thesis to build microfluidic sensors for different applications, as illustrated in Figure 3.16. The proposed resonators are double split ring resonator DSRR, split ring resonator SRR, and dual mode resonator DMR. The details of their designs and fabrications are explained in detail in the following chapters. The choice of using the microstrip structure is because of many advantages, which can be summarized as: the low cost of realization, fast time fabrication, ability to miniaturize the structure to the micro scale, easy adaptation with microfluidic systems, and low loss (giving acceptable quality factors of a few hundred).

3.6.4. Input/output couplings

The two port resonator connected to the network analyser can be presented by the equivalent circuit shown in Figure 3.17, where the resonator is modelled by RLC series circuit and g_1 and g_2 are the coupling coefficients of the input and output microstrip coupling lines, respectively. The coupling can be either mostly inductive or mostly

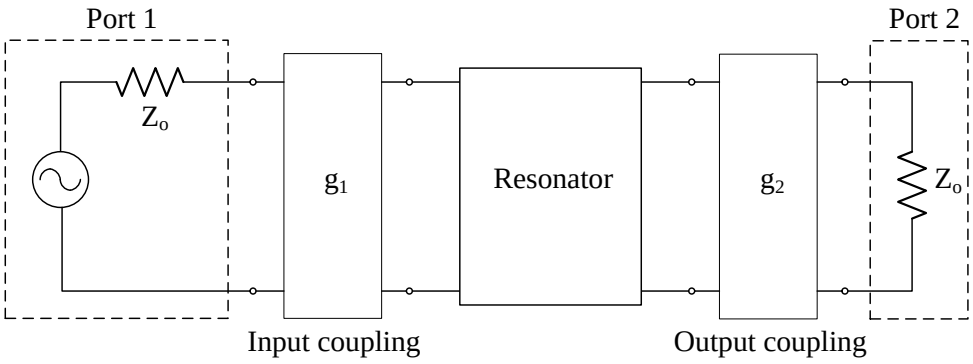

Figure 3.17: Equivalent circuit of the resonator connected to two ports of a network analyser. The coupling is represented by two blocks g_1 and g_2.

capacitive, depending on the shape of the coupling line and the distance between it and the resonator. In case of mostly inductive coupling, the coupling circuit can be approximated as shown in Figure 3.18, where the microwave resonator and the coupling line can be presented as transformer which has the transfer function shown in Figure 3.18. The transfer matrix of the full equivalent resonator circuit of Fig. 3.17 is found using

$$\begin{pmatrix} a & b \\ c & d \end{pmatrix} = \pm \begin{pmatrix} 0 & -j\omega m_1 \\ \frac{1}{j\omega m_1} & 0 \end{pmatrix} \cdot \begin{pmatrix} 1 & Z \\ 0 & 1 \end{pmatrix} \cdot \begin{pmatrix} 0 & -j\omega m_2 \\ \frac{1}{j\omega m_2} & 0 \end{pmatrix} = \pm \begin{pmatrix} m_1/m_2 & 0 \\ \frac{Z}{\omega^2 m_1 m_2} & m_2/m_1 \end{pmatrix} \quad 3.43$$

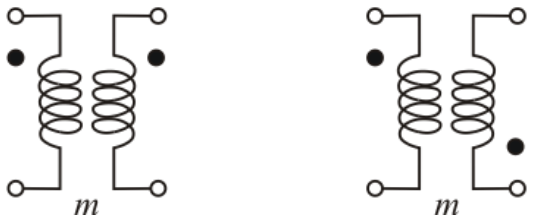

$$\begin{pmatrix} 0 & -j\omega m \\ \frac{1}{j\omega m} & 0 \end{pmatrix} \qquad \begin{pmatrix} 0 & j\omega m \\ -\frac{1}{j\omega m} & 0 \end{pmatrix}$$

Figure 3.18: Transfer matrices for the magnetic coupling loops, which act as transformers with one arm representing the coupling loop, the other the resonator. Note the sign change depending on the sense (i.e. phase) of the loop windings.

where m_1 and m_2 are the mutual inductances at ports 1 and 2, respectively, of the resonator and the positive sign is used for coupling loops wound in the same sense, the negative sign is used for coupling loops wound in the opposite sense. The series impedance *Z* of the resonator is given as:

$$Z = R + j\omega L + \frac{1}{j\omega C} = R + j\omega_0 L\left(\frac{\omega}{\omega_0} - \frac{\omega_0}{\omega}\right) \qquad 3.44$$

where $\omega_0 = \frac{1}{\sqrt{LC}}$ is the resonant frequency. Equation 3.20 can be simplified as

$$Z \approx R + 2jL\,\Delta\omega \approx R\left(1 + 2j\frac{\omega_0 L}{R}\,\frac{\omega - \omega_0}{\omega_0}\right) \approx R\left(1 + 2jQ_0\,\frac{\omega - \omega_0}{\omega_0}\right) \qquad 3.45$$

where $\Delta\omega = \omega - \omega_0$, for frequencies close to resonance (i.e. $\Delta\omega << \omega - \omega_0$, an almost exact approximation for a high *Q* resonator), and $Q_0 = \omega_0 L / R$ is the unloaded quality factor of the resonator. Hence, the four elements of the coupled resonator's transfer matrix are:

$$a = \pm\frac{m_1}{m_2}, \quad b = 0, \quad c = \pm\frac{Z}{\omega^2 m_1 m_2} \approx \frac{R}{\omega^2 m_1 m_2}\left(1 + 2jQ_0\,\frac{\omega - \omega_0}{\omega}\right), \quad d = \pm\frac{m_2}{m_1}$$

Then the transmission coefficient S_{21} can be given in terms of the transfer matrix elements as in Equation 3.46.

$$S_{21} = S_{12} = \pm\frac{2\sqrt{g_1 g_2}}{g_1 + g_2 + 1 + 2jQ_0\,\frac{\omega - \omega_0}{\omega_0}} \rightarrow |S_{21}|^2 = \frac{4g_1 g_2}{(g_1 + g_2 + 1)^2 + 4Q_0^2\left(\frac{\omega - \omega_0}{\omega_0}\right)^2} \qquad 3.46$$

and the coupling coefficients at ports 1 and 2 are defined by

$$g_1 = \frac{\omega_0^2 m_1^2}{Z_0 R} = \frac{\omega_0 m_1^2 Q_0}{L}, \quad g_2 = \frac{\omega_0^2 m_2^2}{Z_0 R} = \frac{\omega_0 m_2^2 Q_0}{L}$$

In the case of symmetric coupling (i.e. $g = g_1 = g_2$) and at resonant frequency, Equation 3.46 can be rewritten as:

$$|S_{21}(f_o)| = |S_{12}(f_o)| = \frac{2g}{1+2g} \qquad \text{or} \qquad P_o = \left(\frac{2g}{1+2g}\right)^2 \tag{3.47}$$

and

$$P(f) = \frac{P_0}{1 + 4Q_L^2\left(\frac{f - f_0}{f_0}\right)^2} \tag{3.48}$$

where P_0 is the peak power at resonance.

3.6.5. Quality factor

Three types of losses determine the quality factor of the microstrip resonator. These parameters are: conduction loss, dielectric loss, and radiation loss [146]. Therefore the quality factor of the microstrip resonator can be expressed as:

$$Q_o = \omega_o \frac{U}{P_T} = \omega_o \frac{U}{P_c + P_d + P_r} \tag{3.49}$$

where Q_o is unloaded quality factor, U is the stored energy in the resonator, P_T is the total dissipated power in the resonator which consists of the dissipated power in conductors P_c, in dielectric P_d, and in radiation P_r. In some cases, the microstrip resonator is put inside a metallic box to increase the quality factor. In this case, the loss of the wall surfaces of the box is considered in the quality factor determination. P_c and P_d depend on the conductor materials and the dielectric, respectively. Moreover, the quality factor also depends on the frequency, the dielectric thickness, and the conductor thickness and width. The measured quality factor, is called the loaded quality factor Q_L in which the external circuits of the input and output coupling are taken into account. Therefore the Q_L can be defined as:

$$\frac{1}{Q_L} = \frac{1}{Q_o} + 2 \cdot \frac{1}{Q_{ex}} \tag{3.50}$$

where Q_{ex} is the quality factor of the external circuit of the input or output circuit (identical coupling circuits), and Q_L the quality factor that can be measured directly by network analyzer. Equation 3.50 can be written in term of the coefficient coupling g as:

$$Q_o = Q_L(1 + 2\mathrm{g}) \qquad 3.51$$

g can be defined as the ratio of the power dissipated in the external circuit to the power dissipated in the resonator and can be classified into three cases: critical coupling when g = 1, where the power dissipated in the external circuit is equal to the power dissipated in the resonator; under-coupling when g < 1, and over-coupling when g > 1. From Equations 3.47 and 3.51, Q_L can be given as:

$$Q_L = Q_o(1 - |S_{21}(f_o)|) \qquad 3.52$$

and so the conversion of the loaded Q to unloaded Q is achieved by using the voltage transmission coefficient at resonance (i.e. the insertion loss).

CHAPTER 4 - SOLVENTS SENSING USING MICROSTRIP SPLIT RING RESONATORS

In this chapter a new type of the microwave microfluidic sensor has been proposed. The concept of the design is based on a microstrip microwave resonator in which the resonant frequency and quality factor are perturbed by the liquid sample. The resonant microwave measurements can give more accurate results with a large dynamic range when compared with broadband measurements. The measurements do not need careful calibration as the results are the difference between two states; i.e., with and without the sample, which increase the sensitivity, reduced systematic errors and reduces the time for measurement.

To achieve high accuracy, sensitivity and simplicity of analysis, the resonant circuits of the sensors should have a high quality factor (Q) and small size. The small size means that the sample filling factor must be high (i.e. a high fraction of the electric field energy will be in the sample), so the resonator will be more sensitive to the presence of the sample. High Q can be achieved using cavity-type resonators (typically $Q \approx 10^4$), but this also means large size and mass in the frequency range 1-10 GHz. One of the big issues in designing and developing resonant sensors based on lumped element circuits (which can be much more compact) is the problem of achieving a suitably high Q factor. From the fundamental definition of Q as the ratio of stored to dissipated energy, the conductor quality factor is then seen to the ratio of field volume to exposed surface area, which is proportional to the typical "size" of the resonator (e.g. its diameter). A size reduction then leads to the inevitable reduction in Q. However, as long as the Q

factor remains above about 100, reliable and accurate measurements of dielectric properties are possible, as will be demonstrated in this chapter.

Split ring resonators are compact structures that have found many sensing applications from microwave through to THz applications [147], [148]. These, like the sensor circuit we use here, are lumped element circuits whose size is not wavelength limited. The capacitance is determined by the gap and the surface of the ring adjacent to the gap. The inductance is provided by the ring. Although the *Q* factor is not as high as for cavity-type resonators, since it is a small planar device, this is compensated by the reduced resonator volume which gives a much increased sample filling factor; this maintains a high sensitivity for dielectric measurements. In our work we need to interrogate planar microfluidic circuits, so we have decided to employ a two-gap split ring resonator, i.e. the double split ring resonator (DSRR). The novel structure has many benefits over the more conventional, single gap split ring resonators (SRR) for our microfluidic application in that the microwave circuit is all in the same plane as the microfluidic circuit, and the two gaps also allows us to measure properties such as fluid velocity and to interrogate multiphase flow (where there will be discrete fluid packets of more than one type of liquid, or solid:liquid flows, for example, microspheres in solution).

Moreover, multi- phase liquids characterization and measurements are required in many applications medicine and chemistry, including features such as the length, volume, speed and dielectric properties of the segments. A new approach using the DSRR is presented in this chapter to characterize and measure multi-phase liquids properties, where the previous works use the optical and electrical approaches to detect the segments' properties, as has been previously described in Section 2.3. Two microfluidic DSRR models C and D are proposed in Section 4.4 for measuring multi-phase liquids with high degree of accuracy.

4.1. Brief theory and concepts

Many modes can be supported by ring resonators such as the double split ring resonators considered here. The excitation of these modes depends on the perturbation and coupling methods [149], [150].

4.1.1. Regular resonant modes

A regular mode is obtained by applying symmetric input and output feed lines on the annular ring element [149], [150]. The positions of maximum electric field for the first two modes are shown in Figure 4.1. Fundamentally, the ring involves two half-wavelength linear resonators connected in parallel. Resonance occurs when the ring circumference is an integral multiple of the guided wavelength.

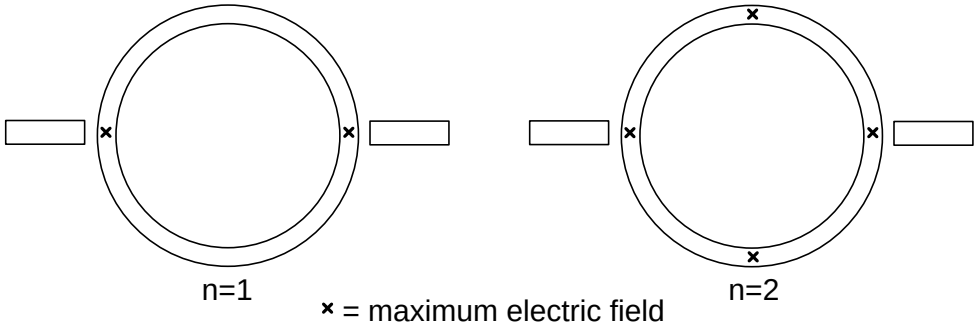

Figure 4.1: Maximum electric field points for the first two modes.

4.1.2. Split Perturbations (two gaps)

Hence the odd modes in the double split ring resonator disappear while the even modes remain unaffected. Figure 4.2 can be used to explain this mode phenomenon. This figure displays the positive maximum and negative maximum electric field distribution on the double split ring resonator. The first situation occurs when the length of half of the ring and the electric length of one of the gap capacitors is equal to the wavelength, while the second situation happens when the length of the half ring equals the wavelength. If the capacitance between the two edges of the ring resonator is neglected, the resonant frequency will be determined by the ring length. By adding the effect of the gap capacitors, the resonant frequency will reduce due to the variation in the electrical length of the ring resonator [151].

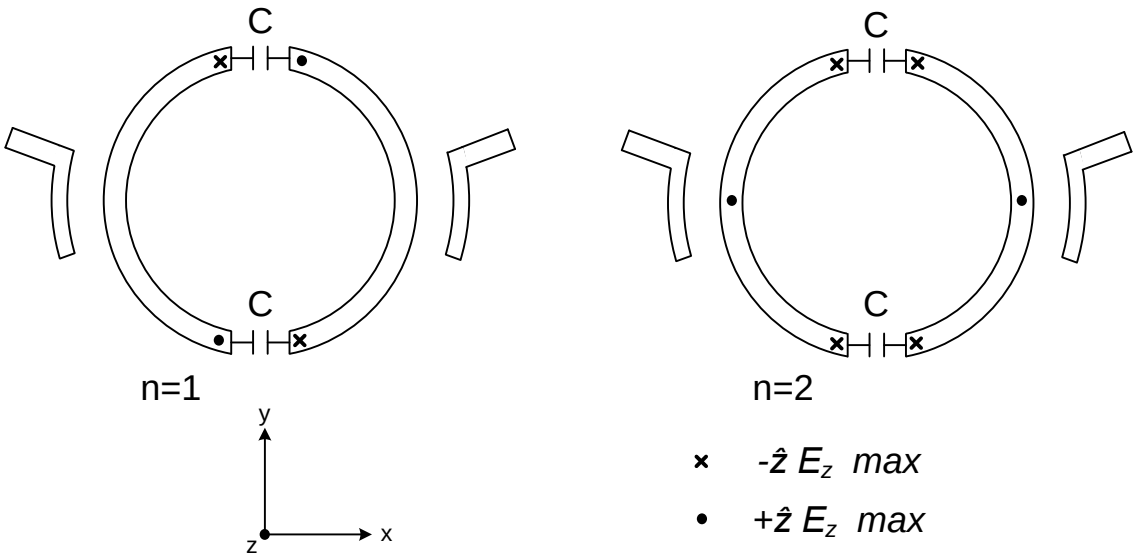

Figure 4.2: Mode chart for the DSRR: (a) first situation at odd mode, (b) second situation at even mode (see the text for full description).

The value of this capacitor depends on the thickness of the ring, the width of the gap, the ring width, and the material inside the gap. The capillary is inserted into the gap between the ends of the rings as illustrated in Figure 4.4, which makes the capacitance associated with the gap regions highly dependent on the permittivity of the capillary and the liquid inside it.

4.1.3. Coupling

The input and output power couplings of the resonator are mostly inductive owing to their positioning at a magnetic field antinode, with a smaller degree of capacitive coupling arising from the fact that they are extended structures and are made of open-circuit, microstrip sections. Circuit analysis of the resonator in the limit of high Q (i.e. much larger than 1, in practice above than 10) gives the following results for the transmission coefficient S_{21} and the resulting power transmission coefficient $P(f)$ in the frequency domain ($f = \omega/2\pi$) [152]

$$S_{21}(f) = \frac{2\sqrt{g_1 g_2}}{1+g_1+g_2+2jQ_0\frac{f-f_0}{f_0}} \qquad 4.1$$

$$\rightarrow \quad P(f) = |S_{21}|^2 = \frac{4g_1 g_2}{(1+g_1+g_2)^2+4Q_0^2\left(\frac{f-f_0}{f_0}\right)^2} \qquad 4.2$$

The dimensionless *coupling coefficients* are defined in terms of the unloaded quality factor Q_o by

$$g_1 = f_0 k_1^2 Q_0 \,, \qquad g_2 = f_0 k_2^2 Q_0 \tag{4.3}$$

where k_1 and k_2 are constants, depending on the geometrical properties of the coupling structures. Usually it is assumed *symmetric coupling* (i.e. $g = g_1 = g_2$, when there are identical input and output coupling structures), which it is sought to achieve in practice. The coupling circuit is realized as a microstrip semi-ring which is centered at the same center of the resonator, as depicted in Figure 4.2. Connections to the input/output ports are made via the dielectric layer and the ground of the microstrip board using a pair of surface-mounted coaxial (SMA) launchers as shown in Figure 4.4. This arrangement ensures that the device and microfluidic interface are in the same plane, for ease of bonding to further PTFE/PFA microfluidic modules in the space above the sensor.

4.1.4. Use of COMSOL Multiphysics

COMSOL Multiphysics® 4.4 was used to perform 3D simulations of the electromagnetics. The electromagnetic waves model was used to simulate the S-parameters and the distribution of the electric field. The wave equation in the frequency domain was computed in the electromagnetic waves model as described in the software as:

$$\nabla \times \mu_r^{-1}(\nabla \times \bar{E}) - k_o^2 \left(\varepsilon_r - \frac{j\sigma}{\omega \varepsilon_o}\right) \bar{E} = 0 \tag{4.4}$$

μ_r is the permeability, ε_r the permittivity and σ the electric conductivity of the material; ε_o is the permittivity of the vacuum, k_o is the wave number in free space, and ω the wave angular frequency. The impedance boundary condition is used for the copper surfaces of the resonator and ground in order to consider the copper losses. The scattering boundary condition was utilized for the faces of the volume $80 \times 80 \times 80$ mm^3 (enclosing the device) to make the boundaries transparent for the scattered waves. Coaxial ports were used to feed the electromagnetic energy to the resonator.

4.2. Methods of solvents characterization

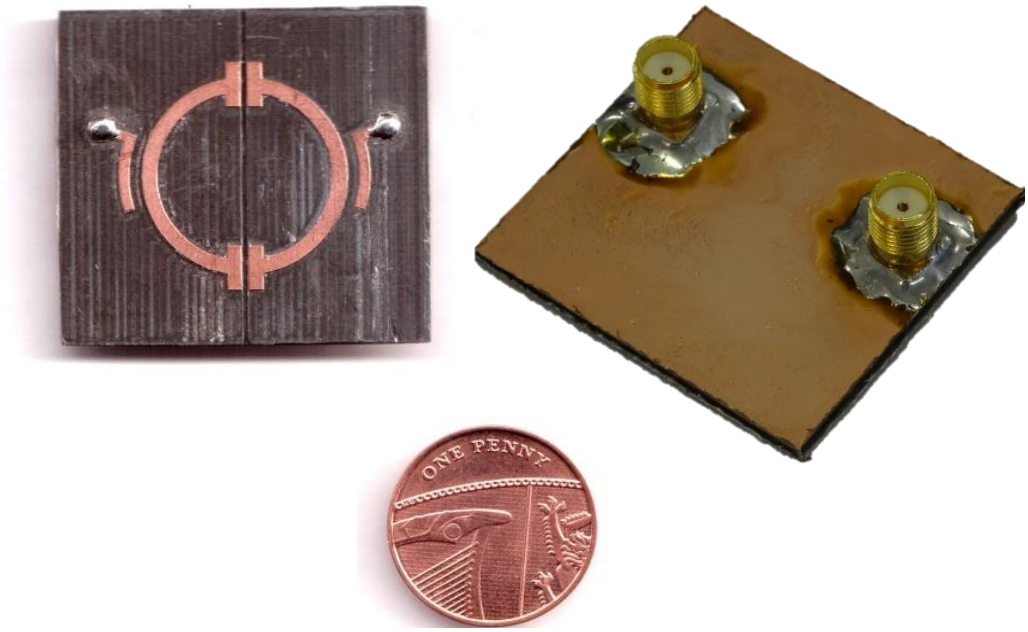

Figure 4.3: Photograph of the DSRR sensor, realized using a microstrip structure.

Figures 4.3, 4.4, and 4.5 show the configuration of the double split ring resonator with a micro-capillary passing through the two gaps. The resonator is made from microstrip using Rogers Corporation RT/duroid® 5880 laminate, which is constructed on a dielectric of a thickness h of 1.57 mm and relative permittivity of 2.20 ± 0.02 and loss tangent 0.0009. The thickness of the copper t is chosen as 70 µm to ensure the highest possible quality factor. The outer radius of the ring is r_1=1 cm, while the inner ring has r_2=0.85 cm. The width of the gap g is 0.7 mm. The other dimensions shown are $W_1 = W_3$ = 1.5 mm, W_2 = 4.5 mm, W_4 = 1.2 mm, W_5 = 1mm, p_1 = 4 mm, and p_2 = 1.3 mm. The area of the sensor is 3.6×3.6 cm^2. A duct with depth of d = 0.165 mm and width of 0.5 mm has been milled to accommodate the capillary. A photograph of the sensor is shown in Figure 4.3.

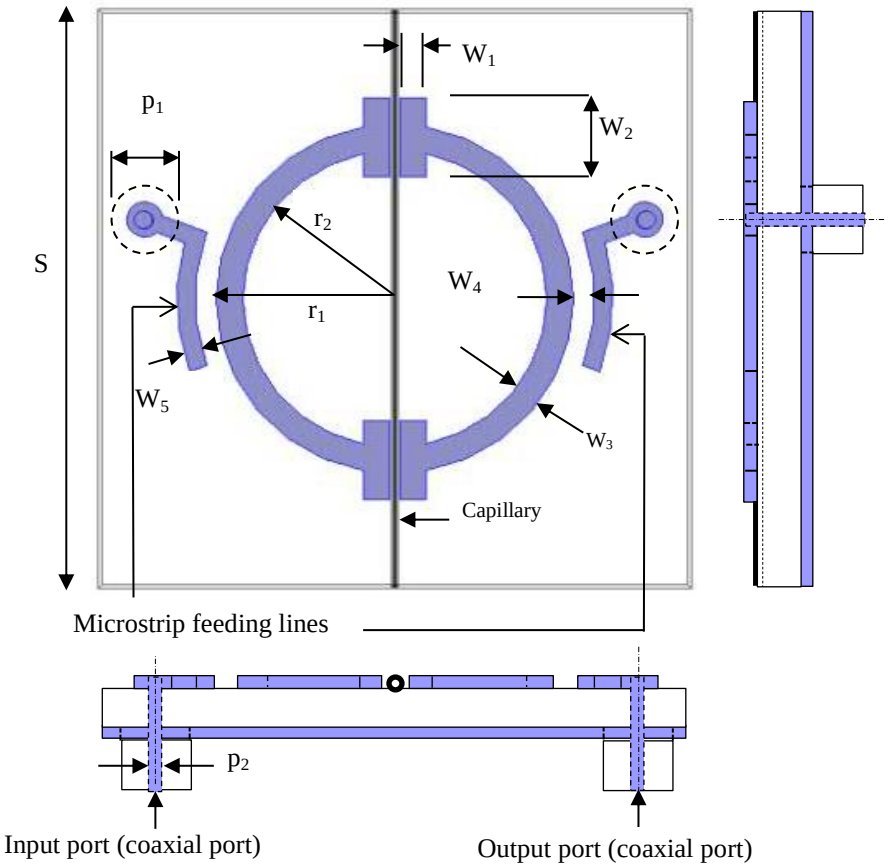

Figure 4.4: Definition of the labelling dimensions of the DSRR, and expanded views of the microwave coupling structures.

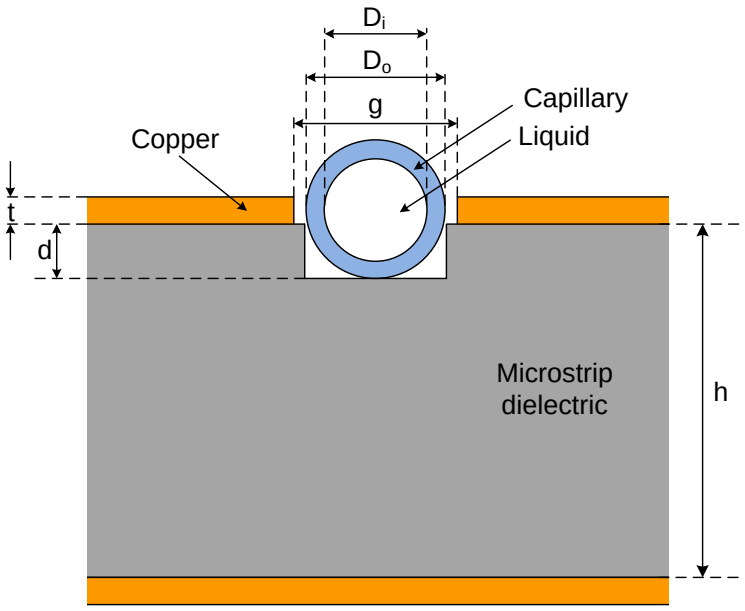

Figure 4.5: A cross section of the capillary inside the resonator gap.

A quartz capillary or PFA (perfluoralkoxy) tube are used for the liquids (models A and B), depending on whether static or flowing liquids are measured, respectively. The inner diameter of the quartz capillary is D_i = 0.3 mm and outer diameter D_0 = 0.4 mm, where the comparable diameters of PFA tubes are 0.15 and 0.36 mm, respectively. The permittivity of the quartz and PFA are assumed to be 3.8 and 2.1, respectively.

All electromagnetic simulations have been performed using COMSOL Multiphysics software. The electric field distribution in one of the gaps at the resonant frequency is presented in Figures 4.6 and 4.7, for three cases: without capillary, with an empty quartz capillary, and with a water-filled quartz capillary (model A). As shown in Figures 4.6(a) and 4.7(a), for the case with no capillary, the electric field concentrates at the edges of the rings. When the empty capillary is inserted, the electric field adopts a new distribution, as illustrated in Figures 4.6(b) and 4.7(b).

The presence of the capillary will increase the intensity of electric field at the ring edges and the field inside the capillary will be reduced compared to outside. When the capillary is filled with water, the electric field is strongly concentrated between the edges of the rings and the capillary (yielding field amplitudes much larger than for the two previous cases) and the field inside the capillary is much less than outside it, owing to the depolarizing effects due to the highly polar nature of water molecules. The simulated results using liquid-filled quartz capillaries (model A) and PFA tubes (model B) are illustrated in Figure 4.8 and 4.9, respectively (dashed lines).

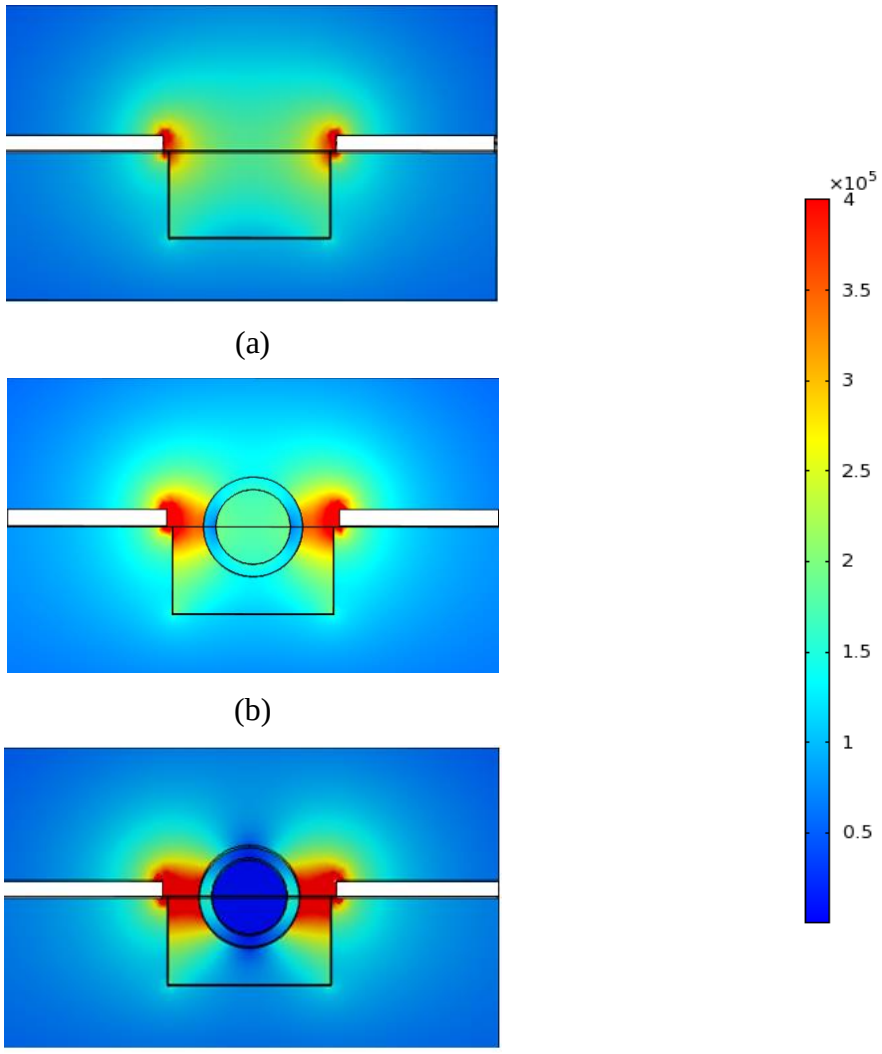

(a)

(b)

(c)

Figure 4.6: Electric field distribution (V/m) in the gap of the DSRR (model A), shown as a cross section of one of the gap regions : a- without capillary, b- with empty quartz capillary, c- with water-filled quartz capillary (note the strong depolarization of the electric field within the water).

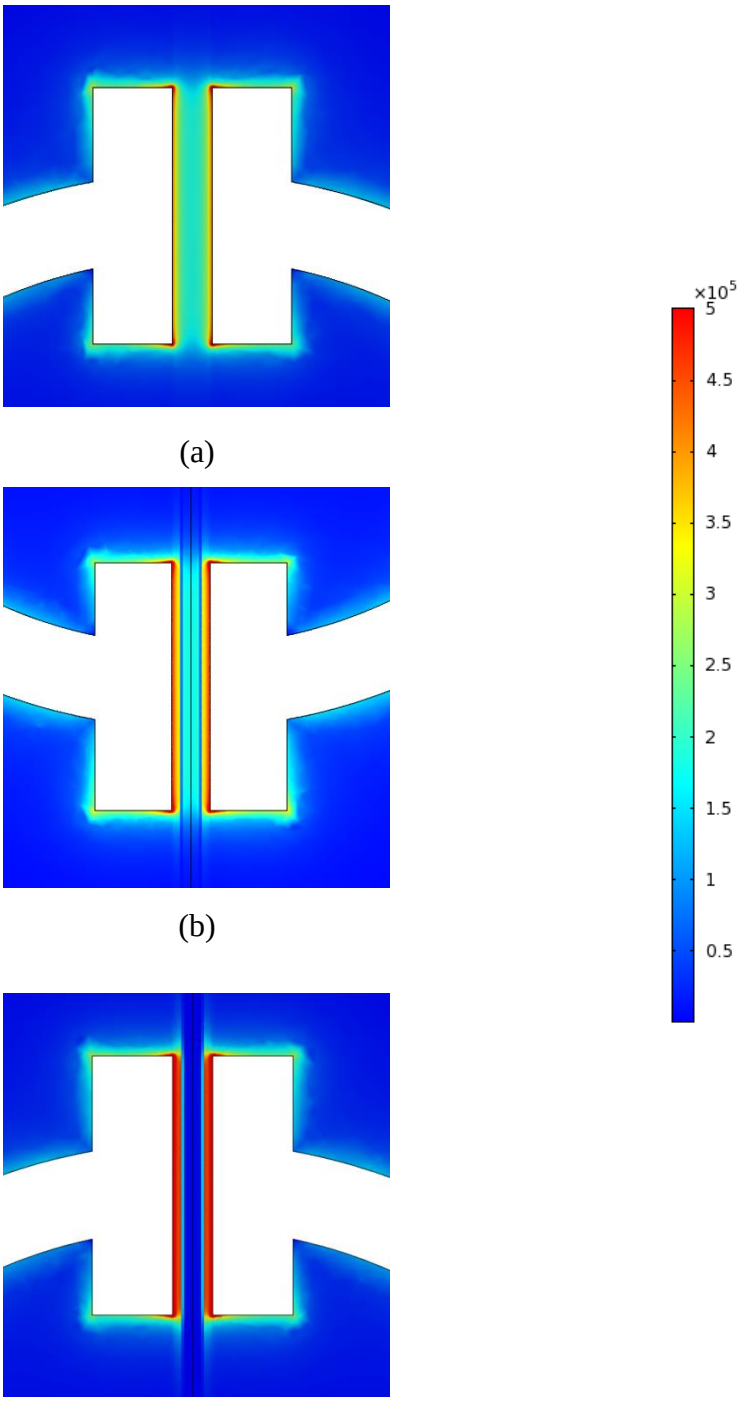

Figure 4.7. Electric field distribution (V/m) in the gap of the DSRR (model A), (in plane view, i.e. viewed from the top) : a- without capillary, b- with empty quartz capillary, c- with water-filled quartz capillary.

The simulation includes the interaction between the electromagnetic field and the solvents, which have the values of complex permittivity, calculated using the Debye model. For every solvent, the complex relative permittivity as a function of frequency

was defined in the simulation. As seen in Figure 4.8 and 4.9, the resonant frequency and quality factor have changed clearly, as a result of changes in the complex permittivity of the solvent. The simulation includes calculating the voltage transmission coefficient $|S_{21}|$ in the frequency domain for the empty capillary, and when it is filled with several types of common solvents (hexane, chloroform, methanol, ethanol, and water). Values of the Debye parameters for these solvents at an ambient temperature of 25^{o}C were taken from [128], [153], and [154].

To make the simulated results approximately identical to the measured results as shown in Figure 4.8 and 4.9, the corrected values of all parameters must be used in the simulation. These values include the new thickness of the microstrip dielectric after milling processing, the value of exact dimensions of the gapes, ring, and coupling elements after fabricating the DSRR (where there is an error of ±30 µm due to the milling cutting). Moreover, the real value of copper conductivity is different from the ideal value due to the roughness. Adding to that the error on the microstrip dielectric and capillary permittivities, and the error due to the position of the capillary inside the gape. Table 4.1 illustrates the real values of the all parameters that were used in the simulation. These values were obtained either by measuring them by microscope in case of the dimensions of the DSRR or by trial and error in case of the material permittivity. The procedure of matching between the simulated and measured results starts by matching the simulated $|S_{21}|$ in case of empty capillary with the measured results which involves using the values of DSRR that were measured by microscope and the slightly change the permittivity values of all materials. Once the acceptable matching between the simulated and measured responses of the empty capillary is achieved then the solvents are simulated. In case if the responses of the solvents are not exactly match with the measured results, that is because the temperature is not exactly 25^{o}C where the solvent permittivity is very sensitive to the temperature variation.

Table 4.1: DSRR dimensions and material properties using in the simulation. All dimensions are in mm.

r_1	r_2	w_2	w_4	g	d	h	$\varepsilon_{capillary}$	$\varepsilon_{dielectric}$	σ_{copper} (S/m)
9.93	8.43	4.36	1.25	7.1	0.4	1.5	3.4	2.15	2×10^{7}

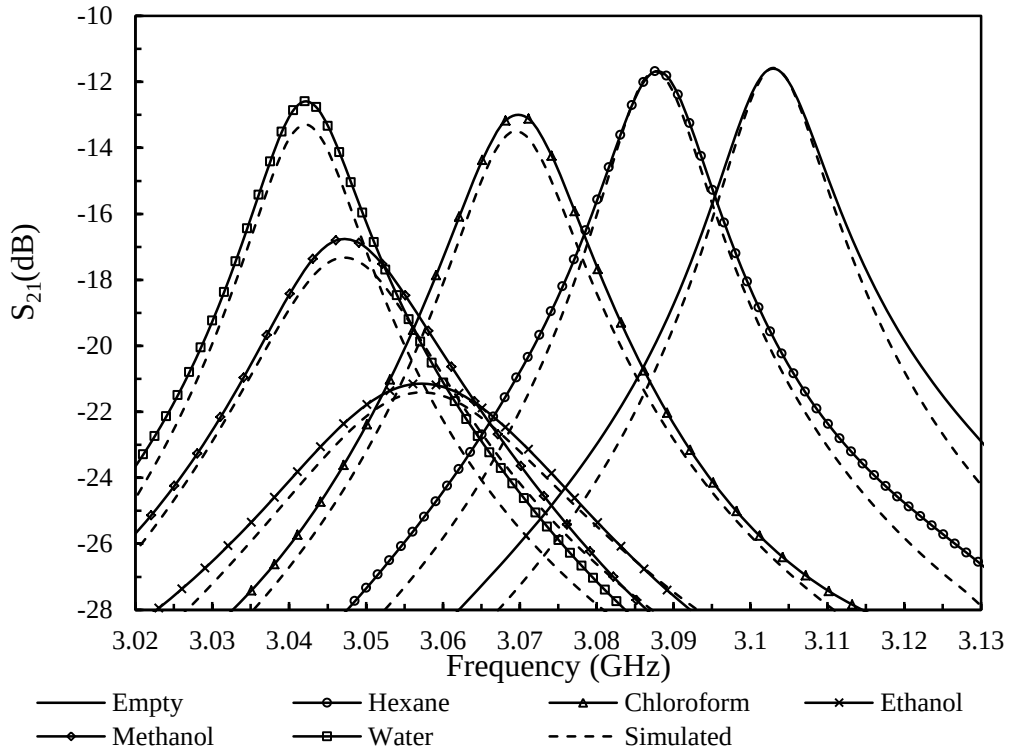

Figure 4.8: $|S_{21}|$ of the sensor using a quartz tube (model A): simulated results by COMSOL Multiphysics Software (dotted lines), and measured results (solid lines and symbols).

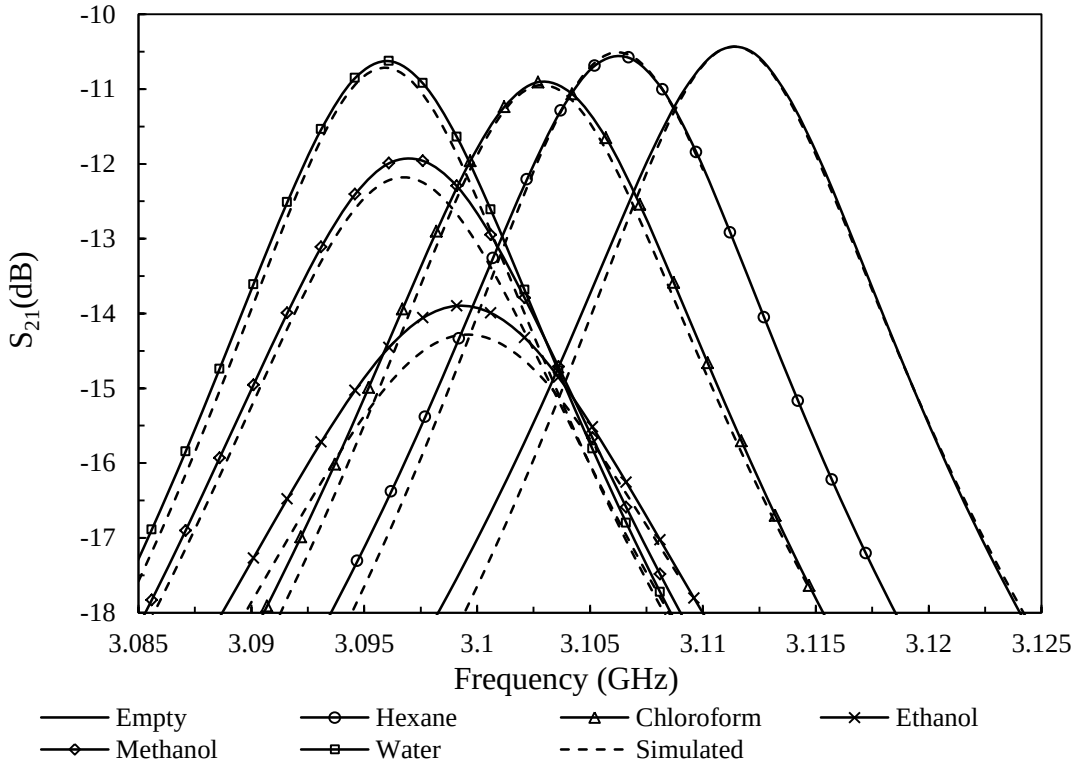

Figure 4.9: $|S_{21}|$ of the sensor using PFA tube (model B): simulated results by COMSOL Multiphysics Software (dotted lines), and measured results (solid lines and symbols).

4.3. Results and discussion

To validate the sensor performance experimentally, $|S_{21}|$ was measured for both the empty capillary and when it was filled with several types of solvents using the two types of capillaries and tubes (quartz and PFA). Several common solvents with different values of complex permittivities and relaxation times were chosen to test the sensor sensitivity for different materials, also in line with those used in the simulations. The results are illustrated in Figures 4.8 and 4.9, and Tables 4.2 and 4.3 for both types of capillary. Measurements were performed using an Agilent E5071B microwave network analyzer. As seen in Figures 4.8 and 4.9, there is good agreement between simulated and measured results. Small differences in the values of resonant frequencies from the simulation and measurement result from all parts of the prototype, but are mainly caused by the measurement uncertainties of the dimensions of the capillary, gaps, and copper thickness, the relative permittivity of the substrate, as well as the temperature.

We have designed the coupling structures to give insertion losses at resonance in the range of 10 to 20 dB. This is to ensure a large signal to noise ratio for measurement, to offset the fact that such microstrip resonators have inherently a low *Q*. The difference in the amplitude of the simulated and measured $|S_{21}|$ is about 0.5 dB, which is due to uncertainties in the dimensions of the coupling structures. Moreover, simulation with such small dimensions of the inner radius of the capillary and capillary wall thickness requires a very small mesh size and large number of mesh modes to obtain acceptable results, and so are limited by the computer and software capabilities. For each type of capillary, we have three sets of results:- simulated results that have been generated by COMSOL software, measured results that have been collected from the tests in the lab, and calculated results from the perturbation Equations 3 and 6 in appendix I.

All these results are listed in Tables 4.2 and 4.3. For the measured results using the quartz capillary, it can be seen that the maximum resonant frequency shift occurs with water, which is 61.5 MHz, while the hexane causes the minimum shift. This is what we expect from the known permittivity of these liquids. On the other hand, the maximum quality factor is when the capillary is empty (approximately 250) and minimum value results with ethanol, as shown in Table 4.2. The ratios of the change in resonant frequency and the change in bandwidth, normalized to the unperturbed resonant frequency $\Delta f_r/f_r$ and $\Delta f_B/f_r$ for the measured results are shown in Figures 4.10 and 4.11, respectively. These measured results are used to calculate the constants in Equations 3

and 6 (appendix I). To obtain optimal agreement between measured and calculated results, the constants k_1 and k_2 are calculated from averaged values obtained from measurements of several pairs of solvents. We selected chloroform-methanol, hexane-water, and ethanol-water for this process. The averaged values of k_1 and k_2 are used to extract the calculated values of $\Delta f_r/f_r$ by substituting them in Equation 3, and are as illustrated in Table 4.2.

To calculate the constants A_1, A_2 and A_3 of Equation 6 (Appendix I), the measured values of $\Delta f_B/f_r$ for hexane, ethanol, and water were selected and substituted in Equation 6, giving a system of three linear equations, which were solved to obtain the values of the constants. These three constants were utilized to calculate the values of $\Delta f_B/f_r$ of other solvents (chloroform and methanol) which are listed in Table 4.3. The results show that there is an acceptable agreement between calculated and measured sets of $\Delta f_r/f_r$ as well as $\Delta f_B/f_r$. The same procedure was applied to the results obtained using the PFA tube and are listed in Table 4.3. Systematic errors between calculated and measured results in the case of using the PFA tube are less those when using the quartz capillary. This is because single quartz capillaries are used each time, with the liquid filling by capillary action. There is a small variation in the capillary volume (of about 2%) from capillary to capillary, and also a slight variation in the capillary position each time. The PFA tube was permanently in place with the liquid filling done by pump or syringe, thus removing these systematic errors owing to differences in tube geometries. Furthermore, the changes in $\Delta f_r/f_r$ and $\Delta f_B/f_r$ for the case of PFA tube are less than for the quartz capillary because the volume of the liquid inside the PFA tube (inner diameter is 150μm) is smaller than that in the quartz capillary (inner diameter is 300 μm) for a fixed tube length.

Table 4.4 contains a comparison between the calculated and measured values of the complex permittivity of the liquids and the error ratio between them. The complex permittivity is extracted from the measurements using an optimization routine based on matching the simulated and experimental results. Good agreements between such measured values of complex permittivity and those calculated from the Debye model are observed and so our sensors permit absolute values of complex permittivity to be deduced within the microfluidic environment.

In general, the differences between calculated and measured values of $\Delta f_r/f_r$ and $\Delta f_B/f_r$ are caused by several factors. Firstly, there are accuracy limitations of the calculation in Equations 3 and 6 (Appendix I). One of the main approximations in these equations is the uniform electric field in the gap, and simulations demonstrate that this not the case in practice. Secondly, some of the values of Debye parameters $\varepsilon_s, \varepsilon_\infty$, and τ of the liquids used in the calculations and simulations vary within the academic literature [129], and are also highly temperature dependent. All measurements here were done at a lab temperature of 25 ± 1ºC, but there might be short term variations in temperature of to 1ºC during the course of a measurement. It should be noted that all of these errors in absolute permittivity are systematic and are due to systematic uncertainties in sensor geometry and sensor material properties (e.g. permittivity of substrate and surface resistance of copper). Percentage changes in complex permittivity (such as those due to chemical reactions or multiphase flow, to name both two examples) have much smaller random errors, typically less than 0.1%, so can be studied very precisely with our sensors.

Table 4.2: A comparison between simulated, measured, and calculated values of $\Delta f_r/f_r$ and $\Delta f_B/f_r$ for quartz tube (model A).

Liquid	Simulated f_r(GHz)	Simulated Δf_r(MHz)	Simulated $\Delta f_r/f_r$	Simulated Q	Measured f_r(GHz)	Measured Δf_r(MHz)	Measured $\Delta f_r/f_r$	Calculated $\Delta f_r/f_r$	Measured Q	Measured $\Delta f_B/f_r$	Calculated $\Delta f_B/f_r$
Empty	3.1035	-------	-------	258.6	3.1035	------	------	------	250	------	------
Hexane	3.0875	16	5.18×10^{-3}	250	3.088	15.5	5.02×10^{-3}	6.26×10^{-3}	249	1.606×10^{-5}	1.606×10^{-5}
Chloroform	3.0695	34	0.0109	211.7	3.07	33.5	0.0103	9.24×10^{-3}	203.5	9.140×10^{-4}	1.018×10^{-3}
Ethanol	3.0575	46	0.0148	87.8	3.0561	47.4	0.01551	0.01619	84.4	7.848×10^{-3}	7.848×10^{-3}
Methanol	3.0475	56	0.01837	142	3.047	56.5	0.01854	0.01857	142	3.042×10^{-3}	2.900×10^{-3}
Water	3.0420	61.5	0.02021	226	3.042	61.5	0.02021	0.01951	231.5	3.196×10^{-4}	3.196×10^{-4}

Table 4.3: A comparison between simulated, measured, and calculated values of $\Delta f_r/f_r$ and $\Delta f_B/f_r$ for PFA tube (model B).

Liquid	Simulated f_r(GHz)	Simulated Δf_r(MHz)	Simulated $\Delta f_r/f_r$	Simulated Q	Measured f_r(GHz)	Measured Δf_r(MHz)	Measured $\Delta f_r/f_r$	Calculated $\Delta f_r/f_r$	Measured Q	Measured $\Delta f_B/f_r$	Calculated $\Delta f_B/f_r$
Empty	3.1114	------	------	268.5	3.1114	------	------	------	264.7	------	------
Hexane	3.1062	5.17	1.664×10^{-3}	267.8	3.1062	5.17	1.664×10^{-3}	1.841×10^{-3}	262.3	3.456×10^{-5}	3.456×10^{-5}
Chloroform	3.103	8.4	2.707×10^{-3}	260	3.103	8.4	2.707×10^{-3}	2.417×10^{-3}	250	2.221×10^{-4}	2.571×10^{-4}
Ethanol	3.0995	11.9	3.839×10^{-3}	190	3.099	12.4	4.001×10^{-3}	4.226×10^{-3}	181.6	1.728×10^{-3}	1.728×10^{-3}
Methanol	3.0967	14.7	4.747×10^{-3}	227.7	3.097	14.4	4.650×10^{-3}	4.682×10^{-3}	223	7.064×10^{-4}	6.526×10^{-4}
Water	3.0959	15.5	5.007×10^{-3}	266.9	3.0961	15.3	4.942×10^{-3}	4.836×10^{-3}	258	9.810×10^{-5}	9.810×10^{-5}

Table 4.4: A comparison between calculated and measured values of solvents complex permittivity and relative error.

Liquid	ε_s	ε_∞	τ (*ps*)	Quartz Tube			PTEF tube		
				Calculated ε(f)	Measured ε(f)	Error	Calculated ε(f)	Measured ε(f)	Error
Hexane	1.894	1.890	5.8	$1.89\text{-}j4\times10^{-4}$	$1.893\text{-}j7\times10^{-3}$	0.05%	$1.89\text{-j}4.1\times10^{-4}$	$1.893\text{-}j8\times10^{-3}$	0.05%
Chloroform	4.72	2.5	7.96	4.67-*j*0.333	4.71-*j*0.247	0.8%	4.67-*j*0.34	4.67-*j*0.2909	0.3%
Ethanol	24.32	4.2	163	6.06-*j*5.83	6.43-*j*5.72	2.3%	6.02-*j*5.76	6.472-*j*5.623	2.9%
Methanol	32.5	5.6	51.5	19.2-*j*13.4	20.18-*j*12.49	1.4%	19.0-*j*13.5	20.07-*j*12.39	1.2%
Water	78.36	5.16	8.27	76.6-*j*11.3	77.42-*j*5.92	0.3%	76.5-*j*11.5	77.39-*j*6.016	0.33%

The values of $\Delta f_r/f_r$ and $\Delta f_B/f_r$ as function of ε_1 and ε_2 for the specific solvents measured here are shown in Figures 4.10 and 4.11, respectively. The green circles represent the calculated values for the complex permittivities of the specific solvents (hexane, chloroform, ethanol, methanol, and water). The blue circles are the measured values of $\Delta f_r/f_r$ and $\Delta f_B/f_r$. To provide a more complete picture of the use of the DSRR for evaluating dielectric properties of liquids, the values of $\Delta f_r/f_r$ and $\Delta f_B/f_r$ have been replotted as surface plots, with values of ε_1 and ε_2 covering the full range of values expected for almost all solvents; the plots are depicted in Figures 4.12 and 4.13 for case of quartz and PFA tubes, respectively. The red grid is the plot of Equations 3 and 6 (Appendix I) in Figures 4.12 and 4.13, respectively. Figure 4.13 shows that $\Delta f/f_r$ is more sensitive to changes in ε_1 compared with ε_2 , whereas $\Delta f_B/f_r$ the opposite is true (as one would expect from simple first perturbation theory). We can give more explanation by simplifying the dipole moment equation of the sample in 3.23 ignoring the effect of the capillary walls:

$$p \approx A \cdot \left(\frac{\varepsilon_{rL}-1}{\varepsilon_{rL}+1}\right) E_0, \tag{4.5}$$

where A is a constant, and $\Delta f_r/f_r$ and $\Delta f_B/f_r$ can be then approximated as:

$$\frac{\Delta f_r}{f_r} \approx B \cdot Re\left(\frac{\varepsilon_{rL}-1}{\varepsilon_{rL}+1}\right) \tag{4.6}$$

$$\frac{\Delta f_B}{f_r} \approx C \cdot Im\left(\frac{\varepsilon_{rL}-1}{\varepsilon_{rL}+1}\right), \tag{4.7}$$

where B and C are constants. As $\varepsilon_{rL} = \varepsilon_1 - j\varepsilon_2$, then Equations 4.6 and 4.7 are:

$$\frac{\Delta f_r}{f_r} \approx B \cdot \frac{(\varepsilon_1^2-1)+\varepsilon_2^2}{(\varepsilon_1^2+1)+\varepsilon_2^2} \tag{4.8}$$

$$\frac{\Delta f_B}{f_r} \approx C \cdot \frac{2\varepsilon_2}{(\varepsilon_1^2+1)+\varepsilon_2^2} \tag{4.9}$$

From Equation 4.8, the change of $\Delta f_r/f_r$ with $(\varepsilon_1 - 1)$ is similar to the measured results as shown in Figures 4.10 and 4.12, which gives approximately linear relationship when ε_1 is small (less than 20) and constant relationship above 20. On the other hand, it is difficult to describe the relationship between $\Delta f_B/f_r$ and ε_2 in Equation 4.9 as $\Delta f_B/f_r$ changes with both ε_1 and ε_2 at the same time.

Finally, from Figures 4.10 to 4.13, note that the DSRR becomes insensitive to measurements of ε_1 above about 20. This is due to the fact that for such high values of permittivity the depolarization is almost complete, and further increases in ε_1 do not result in increased dipole moment (note that the maximum dipole moment is that for a metal, where can think of ε_1 tending to infinity). The only solution to this lack of sensitivity for high ε_1 is to use a sample geometry which is not depolarizing, for example where the electric field is parallel to the capillary, and another PhD student at Cardiff University (Hayder Hamzah) is investigating such structures for generation of high electric fields within polar liquids such as water.

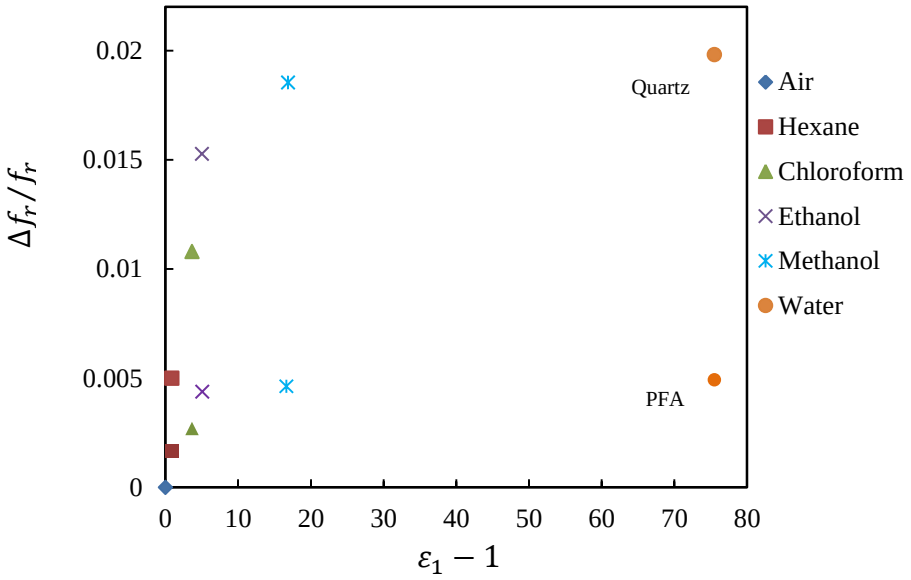

Figure 4.10: Plot the ratio of the measured $\Delta f_r/f_r$ as a function of permittivity ($\varepsilon_1 - 1$).

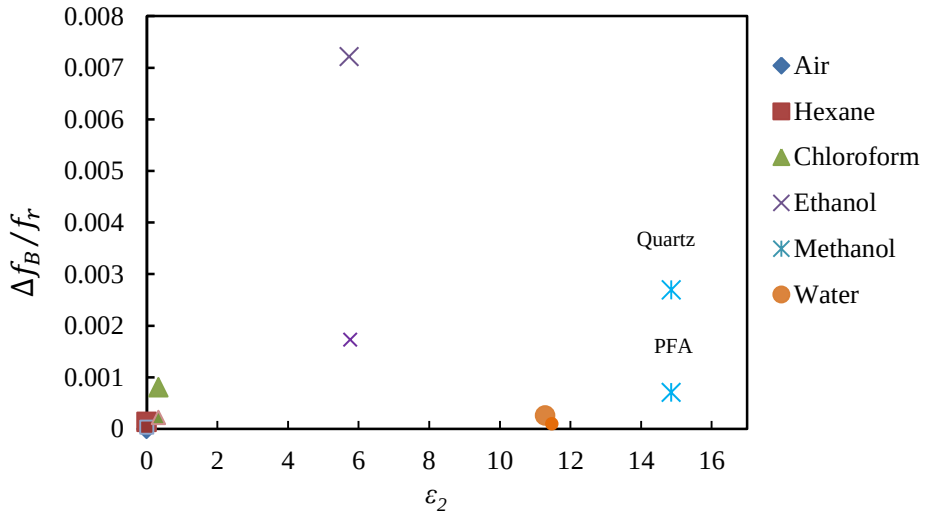

Figure 4.11: Plot the ratio of the measured $\Delta f_B/f_r$ as a function of permittivity ε_2.

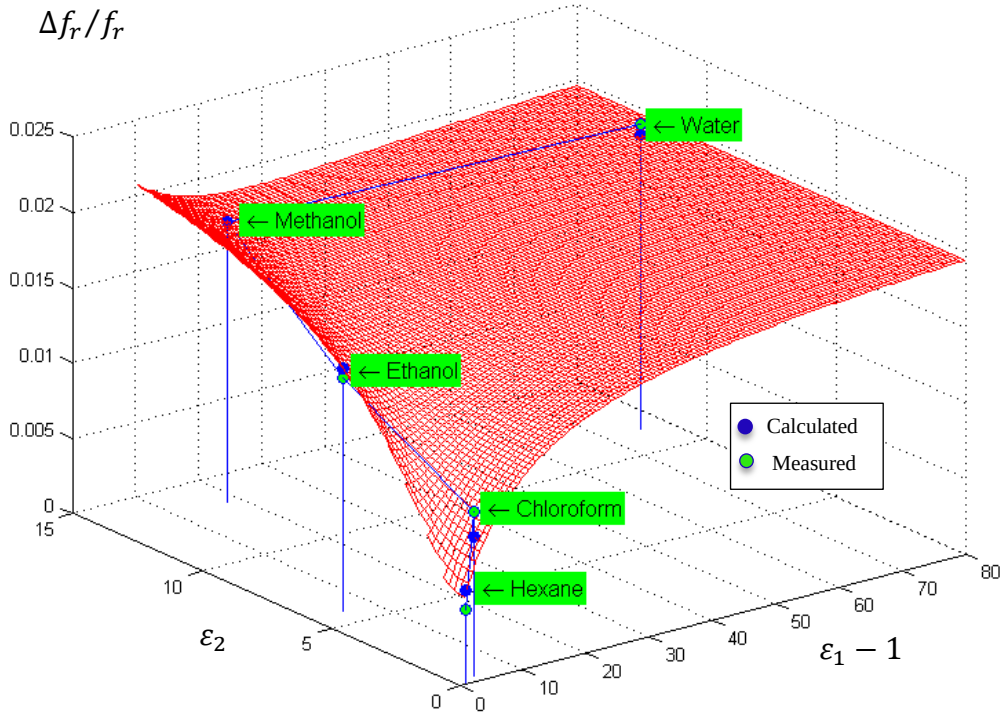

(a)

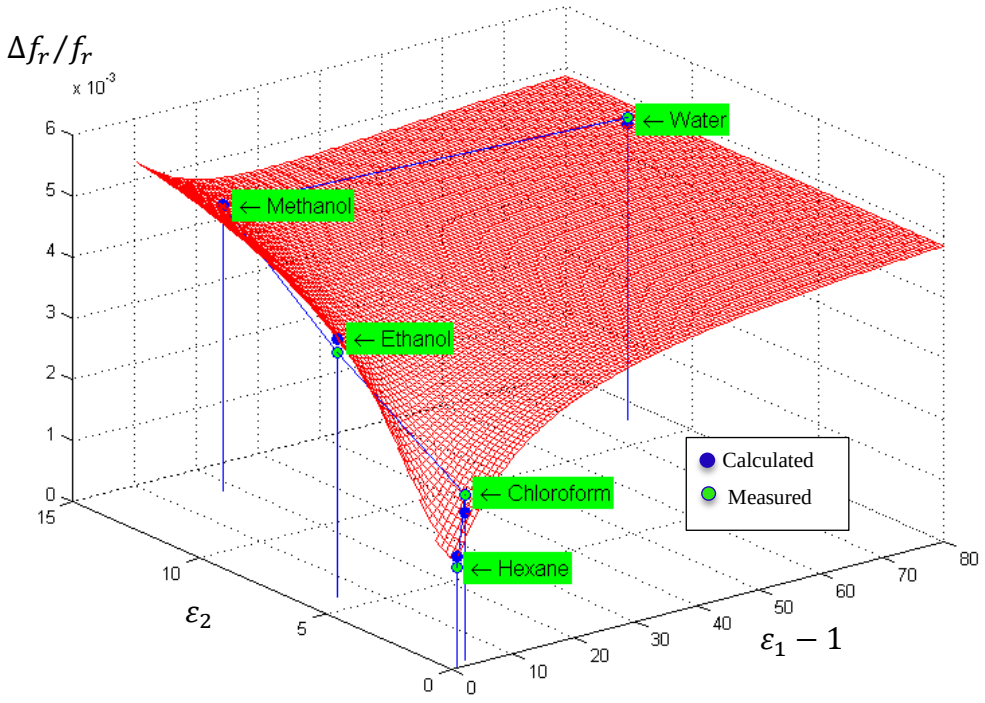

(b)

Figure 4.12: Plot of the measured and calculated ratio of $\Delta f_r/f_r$ as a function of permittivity from Equation 3 (Appendix I), a- using quartz capillary (model A), b- using PFA tube (model B).

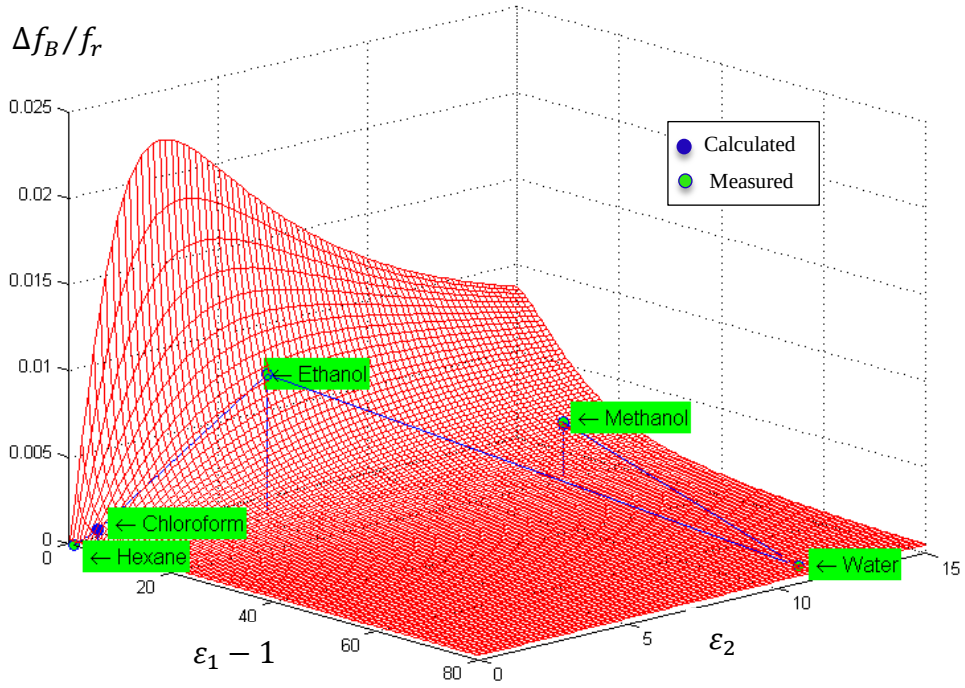

(a)

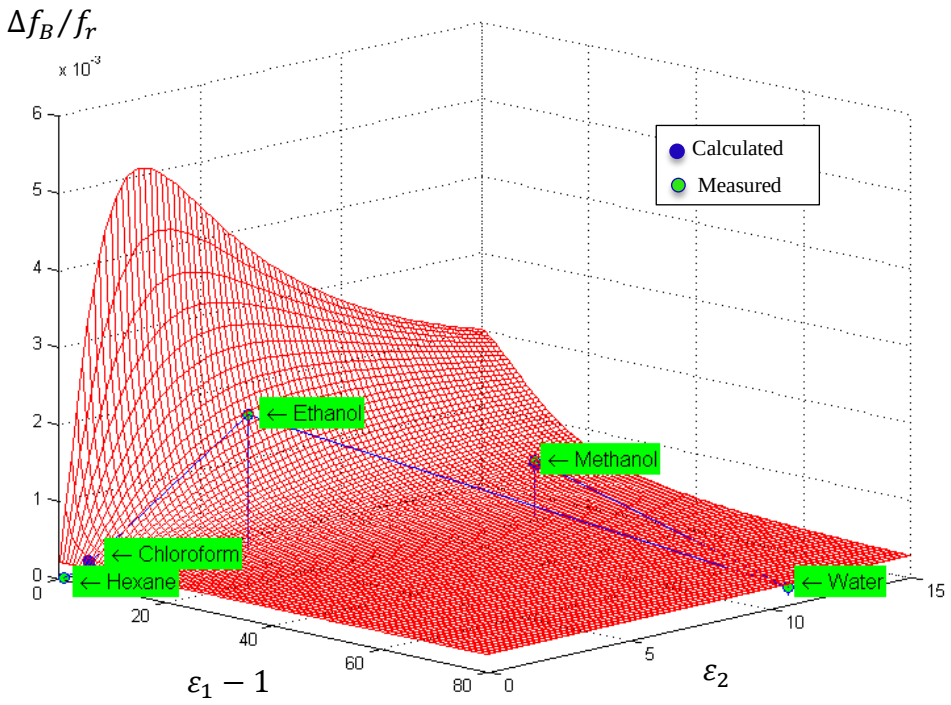

(b)

Figure 4.13: Plot of the measured and calculated ratio of $\Delta f_B/f_r$ as a function of permittivity from Equation 6 (Appendix I), a- using quartz capillary (model A), b- using PFA tube (model B).

4.4. Methods of multi-phase liquids sensing using the DSRR

4.4.1. Electromagnetic and microfluidic design

The DSRR described here can also be used as a microfluidic sensor, whose changes in resonant frequency and bandwidth with time can be used to determine the presence, speed and length of liquid segments, as well as the liquid permittivity (as has just been discussed in detail). The basic system for segment interrogation is shown in Figure 4.14. A segmented flow of discrete water and oil segments is set up inside the PTFE tube using a pump consisting of two syringes (one for oil and the other for water). The lengths of the oil and water segments are controlled by a motorized valve (MXX777-601). LabVIEW software (by National Instruments Ltd.) is used to control both pump and valve. The outer diameter of the PTFE tube is 360 µm and the inner diameter is150 µm.

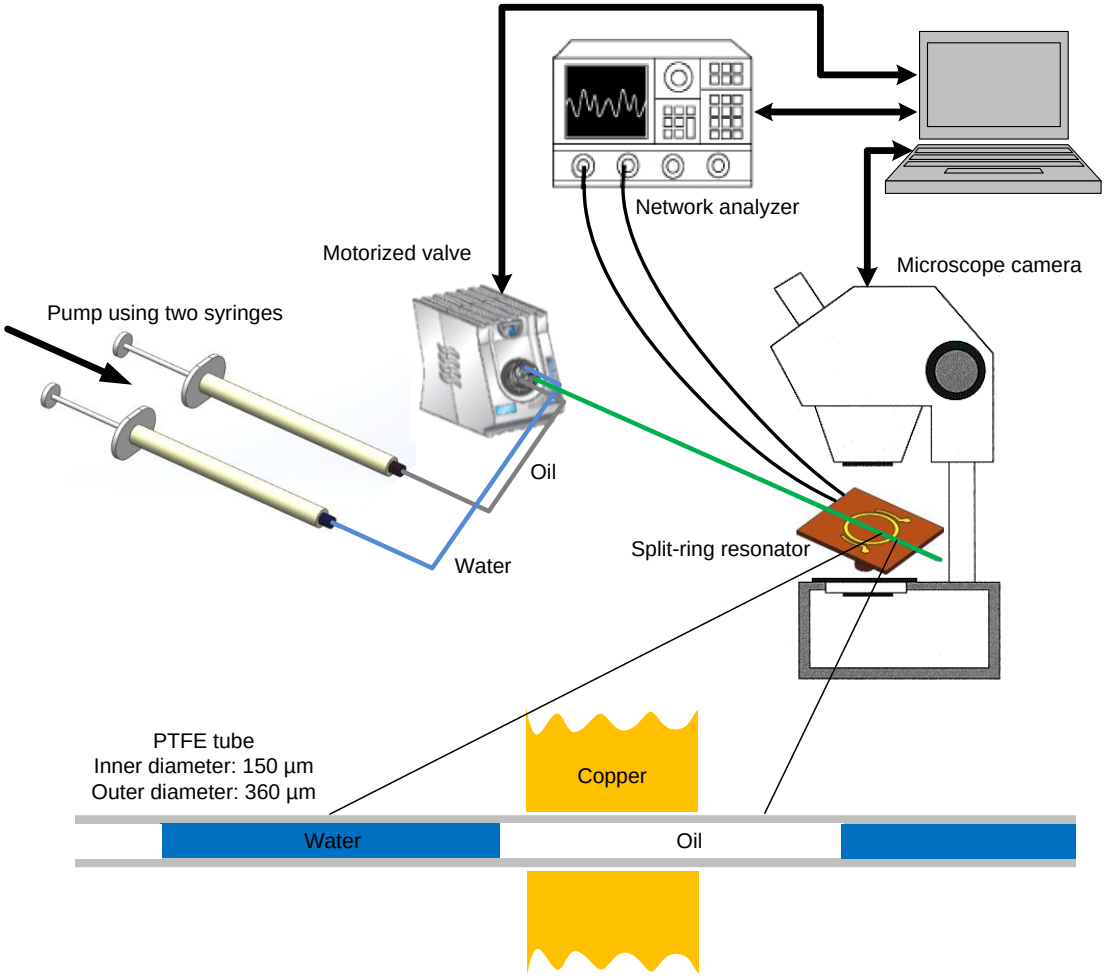

Figure 4.14: Schematic of the microfluidic system and split-ring microstrip resonator (DSRR) connected to network analyzer, all controlled using LabVIEW software. The segmented flow is shown in close-up.

The changes in resonant frequency, bandwidth, and insertion loss of the DSRR due to the liquid perturbations [140] are measured using a network analyzer (Agilent E5071B) under LabVIEW control. The network analyzer is configured to take rapid measurements (every 15 ms). In this system we are also able to record the movement of the oil-water stream using a microscope camera. The schematic of the DSRR is illustrated in Figure 4.15. This is different to the geometry adopted for the permittivity measurements of pure solvents (Figure 4.4), in that the gap regions are less extended, leading to a more localized measurement of permittivity, allowing greater time resolution of segment flow. Two models of the DSRR have been designed to investigate the effect of the gap dimensions on the sensor performance. (C and D, described below). Of these two, model D provides the greatest spatial resolution owing to the shaping of its gap region (Figure 4.19).

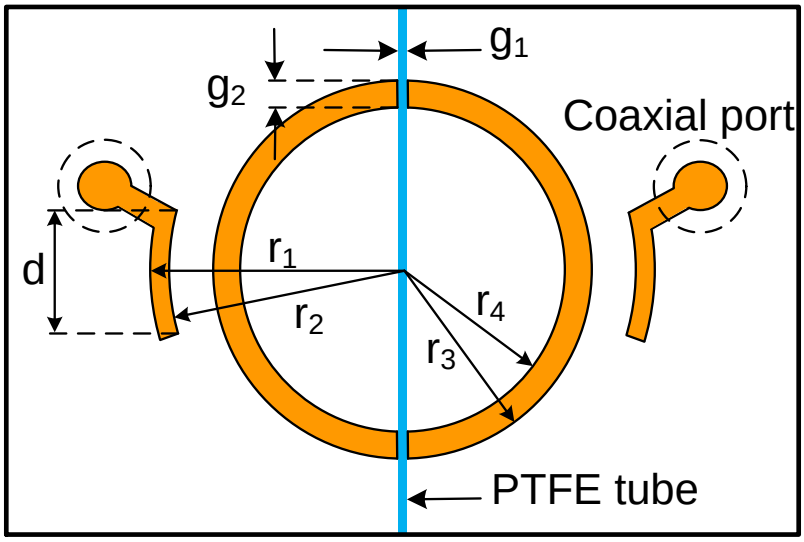

Figure 4.15: Schematic of the double split-ring microstrip resonator (DSRR) with input/output coupling structures, used for multi-phase flow measurements.

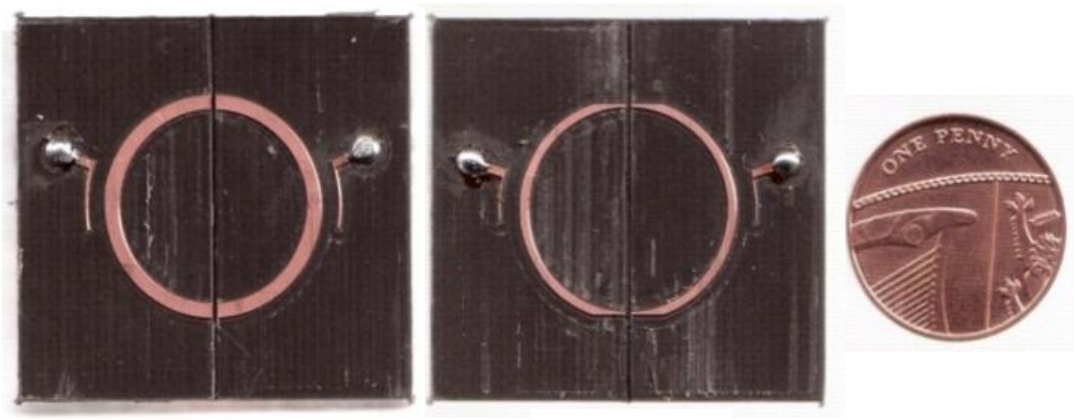

Model C Model D

Figure 4.16: Photograph of the fabricated DSRRs (Models C and D).

Table 4.5: Dimension of models C and D DSRR (all dimensions are in mm)

Model	g_1	g_2	r_1	r_2	r_3	r_4	d
C	0.45	1.25	11.70	11.5	9.87	8.625	6.0
D	0.45	0.20	11.75	11.7	9.87	9.120	4.5

Photographs of both models (C and D) are shown in Figure 4.16, with the dimensions of each listed in Table 4.5. The resonators are fabricated by milling a Rogers Corporation RT/duroid® 5880 laminate, with a dielectric thickness of 1.57 mm, relative permittivity of 2.20±0.02 and loss tangent 0.0009. The thickness of the copper is 70 µm. The simulations of the models with empty, mineral oil, and water filled tubes were performed using COMSOL Multiphysics. This was chosen as a simple immiscible system to demonstrate the proof of concept of the flow sensor with simultaneous measurement of the complex permittivity of the segments, which a completely novel, multi-function sensor. The simulated and measured results of models C and D are shown in Figure 4.17 (a) and (b), respectively. It is clear from the comparison between simulated and measured results that there are good agreements between them for both models. The difference in resonant frequency between simulated and measured results is about 0.1 MHz in both models, while the insertion loss difference is about 0.05 dB.

4.4.2. Performance of the sensor and extraction of segment length, speed, and permittivity

The general response of the sensor (resonant frequency, and insertion loss) as a function of time are shown schematically in Figure 4.18, which also provides an explanation of

the relation between the position and movement of the oil-water segments, and the resulting resonant frequency and insertion loss of the DSRR. There are three possible states of resonant frequency and insertion loss, which we denote as (f_1, IL_1), (f_2, IL_2), (f_3, IL_3), linked to the fluid filling the two gaps of the DSRR, namely water-water (state 1), water-oil or oil-water (state 2) and oil-oil (state 3).

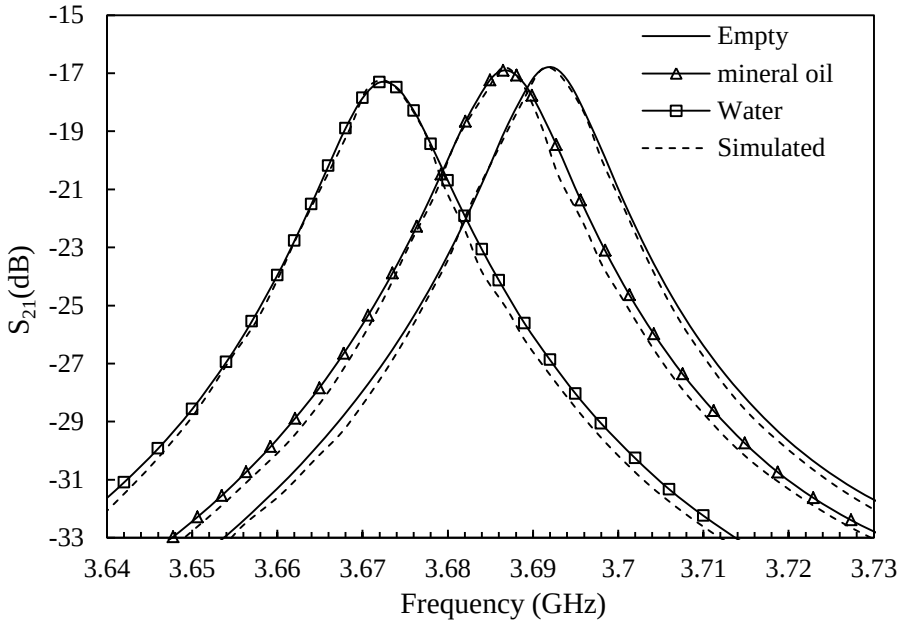

(a)

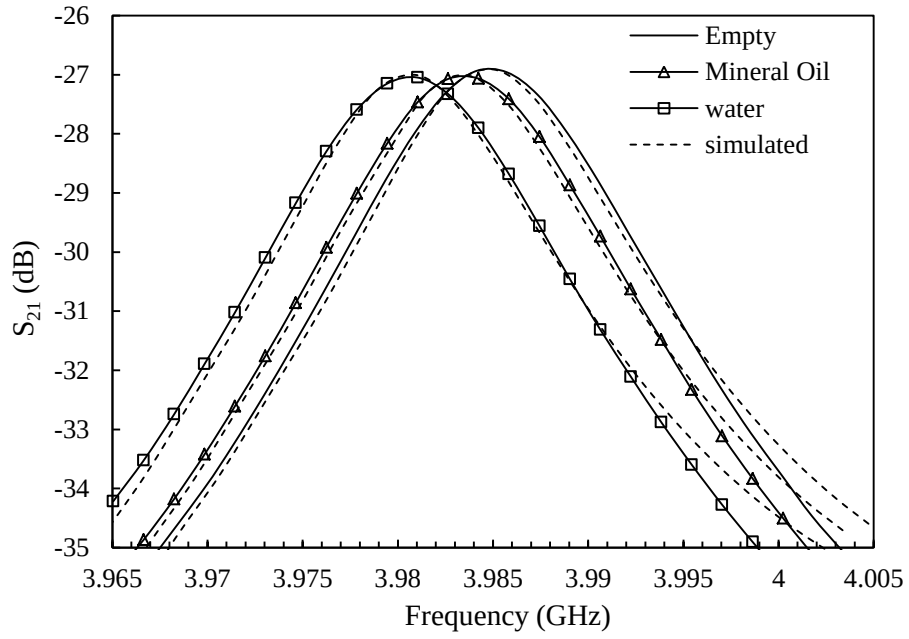

(b)

Figure 4.17: Comparison results between measured and simulated S_{21} for empty, mineral-oil, and water filled PTFE tube : (a) model C sensor, (b) model D sensor.

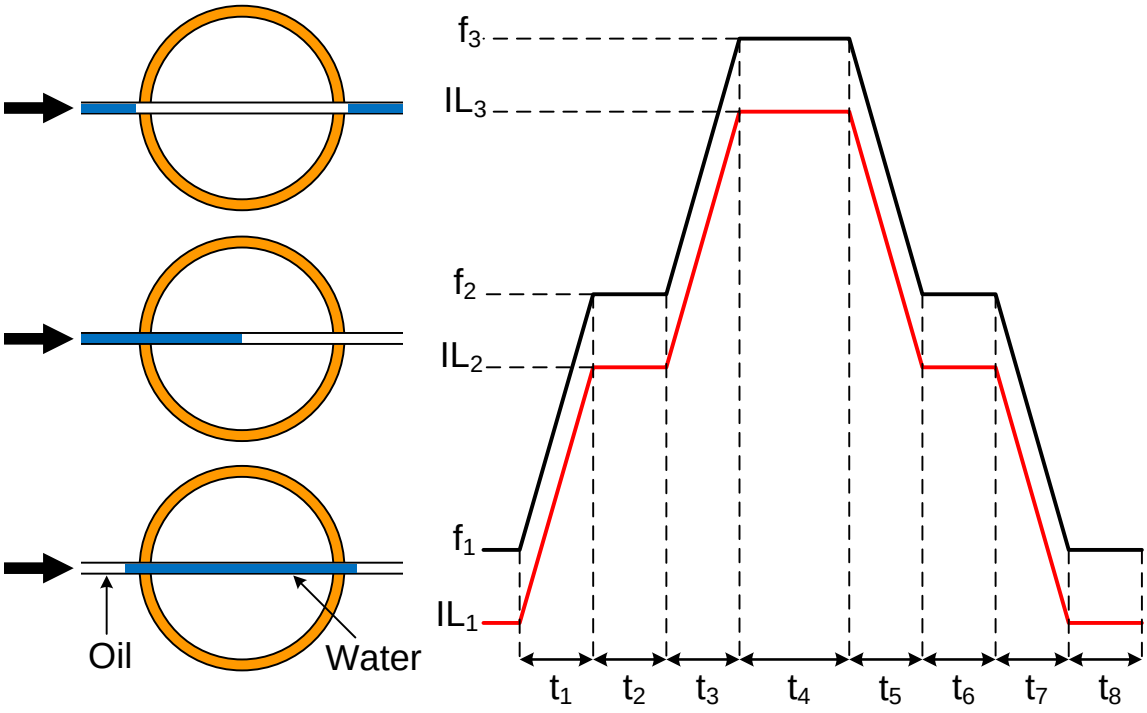

Figure 4.18: A schematic diagram showing the oil and water packets moving between the two gaps of the DSRR sensor, and the corresponding changes in resonant frequency and insertion loss.

Referring again to the states of the DSRR, the values f_1 and IL_1 are the resonant frequency and insertion loss, respectively, when both gap regions are filled by water; we denote this as the initial state of the DSRR. When the oil segment starts to move it will subsequently fill the first gap. The time required to fill the first gap is t_1 and the resonant frequency and insertion loss will increase dramatically from f_1 to f_2, and from IL_1 to IL_2, respectively. Here f_2 and IL_2 are the resonant frequency and insertion loss, respectively, of the DSRR when the first gap is filled by oil and the second gap by water. The time taken for oil to reach the second gap will be t_2 and to fill the second gap is t_3. When both gaps are filled by oil, the resonant frequency and insertion loss are f_3 and IL_3, respectively, and t_4 is the time taken for oil to occupy both gaps. After that the new segment of water will enter and fill the first gap. It takes time t_5 to fill the first gap and the resonant frequency and insertion loss will decrease rapidly from f_3 to f_2, and IL_3 to IL_2. The water segment takes time t_6 to reach to the second gap, after which the resonant frequency and insertion loss will decrease rapidly from f_2 to f_1, and from IL_2 to IL_1. The speed of the liquid can be found from the time required for it to travel the distance between the first and second gap (t_2 or t_6), where the distance between the gaps is well

known (i.e. $2r_4$). By calculating the speed of liquid, the length of oil or water can be calculated from the change in resonant frequency. The volume of oil or water segments are easy to find if the length and radius of tube are known precisely, as is the case here. The permittivity of liquid (oil or water) can be determined by comparing the results frequency shifts and bandwidth changes with the COMSOL simulations of Figure 4.17.

4.5. Results and discussion

In Figure 4.19 (a), the experimental differences in resonant frequency and insertion loss of the model C sensor between mineral-oil and water segments are shown to be 15 MHz and 0.4 dB, respectively. Figure 4.19 (b) shows the response of the model D sensor in which the differences in resonant frequency between oil and water is 2.9 MHz and insertion loss is 0.14 dB, approximately. The differences in resonant frequency and insertion loss are larger for model C than D, as expected since its gap capacitance makes up a smaller fraction of the overall capacitance of the DSRR. This makes model C more accurate in extracting the values of permittivity. Responses of model D offer higher spatial resolution than those of model C since the electric field is more localized to the gap region. Consequently, model D is more precise than C in measuring the length and speed of segments. Moreover, it is clear that the values of resonant frequency and insertion loss in the state when the first gap is filled by water and another by oil are not the same as those

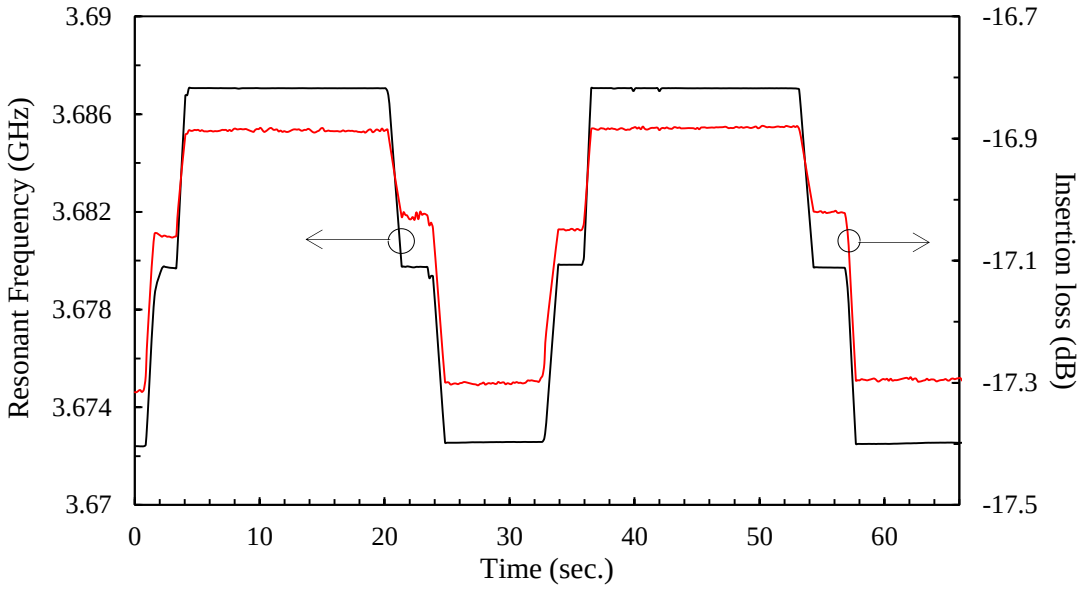

(a)

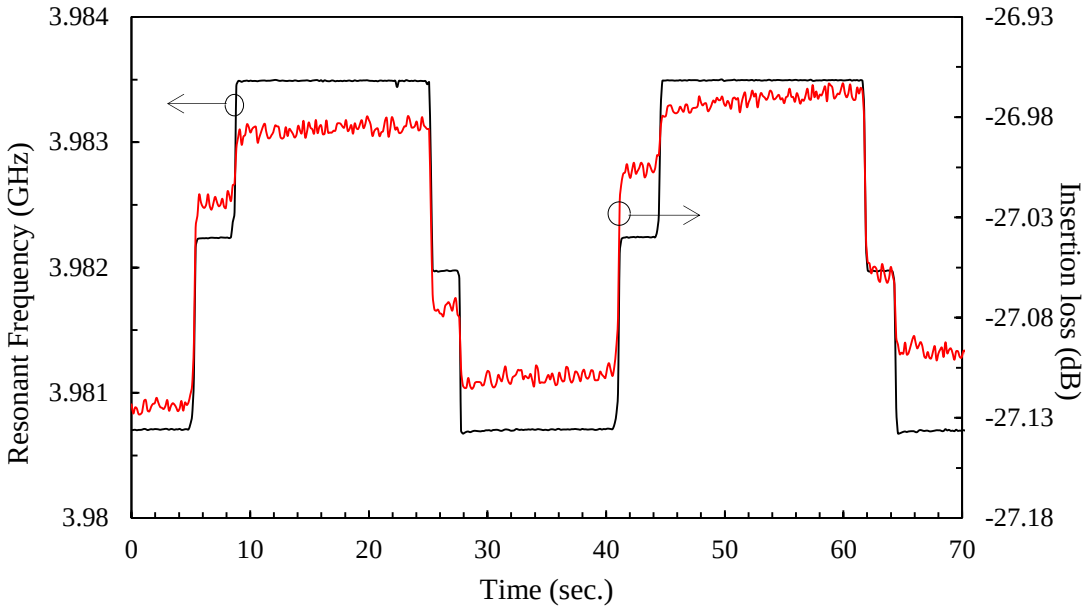

(b)

Figure 4.19: The change in resonant frequency and insertion loss with time for a stream of mineral oil-water segments in a PFTE tube at rate of 8 µL/min: (a) for model C, (b) for model D.

of the converse state (when the first gap is filled by oil and the second gap filled by water), as shown in Figure 4.19 (a) and (b). The reason is that the gaps are not identical in dimensions because of the fabrication process; even a few microns difference in gap dimensions can yield such an asymmetry.

This difference can be exploited to determine the precise position of oil or water. Finally, the value of insertion loss in Figure 4.19 (b) varies slightly with time when the same liquid is within the gaps (oil or water). This variation is due to small temperature drifts and highlights the importance of the need to stabilize the temperature to achieve more accurate and stable results. The two sets of extracted flow rate and length (obtained by the DSRR and also calculated from still images taken by a video camera), and complex relative permittivity (ε) are listed in Table 4.6. The average values and the standard errors are calculated for both sets of data, since the linear velocity of the segments is not constant due to the effect of motorized valve. Here v is the average linear velocity of the oil and water segments (20 samples are taken to measure v), and l_{oil} and l_{water} are the average segment lengths of the oil and water, respectively. The agreement between the measured values of length and velocity from the DSRRs and

camera for the model D is much better than for C, as shown in Table 4.6. This makes model D is more sensitive to measurements of the segment velocity and length, while model C is more sensitive to measurements of the permittivity due to its larger capacitance value. The complex permittivity of both liquid segments is extracted from the sensor measurements using an optimization routine based on matching the simulated and experimental results. The results for water agree with the predictions of the Debye model for water at 25 °C.

Table 4.6: Extracted rate and length of the segment, time in sec., length in mm, and rate in mm/sec.

Model	Microwave measurements (sensed values)			Camera measurements (physical values)			t-test for v
	v	l_{oil}	l_{water}	v	l_{oil}	l_{water}	
C	7.0±0.3	143±6	88±4	5.7±0.3	116±6	72±3	1.62
D	7.3±0.3	146±6	115±5	7.2±0.3	144±6	113±5	0.12
	ε_{oil}			ε_{water}			
C	2.10 – *j*0.00			76.4 – *j*13.6 (at 3.67 GHz)			
D	2.10 – *j*0.00			76.0 –*j*14.7 (at 3.98 GHz)			

CHAPTER 5 – MICRO-SPHERE DETECTION AND CHARACTERIZATION

Recently, microwave techniques have been utilized to build micro-particles and biological cells sensor. The microwave sensing of micro-particles and cells can provide many advantages, most notably the rapid, reliable, and accurate measurements that are obtained. Moreover, microwave cell detection is label-free method in which the cells are maintained in their original state, and easy to reproduce during the measurement [82].

However, most of the previous works have been dedicated to the dielectric assessment of groups of cells, rather than single cell properties. This is restrictive, as to give but one example, there is increasing evidence in other clinical and pre-clinical studies to suggest that the single-cell heterogeneity in the regulation of oncogenic signaling pathways is a general feature of most cancers. In [155] it was shown that the dielectric permittivity, capacitance and conductivity values of cell membranes are higher for normal lymphocytes than for malignant ones. Model-based numerical predictions of the dielectrophoretic behavior of spheroidal biological cells are carried out in [156]. A linear relationship was observed between the DNA content of eukaryotic cells and the change in capacitance in [157] that is evoked by the passage of individual cells across a 1-kHz electric field. Moreover, theoretical analysis and measurement techniques for dielectric spectroscopy of biological cells in the radio frequency range were reviewed in [158].

In this chapter, a new application for a microwave microstrip split ring resonator (SRR) with a narrow, tapered, single-gap section, as a sensor for the dielectric characterization

of microparticles is demonstrated. This is shown schematically in Figure 5.1, illustrating the gap adaption for single cell investigations in medical and biological applications. In section 5.1, a brief theory and concepts of the odd and even resonator modes and the theoretical enhancements in sensitivity that can be expected by tapering and reducing the gap, and that due to reducing the overall size of the SRR. The methods which include the description of the sensor design and fabrication (together with simulation results) are presented in Section 5.2. In Section 5.3, the experimental results are demonstrated and discussed.

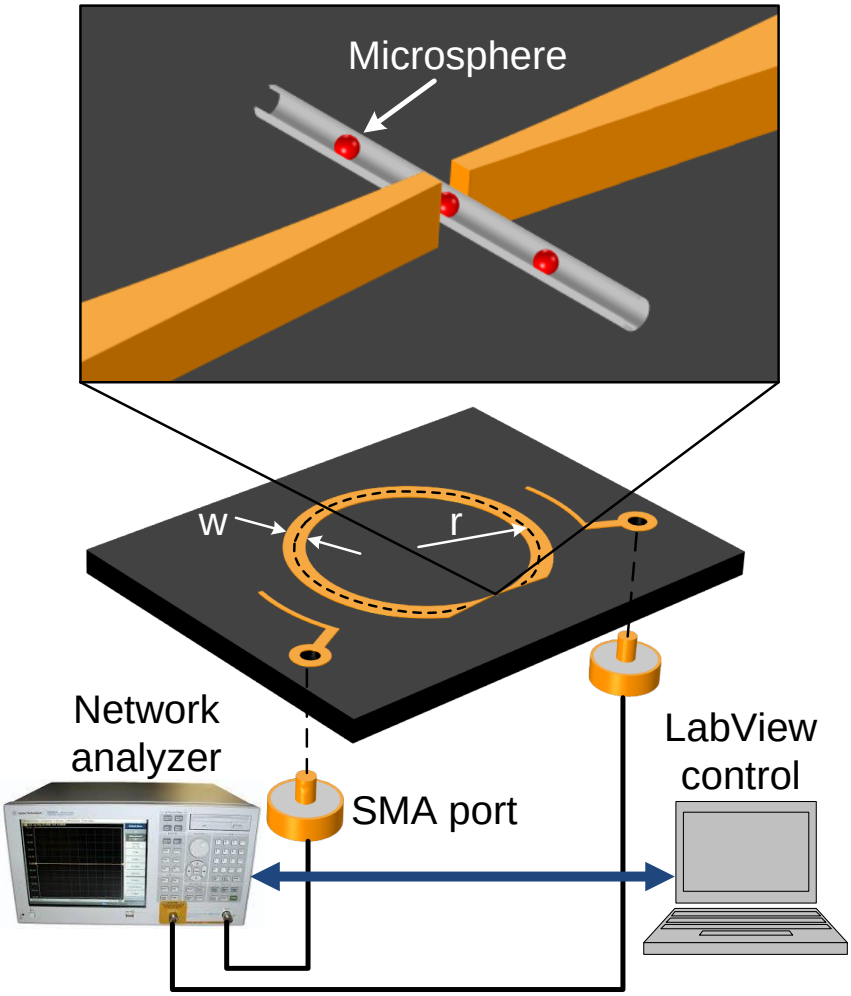

Figure 5.1: Schematic of the split-ring microstrip sensor (the ground plane is on the back surface, not shown), connected to a microwave network analyzer and controlled by a LabVIEW program. Microspheres are passed through the gap region via a water filled, glass capillary.

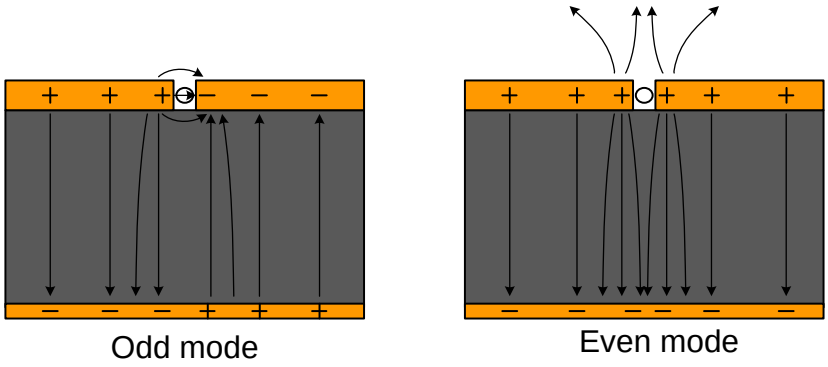

Figure 5.2: Quasi-TEM modes of the SSR. (a) Odd mode (with large electric field in the gap), and (b) even mode (with small electric field in the gap).

5.1. Theory

5.1.1. Odd and even resonator modes

The SRR based on the microstrip geometry (i.e. with ground plane) shown in Figure 5.1 has odd and even mode resonances. The odd mode has the lower resonant frequency and occurs when the wavelength is equal to the electrical length of the ring plus the gap [151]; the even mode has higher frequency and occurs when the wavelength is equal to the ring length only [149]. The distribution of electric field in the gap cross section for both modes is shown schematically in Figure 5.2. In the odd mode configuration the electric field penetrates the gap where the capillary resides, while in even mode the electric field is mostly outside the gap. In our experiments, the odd mode is used to characterize the presence of microspheres whilst the even mode is insensitive to the microspheres but can be used as a useful reference, for example, to account for small changes in temperature. The input and output power couplings of the resonator are mostly inductive owing to their positioning at a magnetic field antinode, with a smaller degree of capacitive coupling arising from the fact that they are extended structures and are made of open-circuit, microstrip sections.

5.1.2. Sensitivity enhancement of the SRR

It can be seen from the perturbation Equations 3.30 – 3.32, and their simplified counterparts Equations 3.34 and 3.35, that greatest SRR sensitivity to the presence of a single microsphere is attained when its mode volume V_m is reduced. This is most easily accomplished by reducing the ring radius r of the SRR. Table 5.1 shows the results of a COMSOL Multiphysics® 4.4 simulation of the SRR shown in Figure 5.1, with varying radii r, giving unperturbed resonant frequencies labelled f_0. As expected, to a good

approximation $f_0 \propto 1/r$ since the SRR's lumped inductance L is proportional to the ring area πr^2, and $f_0 \propto 1/\sqrt{L}$. The gap region is 70 μm deep (defined by the thickness of the copper cladding), with in-substrate gap widths of 35 μm × 35 μm to give a total geometrical volume of the gap of 8.58×10^4 μm^3 (i.e. 8.58×10^{-5} mm^3). We also simulate the perturbation on the SRR region imposed by inserting a single, spherical metal particle of radius 7.5 μm within the gap volume. The sphere volume is 2.1% of the gap volume, thus giving a small perturbation from which the mode volume V_m for SRRs of varying radii can be computed using Equation 3.30. The resulting decrease in resonant frequency Δf is also shown in Table 5.1. A metal sphere of radius a completely depolarises the electric field within it by developing an electric dipole moment $p = 4\pi\varepsilon_0 E_0 a^3 = 3\varepsilon_0 E_0 V_s$, where V_s is the volume of the sphere. This means that the mode volume V_m can be calculated from Δf of a metal sphere using

$$V_\mathrm{m} \approx -\frac{3V_\mathrm{s} f_0}{2\Delta f} \qquad 5.1$$

The resulting values for V_m are also shown in Table 5.1. The fact that V_m increases with increasing radius r is indicative of the fact that the electrical energy is not solely stored within the gap region, but occupies a much larger volume outside of the gap. This is associated with charge storage on the curved ring surfaces itself, which is more effective the larger the radius r. The main results of Table 5.1 are plotted in Figure 5.3, for the resonant frequency f_0 (Figure 5.3(a)) and also the mode volume V_m (Figure 5.3(b)) as a function of ring radius r.

Table 5.1: Dimensions of the split ring resonators showing in Figure 5.1 and the simulated results of the resonant frequency shifts.

r (mm)	w (mm)	Frequency, f_0 (GHz)	Δf (MHz)	$\Delta f/f_0$	V_m (mm^3)
1.75	0.5	9.8150	2.000	0.000204	0.01301
2.25	0.5	7.4280	1.200	0.000162	0.01641
3.50	1.0	4.9420	0.550	0.000111	0.02382
5.50	1.0	3.9093	0.325	0.0000831	0.03188
7.35	1.3	2.5073	0.150	0.0000598	0.04431

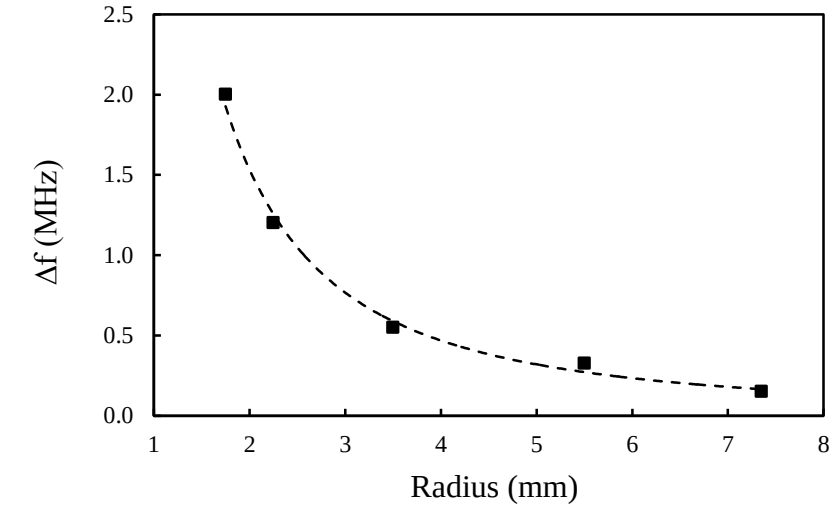

(a)

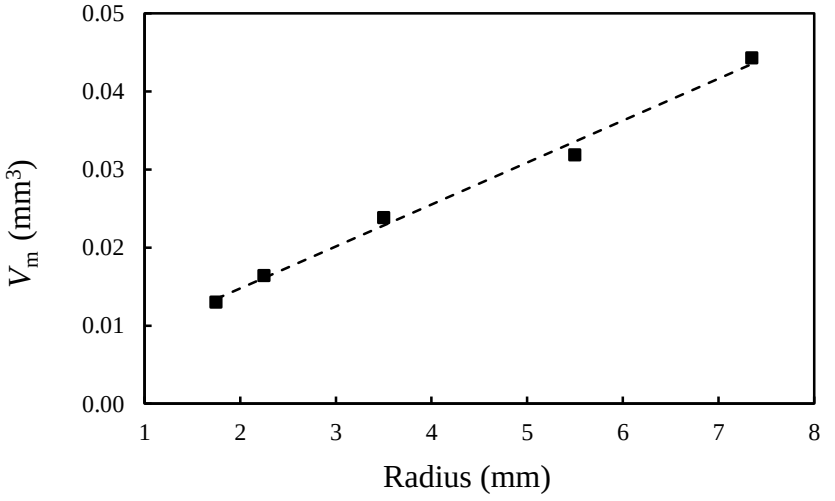

(b)

Figure 5.3: Simulated results of varying the ring radius r of the SSR. (a) Resonant frequency for different ring radii. (b) Effective volume for different ring radii (assuming a constant gap geometry).

5.2. Methods

The SRRs were fabricated by initial cutting of the ring shape and the gap structure using laser micromachining followed by fine finishing with a milling machine. The gap is defined in this way to a tolerance of 1 to 2 microns. A Rogers Corporation RT/duroid® 5880 laminate was used with a substrate (dielectric) thickness of 1.57 mm, relative permittivity of 2.20 ± 0.02 and loss tangent 0.0009. The thickness of the copper is 70 μm, which is chosen to be as thick as possible to ensure a higher quality factor *Q*. Polystyrene microspheres (*Alfa Aesar,* A Johnson Matthey Company) were chosen to

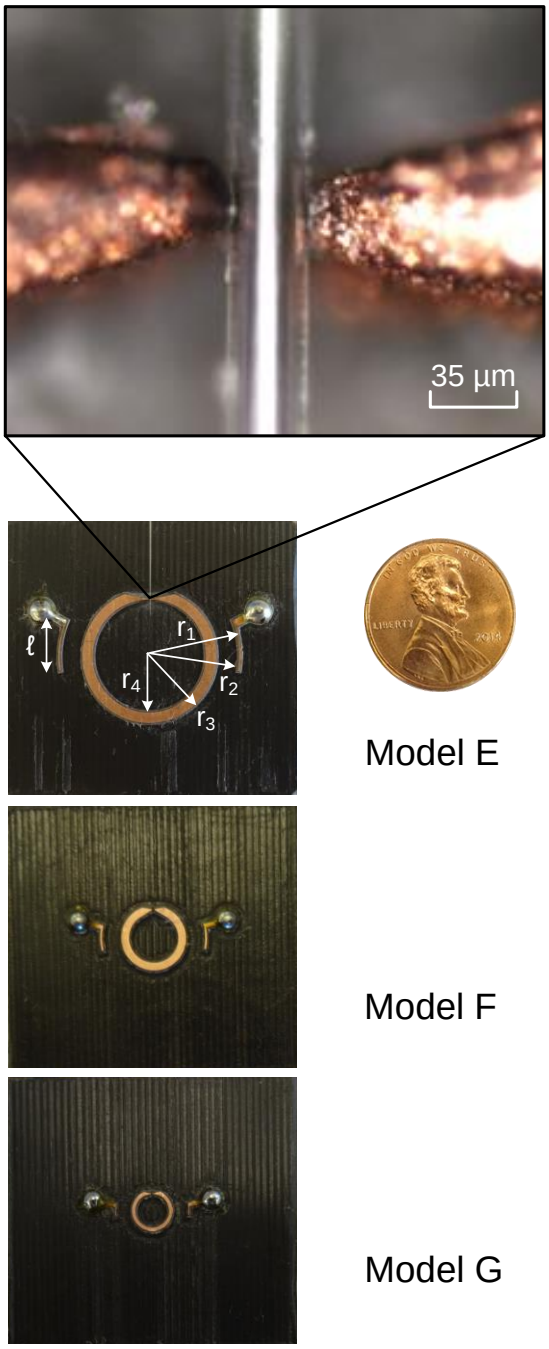

Figure 5.4: Photographs of the fabricated sensors E – G, with a magnified view showing the position of the glass capillary within the gap region.

validate the sensor, of 15 and 25 µm diameters. These were dispersed in water and passed through the glass micro-capillary with the aid of a syringe.

Three sizes of SRRs were designed to study the effect of the ring radius on the microsphere detection, here denoted models E, F and G; their dimensions are listed in Table 5.2. By changing the dimensions we change the mode volume V_m, which reduces

in going from model E to F to G, thus increasing their sensitivity to microsphere detection. In model E the gap was designed to be of width 35 μm, which is wide enough for two sizes of microsphere (diameters 25 and 15 μm) to pass through it, while in models F and G the gap and radius were reduced to increase the detection sensitivity of the smaller microspheres (diameter 15 μm).

The soda glass capillary (SAMCO company) with permittivity of 3.8, inner diameter of 1.3 mm, and outer diameter of 2 mm was heated to red hot and then pulled down to an outer diameter of 34 μm and inner diameter of 30 μm in the case of the model E sensor. For the models F and G sensors, the inner and outer capillary diameters are 28 and 23 μm, respectively. Figure 5.4 shows a photograph of the magnified gap region with the capillary, together with the layout for models E to G.

The constructional materials used here for the microwave microfluidic device comprised (i) an RT/duroid® 5880 laminate, with (ii) an integrated soda glass capillary. The laminate was chosen because of its favorable dielectric properties due to its PTFE – glass-fiber construction. Whilst, the method used here for integrating the glass capillary and the circuit board based SRR, do not conform to currently used microfluidic mass-production techniques [159], the proof of principle functional operation does demonstrate that further work is justified in order to more effectively integrate the use of microwave interrogation techniques with microfluidic flows. The materials used to form microfluidic circuits depends hugely on the production volumes required, their disposability, solvent resistance, creep specifications, electro-optical transmission characteristics, and range from silicon, glasses, polymers, metals, elastomers, paper, sapphire, and diamond [160]. PTFE based materials, especially Teflon AF, offer excellent dielectric properties, solvent resistance, and can be light transmissive, but, on the other hand, are more difficult to bond as integrated capillary structures, and are not so amenable to cost-effective micro-structuring as are silicon and glass. It highly likely that the integrated microwave-microfluidic detectors, such as that demonstrated here, could be fabricated as separate small-scale plug-in modules, that could be inserted within more complex electrofluidic motherboards, and that the recent advances in additive 3D manufacturing [161] could enable such hybrid assemblies made from diverse materials sets.

Table 5.2: Dimensions of the spilt ring resonators shown in Figure 5.4 (all dimensions are in mm).

Model	r_1	r_2	r_3	r_4	ℓ	gap
E	10.9	10.6	8.0	6.7	6.0	0.035
F	6.6	6.3	4.0	3.0	3.0	0.030
G	4.6	4.4	2.5	2.0	1.5	0.030

COMSOL Multiphysics® 4.4 was used to perform 3D simulations of the electromagnetic fields of the sensors with and without polystyrene spheres in water at 25 ºC. The EM waves model was used to simulate the S –parameters of the SRRs. The wave equation in the frequency domain was computed in the EM waves model as described in the software [162] according to Equation 4.4. As in previous simulations, the impedance boundary condition is used for the copper surfaces of the resonator and ground in order to incorporate the copper losses. The scattering boundary condition was utilized for the faces of the volume $40 \times 34 \times 40$ mm^3 (enclosing the device) to make the boundaries transparent for the scattered waves. Coaxial ports were used to feed the electromagnetic energy to the resonator. The relative permittivity of water ($\varepsilon = \varepsilon_1 - j\varepsilon_2$) was described in the simulation by using Debye Theory [1] as its permittivity is variable with frequency. The properties of the materials that were used in the simulation are shown in Table 5.3. The simulated and measured results of the three models E- G are illustrated in Figure 5.4.

Table 5.3: Material properties using in the simulation at 25ºC.

Material	ε_1	ε_2	σ (S/m)
Air	1	0	0
Microstrip Dielectric	2.21	0	3.17×10^{-4}
Copper	1	0	2.70×10^{7}
Polystyrene microsphere	2.10	0	0
Glass Capillary	3.80	0	1.00×10^{-12}
Water [128]	ε_s	ε_∞	τ (*p*se)
	78.4	5.16	8.27

In Figure 5.5 (a), the measured and simulated results of $|S_{21}|$ of the model E are shown for three cases: water only, water and 15 μm diameter microsphere, and water and 25 μm microsphere. The measured and simulated results of models F and G are illustrated in Figure 5.5 (b) and (c), respectively, for water and 15 μm diameter microsphere cases. In all models, the results shown in Figure 5.5 demonstrate that there is good agreement between the measured and simulated results.

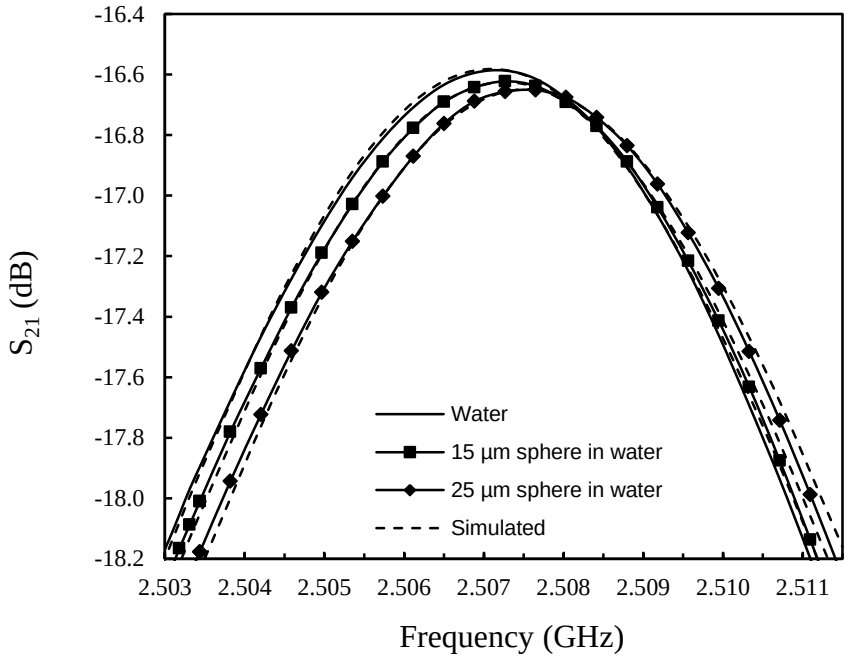

(a)

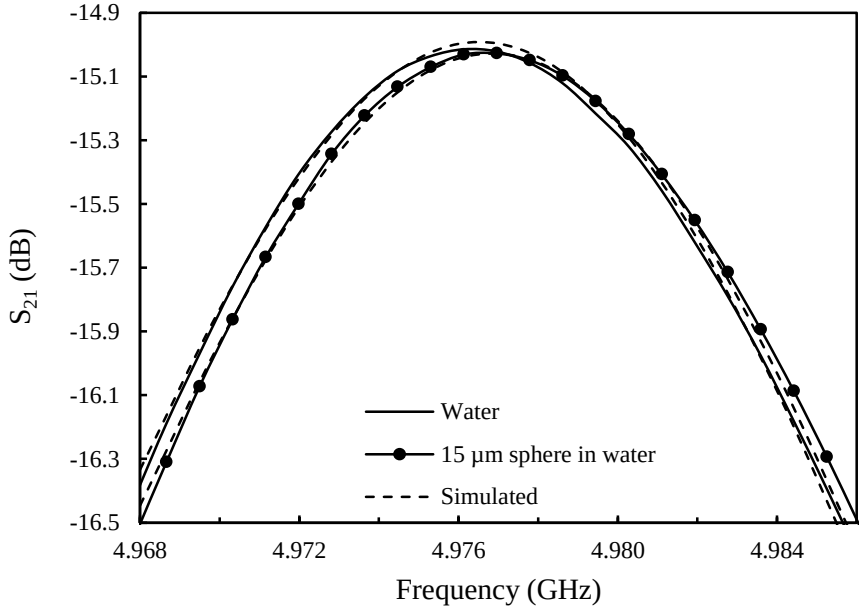

(b)

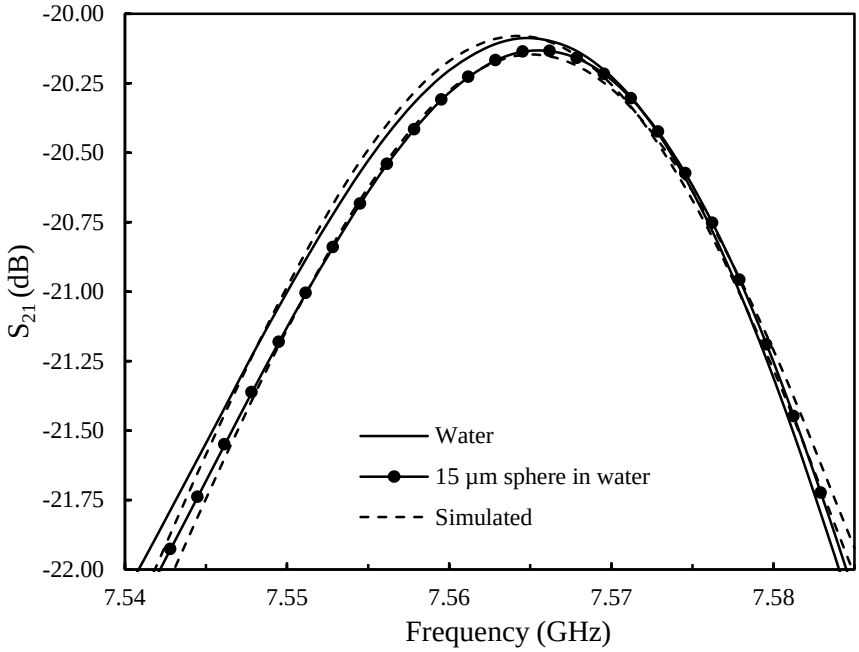

(c)

Figure 5.5: Measured and simulated S_{21} of the sensors with a single microsphere dispersed in water in the gap region. (a) Model E. (b) Model F. (c) Model G.

5.3. Results and discussion

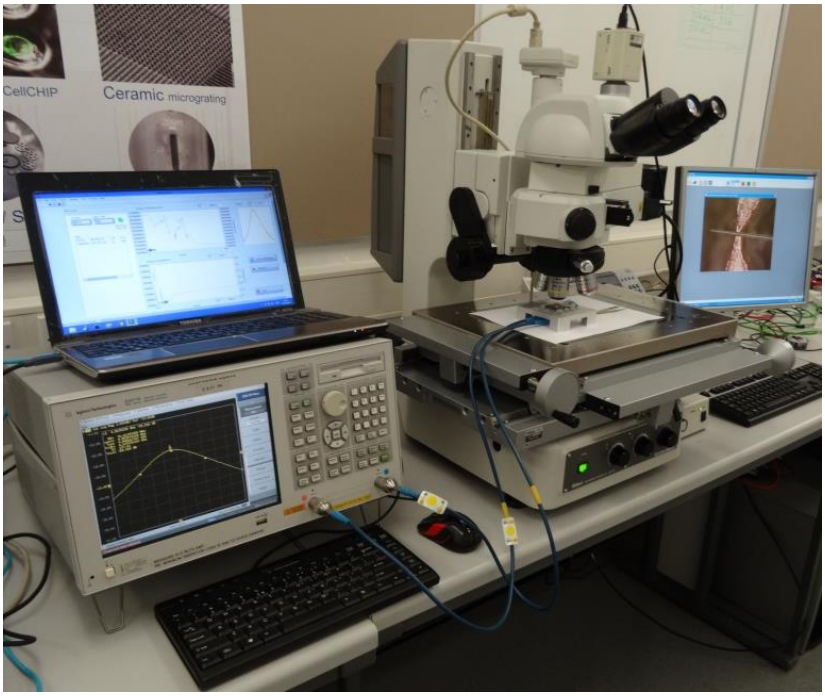

Figure 5.6: Photograph of the assembly of the sensor, network analyzer, laptop computer and optical microscope to aid positioning of the polystyrene microspheres in the gap region.

The bench-top assembly of the split ring resonator with the network analyzer, microscope and computer is shown in Figure 5.6. We consider first the results of model E, with a resonant frequency of approximately 2.5 GHz. Figure 5.7 shows the broadband transmission response (i.e. $|S_{21}|$) of the resonator's first (odd mode) and second (even mode) resonant frequencies.

The odd mode is perturbed by the dielectric properties of the material within the gap as there is a strong electric field there. Conversely, the even mode is almost unperturbed as its electric field is confined mostly between the ring and the ground plane. The changes in the resonant frequency and the insertion loss of the odd mode with time due to a flow of microspheres along the capillary are shown in Figure 5.8 (a) and (b), respectively. The results in Figure 5.8 were collected by a computer running a LabView program to record instantaneously the change in resonant frequency and insertion loss of both modes owing to the movement of the microspheres.

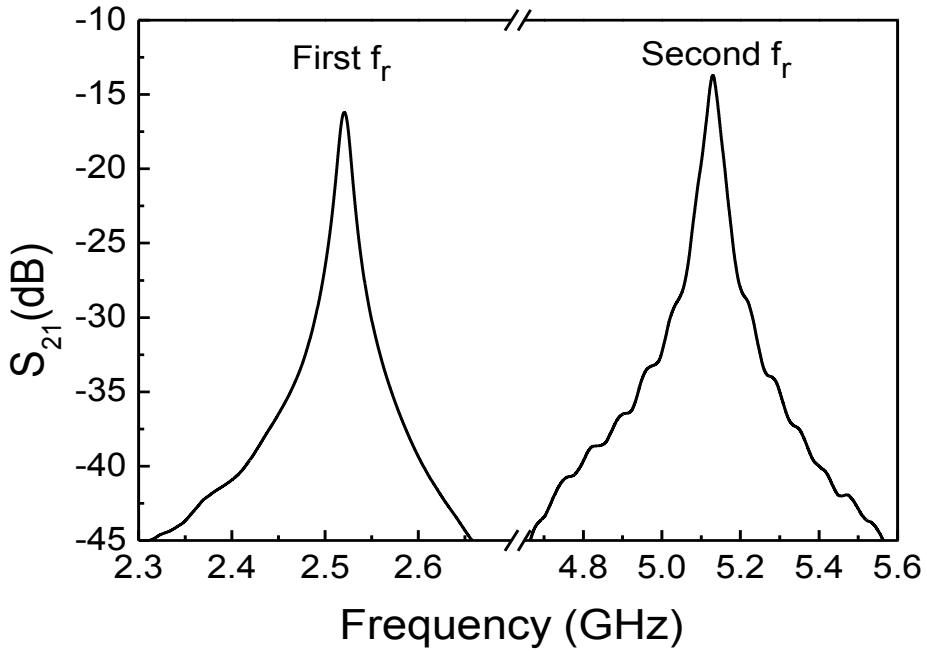

Figure 5.7: Measured broadband $|S_{21}|$ response of the split ring resonator (model E), showing the odd and even mode responses (the even mode has the higher frequency of the two).

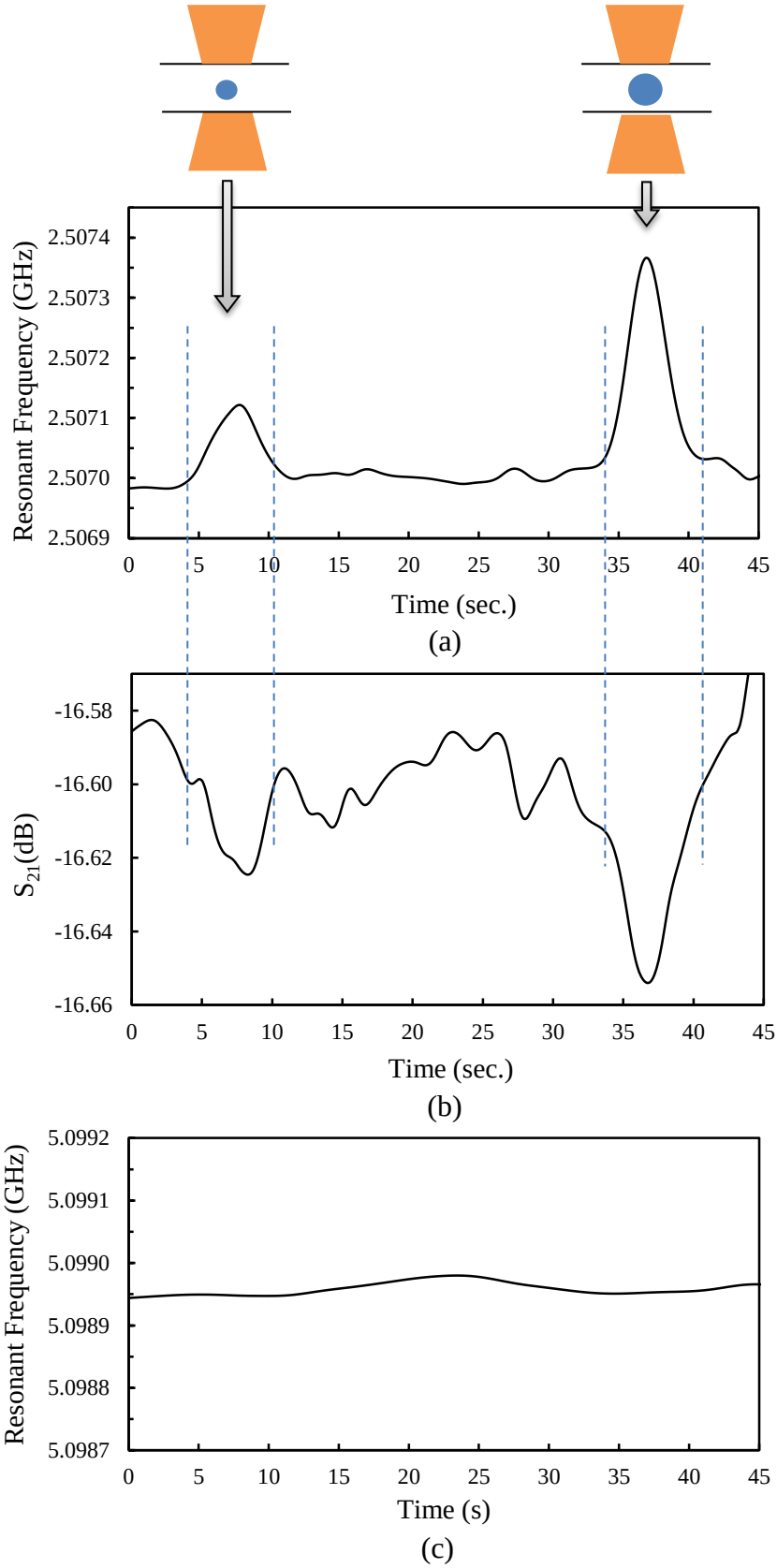

Figure 5.8: Variation of the resonator parameters with respect to time when a 15 µm diameter microsphere enters the gap region of model E (2.5 GHz), followed by a 25 µm diameter microsphere. (a) The resonant frequency of the odd mode, (b) the insertion loss of the odd mode, and (c) the resonant frequency of the even mode.

The $|S_{21}|$ data was fitted to a Lorentzian curve, from which the resonator parameters were extracted. The network analyzer was an Agilent E5071C, with an IF bandwidth of 10 kHz and 401 sweep points to give a sweep time of approximately 0.07 s. This is fast enough to capture enough data during the short time (around 2 s) when the microsphere occupied the gap region of the SRR. Increases in the odd mode resonant frequencies were measured to be 150 ± 8 kHz and 350 ± 18 kHz due to the presence of the 15 and 25 μm diameter microspheres, respectively. The increases in insertion loss were measured to be 0.030 ± 0.002 dB and 0.060 ± 0.003 dB, respectively.

Furthermore, there was no measured perturbation of the even mode with the same microsphere flow, as expected (Figure 5.8 (c)). Therefore, the even mode has the very useful property that its resonant frequency can be used to monitor (and indeed correct for) minute changes in temperature. This is essential in a practical device owing to the highly temperature-dependent complex permittivity of water. Otherwise, small increases in temperature could be inferred as being due to changes in the dielectric properties of the microspheres. The complex permittivity of the microspheres can be extracted from the resonator measurements using approaches in chapter four when the size of the microsphere is known. For example, in model E the extracted relative permittivity of microsphere is 2.1±0.1.

Whilst the perturbations on the resonator are small in the case of Figure 5.8, they can be unambiguously separated from the effects of small temperature changes. A change in temperature would cause the baseline to shift up or down, accordingly. However, this is likely to occur on a timescale which is much longer than the perturbations associated with the presence of the microspheres (typically less than 2 seconds), and these short term changes will be readily separated from the longer term effects of temperature drift.

To verify the usefulness of the even mode in correcting for temperature, the sensor was measured in a temperature-controlled oven (Memmert, Model: IPP 400) with a high degree of temperature control (±0.1 $^{\circ}$C) over the range from 20 to 32 $^{\circ}$C. The resulting fractional changes in resonant frequencies of both modes with temperature are shown in Figure 5.9. The resonant frequencies of both modes increase with temperature as the dielectric thickness expands with increasing temperature. The increase in frequency for the odd mode is some 30% larger than for the even mode due to additional expansion of

the gap width, which causes an additional frequency shift. The results of Figure 5.9 for the even mode can be used to deduce an accurate value of the temperature, and hence also the additional frequency shift in the odd mode caused by a change in temperature.

The increase in insertion loss when a microsphere is present is an interesting result that arises since the microsphere enhances the electric field inside the water filled capillary. This subsequently increases the dielectric losses, as has been discussed in detail in section 5.1.2.

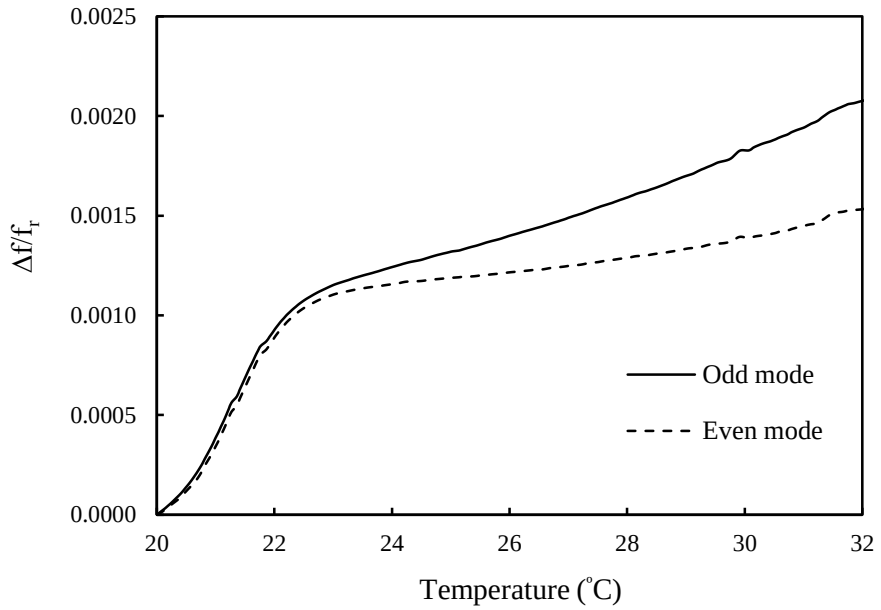

Figure 5.9: Change in the fractional resonant frequency with temperature $\Delta f/f_r$ of both odd and even modes.

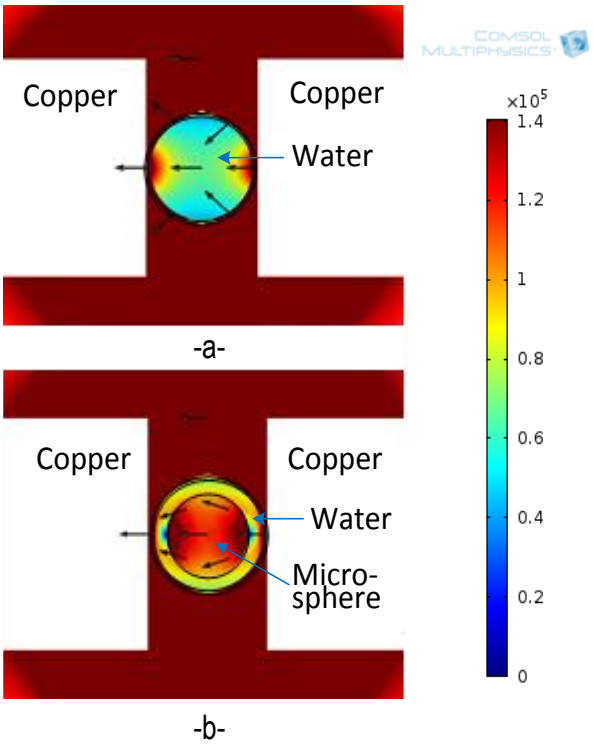

Figure 5.10: Electric field (V/m) in the gap region of the odd mode with a water-filled capillary (a) without microsphere, (b) with microsphere.

This explanation is supported by simulation, as can be seen in Figure 5.10 which shows the simulated electric field distribution on the cross section of the gap region. The simulations show that the volume integrated electric field intensity E^2 within the water surrounding a 25 µm diameter microsphere (Figure 5.10 (b)) is larger than when the microsphere absent (Figure 5.10 (a)).

To increase the ability of the sensor to discriminate the spheres with 15 µm diameter, or to deal with spheres (such as biological cells) which may not have such large differences in their permittivity with that of the host liquid, two smaller models F and G have been designed and tested.

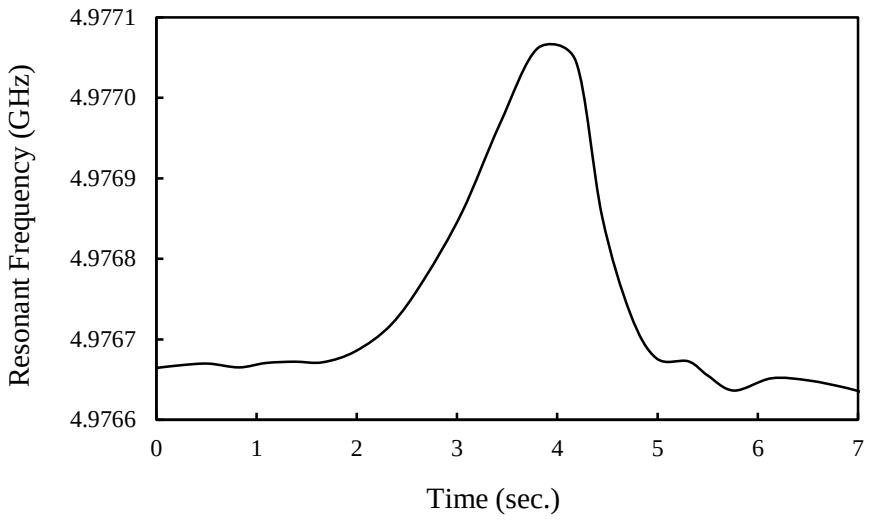

(a)

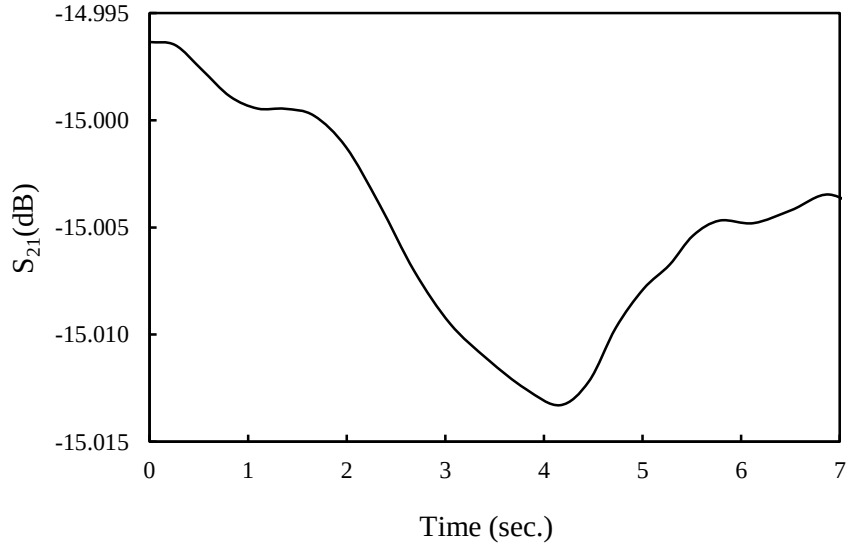

(b)

Figure 5.11: Variation of the resonator parameters with respect to time when a 15 µm diameter microsphere enters the gap region in model F (5 GHz). (a) The resonant frequency, and (b) the insertion loss.

In these two models the gap width was reduced to 30 µm and the ring radii were decreased to 3.5 and 2.25 mm for model F and G respectively, as shown in Table 5.2. In model F, the resonant frequency is set at 5 GHz and its S_{21} is shown in Figure 5.4 (b). The changes in the resonant frequency and amplitude (losses) are shown in Figure 5.11. The shift in resonant frequency is 400 ± 20 kHz and the increase in the insertion loss is 0.012 ± 0.001 dB, which is more sensitive to the 15 µm diameter microsphere than model E.

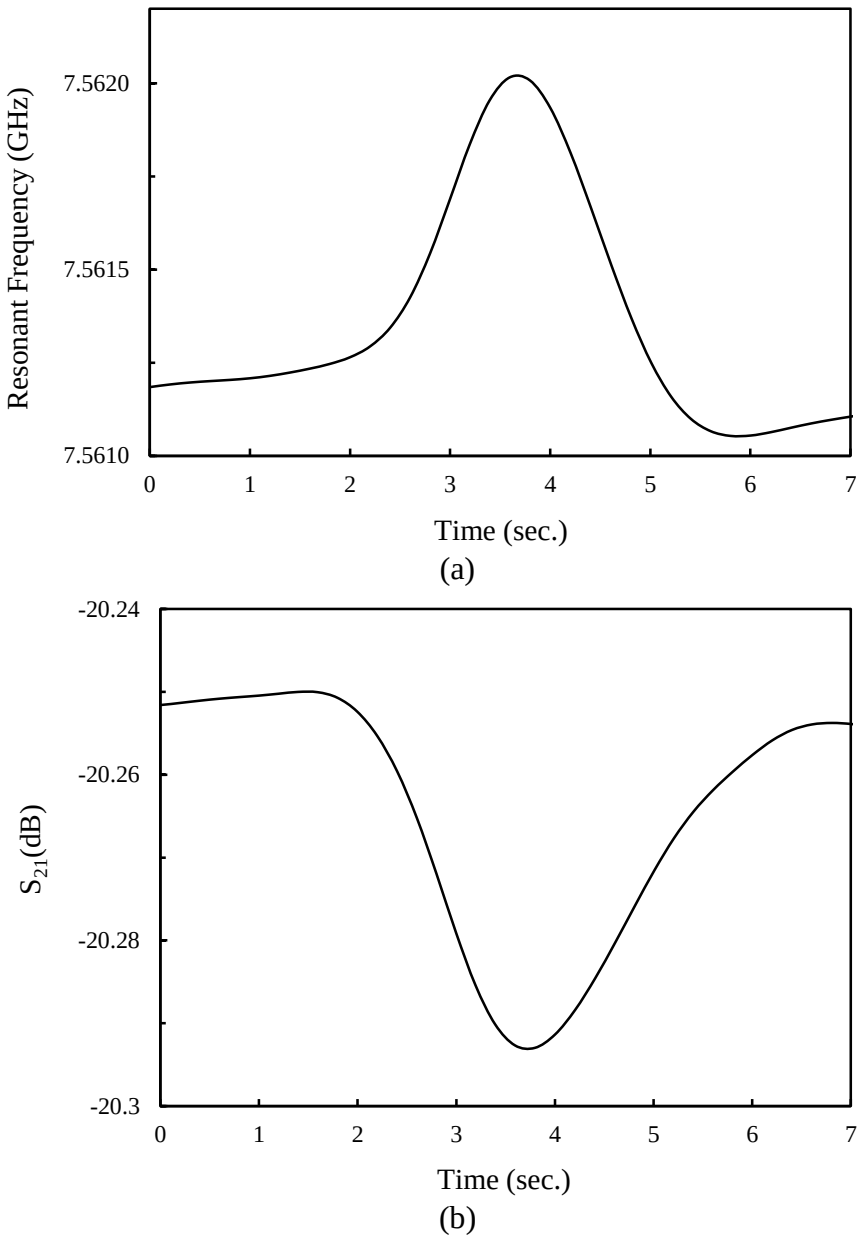

Figure 5.12: Variation of the resonator parameters with respect to time when a 15 μm diameter microsphere enters the gap region in model G (7.5 GHz). (a) The resonant frequency (b) The insertion loss.

More sensitive results have been obtained from model G, as shown in Figure 5.12. The shift in resonant frequency is now 1.00 ± 0.05 MHz and the increase of the insertion loss is 0.040 ± 0.002 dB when the 15 μm diameter sphere passes though the gap of model G.

The results have some variation due to small temperature drifts. The change in temperature arises due to the flow of water inside the capillary; the water needs to reach

thermal equilibrium to achieve stable, and hence accurate, results. In addition, the variation in results comes from the limitation of the network analyzer sensitivity as the changes in S_{21} are very small.

Finally, since the hope is to apply this sensor for the detection of human cells, a simulation has been performed of the SRR with the 15 micron microsphere replaced by a "white blood cell" with diameter of 12 μm [155] of representative permittivity of 10 and conductivity of 0.5 at 7.5 GHz [163] as shown in Figure 5.13. In the smallest SRR (model G) this gives a frequency shift of 0.5 MHz, so we expect our method to be able to quantify both the presence, and measure the complex permittivity, of individual cells.

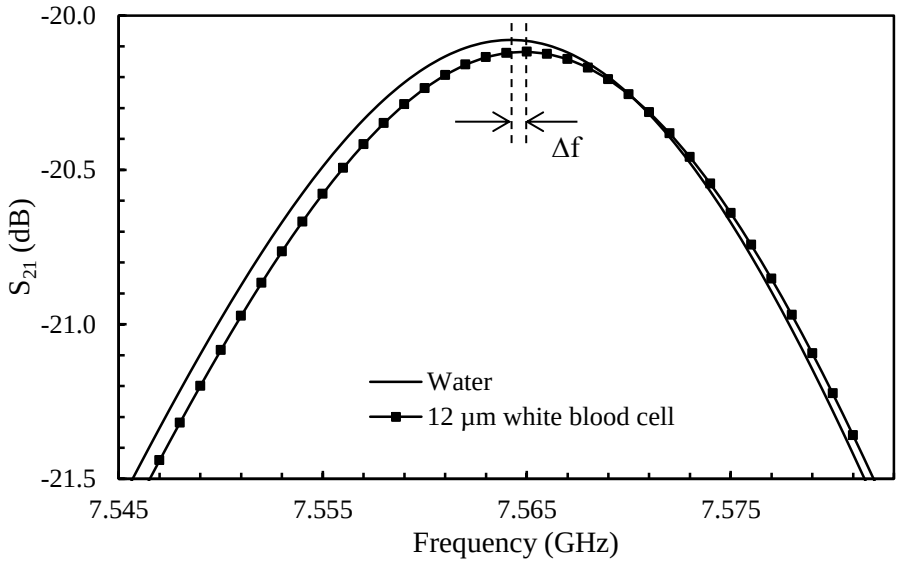

Figure 5.13: Simulated S_{21} of the model G sensor with a single white blood cell dispersed in water in the gap region.

CHAPTER 6 - DUAL MODE MICROWAVE MICROFLUIDIC SENSOR

A common problem in microwave microfluidic sensors is temperature variation, as the liquid permittivity is often very sensitive to the change in temperature (water being an example) which yields to inaccurate measurements. Several works have been dedicated to solve this problem. In [164] the error frequency shift of the resonator due to the temperature effect on the sample dielectric properties was determined by using reference measurements in which the resonator does not need cooling. Another idea was proposed by us in chapter five where the even mode can be used to monitor (and indeed correct for) minute changes in temperature. However, there is still a small influence of the sample on the even mode, which complicates the correction process.

A new, versatile sensor is proposed in this chapter which has an in-built reference resonant frequency which is almost completely insensitive to the presence of the dielectric sample, and so can be used to monitor the temperature changes and hence to calibrate the dielectric measurements accordingly. Such separation of the responses of measurement and reference sensor is accomplished by the design, which uses separate resonators for each function. The block diagram of the sensor is shown in Figure 6.1 that illustrates the principle of using the two resonators; one is for liquid sample characterization and other for temperature calibration.

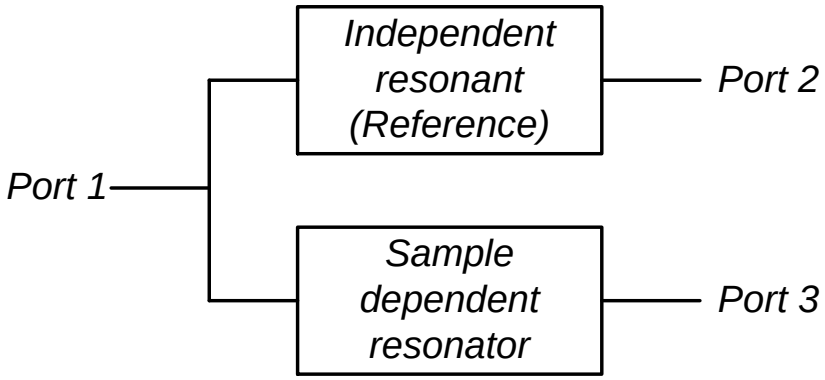

Figure 6.1: A block diagram of the concept of the dual-mode microstrip sensor (DMS), incorporating two independent resonators, only one of which is sensitive to the presence of a liquid sample.

This chapter is structured as follows: in Section 6.1, brief concepts and theory of the perturbation theory, the temperature dependence of liquids and the microstrip resonators adopted, and the use of LabVIEW interface are presented. We label this type of sensor "DMS" i.e. dual-mode mircostrip sensor. Experimental methods, which include the description of the sensor design and fabrication (together with simulation results), are presented in Section 6.2. In Section 6.3, the experimental results are demonstrated and discussed.

6.1. Brief theory and concepts

6.1.1. Resonance perturbation

A half wavelength microstrip resonator is adopted to build the DMS sensor as shown in Figure 6.2. In this structure the electric field energy is stored predominantly in the microstrip's dielectric. If the sample capillary is filled with a liquid sample and is inserted within the dielectric, under the end of the quarter ring (as shown in Figure 6.2), a material perturbation will occur which causes a shift in the resonant frequency [140], estimated to a good approximation by the first order cavity perturbation equations as given in Equations 3.30 and 3.31. As with the sensors described in earlier chapters, a reduction in the resonant frequency and Q can be exploited to measure the permittivity of the liquid within the capillary, with the added benefit for the DMS of the ability to correct for changes in ambient temperature.

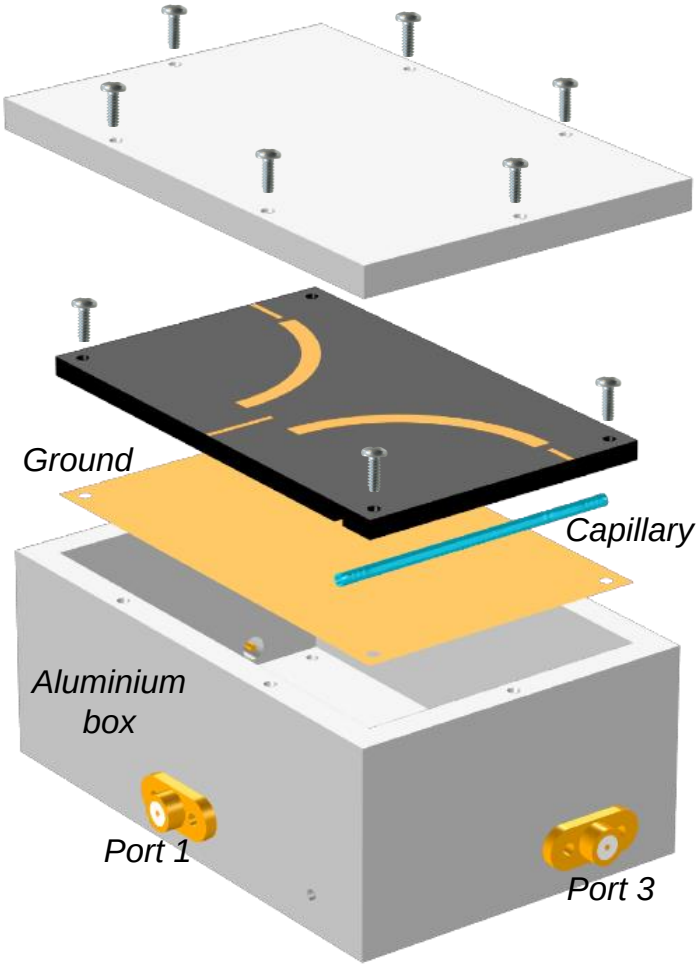

Figure 6.2: Schematic of the dual mode microstrip sensor DMS inside aluminium cavity.

6.1.2. Temperature dependence

There are two temperature-dependent factors that cause inaccurate measurements of dielectric property measurements of liquids when using microstrip-based resonant sensors; the change in liquid permittivity with temperature, and the changes in resonator dimensions and dielectric constant of the microstrip. For polar liquids, the permittivity at certain frequency is given in [1],[138], and [139], also in Equations 3.10 and 3.11. Both real and imaginary parts of the liquid permittivity decrease with temperature, which make Equations 3.30 and 3.31 temperature dependent and so will affect the permittivity measurement.

The length and width of the microstrip line expand with temperature. The change in the microstrip line length Δl with temperature is given (to first order in changes in temperature) by [165], [166] as:

$$\Delta l = l\alpha_l \Delta T \tag{6.1}$$

where α_l is the linear thermal expansion coefficient of the copper making up the microstrip line (where $\alpha_l = 16.5 \times 10^{-6}/^o C$). The value of the substrate dielectric permittivity and the thickness of the dielectric also change with temperature. Similarly to Equation 6.1, the change in the dielectric constant $\Delta\varepsilon_r$ with temperature is given by [165], [166] as:

$$\Delta\varepsilon_r = \varepsilon_r \alpha_r \Delta T \tag{6.2}$$

where α_r is the temperature coefficient of the dielectric constant ($\alpha_r = 173 \times 10^{-6}/^o C$ for RT/Duroid 5870 laminate). The combination of the expansion in the microstrip line dimensions (length and width) and dielectric thickness, and dielectric constant variation with temperature will all increase the resonant frequency [167]-[169] as the temperature is increased.

6.1.3. LabVIEW Interface

As has been described, in order to obtain dielectric measurements, accurate measurement of the resonator Q and frequency is required. Instrument noise is minimized by extracting resonator parameters from the coefficients of a fitted Lorentzian curve to measured power transmission co-efficient in frequency domain. The power transmission coefficients between port 1 and 2, or between 1 and 3, can be written generally as:

$$\left|S_{21,31}\right|^2 = \frac{4g}{(1+2g)^2+4Q_o^2\left(\frac{f-f_0}{f_0}\right)^2} = \frac{P_0}{1+4Q_L^2\left(\frac{f-f_0}{f_0}\right)^2} \tag{6.3}$$

where g is the coupling coefficient (assumed equal, i.e. symmetric, at each port), f_o is the resonant frequency, $Q_L = Q_o(1-\sqrt{P_o})$; P_o is the power transmission coefficient at

resonance, which is related to the value of coupling coefficient. This unloading procedure for Q relies on there being symmetric coupling, which is attained experimentally by having equal coupling gaps between the port feedline and the microstrip line of each resonator. Furthermore, this method is often regarded as the most accurate for low SNR, as is the case here with low resonator Q, unlike a marker based bandwidth approach using data taken directly from the network analyzer.

A program was created in LabVIEW to interface with the network analyzer and simultaneously measure S_{21} and S_{31}. The curve fitting procedure, also implemented in LabVIEW, utilizes the Levenberg-Marquardt algorithm to find a fit minimizing the mean squared error between the data and fit.

In an environment where the temperature is changing, it is important that frequency sweep times are minimized in order to reduce the effect of a changing response during the sweep. This requirement necessitates the reduction of the number of frequency points, which in turn requires the reduction in measurement span in order to maintain accuracy. Therefore, the measurement program was designed to continually adjust the measurement window to track the resonance peak.

6.2. Experimental methods

The DMS design is based on the idea of two microstrip resonator sensors excited simultaneously with one input port. The first sensor is used to characterize the liquid sample and the second one is dedicated to determine the change in the ambient temperature, since the liquid and all resonator elements (copper and dielectric dimensions and material properties) are functions of temperature. A half wavelength microstrip line is adopted for the design of the sensor, which is a half wavelength resonator with open circuit ends (where the electric field will be a maximum). The resonant wavelength is then related to the length of the strip by [170]:

$$l = n\lambda_g/2 \qquad 6.4$$

where $\lambda_g = v_p/f = \lambda_g/\sqrt{\varepsilon_{eff}}$ and n integer, allowing resonant frequency to be calculated. The effective permittivity ε_{eff} can be calculated used standard means (e.g.

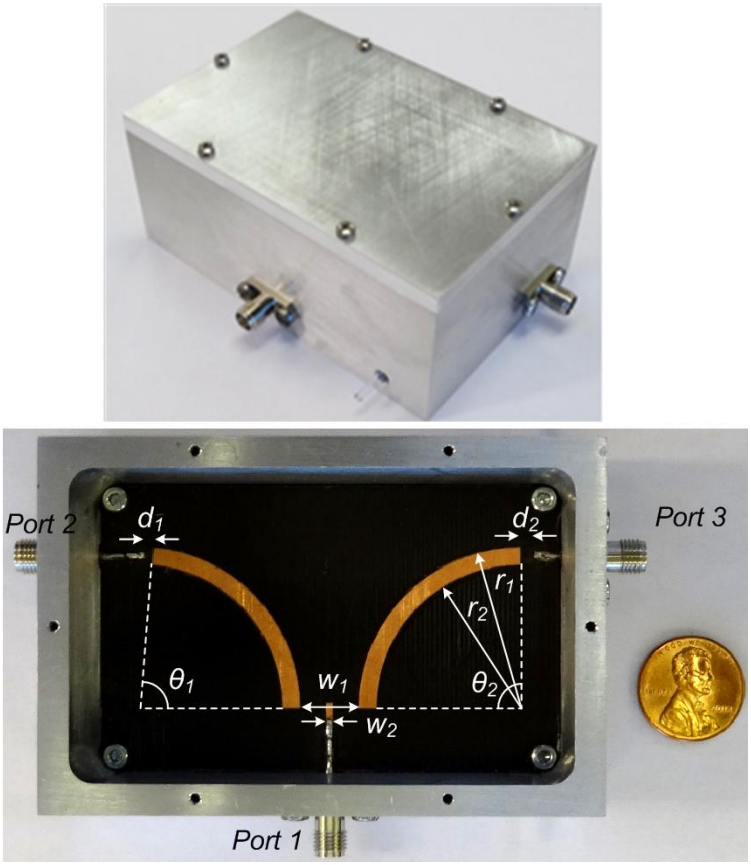

Figure 6.3: Photograph of the fabricated sensor with three ports.

Table 6.1: Dimensions of the sensor shown in Figure 6.3, (all dimensions are in mm).

i	r_i	θ_3(deg.)	w_i	d_i
1	24.9	85	10.2	1.6
2	27.9	90	1.0	1.6

LineCalc, within Keysight's ADS software). The resonators were fabricated by mechanical milling of a Rogers Corporation RT/Duroid 5870 laminate, with a dielectric of thickness of 3.18 mm, relative permittivity of 2.33±0.02, and loss tangent of 0.0012. The thickness of the copper is 35 µm. All of the dimensions are illustrated in table 6.1.

In order to avoid undesirable field coupling between the two resonators [171], they were designed to have two different resonant frequencies (2.53 GHz for the liquid loaded resonator, with the reference resonator at 2.65 GHz, i.e. 120 MHz shift between them). This was done by making them slightly different lengths, as shown in Figure 6.3 and table 6.1. This minimises any interference between them when liquid sample is under test, and brings the frequency of the loaded resonator into the range 2.45 to 2.50 GHz, i.e. one of the industrially important IMS bands.

The position of the capillary was chosen to be between the end of the microstrip line resonator and the ground through the dielectric, as shown in Figure 6.2, to obtain maximum perturbation of the resonator as the electric field will be highest here. A duct of dimensions 2×2×50 mm was milled on the back side of the microstrip board to hold the capillary and then the duct was finally layered by copper sheet. A soda glass capillary (SAMCO company) with inner diameter of 1.4 mm and outer diameter of 2 mm and permittivity of 3.8 is used to hold the liquid.

Several approaches have been used to increase the quality factor of the resonators which helps to increase the sensitivity of the sensor. In [40] a passive ring resonator with an active feedback loop to generate negative resistance and compensate for the resonator's loss was proposed, which in return significantly increases the quality factor of the system. In this work, the microstrip resonator board was set inside rectangular cavity (an aluminum box), which increases the quality factor from 80 to 360 by reducing the radiation loss from the structure. This is approximately the optimal *Q* expected for the resonators, given the loss tangent of the substrate and the surface resistance of the copper conductors, each of which give a dielectric *Q* and conductor *Q* of about 800.

The size of the cavity is designed to be small enough to that its own resonant frequencies are much larger than the resonant frequencies of the sensor to avoid the interference between them. The microstrip board is fixed on the bottom of the box by four metal screws, as shown in Figure 6.2, and the capillary is inserted into the microstrip board through the holes in the outer rectangular cavity. SMA connectors were connected to the sensor via the box to connect to the network analyzer. COMSOL Multiphysics® simulations were performed for the sensor with an empty, chloroform filled, and water filled capillary at 25ºC. The complex permittivities of the liquids (water and chloroform) are assumed to have real and imaginary parts which are well described by Debye theory [1]. Values of the Debye parameters for water and chloroform at an ambient temperature of 25ºC were taken from [128], the same as those used in earlier chapters. The simulated and measured results are illustrated in Figure 6.4, showing good agreement between the two.

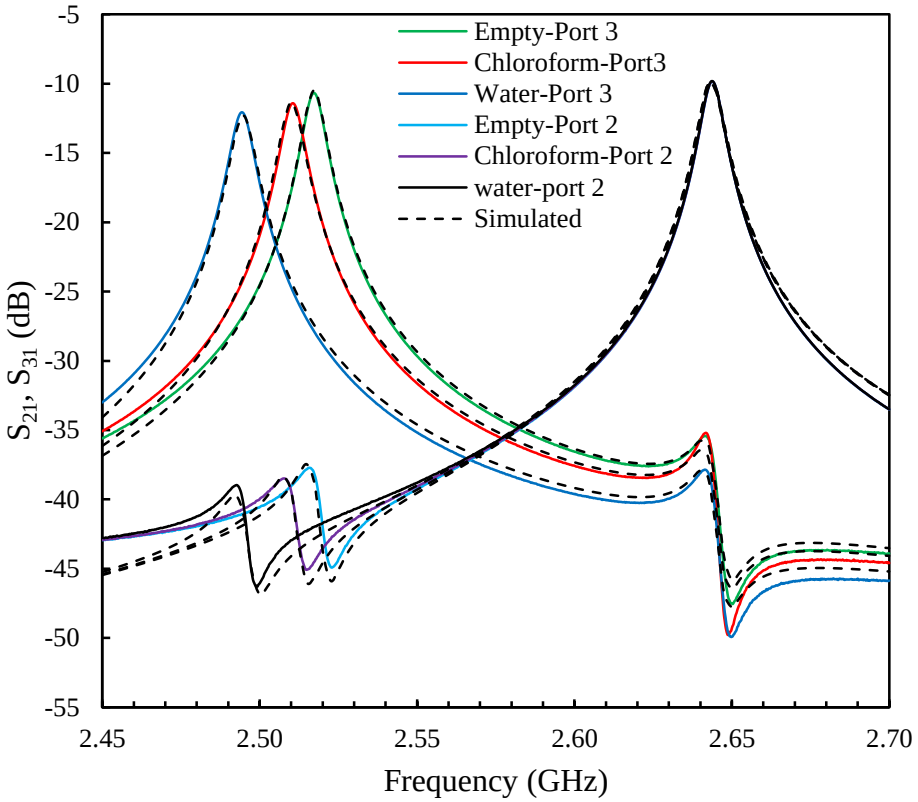

(a)

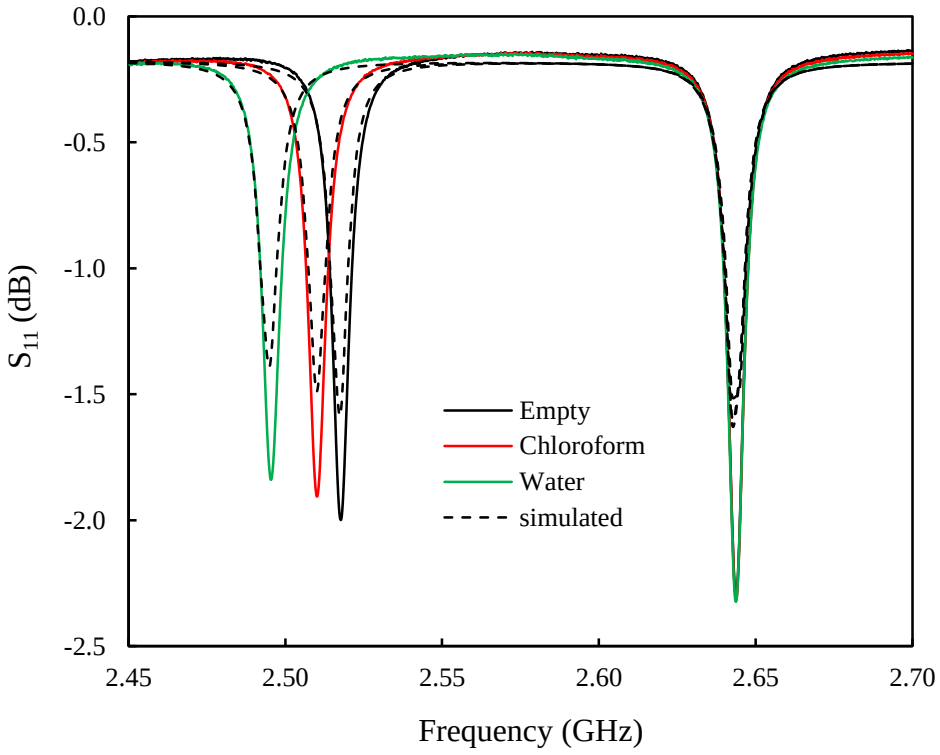

(b)

Figure 6.4: Measured and simulated S-parameter of the sensor with empty, chloroform, and water filled capillary. (a) S_{21} and S_{31}. (b) S_{11}.

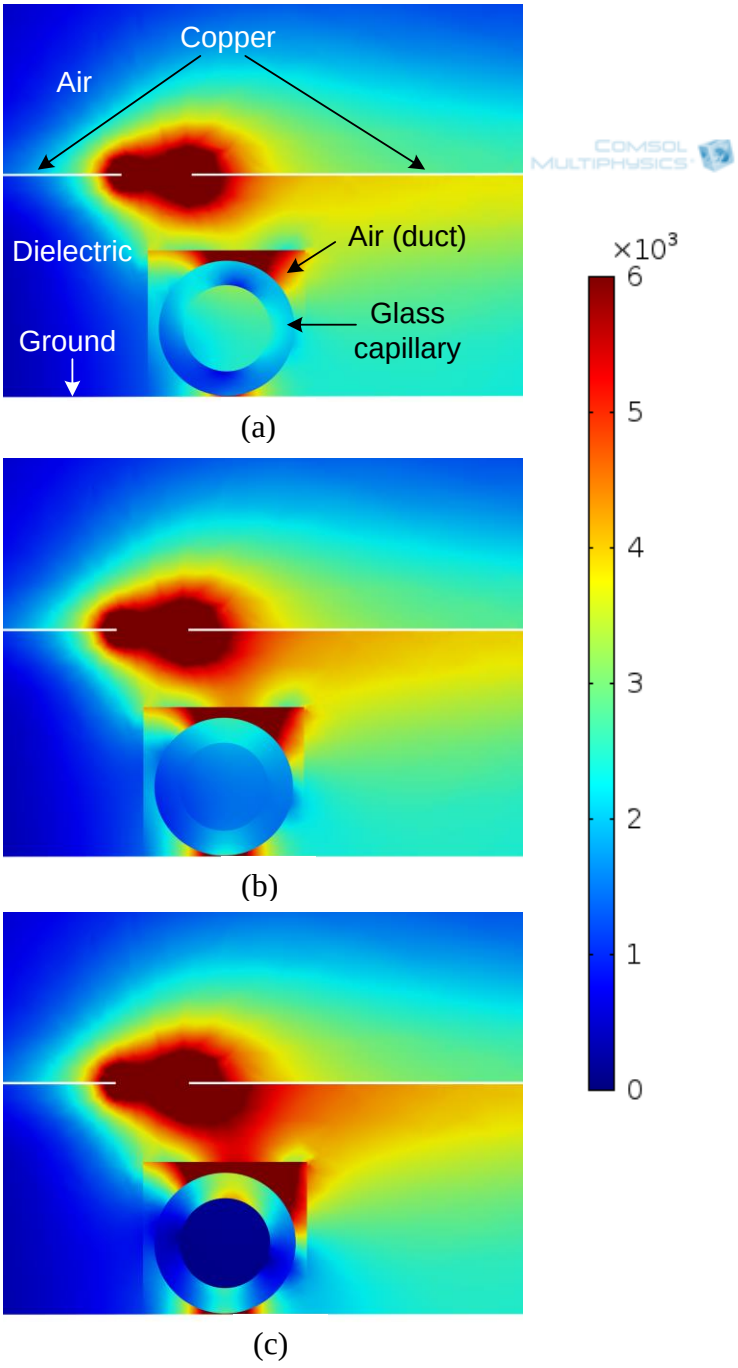

Figure 6.5: Electric field distribution in the cross section of the end of the sensing resonator of the sensor (V/m), generated by a COMSOL simulation: (a) With empty capillary. (b) With chloroform-filled capillary. (c) With water-filled capillary.

The distribution of the electric field of the cross section of the coupling end of the sensing resonator (sensing branch) of the device is illustrated in Figure 6.5, which was performed by using COMSOL Multiphysics®. Figure 6.5 shows three cases: empty capillary, chloroform-filled capillary, and water-filled capillary. In the case of empty capillary, the electric field concentrates between the edges of the resonator and coupling

strips and on the top of the capillary at the 2.517 GHz resonant. The presence of the chloroform in the capillary, as shown in Figure 6.5(b), increases the intensity of the electric field at the polar regions outside of the capillary, and reduces it inside the capillary at the resonant frequency of 2.510 GHz. When the capillary is filled with water, the electric field is strongly concentrated at the resonant frequency of 2.494 GHz between the edges of the resonator and the coupling strip, and the capillary (much more than the values of the two previous cases). The field inside the capillary is much less than outside it and also the previous two cases, due to the highly polar nature of water causing large reduction (depolarisation) of the internal field.

6.3. Results and discussion

To verify the sensor performance, a temperature scan was applied. An oven (Memmert, Model: IPP 400) with a high degree of temperature control (±0.1ºC) was used to heat the sensor from 23 to 35ºC. The rise time was set to be very slow (five hours) to ensure approximate thermal equilibrium among all parts of the sensor, capillary, and the liquid.

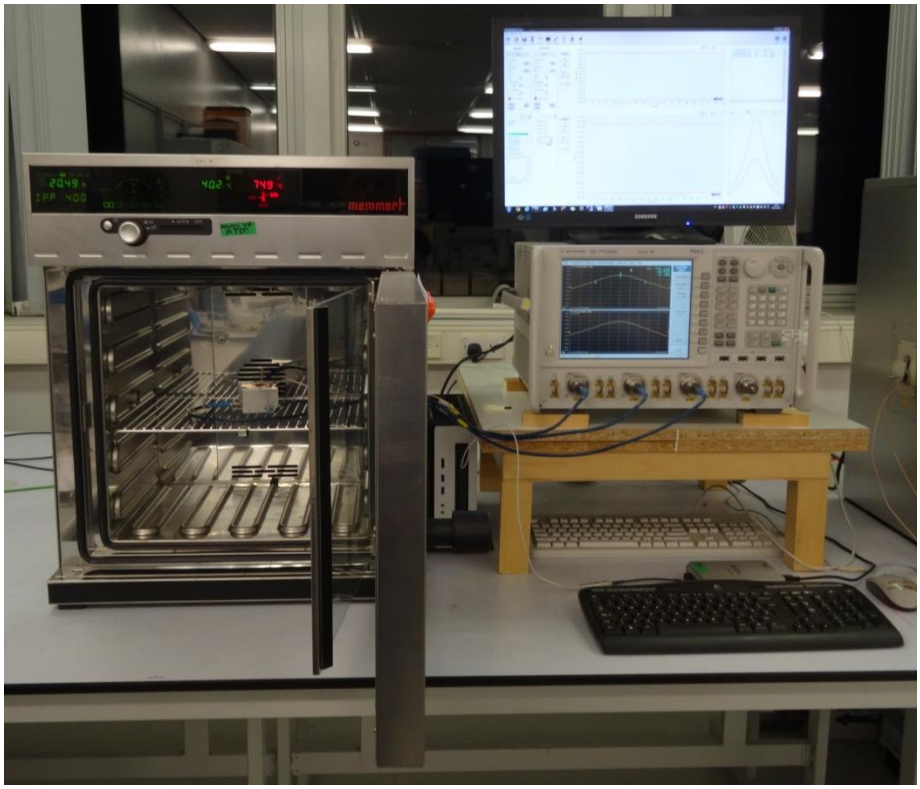

Figure 6.6: Photograph the bench-top experimental assembly. The sensor is put inside a computer-controlled oven and connected to an Agilent PNA-L N5232A network analyzer under LabVIEW program control.

The bench-top assembly of the sensor inside the oven with network analyzer and LabVIEW control program is shown in Figure 6.6. As the sensor has three ports (one for input and two for outputs) the PNA-L N5232A network analyzer (Agilent technologies) with four ports is used to measure the S- parameters (S_{11}, S_{21}, S_{31}) of the sensor as function of temperature. Moreover, a LabVIEW program has been developed to collect the results from the network analyzer and from a temperature sensor, which is a platinum resistance thermometer connected to the microstrip ground.

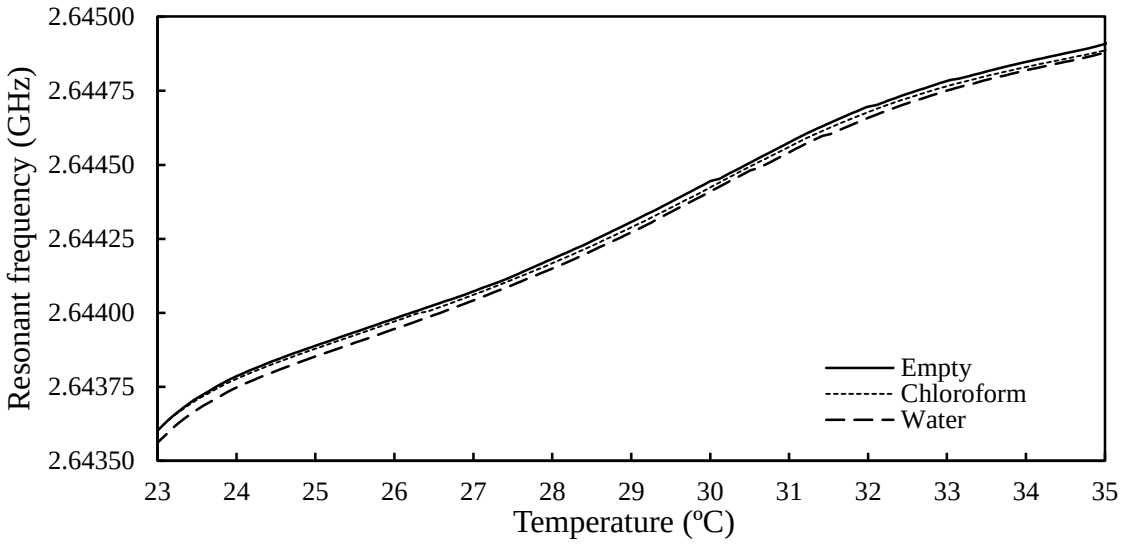

(a)

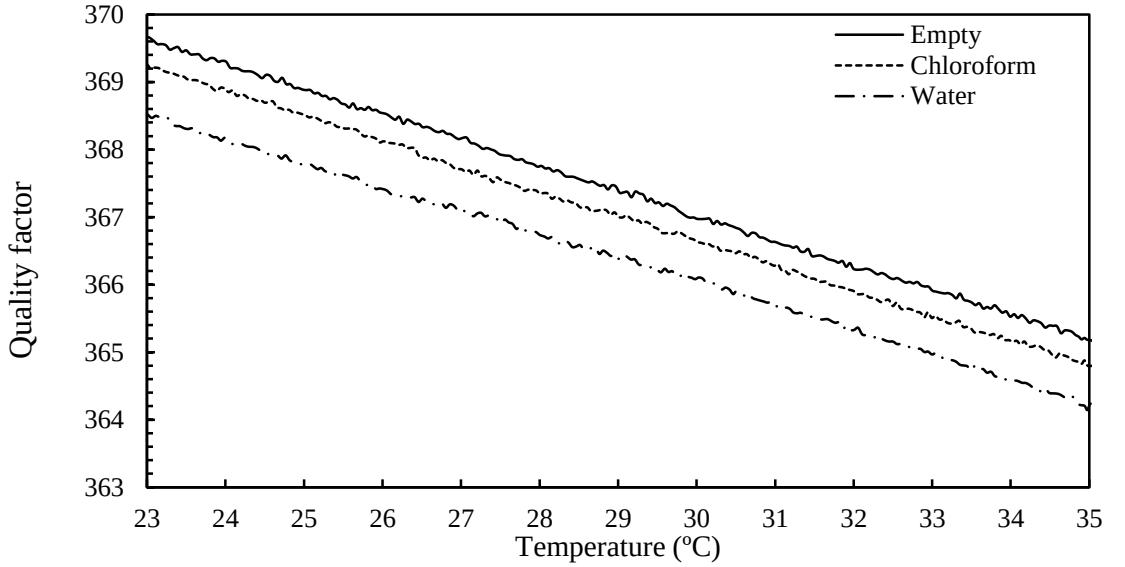

(b)

Figure 6.7: Port 2 measurements of the reference resonator with temperature, when the sensor resonator contains empty, chloroform, and water filled capillaries. (a) Resonant frequency, and (b) quality factor.

As shown in Figure 6.7 (a), when the microwave measurement was taken from port 2 (reference port) when undertaking the temperature sweep, the resonant frequency was found to increase with temperature. This behaviour is explained in Section 6.1.2, as the effect of the thermal expansion of the dielectric thickness expansion with temperature is the dominant over all other parameters (copper thermal expansion and the temperature coefficient of the dielectric constant of the substrate). This decreases the distributed capacitor of the microstrip and so increases the resonant frequency. Moreover, the losses have increased with temperature as shown in Figure 6.7 (b) as the conductivity of the copper decreases.

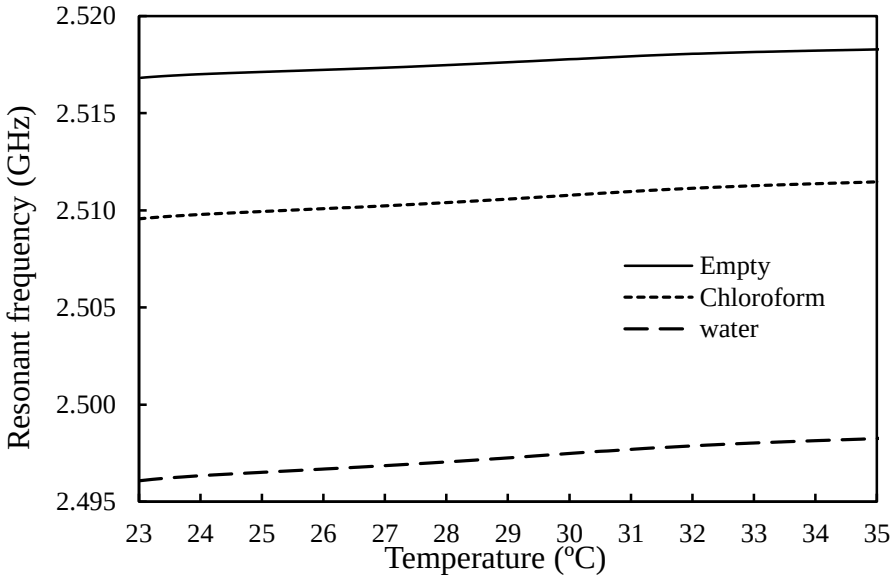

(a)

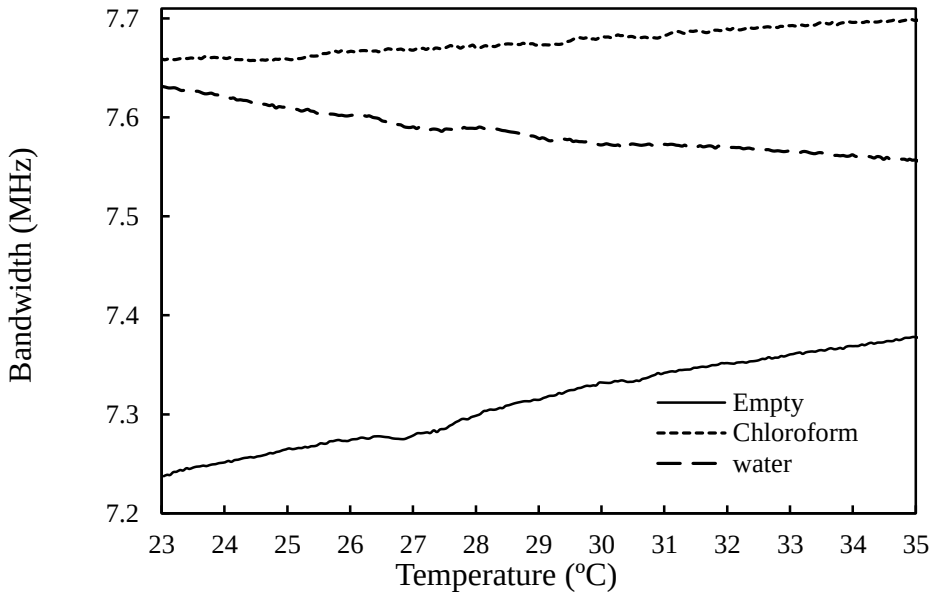

(b)

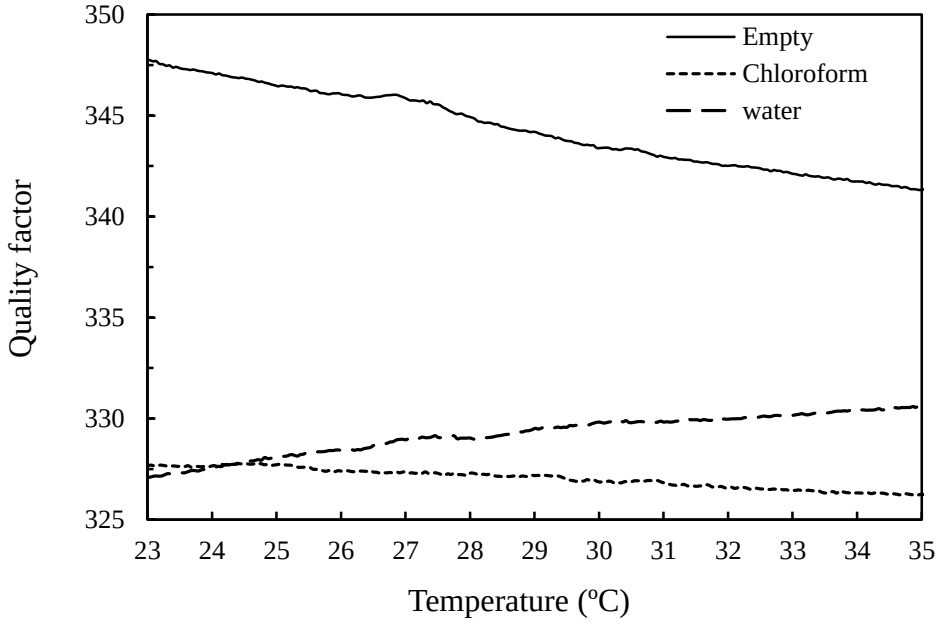

(c)

Figure 6.8: Port 3 measurements with temperature for empty, chloroform, and water sample. (a) Resonant frequency, (b) bandwidth, (c) quality factor.

Comparatively, the changes in resonant frequency measured from port 3 when the capillary is empty are very similar to those from port 2 (for the sensor resonator), with some minor differences as the structures are not identical; e.g. due to the present of the duct in one, as shown in Figure 6.8 (a). The resonant frequency of reference resonator (port2) at 23ºC is 2.6436 GHz, and at 35ºC is 2.6449 GHz which means that the shift in the resonant frequency is +1.3 MHz. In the case of the empty capillary resonator (port 3) the resonant frequencies at 23 and 35ºC are 2.5168 and 2.5183 GHz, respectively, and the shift in this case is +1.5 MHz.

The sensor then was tested with the two liquids chloroform (weakly polar) and water (strongly polar). The change in the resonant frequency, 3 dB bandwidth, and quality factor with temperature from port 3 with chloroform filled capillary are shown in Figure 6.8. The shift in resonant frequency over the range of temperature sweep is about 1.91 MHz. There are also changes in the bandwidth and quality factor. In the case of water, the shifts in resonant frequency, losses, bandwidth, and quality factor will be larger as illustrated in Figure 6.8. The resonant frequency increases from 2.4961 GHz at 23ºC to 2.4983 at 35ºC with shift of 2.2 MHz. The resulting fractional changes in resonant frequencies of both resonators (port 2 and 3) with temperature are shown in Figure 6.9.

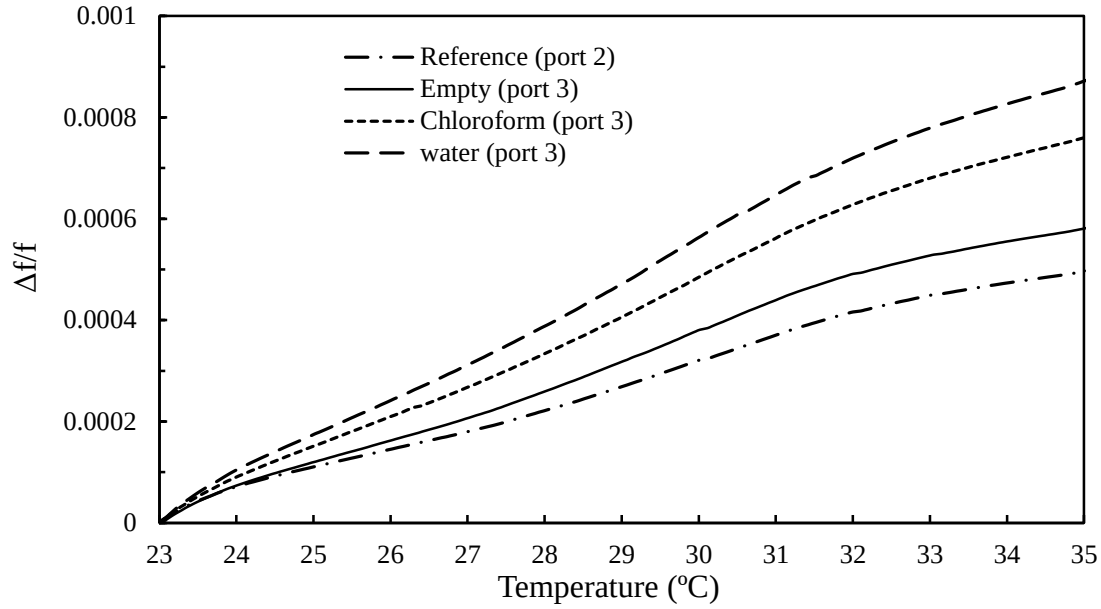

Figure 6.9: Change in the fractional resonant frequency with temperature Δf/fr of both resonators (port 2 and port3).

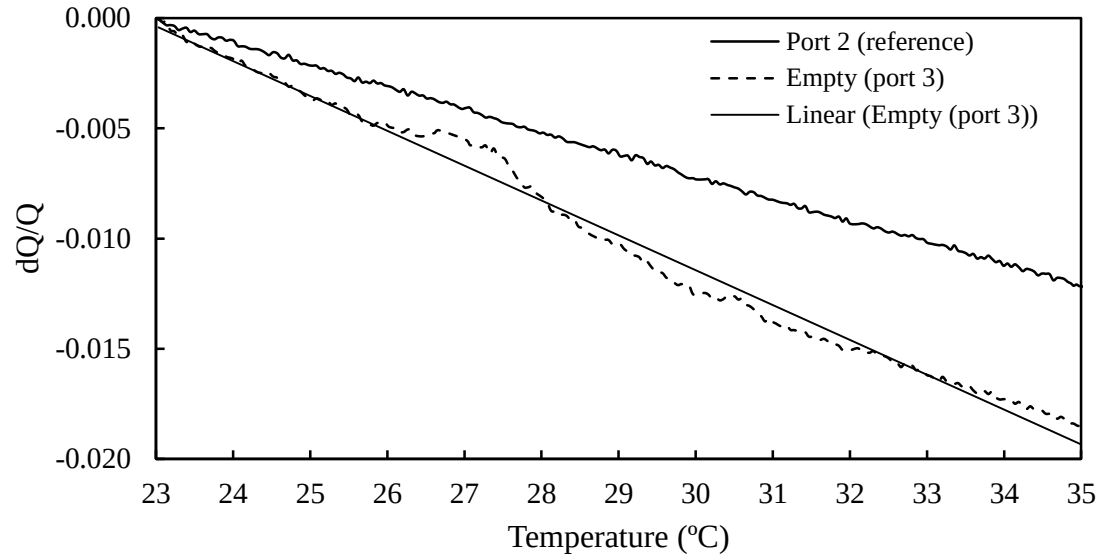

Figure 6.10: Change in the fractional quality factor with temperature ΔQ/Q of both resonators (port 2 and port3).

Moreover, Figure 6.10 shows the change in the fractional quality factor with temperature between the reference resonator (port 2) and the port 3 with empty capillary the results can be approximated to linear relationships in which can be used to determine the losses of the port 3 from the losses of the port 2.

All these results show the need to know the effect of instantaneous temperature on liquid permittivity and sensor materials, to calibrate the measurements. The reference channel (port 2) can provide the information of the value of temperature which can then be used to obtain accurate, corrected values of the liquid permittivity.

The correction of the results can be done by removing the changes in the resonant frequency and quality factor that come from the effect of the temperature on all parts of the resonator except the liquid sample in which the corrected results of the resonant frequency and quality factor must only represent the variation in the complex permittivity of the liquid sample due to the temperature. The changes in resonant frequency and quality factor for all parts of the resonator except the liquid sample can be found from the measurements of the port 2 (reference resonator). As shown in Figure 6.9, the approximate relationship between $\Delta f/f$ of the reference resonator (port 2) and $\Delta f/f$ of the empty capillary (port 3) can be easily found as:

$$\Delta f/f_{emplt(port3)} = K \cdot \Delta f/f_{reference(port2)} \quad 6.5$$

where K is constant which can be calculated from Figure 6.9 (K≈1.15). Similarly, as shown in Figure 6.10, the change in the quality factor ($\Delta Q/Q$) of the reference resonator (port 2) and that for the empty capillary (port 3) can be linked together as:

$$\Delta Q/Q_{empty(port3)} = K \cdot \Delta Q/Q_{reference(port2)} \quad 6.6$$

K in this case is equal to 1.6. From Equations 6.5 and 6.6, the resonant frequency and the quality factor in the case of the empty capillary of port 3 can be found instantaneously from the measurements of port 2 as function of temperature. If we assumed room temperature (25ºC) as the reference temperature to calibrate the results (which is used later to extract the value of the complex permittivity of the liquid) then the changes in the resonant frequency and quality factor of the empty capillary as function of temperature of port 3 can be found as:

$$\Delta f_r(T) = f_r(T) - f_r(25^o) \quad 6.7$$

$$\Delta Q_r(T) = Q_r(T) - Q_r(25^o) \quad 6.8$$

The corrected values of the resonant frequency and the quality factor (for water or chloroform) will be the instantaneous measurements minus the $\Delta f_r(T)$ and $\Delta Q_r(T)$ of the empty capillary, respectively, as:

$$f_{corrected} = f_{measured} - \Delta f_r(T) \quad 6.9$$

$$Q_{corrected} = Q_{measured} - \Delta Q_r(T) \quad 6.10$$

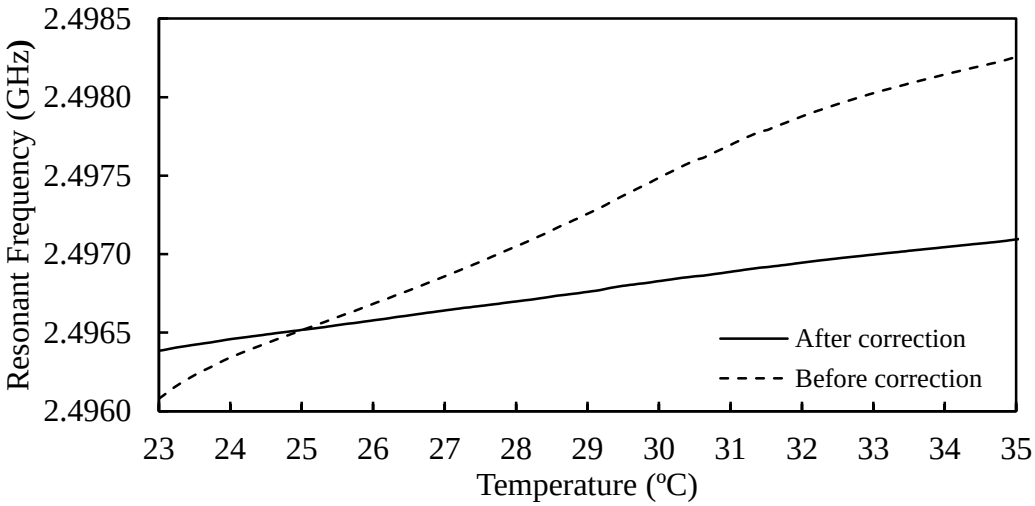

(a)

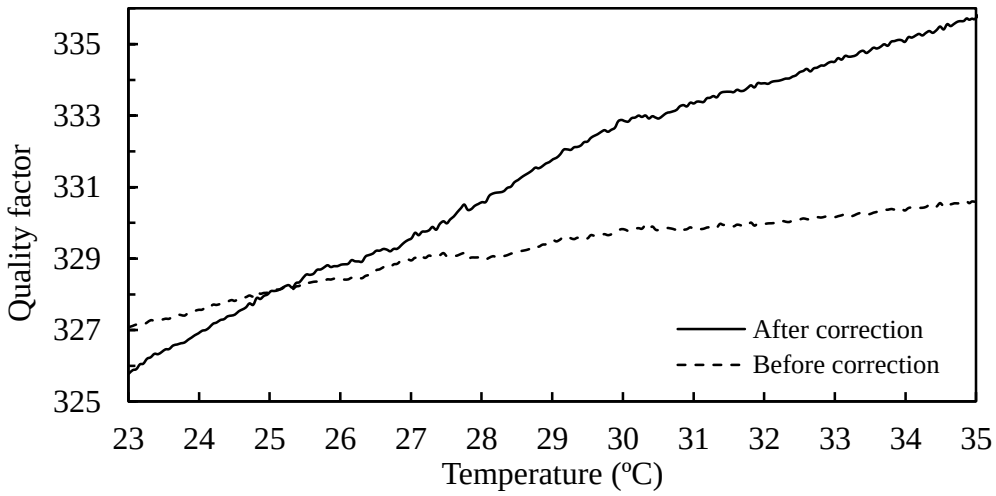

(b)

Figure 6.11: Port 3 corrected measurements with temperature for water sample. (a) Resonant frequency, (b) quality factor.

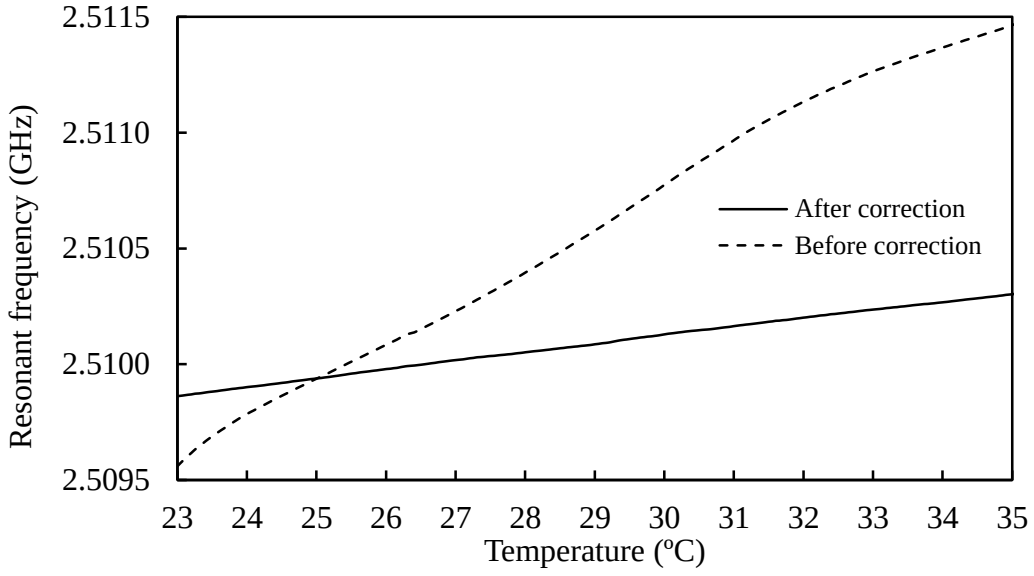

(a)

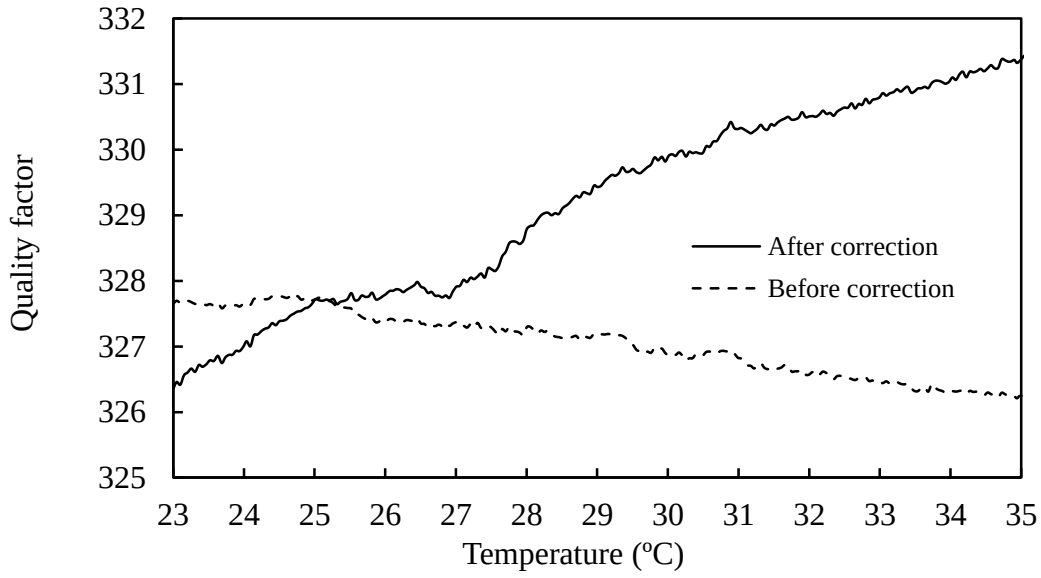

(b)

Figure 6.12: Port 3 corrected measurements with temperature for chloroform sample. (a) Resonant frequency, (b) quality factor.

The corrected results (resonant frequency and quality factor) for water and chloroform are shown in Figures 6.11 and 6.12, respectively, where the effect of temperature on the resonator parts (except the liquid sample) was removed. The complex permittivity is extracted from the measurements using an optimization routine based on matching the simulated and experimental results. In case of water, the values of its complex permittivity as function of temperature is calculated from [130] and used as reference for comparison with the measured and corrected results to find the error. The error of

the complex permittivity values which are calculated from the measured (uncorrected) results is from 2.6% to 11.4% depending on the temperature value, while in the case of corrected results the error reduces to 0.3-0.9%. The same procedure was done to the chloroform.

As there are no reliable, published data about the values of the complex permittivity of chloroform as a function of temperature and frequency, a separate microwave cylindrical waveguide cavity with inner radius a = 46 mm and length d = 40 mm was used to measure the complex permittivity of chloroform using standard cavity perturbation analysis [140], [172]. This can be done over a variable temperature range by placing the cavity in an oven (Memmert, Model: IPP 400) with a high degree of temperature control (±0.1ºC). The complex permittivity of chloroform was measured over the temperature range 23-35ºC at the two resonant frequencies of the TM_{010} and TM_{020} modes of the cylindrical cavity (at 2.5 and 5.7 GHz, respectively), where the two equations of the perturbation theory in case of cylindrical cavity resonator can be approximated and written as a function of temperature as:

$$\frac{\Delta f_r(T)}{f_r} \approx (\varepsilon_1(T) - 1)\frac{V_s}{2V_{eff}}, \tag{6.11}$$

$$\frac{\Delta f_B(T)}{f_r} \approx \varepsilon_2(T)\frac{V_s}{V_{eff}}, \tag{6.12}$$

where V_s is the sample volume and V_{eff} is the effective volume of the electric field energy in the cavity as in [172]. By using Equations 6.11 and 6.12, the value of chloroform complex permittivity is extracted as function of temperature as shown in Figure 6.13 for both two modes. Results at 2.51GHz (the resonant frequency of the DMS when sample is chloroform) were found by linearly interpolating the complex permittivity between 2.5 and 5.7 GHz. These are plotted as a function of temperature in Figure 6.13. The error in this case (chloroform) reduces from the range of 3.1% to 8.5% for the measured results (uncorrected) to the range of 0.2 to 0.4% for the corrected results.

The corresponding calculations of the complex permittivity of water and chloroform before and after the correction are illustrated in Table 6.2 and 6.3, respectively.

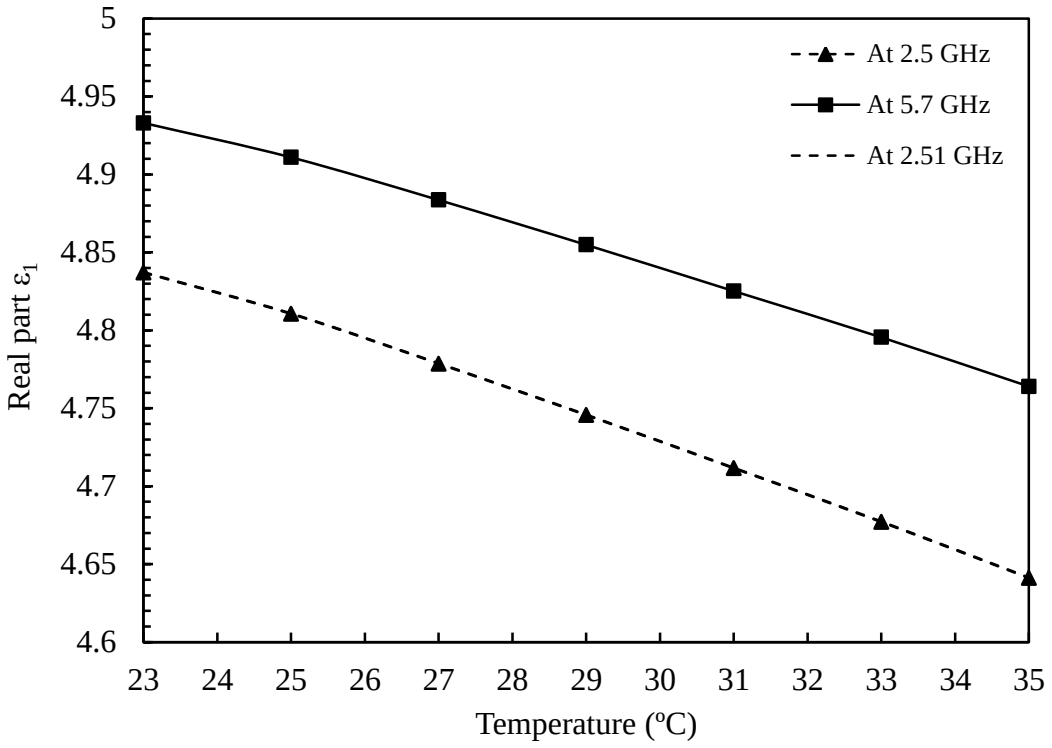

(a)

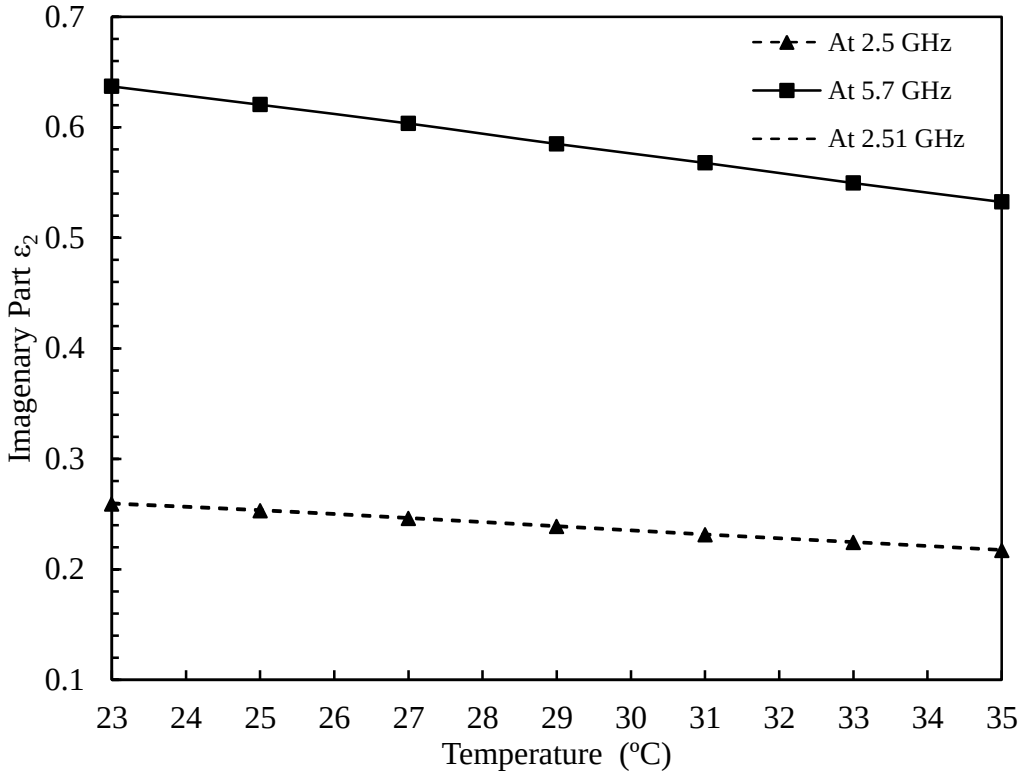

(b)

Figure 6.13: Cavity measurements of the complex permittivity of chloroform with temperature: (a) real part, and (b) imaginary part at frequencies of 2.5 and 5.7 GHz.

Table 6.2: Comparison between calculated and measured values of water complex permittivity before and after correction and relative error.

Temperature (°C)	f_r (GHz) measured	f_r (GHz) corrected	Q measured	Q corrected	$\varepsilon(f,T)$ calculated [130]	$\varepsilon(f,T)$ measured	Error	$\varepsilon(f,T)$ corrected	Error
23	2.496081	2.496385	327.082	325.779	77.74-*j*9.88	81.70-*j*9.80	4.9%	78.50-*j*10.00	0.9%
25	2.496519	2.496519	328.089	328.089	77.15-*j*9.33	77.15-*j*9.33	0.0%	77.15-*j*9.33	0.0%
27	2.496860	2.496642	328.950	329.569	76.54-*j*8.81	74.50-j9.00	2.6%	76.30-j8.80	0.3%
29	2.497259	2.496760	329.516	331.780	75.94-*j*8.30	72.00-j8.60	5.1%	75.50-j8.20	0.5%
31	2.497696	2.496887	329.824	333.340	75.34-*j*7.85	70.00-j8.15	7.0%	75.00-j7.80	0.5%
33	2.498024	2.496997	330.158	334.506	74.75-*j*7.45	68.00-j7.80	8.9%	74.40-j7.40	0.5%
35	2.498257	2.497095	330.606	335.756	74.15-*j*7.05	65.50-*j*7.50	11.4%	73.80-*j*7.00	0.5%

Table 6.3: Comparison between calculated and measured values of chloroform complex permittivity before and after correction and relative error.

Temperature (ºC)	f_r (GHz) measured	f_r (GHz) corrected	Q measured	Q corrected	$\varepsilon(f,T)$ measured (cavity resonator)	$\varepsilon(f,T)$ measured	Error	$\varepsilon(f,T)$ corrected	Error
23	2.509557	2.509862	327.645	326.342	4.84-*j*0.26	5.00-*j*0.25	3.3%	4.83-*j*0.27	0. 2%
25	2.509939	2.509939	327.719	327.719	4.81-j0.25	4.81-j0.25	0.0%	4.81-j0.25	0.0%
27	2.510230	2.510018	327.366	327.911	4.78-j0.25	4.63-j0.26	3.1%	4.77-j0.26	0.2%
29	2.510577	2.510086	327.177	329.431	4.75-j0.24	4.60-j0.27	3.1%	4.74-j0.25	0. 2%
31	2.510965	2.510164	326.827	330.316	4.71-j0.23	4.55-j0.27	3.3%	4.69-j0.24	0. 4%
33	2.511263	2.510235	326.450	330.799	4.68-j0.22	4.40-j0.27	5.9%	4.67-j0.23	0.2%
35	2.511465	2.510302	326.243	331.394	4.64-j0.22	4.24-j0.28	8.5%	4.63-j0.22	0.2%

6.4. DMS design improvement

Due to the interaction between the two channels (the reference and sensing channel) there is some variation in the resonant frequency and the quality factor of the reference channel (port 2) with the changing of the liquid sample at the same temperature as shown in Figure 6.7. This design of the two resonators with common input is similar to a duplexer structure, where the interaction between the two channels is inventible [171], [173]. The variation in the reference frequency due to the presence of different liquids at 25ºC is illustrated in table 6.4, being 20 KHz in the case of the chloroform and 40 KHz in case of water. These small shifts in the resonant frequency and the quality factor of the reference channel may produce some error in the extracting the relative permittivity of the liquid sample. To solve this problem a new design is proposed as shown in Figure 6.14 with the same box dimensions as the first design.

In this improved design of the DMS, two modifications have been added. Firstly, the method of feeding the two channels was changed to a T-junction in order to increase the distance between them and consequently decrease the interaction between their electromagnetic fields. Secondly, the difference between the resonant frequencies of the two resonators was increased as shown in the Table 6.4, from 127 MHz to 289 MHz (this is the minimum separation can be achieved without interaction).

The simulated results of the improved DMS are illustrated in Figure 6.15, where the shift in the resonant frequency of the reference channel with different samples (chloroform and water) is reduced to zero as shown in Table 6.4. Unfortunately, time did not permit the experimental verification of the improved DMS design, so this is left for future work.

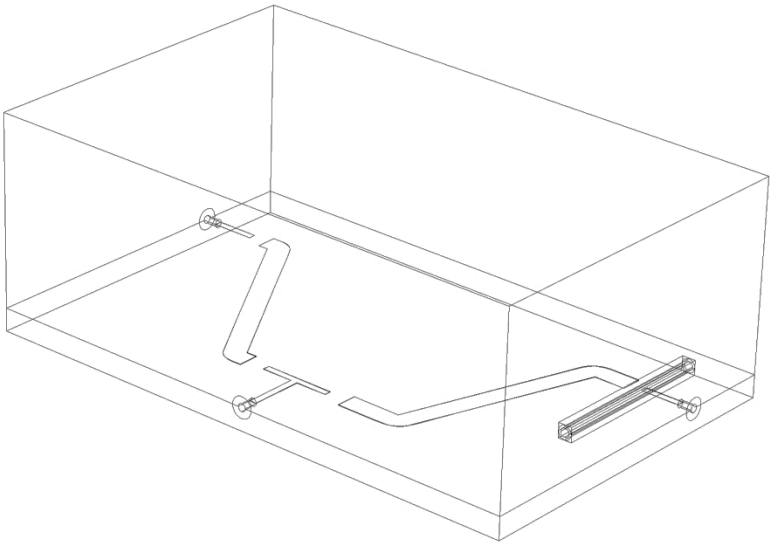

(a)

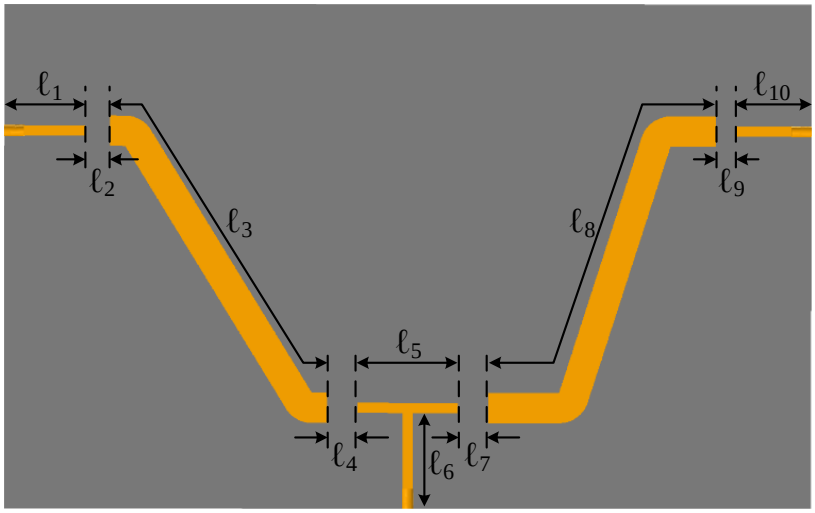

(b)

Fig. 6.14: (a) Schematic of the improved dual mode microstrip sensor inside aluminum cavity and (b) the dimensions of the design, ℓ_1= 8 mm, ℓ_2= 2.5 mm, ℓ_3= 37 mm, ℓ_4= ℓ_7= 3 mm, ℓ_5= 10 mm, ℓ_6= 9.5 mm, ℓ_8= 41 mm, ℓ_9= 2 mm, ℓ_{10}= 7.5 mm, the widths of the strip line are the same in the Figure 6.3.

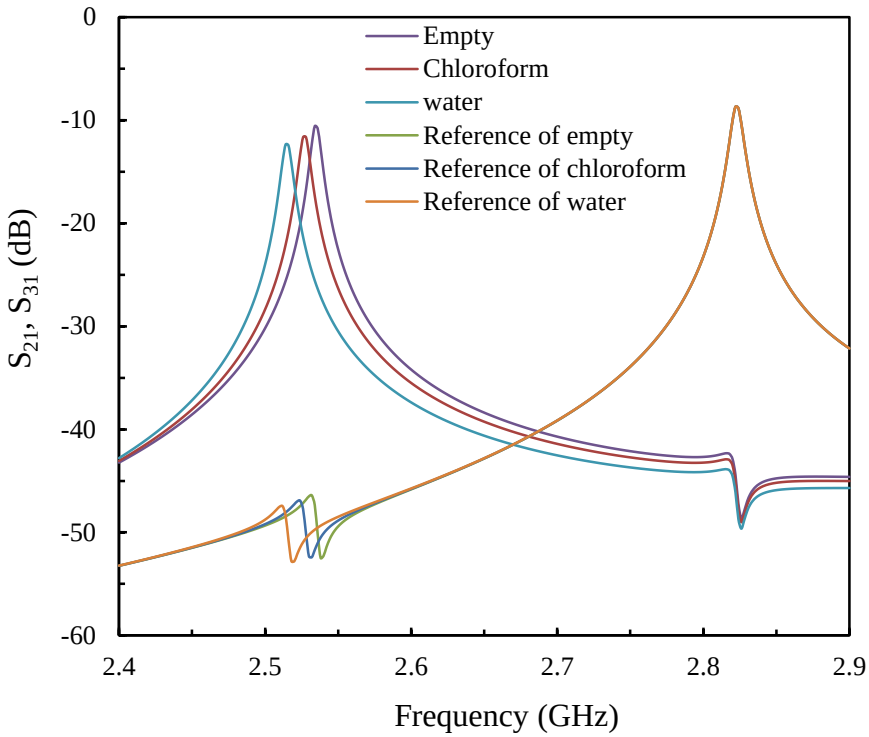

Figure 6.15: Simulated S_{21} and S_{31} of the improved DMS sensor proposed in Figure 6.13 with empty, chloroform, and water filled capillaries.

Table 6.4: Performance comparison between the two designs of the DMS

Design	Sample	f_r (GHz) (port 2)	Δf (KHz)	f_r (GHz) (port3)	Δf (MHz)
DMS (Figure 6.3)	empty	2.64389	-----	2.5170	-----
	chloroform	2.64387	2	2.5100	7
	water	2.64385	4	2.4940	23
Improved DMS (Figure 6.14)	empty	2.82280	-----	2.5350	-----
	chloroform	2.82280	0	2.5270	7
	water	2.82280	0	2.5150	23

CHAPTER 7 - RESONATORS FOR MICROWAVE APPLICATORS WITH ADAPTIVE COUPLING

Microwave heating techniques have been adopted and developed for many industrial, domestic and medical applications. The many advantages of microwave heating can be summarized as: (i) high selectivity to absorbing components, (ii) high efficiency of conversion of electromagnetic energy to heat when using microwave absorbing materials, (iii) non-contacting energy delivery, and (iv) volumetric heating. These advantages can be combined to offer potentially faster heating rates than for any other method [115].

Normally, in a heating application the microwave input circuit is critically coupled to the resonant applicator device, resulting in maximum power transfer from source to applicator. The input impedance of the applicator can be written $Z_{in} = g \cdot Z_0$, where g is the (dimensionless) coupling coefficient and Z_0 is the system impedance (usually 50 Ω, as is the case here). In practice g depends on the geometrical details of the coupling structure, the unloaded Q factor of the resonator and the resonant frequency f_0. Critical coupling corresponds to the condition $g = 1$, which is achieved for arbitrary values of Q and f_0 by mechanical adjustment of the coupling structure. There are major challenges in heating materials in this way imposed by the temperature dependence of the properties of the materials themselves, which causes the Q and (more seriously for a high Q resonator) f_0 to drift. For example, for the heating of aqueous samples, this is a result of

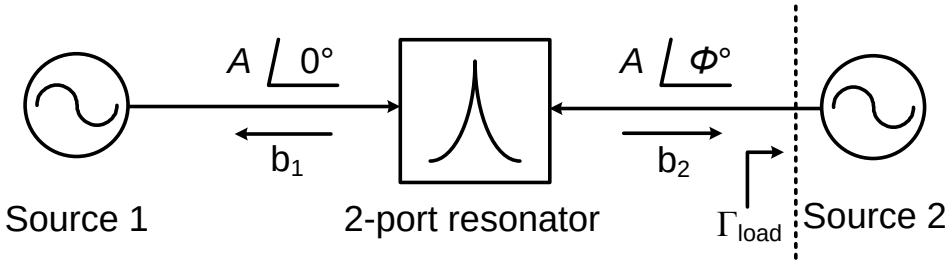

Figure 7.1: Block diagram of a two-port resonator fed by two synchronized sources of the same frequency (equal to the resonant frequency) and with a phase shift of ϕ. A is the magnitude of the incident wave to the both ports of the resonator and b_1 and b_2 are the reflected waves from the resonator.

the strong temperature dependence of the complex microwave permittivity of water. In summary, to maintain maximum efficiency during the heating process, we should be able to control a) excitation frequency and b) coupling strength of the heating system simultaneously for continuous critical coupling condition. The excitation frequency can be easily controlled by signal source control while monitoring the response of the resonator. However, controlling coupling strength on a printed circuit board is not an easy task.

In this chapter, a novel adaptive coupling topology is proposed that offers the ability to electronically adjust the coupling between the source and the heating resonator. The system consists of the resonator and two synchronized power sources with a variable phase shift between them, as shown in Figure 7.1. A double split-ring resonator (DSRR) designed in chapter four was adopted as the host resonator and is connected to the two outputs of a variable phase-shift source. The adaptive coupling method was verified by heating chloroform as a test liquid within a quartz micro-capillary.

7.1. Brief theory and concepts

7.1.1. Microwave heating of polar liquids in capillaries

When placed in an oscillating electric field, the molecules of a polar liquid rotate owing to the torque generated by the field. This rotation, which continually changes its sense, results in dielectric heating due to friction. For common solvents the heating is often most intense in the microwave frequency range. The relative permittivity of the liquid can be written as a complex number $\varepsilon = \varepsilon_1 - j\varepsilon_2$, with real and imaginary parts well described by the Debye theory.

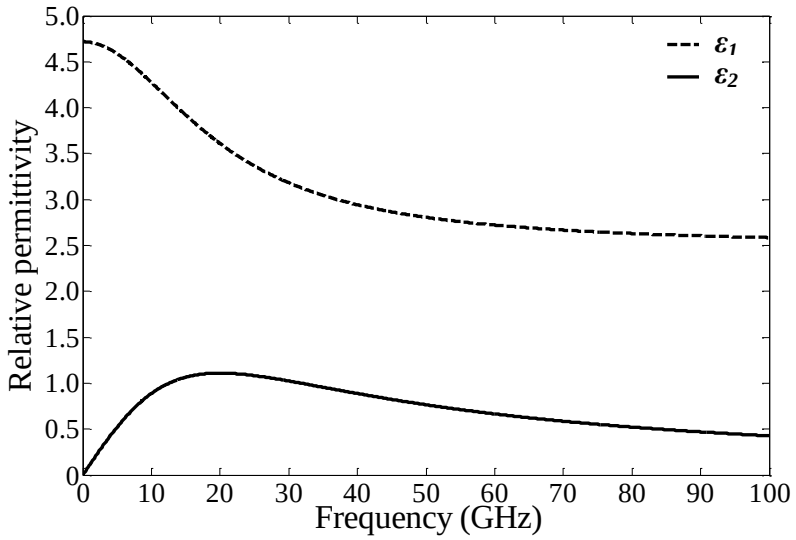

Figure 7.2: The complex relative permittivity of chloroform at 25ºC, calculated from its Debye parameters listed in Table 7.1.

The complex permittivity of our test liquid chloroform is plotted in Figure 7.2, based on its Debye parameters listed in Table 7.1. From Figure 7.2, the maximum loss occurs at 20 GHz, where $\varepsilon_2 = 1.11$. The dissipated power density within the liquid is given by [174]:

$$p = 2\pi f \varepsilon_o \varepsilon_2 |E|^2 \qquad 7.1$$

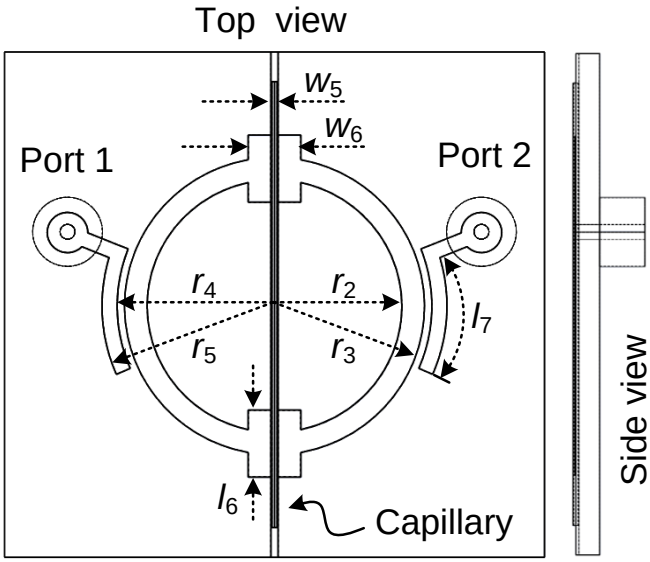

Figure 7.3: Definition of the symbols used to define the dimensions of the DSRR structure, also including the coupling ports.

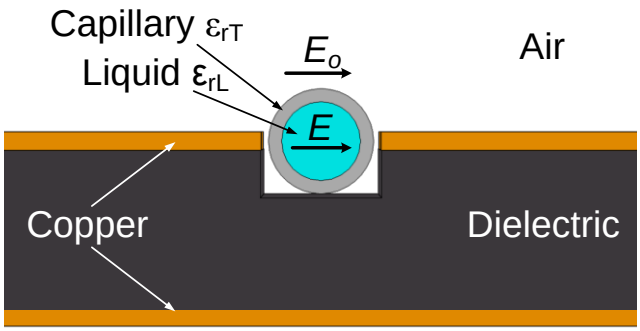

Figure 7.4: Cross section of the capillary inside the resonator gap, showing schematically the applied electric field E_0 and the resulting electric field E within the capillary.

where E is the electric field amplitude **within** the liquid and f is the excitation frequency. The DSRR used in this heating study is shown diagrammatically in Figure 7.3, similar to that described in chapter four for microwave sensing but with modifications for this heating application. The two portions of liquid within the two gap regions will be heated. In our DSRR the electric field is perpendicular to the axis of the liquid sample as shown in Figure 7.4 (assumed cylindrical since it is held within a cylindrical capillary), which means that E is reduced greatly compared to the amplitude of the applied field E_o owing to the effects of depolarisation. This is dealt with in detail in [28], but to a good approximation E is found to be in Equation 3.22. It is clear from Equations 7.1 and 3.22 that the heat efficiency is inversely proportional to the real part of the liquid and directly proportional to the imaginary part of the liquid's relative permittivity.

7.1.2. Adaptive coupling method

The aim of our adaptive coupling method is to decrease or increase the coupling between the resonator and the input ports electronically, and hence precisely maintain the critical coupling condition. Many factors may affect this, not least the change in both frequency and Q as the liquid heats, owing to the highly temperature dependent complex permittivity of polar liquids (water being the classic example). This provides the ability to control the power delivery to the resonator and, consequently, the ability to the control heating without changing the source power. On varying the phase shift between the two, equal-power inputs at ports 1 and 2 (as in the schematic of Figure 7.1), the total delivered power to the resonator changes. To verify this concept of adaptive

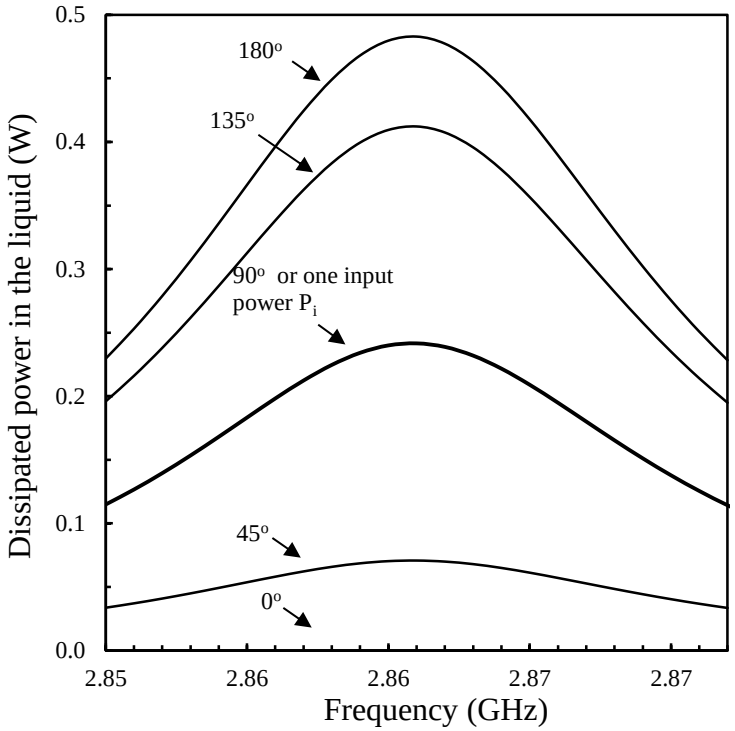

Figure 7.5: The simulated power dissipation in the liquid (chloroform) as a function of frequency with respect to the phase shift between the two microwave inputs, calculated using COMSOL Multiphysics®.

resonator coupling, a simulation of the DSRR shown schematically in Figure 7.3 (with dimensions shown in Table 7.2 in the next section) was performed using COMSOL Multiphysics® for the microwave heating of chloroform. If an input power of P_i is applied to one of the input ports of the resonator, the dissipated power in the liquid is calculated to be $0.24P_i$ at the resonant frequency (2.861 GHz), while the rest of the power $0.76P_i$ is dissipated in the rest of the DSRR structure (mostly the copper parts) and also lost by radiation. If the power P_i is halved to two parts ($P_i/2+P_i/2$) and fed into the two inputs simultaneously with variable phase-shift between them, then the delivered dissipated power in the liquid can be controlled by varying the phase. It is clear from Figure 7.5 that if the phase-shift between two inputs is 0º, the dissipated power in chloroform will be zero, and can be increased to up to $0.48P_i$ when the phase shift is 180º at the resonant frequency (2.861 GHz). This is double the value of dissipated power compared with the case when the same value of power is applied to one port only. For 90º phase difference, the same power is dissipated in the liquid as when the power is applied to one port only.

To explain why maximum power dissipation happens when the two sources are 180º out of phase, the source that feeds port two with variable phase is used as variable load impedance. If we assume the two port S-parameters of the resonator as S_{11}, S_{12}, S_{21}, S_{22}, as shown in Figure 7.1, the reflection coefficient of the load Γ_{load} can be written as:

$$\Gamma_{load} = \frac{Ae^{j\phi}}{b_2} = \frac{1}{S_{21}\frac{A}{Ae^{j\phi}}+S_{22}} = \frac{1}{S_{21}e^{-j\phi}+S_{22}}. \quad 7.2$$

It can be seen from Equation 7.2 that the value of the Γ_{load} can be controlled by varying the value of the phase shift ϕ. Therefore the source of port two is utilized to change the load impedance of the resonator to the optimum value in order to increase the matching between the sources and the two inputs of the resonator. The load impedance which obtained from the simulation with different phase shift between ϕ two sources (from 0º to 360º) at the resonant frequency 2.861 GHz, is plotted on Smith chart as a function of ϕ in Figure 7.6. From this it can be seen that the optimum matching occurs at ϕ=180º, where maximum power is delivered to the resonator.

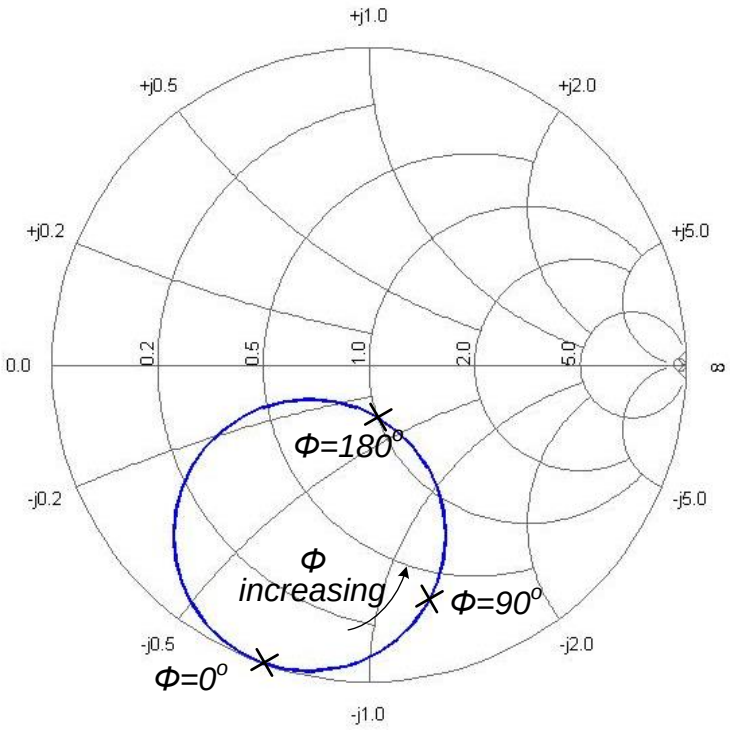

Figure 7.6: Simulated load impedance (blue line) of the DSRR with variable phase output source.

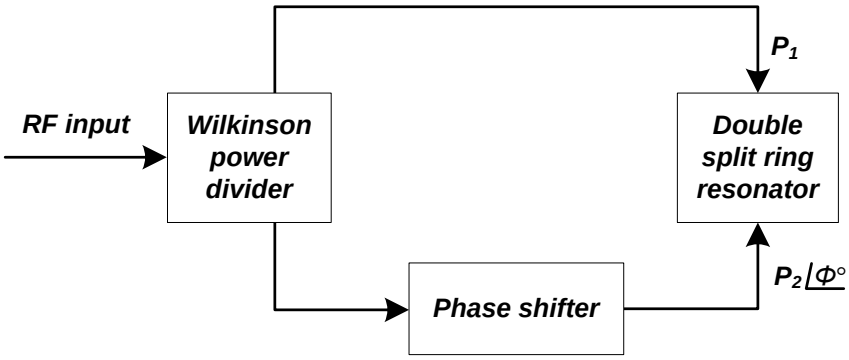

Figure 7.7: A block diagram of the DSRR fed with input signals with different phases, achieved by using an adjustable phase shifter circuit.

The experimental realization of a variable phase-shift, two-input resonator can be achieved by using a Wilkinson power divider (to split the power into two equal parts) and a quadrature phase-shifter connected to varactors [175]. The varactor capacitance is varied with an applied dc bias voltage, which changes the phase by imbalancing the otherwise equal electric lengths of the microstrip sections [176]. The block diagram illustrating this type of adaptive coupling is shown in Figure 7.7.

7.1.3. Use of COMSOL Multiphysics

COMSOL Multiphysics® 4.4 was used to perform 3D simulations of the electromagnetics, electromagnetics with lumped elements, and coupled electromagnetic-thermal effects. The electromagnetic waves model was used to simulate the S-parameters, dissipated power in the liquid (chloroform), and the input/output impedances of the resonator. Coaxial ports were used to feed the electromagnetic energy to the resonator and lumped elements were used to set the variable reactor of the varactors. The microwave heating model was used to obtain the heat distribution in the liquid as defined in the software:

$$\rho C_p \bar{u}.\nabla T = \nabla.(k\nabla T) + Q \qquad 7.3$$

where ρ is the density of the material, C_p the heat capacity at constant pressure and k the thermal conductivity of the material. $\bar{u}$ is the spatial displacement vector, T is the temperature and Q is the heat source. For Joule heating, this is driven by the electric field and is added in the Electromagnetic Heat Source node.

The relative permittivity of chloroform was described in the simulation by using Debye theory as its permittivity is variable with frequency. The properties of the materials that used in the simulation are shown in Table 7.1.

Table 7.1: Material properties using in the simulation at 25 ℃.

Material		ε_1	ε_2	σ (S/m)		
Air		1	0	0		
Microstrip Dielectric		2.21	0	3.17×10^{-4}		
Copper		1	0	2.7×10^{7}		
Quartz Capillary		3.4	0	1×10^{-12}		
Chloroform [154]						
ε_s	ε_∞	τ (*p*s)	k (W/(m·K))	ρ (kg/m^3)	C_p (J/(kg·K))	γ
4.72	2.5	7.96	0.1152	1489	1050	1.11

In Table 7.1, ε_s and ε_∞ are the values of permittivity in the static ($\omega\tau \ll 1$) and VHF ($\omega\tau \gg 1$) limits, respectively, τ is the relaxation time, and γ is the ratio of specific heats. A maximum mesh size for the simulations was set to be 3 mm, while the minimum mesh size is 0.24 mm which produced 211,166 mesh elements.

7.1.4. Temperature and complex permittivity measurements

There are several methods to measure the temperature of liquid in the microfluidic systems, such as the microscopy fluorescence thermometry technique [177]. Our approach is based on the fact that the complex permittivity varies with temperature as well as frequency. Complex permittivity can be defined as in [1], [138], and [139] as in Equations 3.10 and 3.11. Then the value of the complex permittivity can be linked with the temperature. In polar liquids such as chloroform, both ε_1 and ε_2 values decrease with temperature. In our design, the resonant frequency and quality factor depend on the liquid sample, modelled by first order cavity perturbation concepts [140]. Therefore, the change in temperature causes a shift in resonant frequency and change in quality factor (or, equivalently, 3 dB bandwidth) as shown in Figure 7.8, due to the change in liquid complex permittivity, which can then be used to obtain the liquid's average temperature.

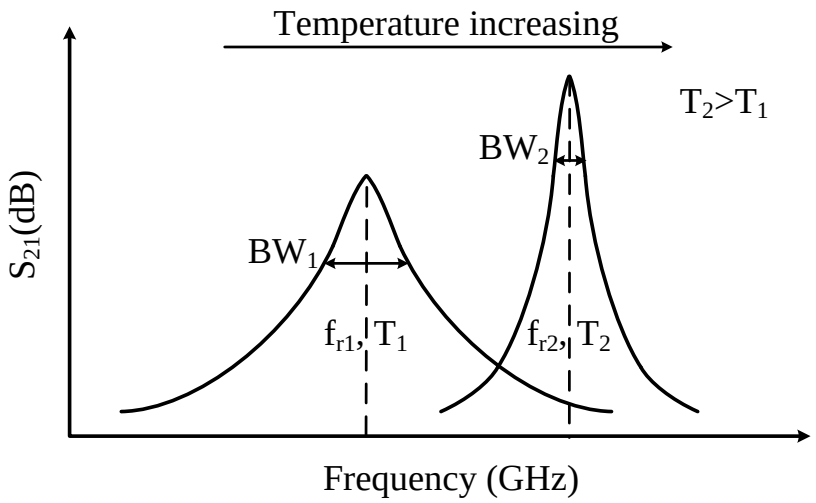

Figure 7.8: Schematic plot, showing the expected variation of $|S_{21}|$ with temperature due the change in complex permittivity of the liquid filling the resonator.

We measured the complex permittivity of chloroform as a function of temperature at a frequency of 2.86 GHz (set by the resonant frequency of the resonator) as described in section 7.3. When the liquid is heated by the resonator, the resonant frequency increases from f_{r1} to f_{r2} and in addition the bandwidth decreases from BW_1 to BW_2, as illustrated in Figure 7.8. From these shifts in resonant frequency and bandwidth, the corresponding change in the complex permittivity can be determined. A routine involving simulation has been applied to find the exact value of the complex permittivity for the new value of the resonant frequency and bandwidth ($f_{r2,}$ BW_2). A new value of complex permittivity found from the simulation is compared with the measured values of complex permittivity in order to deduce the temperature.

7.2. Methods

The DSRR described in chapter four was adopted and modified for this study. The input/output coupling was strengthened by reducing the gap between it and the DSRR, to increase the delivered power to the liquid. The design of the resonator was aided by COMSOL Multiphysics® simulations. A photograph of the fabricated DSRR is shown in Figure 7.9, designed to heat chloroform within a quartz capillary at 2.861 GHz (at 25ºC). The design procedures of the Wilkinson power divider and the quadrature phase-shifter were taken from [140], also to operate at the center frequency of 2.861 GHz (the resonant frequency of the DSRR).

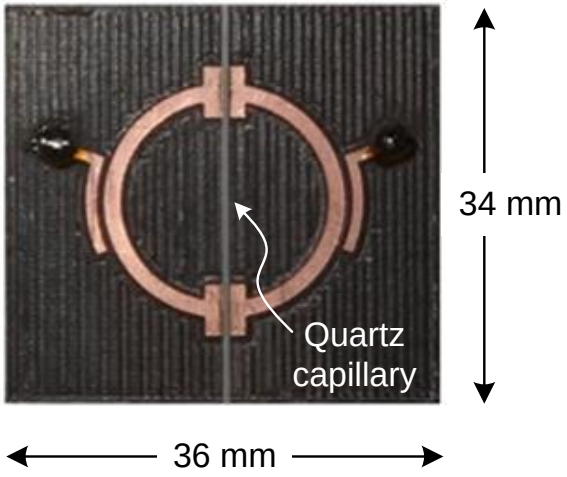

Figure 7.9. Photograph of the microstrip heating resonator (DSRR), fabricated by milling a Rogers RT/Duroid 5880 laminate.

The circuits were fabricated by the mechanical milling of a Rogers Corporation RT/Duroid 5880 laminate, with a dielectric of a thickness of 1.57 mm, relative permittivity of 2.20±0.02 and loss tangent of 0.0009. The thickness of the copper was chosen as 70 µm to ensure the highest possible quality factor for the DSRR. The dimensions of Wilkinson power divider and quadrature phase-shifter were calculated by line calculation tool in Advanced Design System 2014 (Keysight Technology). However, due to discontinuities, junction effects, or unequal even- and odd-mode velocities, the performances of Wilkinson power divider and quadrature phase shifter became degraded in the simulation [171], [178]. Slight modifications of their lengths ℓ, and widths w, were made to improve their simulated performances. Table 7.2 shows the dimensions of all designed components.

Table 7.2: Dimensions of the adaptive coupling DSRR showing in Figures 7.3 and 7.14. All dimensions are in mm.

i	1	2	3	4	5	6	7
ℓ_i	28.00	16.20	20.75	18.45	46.85	4.50	8.04
w_i	4.77	2.78	7.33	4.96	0.46	3.50	5.02
r_i	10.84	8.50	10.00	10.50	11.50	------	------

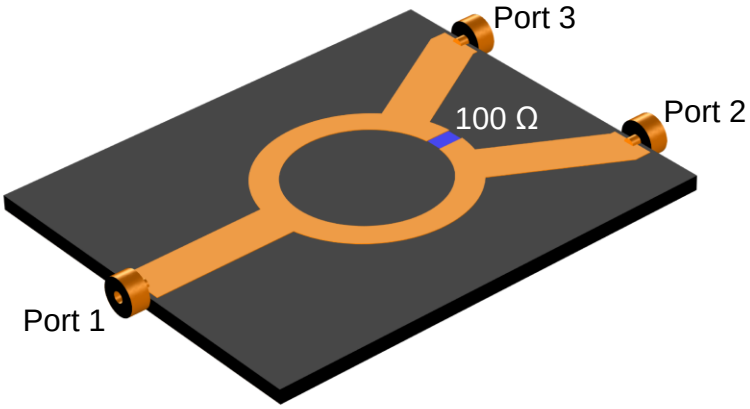

Figure 7.10. The model of the Wilkinson power divider, which was simulated using COMSOL Multiphysics®.

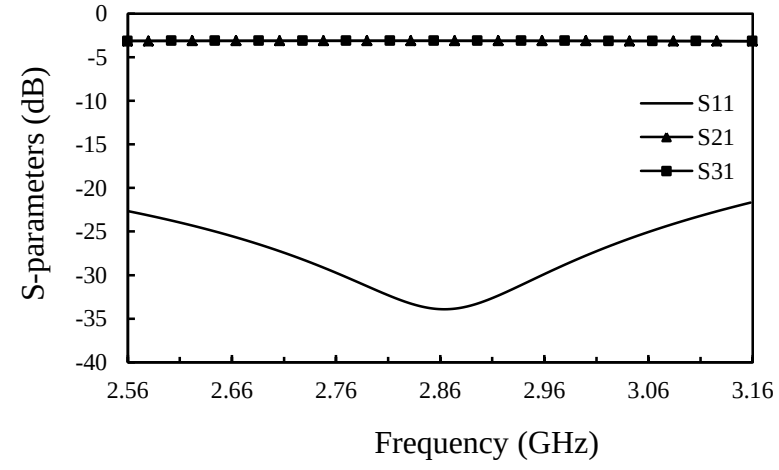

(a)

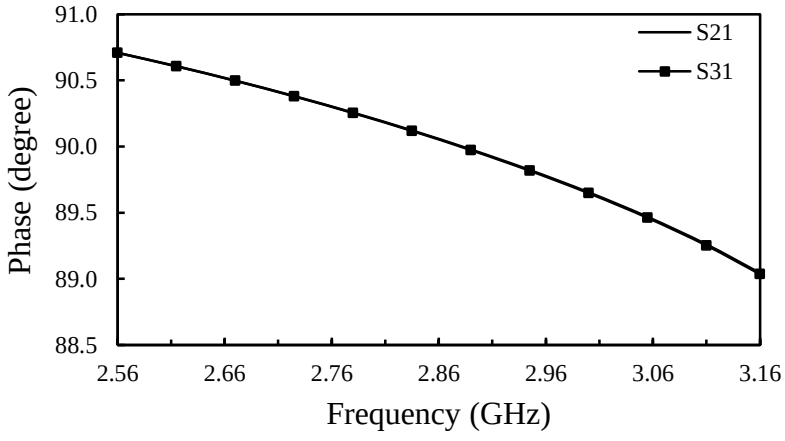

(b)

Figure 7.11. (a) The S-parameters of the Wilkinson power divider are simulated using COMSOL Multiphysics®, show good input matching at 2.861 GHz and evenly divided power at the two output ports, (b) The phases of the two output ports show approximately 90º difference at 2.861 GHz.

The simulated S-parameters of the Wilkinson power divider illustrated in Figure 7.10 are shown in Figure 7.11, where good input impedance matching characteristics are observed and the coupled power at each output port is about -3.2 dB around 2.861 GHz, with a phase delay of 90º. The dimensions of the Wilkinson power divider are illustrated in Table 7.2. The form of the quadrature (90º) hybrid coupler is shown schematically in Figure 7.12 which is tuned to operate at 2.861 GHz. The simulated S-parameters of the quadrature hybrid coupler are shown in Figure 7.13 (using COMSOL Multiphysics®). The S-parameters of the branch line coupler show good input matching S_{11} and isolation S_{41} around 2.861 GHz, where the coupled signal at the two output ports (S_{21} and S_{31}) is at about -3.2 dB at 2.861 GHz. Figure 7.13(b) shows the phase shift (in degree) between the outputs (port 2, 3, and 4) and the input port 1. The phase shift between port 2 and 3 is 89.8º at 2.861 GHz, where in the ideal phase shift is equal to 90º.

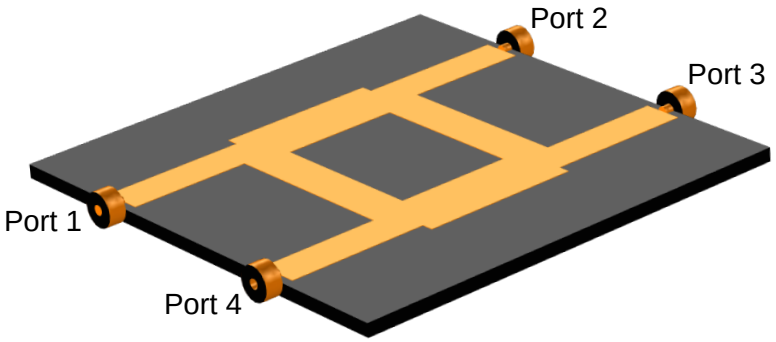

Figure 7.12. The model of a quadrature (90º) hybrid coupler is simulated by COMSOL Multiphysics®.

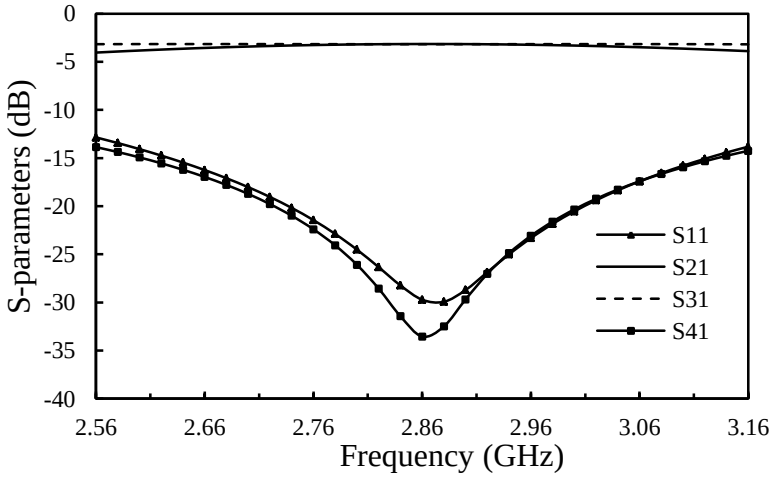

(a)

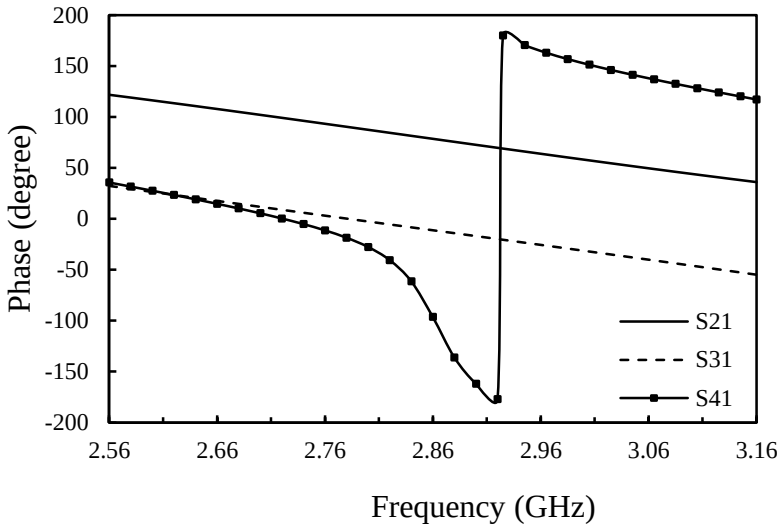

(b)

Figure 7.13. (a) The S-parameters of a quadrature (90º) hybrid coupler are simulated by COMSOL Multiphysics®, (b) A similar plot for the phases.

A phase shifter can be achieved by incorporating the quadrature hybrid coupler with variable capacitors or inductors to obtain a variable phase shifter. Variable capacitors or inductors were connected to ports 2 and 3 of the quadrature hybrid coupler, which act as short circuits to reflect the incident energy back towards port 4 with phase shift depending on the their values. A variable capacitor can be realized by a varactor diode, in which the variable phase can be controlled electronically as shown in the full circuit topology illustrated in Figure 7.14, which also shows a photograph of the final circuit.

As the active volume of liquid in our system is tiny, only 0.64 µL in both gaps, so the dissipated power required to heat chloroform is small; for example, 1 W dissipated power produces a heating rate of around 60ºC/s. A varactor diode 1T362A (Sony Corporation) was chosen which can handle this small amount of power. In reverse bias this varactor diode yields a capacitance range of approximately 2.3 to 100 pF over the voltage range of 25 to 0 V at 900 MHz, respectively [179]. However, at 2.861 GHz the variable reactor of the diode has an inductive effect as the frequency of operation is higher than the self-resonant frequency, which makes the package inductance of the diode dominant. The measured reactance of the diode in reverse bias at 2.861 GHz is shown in Figure 7.15. In the design it was required to set the phase shift range with the range of the variable inductor.

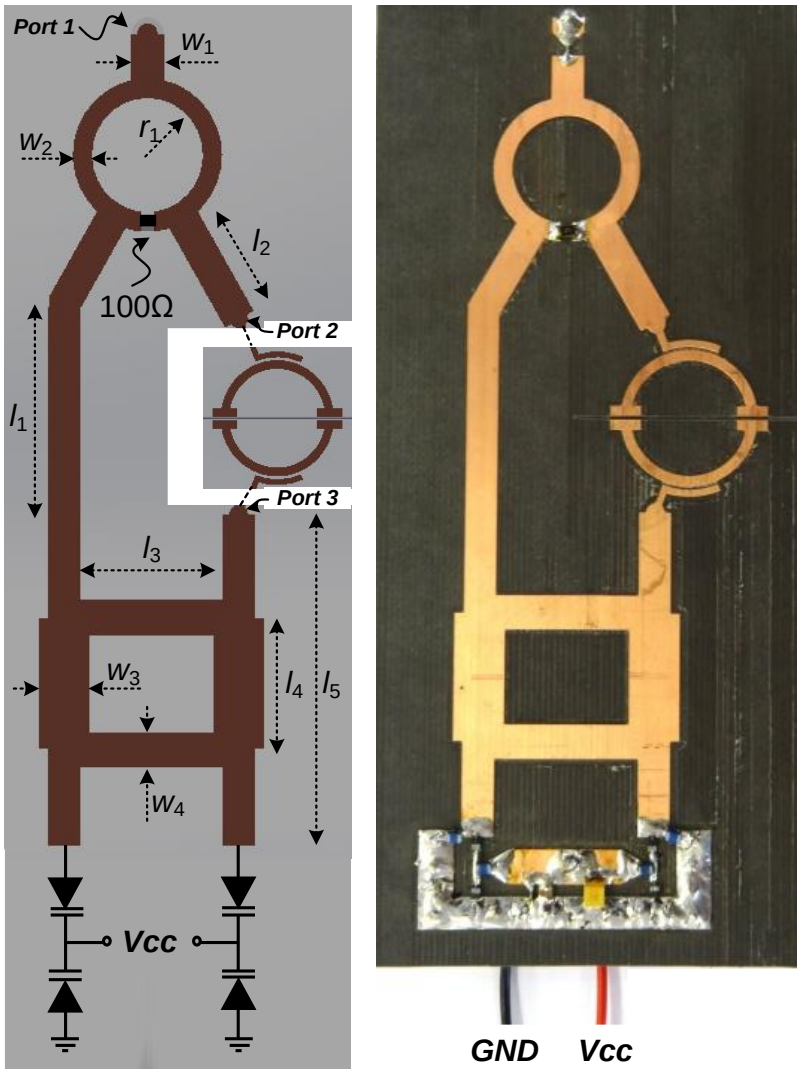

Figure 7.14. The circuit topology and photograph of the DSRR connected to the two outputs of a variable phase-shift power source, that consisted of the Wilkinson power divider, quadrature phase-shifter and varactor circuit.

An 180^{o} phase shift between ports 2 and 3 was achieved by setting the diode's effective inductance to value of 0.7 nH. This setting is realized by carefully choosing ℓ_1 to be 28 mm, which gives a phase shift of 132º at 2.861 GHz. Together with the quadrature (90º) hybrid coupler and the two parallel diode inductors, the phase shift between ports 2 and 3 at 2.861 GHz will be then 180º. The groove for the quartz capillary was fabricated using laser micromachining, with a width of w_5 (i.e. 0.46 mm) and depth of 0.235 mm. Microwave connection to the input port (port 1 at the top of Figure 7.14) was made via the dielectric layer and the ground of the microstrip board using a surface-mounted coaxial (SMA) connector. The quartz capillary has an inner diameter of 0.3 mm and outer diameter of 0.4 mm.

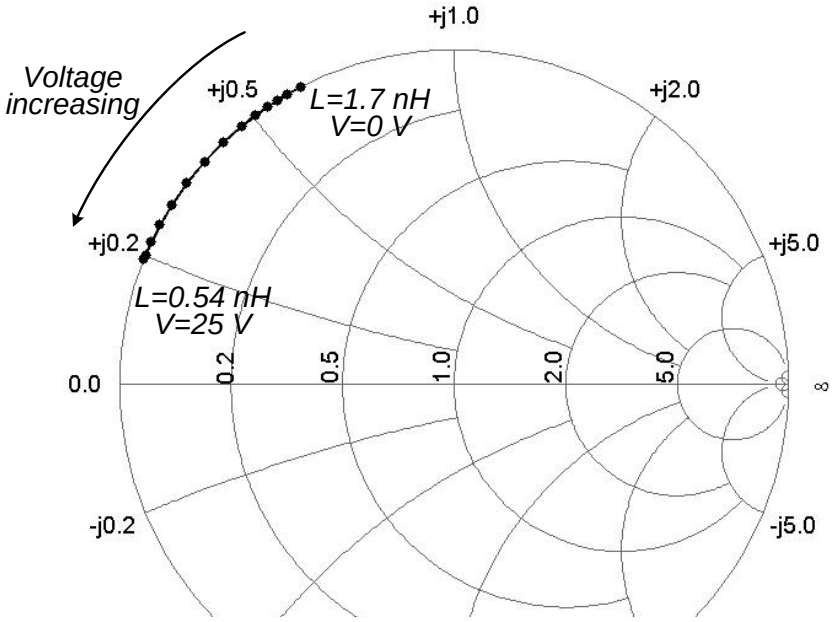

Figure 7.15: Measured variable inductance of the varactor 1T362A at 2.861 GHz.

The capillary was inserted in the groove and filled by liquid using capillary action. Chloroform was selected as the test liquid, as it is a high loss, polar-liquid with a low boiling point (61.5ºC) which does not demand a high-power microwave source to heat it. Separate resonant cavity measurements of chloroform were used to determine its complex permittivity of $\varepsilon = 4.80 - j0.30$ (with an error of about 2% in both real and imaginary parts) at 25ºC at 2.861 GHz. This value was used in the COMSOL simulations for the design of the DSRR. The resulting DSRR with chloroform sample was measured to have a resonant frequency of 2.861 GHz and an unloaded quality factor of 150 at 25ºC.

To deliver the power to the adaptive coupling resonator circuit, a power amplifier ZHL-42 (manufactured by Mini-Circuits) was used to amplify the signal from an Agilent E5071B network analyzer. The power amplifier gain is 29.6 dB and the range of delivered power from the network analyzer is from −10 to 0 dBm. The resulting input power to the circuit is from 20 to 30 dBm, which covers the power range required to boil the chloroform sample. A circulator was used to protect the power amplifier from the reflected power. Figure 7.16 shows the bench-top assembly of the adaptive coupling resonator with the power amplifier and the network analyzer.

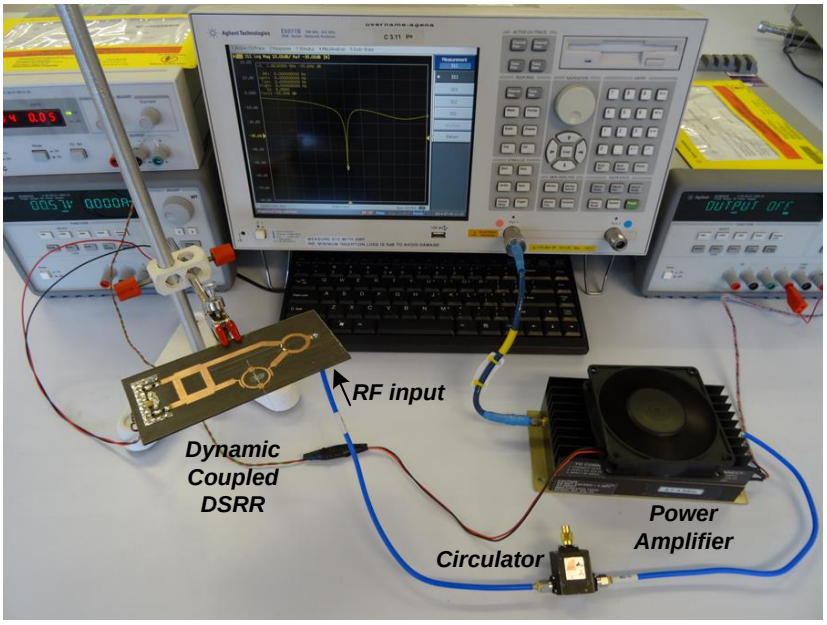

Figure 7.16: Photograph the bench-top experimental assembly. The microwave source was provided by an Agilent E5071B network analyzer. Other components are labelled.

7.3. Results and discussion

To verify the ability of the resonator with adaptive coupling to increase the heating efficiency, as well as controlling strength of the coupling, tests were undertaken. Firstly, this was by feeding only one input port of the resonator, which incorporated a chloroform filled capillary. This was heated to boiling at different values of input power.

Due to the difficulty of measuring the liquid temperature inside the resonator-integrated capillary, the shift in the resonant frequency was used to measure the temperature of chloroform, as the permittivity of a polar liquid is a strong function of temperature [180]. The complex permittivity of heated chloroform can be calculated by applying an optimization routine based on matching the simulated and experimental results (section 7.1.4 above). The temperature can then be determined from the new value of liquid permittivity.

As previously mentioned, a separate microwave cavity was used to measure the complex permittivity of chloroform using standard cavity perturbation analysis [140], [172]. This can be done over a variable temperature range by placing the cavity in an oven (Memmert, Model: IPP 400) with a high degree of temperature control (±0.1ºC).

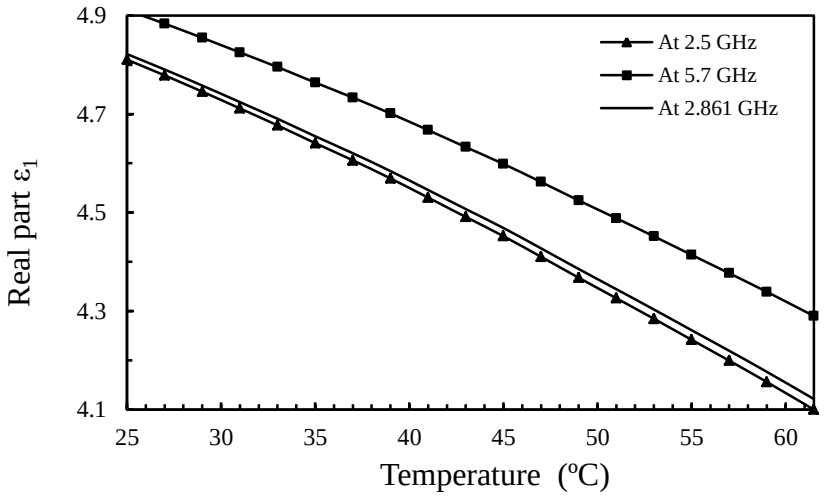

(a)

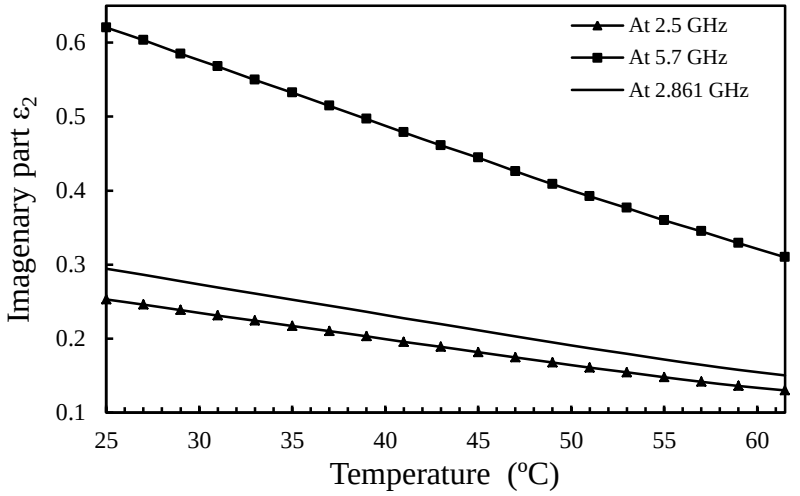

(b)

Figure 7.17: Cavity measurements of the complex permittivity of chloroform with temperature: (a) real part, and (b) imaginary part at frequencies of 2.5 and 5.7 GHz. The values shown at 2.861 GHz are linearly interpolated between these two measurement frequencies.

The complex permittivity of chloroform was measured over the temperature range 25.0-61.5ºC (i.e. to boiling) at the two resonant frequencies of the TM_{010} and TM_{020} modes of the cylindrical cavity (at 2.5 and 5.7 GHz, respectively). Results at 2.861 GHz were found by linearly interpolating the complex permittivity between 2.5 and 5.7 GHz. These are plotted as a function of temperature in Figure 7.17. By knowing the complex permittivity of chloroform as a function of temperature, the temperature of the chloroform can be inferred with a high degree of accuracy from measuring the resonant frequency of the DSRR (or indeed any type of resonant applicator used to heat it).

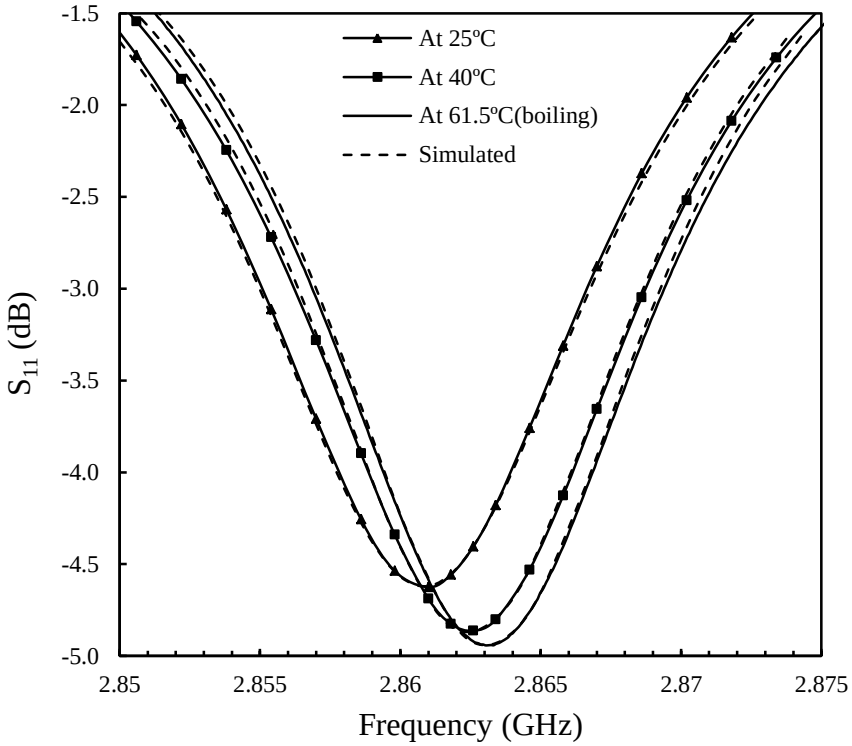

Figure 7.18: Simulated and measured magnitudes of the voltage reflection coefficients S_{11} for the single port DSRR at different temperatures degrees.

As shown in Figure 7.18, the resonant frequency is 2.8610 GHz when 1 mW of power was applied to only one input port of DSRR. This means that there was negligible heating of the chloroform at such low powers and the chloroform temperature remained at 25ºC (room temperature). By increasing the input power to 180 mW, boiling occurred when the resonant frequency increased to 2.8631 GHz, which accurately predicts the boiling point of chloroform of 61.5ºC (where the real permittivity is 4.10).

In the second part of the experiments the DSRR was fed with two input signals of variable phase difference, with the circuits shown in Figures 7.14 and 7.16. The phase shift between ports 2 and 3 shown in Figure 7.14 was measured with variable bias voltages applied to the varactor diode, as shown in Figure 7.19. Here the DSRR was removed and the output terminated with a 50 Ω load. At the resonant frequency of the DSRR (2.861 GHz) with the chloroform at 25ºC, the circuit provides a range of phase shifts from 128º at 0 volt to 190º at 25 volts. This covers the condition for maximum power transfer into the DSRR that occurs at 180º, according to the simulation shown in Figure 7.5.

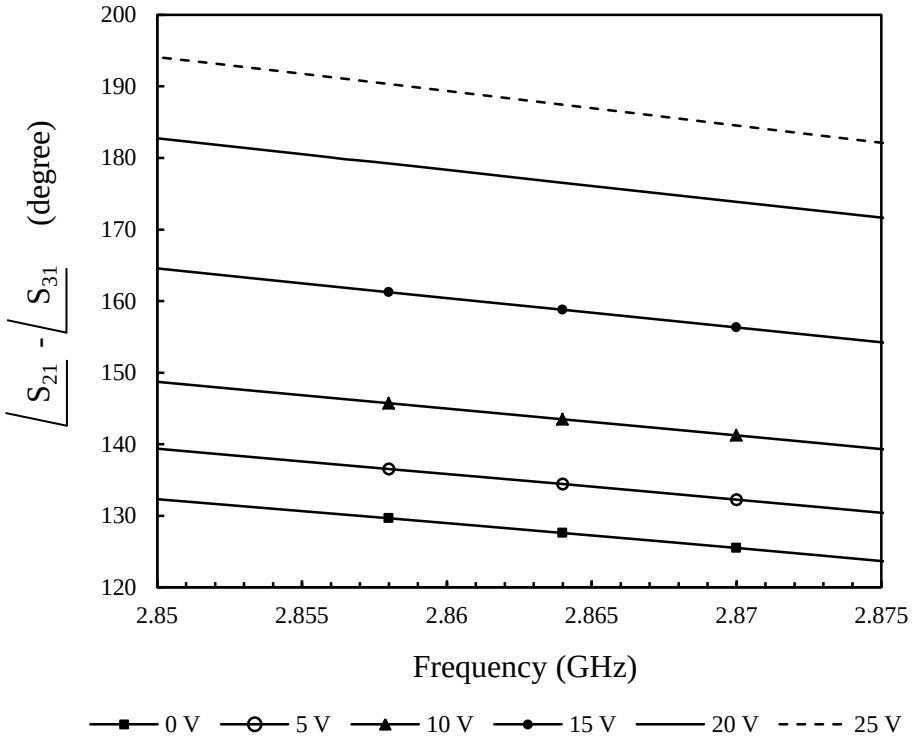

Figure 7.19: The measured phase of S_{23} between Ports 2 and 3 of Figure 7.14, for different values of the applied bias voltage.

To determine the performance of the adaptive coupling resonator shown in Figure 7.14 for optimum heating efficiency, microwave power was fed to the input port of the circuit shown in Figure 7.16. At each input power the bias voltage was adjusted to give the maximum coupling, i.e. maximum power transfer, corresponding to a phase difference of 180º, as shown in Figure 7.20. The input power required for boiling (where the DSRR's resonant frequency was shifted to 2.6831 GHz due to the change in permittivity), was 45 mW at each port (port 2 or 3) of the DSRR, or 90 mW when fed at both ports. After heating the chloroform to 61.5ºC, the return loss decreased by 4 dB due to a combination of the increase in resonant frequency and increased value of quality factor.

The coupling can be re-adjusted to return to the same value of return loss (49 dB) attained before heating. Moreover, as shown in Figure 7.20, the three dotted lines and maximum coupling line correspond to the magnitudes of S_{11} with different values of diode DC voltage and 0 dBm input power. This means that the coupling changes with the value of the DC bias voltage, demonstrating the ability to control the coupling electronically.

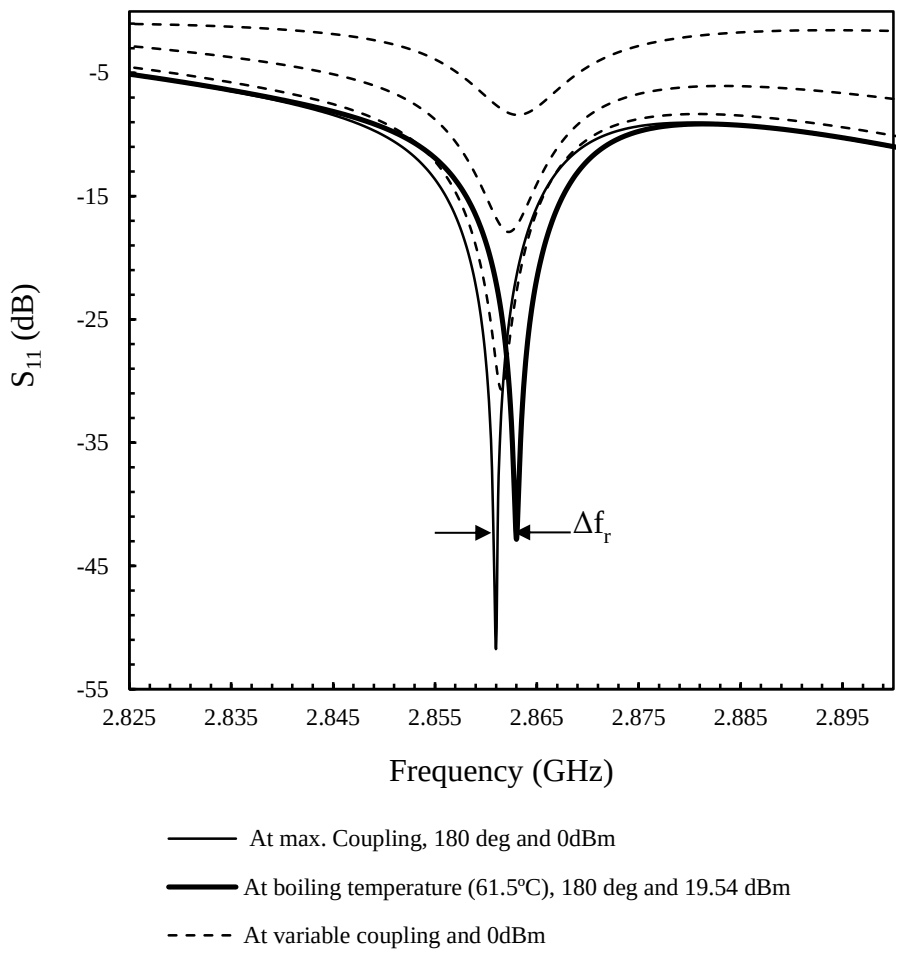

Figure 7.20: Measured values of S_{11} of the adaptive coupling resonator in Figure 7.16.

A summary of the adaptive coupling circuit performance is illustrated in Table 7.3. As shown in Figure 7.20, there is a change in resonant frequency due to the coupling variation. The resonant frequency changes are approximately 2.0 ± 0.1 MHz, which is well within the bandwidth of the power amplifier. Finally, a simulation of the heat distribution along the chloroform sample was undertaken using COMSOL Multiphysics® to illustrate the distribution of the temperature along the gap area, as shown in Figure 7.21. This simulation is when the DSRR is fed with 180 mW at one port, or 45 mW at two ports, with a phase shift of 180º between them (total input power is 90 mW). In both cases the chloroform was heated to boiling along the center region (61.5ºC).

Table 7.3: Performance comparison between the two types of power feeding.

	Input power (mW)	Δf (MHz)	Complex permittivity	Temperature (ºC)
One port feeding	90	1.2±0.1	4.55-j0.23	40.0
	180	2.0±0.1	4.10-j0.15	61.5
Two ports feeding	90 (both ports)	2.0±0.1	4.10-j0.15	61.5

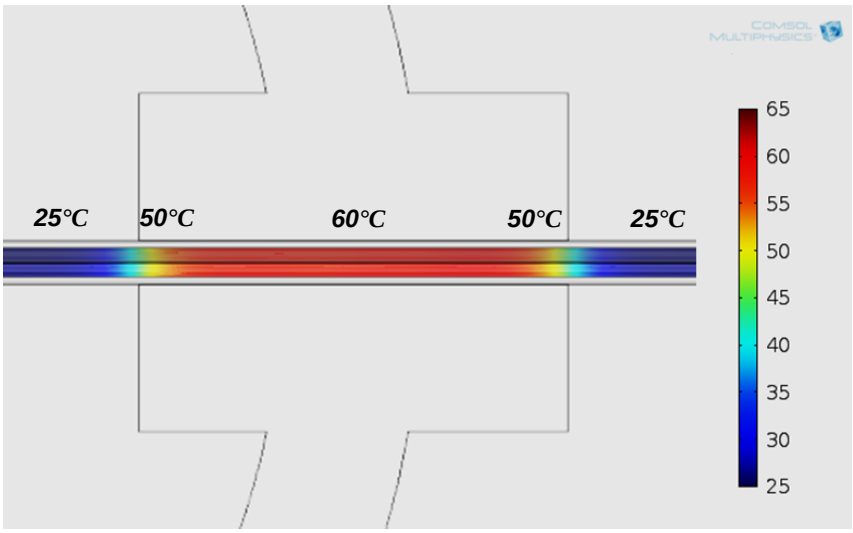

Figure 7.21: The simulated temperature distribution over the channel for the one input DSRR with 180 mW, or two input DSRR with 45 mW at each input.

CHAPTER 8 - CONCLUSIONS AND FUTURE RESEARCH

8.1. Conclusions

This thesis has focused on the design of several types of the microfluidic sensors and applicators using microstrip resonator structures. The sensing concept of all sensors is the resonator perturbation due to the presence of the liquid or micro-sphere sample in which the changes in the resonant frequency and the quality factor are exploited to extract the value of the sample's complex permittivity.

In chapter two, a literature review of all types of microwave microfluidic sensors, microwave cell sensors, and microwave microfluidic applicators was provided. Chapter three illustrated briefly the background theory of the liquid complex permittivity, microwave heating, microstrip resonators, and perturbation theory.

In chapter four, a new resonant microstrip technique has been realized and tested to measure the dielectric permittivity of liquids. The method is based on resonator perturbation theory in which the resonant frequency and the bandwidth change by adding a liquid sample in a microfluidic circuit. A planar double split-ring resonator is adopted and designed to reduce the size and weight of the sensor, which makes it suitable to be incorporated into microfluidic and lab-on-a-chip implementations. The sensor was simulated by COMSOL Multiphysics Software and optimized to improve its quality factor. Moreover, a theoretical model has been developed that gives good comparison with the measured values for a range of different liquids. Several solvents were tested inside two types of tubes. The sensor sensitivity is limited at high permittivity by the effects of depolarization, but for low permittivity gives very

sensitive results for small changes in the permittivity of liquids, thus provided a means of liquid identification and tracking of small variations in liquid property due to, for example, chemical or physical change.

Moreover, a new method to measure length, speed, volume and permittivity of liquids in a microfluidic system with segmented flow is also proposed in chapter four. A double split-ring microwave resonator is used as the resonant sensor element. Two models were designed and fabricated to study the effect of the gap on the sensor performance. Experimental results demonstrate their promising ability to detect (non-invasively) the segment properties, making them adaptable and attractive for medical, biological and chemical real-time, lab-on-chip applications.

In chapter five, three models of microwave sensor based on a microstrip split ring resonator were developed and tested for the dielectric measurement, size measurement and counting of microspheres. Model A had very high sensitivity due to the small size of its gap region, here 35 μm. Two sizes of polystyrene microspheres (15 and 25 μm) have been used to verify the odd mode's perturbation when a microsphere is present in the gap. Furthermore, it has been demonstrated that the even mode is insensitive to the presence of microspheres and so can be used for temperature compensation. There is a need to increase the sensitivity further since for real cells in aqueous solution there is little contrast in permittivity, hence the gap and ring radii have been reduced in models B and C. Their increased sensitivity is simply due to the associated reduction in mode volume V_m, which quantities the volume of the resonator over which the electric field is distribution. The observed changes in resonant frequency and insertion loss of the odd mode were due to the dielectric contrast between the microspheres and their host solvent (water). The complex permittivity of the microspheres can be extracted from the resonator measurements either using an optimization routine based on matching the simulated and experimental results, or by using the theoretical method in chapter four.

Chapter six proposes a new type of microwave microfluidic sensor with two modes. The sensor was based on half wavelength quarter ring microstrip resonators, where two resonators were designed and fabricated to measure the liquid permittivity with temperature variation. A temperature sweep from 23 to 35 ºC was conducted to verify its performance. Two polar liquids (water and chloroform) were tested with the sensor

to show the effect of varying temperature on the measurements and how these can be corrected using by the reference resonator.

Chapter seven presents a novel adaptive coupling method that provides the ability to change (and, in principle, control) the coupling of a microwave resonator electronically. This approach can be exploited in microfluidic heating applications, where the heating rate can be optimized without changing the source power. The power gain, or the extent of heating, can be increased to double the power value of that used when using a one-port feed. For example, with chloroform, the total power (applied to both ports) required to reach the boiling temperature was half the value needed in the one-port configuration. The verification of this new concept was achieved by simulation and experiment, including the assessment of the dissipated power, the heat distribution of the liquid, S-parameter measurements, and the associated shifts in resonant frequency. The proposed topology is used for proof-of-principle.

8.2. Further research

According to the conclusions drawn and the ability to develop the approaches proposed in this thesis, several future works can be proposed to improve the sensitivity, accuracy, and performance of the present works. The suggestions can be listed related to the work chapters, as follows:

In chapter four, the performance of the sensor can be increased by adjusting the geometry of the gap, to enable more localized dielectric measurement, suitable for the evaluation of the material properties and geometry for small particles in a microfluidic flow stream. Moreover, the sensitivity of the sensor can be increased by raising the quality factor of the resonator DSRR. This is can be done by increasing the thickness of the copper of the DSRR and/or fabricate the sensor inside metal box to reduce the radiation. This sensor can be used to design microwave applicator for microfluidic system in which the input coupling can be enhanced to deliver more power to the resonator. With regard to multi-phase liquids measurements, the sensors can by modified to measure the contact angle between two types of the liquids and the capillary. The contact angle is determined by measuring the rate of change in the resonant frequency when the liquid changes in the resonator gap under constant flow rate.

In chapter five, the ability of the SRRs to count microspheres, as well as determine their complex permittivity, can be next applied to human cell detection and diagnostics. As mentioned above, the sensitivity of the cell detection can be improved by increasing the copper thickness of the split ring, where the selectivity of the resonator is increased. Additionally, the fabrication of the resonator can be improved in terms of patterning resolution, which will yield an increase in the sensitivity of cell detection. More advanced technology can be adopted to fabricate the split ring such as photolithography techniques. Another application of the split ring resonator sensor is for multi-phase segmented liquids measurements (velocity, length, size, and complex permittivity) where the proposed sensors in chapter five can be redesigned for this purpose.

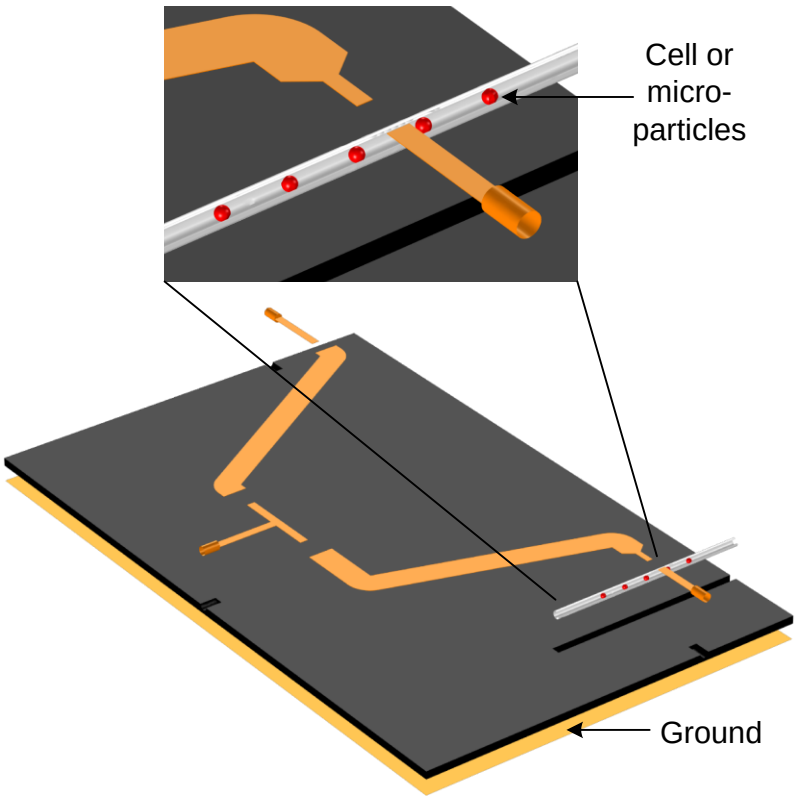

Figure 8.1: The proposed dual mode sensor for cells and micro-particles detection.

Work presented in chapter six can be developed to measure the permittivity of two or more liquids by adding more branches which gives the ability to monitor several liquids permittivity with temperature. This sensor is simply a microstrip resonator which can be miniaturized to provide a compact sensor also with use as a microwave applicator. Moreover, this type of sensor can be modified to cell detection sensor by miniaturizing

the end of the half wave microstrip resonator and the thickness of the microstrip dielectric to the dimension of the targeted cell to maximize the perturbation as shown in Figure 8.1.

Finally, in chapter seven, miniaturization will be achieved by using commercially available power dividers and quadrature hybrid couplers. Moreover, the phase shifter circuit can be improved to increase the range of the phase shift variation (from 0º to 180º). The concept of adaptive coupling can be generalized to apply to several types of resonators for heating application in which the required energy can be saved by half. For example, a cylindrical cavity can be fed by two inputs with variable phase shift between them as shown in Figure 8.2. This is just one example that will benefit from the adaptive electronic coupling technique presented in this thesis.

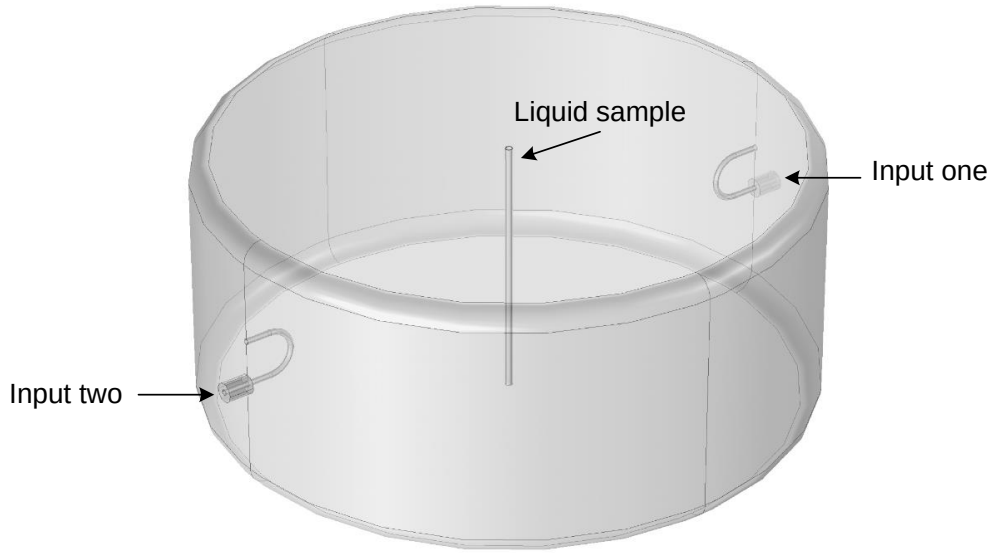

Figure 8.2: The proposed cylindrical cavity with two inputs for microfluidic heating applications.

APPENDIX I

EXTRACTION OF $\Delta f_r/f_r$ *AND* $\Delta f_B/f_r$

In Chapter 3, section 3.4, the capillary-perturbed DSRR resonator was introduced as a method for quantifying the dielectric properties of a liquid sample. This appendix is dedicated to the extraction of approximate analytic equations relating the change in the resonant frequency and the bandwidth due to the perturbation of the presence of the liquid sample to its dielectric properties.

It can be assumed that the stored energy U_{tot} consists of two parts; that in the liquid U_L and that in the other parts of the resonator U_R (tube, dielectric, and air), so

$$U_{tot} = U_L + U_R \qquad 1$$

where $U_L = \frac{1}{2} Re(\varepsilon_{rL}) \int E^2 dV$, where ε_{rL} is the complex permittivity of the test liquid. By substituting Equation 3.25 and Equation 1 in equation 3.24, Equation 2.24 can be written as

$$\frac{\Delta f_r}{f_r} = -\frac{1}{4} \frac{Re(pE_0^*)}{U_L + U_R} \qquad 2$$

or

$$\frac{\Delta f_r}{f_r} \approx -\frac{1}{4} \frac{Re\left(2\pi\varepsilon_o b^2 l \left(\frac{(\varepsilon_{rT}-1)(\varepsilon_{rT}+\varepsilon_{rL})+(\varepsilon_{rT}+1)(\varepsilon_{rT}-\varepsilon_{rL})a^2/b^2}{(\varepsilon_{rT}+1)(\varepsilon_{rT}+\varepsilon_{rL})+(\varepsilon_{rT}-1)(\varepsilon_{rT}-\varepsilon_{rL})a^2/b^2}\right) E_0^2\right)}{\frac{1}{2} Re(\varepsilon_{rL}) \int Re\left(\frac{4\varepsilon_{rT} E_0}{(\varepsilon_{rT}+1)(\varepsilon_{rT}+\varepsilon_{rL})+(\varepsilon_{rT}-1)(\varepsilon_{rT}-\varepsilon_{rL})a^2/b^2}\right)^2 dV + U_R}$$

which can be simplified to

$$\frac{\Delta f_r}{f_r} = \frac{k_1 Re\left(\frac{(\varepsilon_{rT}-1)(\varepsilon_{rT}+\varepsilon_{rL})+(\varepsilon_{rT}+1)(\varepsilon_{rT}-\varepsilon_{rL})a^2/b^2}{(\varepsilon_{rT}+1)(\varepsilon_{rT}+\varepsilon_{rL})+(\varepsilon_{rT}-1)(\varepsilon_{rT}-\varepsilon_{rL})a^2/b^2}\right)}{Re\left(\frac{\varepsilon_{rL}}{(\varepsilon_{rT}+1)(\varepsilon_{rT}+\varepsilon_{rL})+(\varepsilon_{rT}-1)(\varepsilon_{rT}-\varepsilon_{rL})a^2/b^2}\right)^2+k_2} \quad 3$$

where k_1 and k_2 are constants. The change in bandwidth Δf_B of the resonator can be written as

$$\frac{\Delta f_B}{f_r} = \frac{1}{Q_L} - \frac{1}{Q_o} \quad 4$$

where Q_o is the quality factor of the resonator when the tube is empty and Q_L is the quality factor when liquid filled. The quality factor is given as [140], where the dissipated power consists of two parts as

$$Q = \omega \frac{time\ averaged\ energy}{time\ average\ power\ dissipated} = \frac{\omega U_{tot}}{\langle P\rangle + P_R} \quad 5$$

where $\langle P\rangle = -\frac{1}{2}\omega Im(pE_o)$, and P_R is the power dissipated in other parts of the resonator (tube, dielectric, and metal). Equation 4 then becomes

$$\frac{\Delta f_B}{f_r} = \frac{\langle P\rangle + P_R}{\omega U_{tot}} - \frac{1}{Q_o} = \frac{-\frac{1}{2}\omega Im(pE_o)+P_R}{\omega(U_L+U_R)} - \frac{1}{Q_o} =$$

$$\frac{-\frac{1}{2}\omega Im\left(2\pi\varepsilon_o b^2 l\left(\frac{(\varepsilon_{rT}-1)(\varepsilon_{rT}+\varepsilon_{rL})+(\varepsilon_{rT}+1)(\varepsilon_{rT}-\varepsilon_{rL})a^2/b^2}{(\varepsilon_{rT}+1)(\varepsilon_{rT}+\varepsilon_{rL})+(\varepsilon_{rT}-1)(\varepsilon_{rT}-\varepsilon_{rL})a^2/b^2}\right)E_o^2\right)+P_R}{\omega\left(\frac{1}{2}VRe(\varepsilon_{rL})Re\left(\frac{4\varepsilon_{rT}E_O}{(\varepsilon_{rT}+1)(\varepsilon_{rT}+\varepsilon_{rL})+(\varepsilon_{rT}-1)(\varepsilon_{rT}-\varepsilon_{rL})a^2/b^2}\right)^2+U_R\right)} - \frac{1}{Q_o}$$

or

$$\frac{\Delta f_B}{f_r} = \frac{A_1 Im\left(\frac{(\varepsilon_{rT}-1)(\varepsilon_{rT}+\varepsilon_{rL})+(\varepsilon_{rT}+1)(\varepsilon_{rT}-\varepsilon_{rL})\,a^2/b^2}{(\varepsilon_{rT}+1)(\varepsilon_{rT}+\varepsilon_{rL})+(\varepsilon_{rT}-1)(\varepsilon_{rT}-\varepsilon_{rL})\,a^2/b^2}\right)+\frac{A_2}{\omega}}{Re\left(\frac{\varepsilon_{rL}}{(\varepsilon_{rT}+1)(\varepsilon_{rT}+\varepsilon_{rL})+(\varepsilon_{rT}-1)(\varepsilon_{rT}-\varepsilon_{rL})\,a^2/b^2}\right)^2+A_3} - \frac{1}{Q_o} \quad 6$$

where A_1, A_2, and A_3 are constants. The constants of Equation 3 and 6 depend on the structure of the resonator and the volume of the capillary, which can be calculated from the measured values of $\Delta f_r/f_r$ and $\Delta f_B/f_r$.

APPENDIX II

Effective medium theory applied to micro-sphere detection

In Chapter 3, section 3.4, the micro-sphere-perturbed SRR resonator was introduced as a method for simultaneously quantifying the dielectric properties of a microsphere. This appendix is dedicated to the extraction of an analytic formula for the effective permittivity of the liquid with a micro-sphere inside.

To find the formula of the polarization of the sphere and liquid in the capillary inserted in the split ring resonator gap, firstly, it is assumed that the sphere is surrounded by the liquid as shown in Figure II.1.

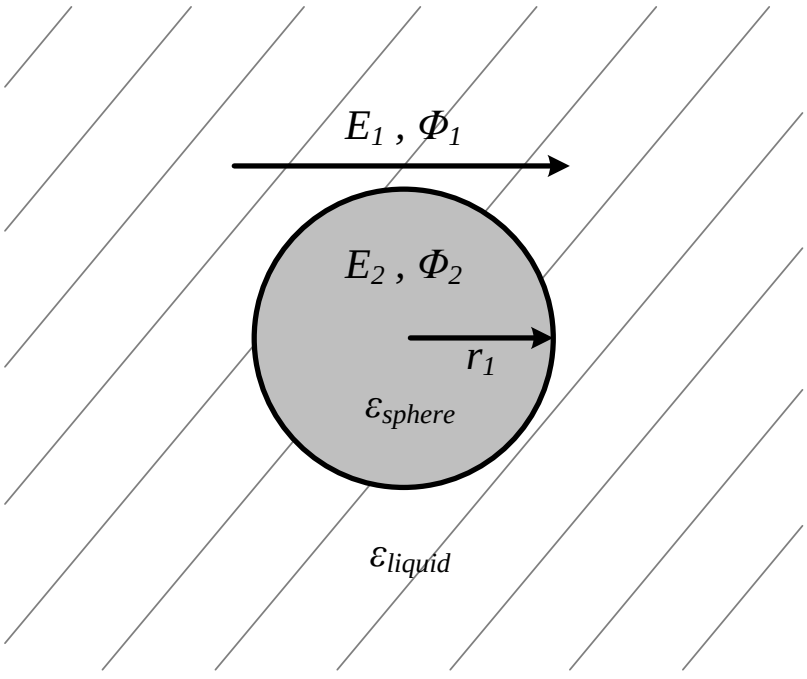

Figure II.1: Cross section of the sphere in the liquid.

The electric potential inside and outside the sphere can be written as:

$$\phi_1 = -E_1 r cos\theta + \frac{A}{r^2} cos\theta \qquad r \geq r_1 \qquad 1$$

$$\phi_2 = -E_2 r cos\theta \qquad r < r_1 \qquad 2$$

where *A* is a constant, proportional to the induced dipole moment of the sphere. At $r = r_1$ the boundary conditions are:

$$\phi_1 = \phi_2 \qquad \text{and} \qquad \varepsilon_{liquid} \frac{\partial \emptyset_1}{\partial r} = \varepsilon_{sphere} \frac{\partial \emptyset_2}{\partial r}$$

From Equations 1 and 2, A and E_2 can be found as:

$$A = \frac{r_1^3}{3\varepsilon_{liquid}} (\varepsilon_{sphere} - \varepsilon_{liquid}) E_2 \qquad 3$$

$$E_2 = \frac{3\varepsilon_{liquid}}{\varepsilon_{sphere} + 2\varepsilon_{liquid}} E_1 \qquad 4$$

Then, the dipole moment due to the liquid is :

$$p = 4\pi\varepsilon_o \varepsilon_{liquid} A = 3\upsilon\varepsilon_o \varepsilon_{liquid} \left(\frac{\varepsilon_{sphere} - \varepsilon_{liquid}}{\varepsilon_{sphere} + 2\varepsilon_{liquid}}\right) E_1 \qquad 5$$

where υ is the sphere volume (i.e $\upsilon = 4\pi r_1^3/3$). The total dipole moment can be given as:

$$p_{total} = \left(\varepsilon_{liquid} - 1\right)\varepsilon_o V E_1 + 3\upsilon\varepsilon_o \varepsilon_{liquid} \left(\frac{\varepsilon_{sphere} - \varepsilon_{liquid}}{\varepsilon_{sphere} + 2\varepsilon_{liquid}}\right) E_1 \qquad 6$$

The total dipole moment can be simplified as:

$$p_{total} = \left(\varepsilon_{eff} - 1\right)\varepsilon_o V E_1 \qquad 7$$

where ε_{eff} is the effective permittivity of the liquid and micro-sphere which is written as:

$$\varepsilon_{eff} \approx \varepsilon\left(1+\frac{3\beta(\varepsilon_s-\varepsilon)}{\varepsilon_s+2\varepsilon}\right) \quad 8$$

Here, ε_s is the permittivity of the microsphere, ε the permittivity of the host solution and β is the volume fraction of microspheres.

APPENDIX III

Extract of Equation 3.33

The evaluation of Equation 3.33 in Chapter 3, section 3.4 is illustrated in this appendix. The change in the polarization Δp before and after the presence of the sphere in the gape can be given as in Equation 3.29 as:

$$\Delta p = p(\varepsilon_{eff}) - p(\varepsilon), \quad 1$$

or

$$\Delta p = \varepsilon_o(\varepsilon_{eff} - 1)E_1 V - \varepsilon_o(\varepsilon - 1)E_1 V, \quad 2$$

where ε is the permittivity of the liquid, ε_{eff} is the effective permittivity of the liquid with sphere, and V is the volume of the sample. Equation 2 can be simplified in term of the external electric field E_o as:

$$\Delta p = \varepsilon_o(\varepsilon_{eff} - 1)\frac{2E_o}{(\varepsilon_{eff}+1)}V - \varepsilon_o(\varepsilon - 1)\frac{2E_o}{(\varepsilon+1)}V \quad 3$$

ε_{eff} can be approximated by assuming the permittivity of the liquid (water in this case which is $\varepsilon \approx 80$) is much larger than the permittivity of the sphere (polystyrene in this case which is $\varepsilon_s \approx 2$) as:

$$\varepsilon_{eff} \approx \varepsilon\left(1 + \frac{3\beta(\varepsilon_s - \varepsilon)}{\varepsilon_s + 2\varepsilon}\right) \approx \varepsilon\left(1 - \frac{3}{2}\beta\right), \quad 4$$

by substituting Equation 4 in 3, Equation 3 then becomes:

$$\Delta p \approx \varepsilon_o[\varepsilon\left(1-\frac{3}{2}\beta\right)-1]\frac{2E_o}{[\varepsilon\left(1-\frac{3}{2}\beta\right)+1]}V-\varepsilon_o(\varepsilon-1)\frac{2E_o}{(\varepsilon+1)}V,$$

or

$$\Delta p \approx 2\varepsilon_o E_o V\left[\frac{\varepsilon-\frac{3}{2}\cdot\beta\varepsilon-1}{\varepsilon-\frac{3}{2}\cdot\beta\varepsilon+1}-\frac{\varepsilon-1}{\varepsilon+1}\right]$$

$$\Delta p \approx 2\varepsilon_o E_o V\left[\frac{(\varepsilon-1)}{(\varepsilon+1)}\cdot\frac{(1-\frac{3}{2}\cdot\frac{\beta\varepsilon}{\varepsilon-1})}{(1-\frac{3}{2}\cdot\frac{\beta\varepsilon}{\varepsilon+1})}-\frac{\varepsilon-1}{\varepsilon+1}\right] \quad 5$$

As $\beta \ll 1$, then Equation 5 can be simplified as:

$$\Delta p \approx 2\varepsilon_o E_o V\cdot\frac{(\varepsilon-1)}{(\varepsilon+1)}\left[\left(1-\frac{3}{2}\cdot\frac{\beta\varepsilon}{\varepsilon-1}\right)\cdot\left(1+\frac{3}{2}\cdot\frac{\beta\varepsilon}{\varepsilon+1}\right)-1\right]$$

$$\Delta p \approx 2\varepsilon_o E_o V\cdot\frac{(\varepsilon-1)}{(\varepsilon+1)}\left[1-\frac{3}{2}\cdot\frac{\beta\varepsilon}{\varepsilon-1}+\frac{3}{2}\cdot\frac{\beta\varepsilon}{\varepsilon+1}-\frac{3}{2}\cdot\frac{\beta\varepsilon}{\varepsilon-1}\cdot\frac{3}{2}\cdot\frac{\beta\varepsilon}{\varepsilon+1}-1\right],$$

or

$$\Delta p \approx 2\varepsilon_o E_o V\cdot\frac{(\varepsilon-1)}{(\varepsilon+1)}\left[-\frac{3}{2}\cdot\frac{\beta\varepsilon}{\varepsilon-1}+\frac{3}{2}\cdot\frac{\beta\varepsilon}{\varepsilon+1}\right]$$

$$\Delta p \approx 2\varepsilon_o E_o V\cdot\frac{(\varepsilon-1)}{(\varepsilon+1)}\left[-\frac{3}{2}\cdot\frac{2\cdot\beta\varepsilon}{\varepsilon^2-1}\right]$$

$$\approx -6\varepsilon_o E_o V\cdot\frac{\beta\varepsilon}{(\varepsilon+1)^2}$$

As $\varepsilon \gg 1$ and $V=\pi a^2 l$, then:

$$\Delta p \approx -\frac{6\pi l a^2\beta}{\varepsilon}\varepsilon_o E_o \quad 6$$

BIBLIOGRAPHY

[1] H. Frohlich, *Theory of Dielectric*. New York. NY, USA: Oxford Univ., 1958.

[2] O. Shaforost, *Microwave whispering-gallery resonators for nanolitre liquid sensing*, Institut für Bio- und Nanosysteme Bioelektronik (IBN-2), Diss., Dortmund, Univ., 2009.

[3] A.R. Von Hippel, *Dielectrics and Waves*, MIT Press, 1954.

[4] M. S. Boybay and C. L. Ren, Microwave in Microfluidics, in: D. Li (Ed.), Encyclopedia of Microfluidics and Nanofluidics, Springer, 2014, ISBN: 978-3-642-27758-0

[5] D. Stuerga, Microwave–Material Interactions and Dielectric Properties, Key Ingredients for Mastery of Chemical Microwave Processes, in: A. Loupy (Ed.), Microwaves in Organic Synthesis, Wiley-VCH, 2002, ISBN 3-527-30514-9

[6] R. Meredith, *Engineers' Handbook of Industrial Microwave Heating*. The institution of electrical engineers, London, UK, 1998.

[7] M. V. Rao, J. J. Shah, J. Geist and M. Gaitan, *Microwave Dielectric Heating of Fluids in Microfluidic Devices, in: W. Cao (Ed), The Development and Application of Microwave Heating*, INTECH, 2012, ISBN 978-953-51-0835-1

[8] D.J. Marchiarullo, A. Sklavounos, N.S. Barker and J.P. Landers, "Microwave-mediated microchip thermocycling: pathway to an inexpensive, handheld real-time PCR instrument," 11th Int. Conf. on Miniaturized Systems for Chemistry and Life Sciences, 2007.

[9] K. Grenier, D. Dubuc, T. Chen, T. Chrétiennot, M. Poupot, and J-J. Fournié, "Microfluidic on-chip for biomedical applications," in *Proc. Bipolar/BiCMOS Circuits Technol. Meeting*, Atlanta, GA, USA, 2011, pp. 129–132.

[10] K. Grenier, D. Dubuc, et. al., "New broadband and contact less RF / microfluidic sensor dedicated to bioengineering", *2009 IEEE MTT-S Int. Microwave Symp. Dig.*, June 2009.

[11] M. Kent, "A simple flow through cell for microwave dielectric measurements," *Phys. Sci. Instrum.*, vol. 22, pp. 269-271, 1989.

[12] Q. Chen, J. McMurdie, D. Roitman, and A. Knoesen, "Microwave transmission line dielectric probe to detect biomolecular surface interactions,"in *Proc. 26th Annu. Int. Conf. IEEE EMBS*, New Orleans, LA, USA, 2004, pp. 1990–1993.

[13] K. Grenier, D. Dubuc, P. Poleni, M. Kumemura, H. Toshiyoshi, T. Fujii, and H. Fujita, "Integrated broadband microwave and microfluidic sensor dedicated to bioengineering," *IEEE Trans. Microw. Theory Techn.*, vol. 57, no. 12, pp. 3246–3253, Dec. 2009.

[14] J. Booth, N. Orloff, J. Mateu, M. Janezic, M. Rinehart, and J. Beall,"Quantitative permittivity measurements of nanoliter liquid volumes in microfluidic channels to 40 GHz," *IEEE Trans. Instrum. Meas.*, vol. 59, no. 12, pp. 3279–3288, Dec. 2010.
[15] J. Mateu, N. Orloff, M. Rinehart, and J. C. Booth, "Broadband Permittivity of Liquids Extracted from Transmission Line MEasurements of Microfluidic Channels," *2007 IEEE MIT-S Int. Microwave Symp. Dig.*, pp. 523-526, June 2007.
[16] T. Chen, D.Dubuc, and K. Grenier, "Accurate nanoliter liquid complex admittance characterization up to 40 GHz for biomedical applications," in *IEEE MTT-S Int. Microw. Symp. Dig.*, Montréal, QC, Canada, Jun. 2012, pp. 1–3.
[17] T. Chen, D. Dubuc, M. Poupot, J. Fournié, and K. Grenier, "Accurate nanoliter liquid characterization up to 40 GHz for biomedical applications: Toward noninvasive living cells monitoring," *IEEE Trans. Microw. Theory Techn.*, vol. 60, no. 12, pp. 4171–4177, Dec. 2012.
[18] M. Olapinski, S. Manus, M. George, A. Brüggemann, N. Fertig, and F. C. Simmel, "Detection of lipid bilayer and peptide pore formation at gigahertz frequencies," *Appl. Phys. Lett.*, vol. 88, no. 1, pp. 013902-1– 013902-3, Jan. 2006.
[19] J. C. Booth, J. Mateu,M. Janezic, J. Baker-Jarvis, and J. A. Beall, "Broadband permittivity measurements of liquid and biological samples using microfluidic channels," in *Proc. IEEE MTT-S Int. Microw. Symp. Dig.*, 2006, pp. 1750–1753.
[20] N. Meyne, W. Müller-Wichardsy, H. K. Trieuy, and A. F. Jacob, "Quasi-lumped coplanar transmission-line sensors for broadband liquid characterization," in *Microwave Conference (EuMC), 2014 44th European*, Rome, 2014, pp. 687 – 690.
[21] Y. Cui, Y. He, and P. Wang, "A quadrature-based tunable radio frequency sensor for the detection and analysis of aqueous solutions," *IEEE Microwave and Wireless Components Letters*, vol. 24, no. 7, pp. 490-492, Jul. 2014.
[22] Y. Cui, J. Sun, Y. He, Z. Wang, and P. Wang, "A simple, tunable, and highly sensitive radio-frequency sensor," *Applied Physics Letters*, vol. 103, no. 6, pp. 062906, Aug. 2013.
[23] M. a. Suster and P. Mohseni, "An RF/microwave microfluidic sensor based on a center-gapped microstrip line for miniaturized dielectric spectroscopy," *2013 IEEE MTT-S Int. Microw. Symp. Dig.*, pp. 1–3, Jun. 2013.
[24] F. Duhamel, I. Huynen, and A. Vander Vorst, "Measurement of complex permittivity of biological and organic liquids up to 110 GHz," in *IEEE MTT-S Int. Microw. Symp. Dig.*, 1997, vol. 1, pp. 107–110.
[25] Y. Wang and M. N. Afsar, "Measurement of complex permittivity of liquids using waveguide techniques," *Progr. Electromagn. Res.*, vol. 42, pp. 131–142, 2003.
[26] M. A. Suster, B. Blackburn, U. Gurkan, and P. Mohseni1, "An RF/microwave microfluidic sensor based on a 3D capacitive structure with a floating electrode for miniaturized dielectric spectroscopy," in *SENSORS, 2014 IEEE*, Valencia, 2014, pp. 1784 – 1787.
[27] R. Göritz, A. Masood, O. Castell, D.A. Barrow, C. Allender, and A. Porch, "Microwave compositional analysis of solvent matrices in microcapillary manifold systems," *Proc. MicroTAS 2007*, Paris, 2007, pp.1689-1691.
[28] A. Masood, A. Porch, and D. Barrow, *Microwave Resonators for Highly Sensitive Compositional Analysis*. Saarbrücken, Germany: LAMBERT, 2010.
[29] O. Castell, A. Masood, R. Göritz, D. Barrow, C. Allender, and A. Porch, "Microwave technique for monitoring phase separation of a multiphase-flow regime utilised for continuous molecular enrichment," *in Proc. MicroTAS*, San Diego, CA, USA, 2008, pp. 137-139.

[30] H. Kawabata and Y. Kobayashi, "Accurate measurements of complex permittivity of liquid based on a TM_{010} mode cylindrical cavity method," in *Eur. Microw. Conf.*, 2005, pp. 1–4.
[31] B. Kapilevich and B. Litvak, "Optimized microwave sensor for online concentration measurements of binary liquid mixtures," *IEEE Sens. J.*, vol. 11, no. 10, pp. 2611–2616, Oct. 2011.
[32] K. B. Yu, S. G. Ogourtsov, V. G. Belenky, A. B. Maslenikov, and A. S. Omar, "Accuratemicrowave resonantmethod for complex permittivity measurements of liquids," *IEEE Trans.Microw. Theory Techn.*, vol. 48, no. 11, pp. 2159–2164, Nov. 2000.
[33] G. Gennarelli, S. Romeo, M. Scarfi, and F. Soldovieri, "A microwave resonant sensor for concentration measurements of liquid solutions," *IEEE Sensors J.*, vol. 13, no. 5, pp. 1857–1864, May 2013.
[34] A. Porch, A. Masood, J. Naylon, A. Sulaimalebbe, and D. A. Barrow, "Sapphire dielectric resonators for microfluidic compositional analysis," *in Proc. MicroTAS, Groningen*, The Netherlands, 2010, pp. 2011–2013.
[35] E. N. Shaforost, N. Klein, S. A. Vitusevich, A. A. Barannik, and N. T. Cherpak, "High sensitivity microwave characterization of organic molecule solutions of nanoliter volume," *Appl. Phys. Lett.*, vol. 94, no. 11, p. 112901, Mar. 2009.
[36] E. McKeever, S. K. Pavuluri, R. Lopez-Villarroya, G. Goussetis, D. M. Kavanagh, M. I. Mohammed, and M. P. Y. Desmulliez, "Label-free chemical/biochemical sensing device based on an integrated microfluidic channel within a waveguide resonator," *in Proc. IEEE 3rd Electron. Syst. Integration Technol. Conf.*, Berlin, Germany, 2010, pp. 1–3.
[37] A. Masood, O. K. Castell, D. A. Barrow, C. J. Allender, and A. Porch, "Split ring resonator technique for compsitional analysis of solvent matrices in microcapillary systems," *in Proc. MicroTAS*, San Diego, CA, USA, 2008, pp. 1636–1638.
[38] M. S. Boybay, A. Jiao, T. Glawdel, and C. L. Ren, "Microwave sensing and heating of individual droplets in microfluidic devices," *Lab Chip*, vol. 13, no. 19, 13, pp. 3840-3846, Oct. 2013.
[39] C. Song and P. Wang. (2009, Jan.). A radio frequency device for measurement of minute dielectric property changes in microfluidic channels. *Appl. Phys. Lett.* [Online]. *94(2)*, p. 023901. Available: http://link.aip.org/link/?APL/94/023901/1.
[40] M. H. Zarifi, and M. Daneshmand, "Non-contact liquid sensing using high resolution microwave microstrip resonator," in *IEEE MTT-S Int. Microw. Symp. Dig. (IMS)*, Phoenix, AR, 2015, pp. 1-4.
[41] G. McKerricher, D. Conchouso, B.S. CooK, I. Fould, and A. Shamim, "Crude oil water-cut sensing with disposable laser ablated and inkjet printed RF microfluidics," in *IEEE MTT-S Int. Microw. Symp. Dig. (IMS),*Tampa, FL, 2014, pp. 1-3.
[42] K. Saeed, A. C. Guyette, R. D. Pollard, and I. C. Hunter, "Microstrip resonator technique for measuring dielectric permittivity of liquid solvents and for solution sensing," in *IEEE MTT-S Int. Microw. Symp. Dig.*, Honolulu, HI 2007, pp. 1185–1188.
[43] U. Schwerthoeffer, R. Weigel, and D. Kissinger, "Microwave sensor for precise permittivity characterization of liquids used for aqueous glucose detection in medical applications," *In GeMiC 2014*, Aachen, Germany, 2014, pp. 1-2.
[44] C. Song, J. E. Harriss and P. Wang, "Compensating on-chip transmission line losses for a high-sensitivity microwave sensor," *Sens. Actuators, A Phys.*, vol. 154, no. 1, pp. 7-11, Aug. 2009.

[45] D. J. Rowe, A. Porch, D. A. Barrow, and C. J. Allender, "Dielectric analysis of microfluidic systems with an integrated microwave resonant device," *in Proc. 41st Eur. Microw. Conf.*, Manchester, U.K., 2011, pp. 607–610.
[46] D. J. Rowe, A. Porch, D. A. Barrow, and C. J. Allender, "Microfluidic device for compositional analysis of solvent systems at microwave frequencies," *Sens. Actuators B, Chem.*, vol. 169, pp. 213–221, 2012.
[47] D. J. Rowe, *Microfluidic microwave resonant sensors*, PhD thesis, Cardiff University, 2012.
[48] D. J. Rowe, A. Porch, D. A. Barrow, and C. J. Allender, "Integrated microwave resonant device for dielectric analysis of microfluidic systems," *in J. Physics: Conf. Series*, Aug. 2011, vol. 310, Art. ID 012004.
[49] D. J. Rowe, J. Naylon, A. Porch, D. A. Barrow, and C. J. Allender, "Microwave resonant sensor for real-time continuous-flow measurements of microfluidic systems," in *Proc. 15th Int. Conf. Miniaturized Syst. Chemistry and Life Sci.*, Groningen, Germany, 2010, pp. 1004–1006.
[50] D. J. Rowe, A. Porch, D. A. Barrow, and C. J. Allender, "Non-contact label-free dielectric spectroscopy of single-and multi-phase microfluidic systems," in *Proc. 16th Int. Conf. Miniaturized Syst. Chemistry and Life Sci.*, Seattle, WA, 2011, pp. 891–893.
[51] D. J. Rowe, A. Porch, D. A. Barrow, and C. J. Allender, "Novel coupling structure for the resonant coaxial probe," *IEEE Trans. Microw. Theory Tech.*, vol. 60, no. 6, pp. 1699–1708, Jun. 2012.
[52] D. Rowe, A. Porch, D. Barrow, and C. Allender, "Microfluidic microwave sensor for simultaneous dielectric and magnetic characterization," *IEEE Trans. Microw. Theory Techn.*, vol. 61, no. 1, pp. 234–243, Jan. 2013.
[53] T. Chretiennot, D. Dubuc, and K. Grenier, "A microwave and microfluidic planar resonator for efficient and accurate complex permittivity characterization of aqueous solutions," *IEEE Trans. Microw. Theory Tech.*, vol. 61, no. 2, pp. 972–978, 2013.
[54] J. A. Gordon, C. L. Holloway, J. Booth, S. Kim, Y. Wang, J. Baker-Jarvis, *et al.*, "Fluid interactions with metafilms/metasurfaces for tuning, sensing, and microwave-assisted chemical processes," *Phys. Rev. B*, vol. 83, pp. 205130-1–205130-5, May 2011.
[55] A. Ebrahimi, W. Withayachumnankul, S. Al-Sarawi, and D. Abbott, "High-Sensitivity Metamaterial-Inspired Sensor for Microfluidic Dielectric Characterization," *IEEE Sens. J.*, vol. 14, no. 5, pp. 1345– 1351, May 2014.
[56] W. Withayachumnankul, K. Jaruwongrungsee, A. Tuantranont, C. Fumeaux, and D. Abbott, "Metamaterial-based microfluidic sensor for dielectric characterization," *Sens. Actuators A, Phys.*, vol. 189, pp. 233–237, Jan. 2013.
[57] K. Grenier, D. Dubuc, P.-E. Poleni, M. Kumemura, T. Fujii, H. Toshiyoshi, and H. Fujita, "Resonant based microwave biosensor for biological cells discrimination," in IEEE Radio Wireless Symp., New Orleans, LA, USA, Jan. 2010, pp. 523–526.
[58] S. Pinon, D. L. Diedhiou, A. Boukabache, V. Conedera, D. Bourrier, A.-M. Gue, G. Prigent, E. Rius, C. Quend, B. Potelon, and J.-F. Favennec, "Fabrication and characterization of a fully integrated biosensor associating microfluidic device and RF circuit," in IEEE MTT-S Int. Microw. Symp. Dig., Montreal, QC, Canada, 2012, pp. 1–3.
[59] N. Wiwatcharagoses, K. Y. Park, and J. Hejase, "Microwave artificially structured periodic media microfluidic sensor," in *Proc. IEEE Electron. Compon. Technol. Conf.*, Lake Buena Vista, FL 2011, pp. 1889–1893.

[60] C. Elbuken, T. Glawdel, D. Chan, and C. L. Ren, "Detection of microdroplet size and speed using capacitive sensors," *Sensors and Actuators A*, vol. 171, no. 2, pp. 55– 62, Nov. 2011.
[61] V. Srinivasan, V. K. Pamula, and R. B. Fair, "Droplet-based microfluidic lab-on-a-chip for glucose detection," *Analytica Chimica Acta*, vol. 507, no. 1, pp. 145–150, Apr. 2004.
[62] N. Nguyen, S. Lassemono, and F. A. Chollet, "Optical detection for droplet size control in microfluidic droplet-based analysis systems," *Sensors and Actuators B*, vol. 117, no. 2, pp. 431–436, Oct. 2006.
[63] V. Lien and F. Vollmer, "Microfluidic flow rate detection based on integrated optical fiber cantilever," *Lab Chip*, vol. 7, no. 10, pp. 1352–1356, Jul. 2007.
[64] N. Damean, L. F. Olguin, F. Hollfelder, C. Abella and W. T. S. Huck, "Simultaneous measurement of reactions in microdroplets filled by concentration gradients," *Lab Chip*, vol. 9, no. 12, pp. 1707–1713, Mar. 2009.
[65] S. Jakieła, P. M. Korczyk, S. Makulska and P. Garstecki, "Speed of droplets in microfluidic channels," *15th International Conference on Miniaturized Systems for Chemistry and Life Sciences*, Seattle, Washington, 2011, pp. 671- 673.
[66] M. G. Pollack, R. B. Fair, and A. D. Shenderov, "Electrowetting-based actuation of liquid droplets for microfluidic applications," *Appl. Phys. Lett.*, vol. 77, no. 11, Sep. 2000.
[67] S. Gawad, L. Schild, and P. Renaud, "Micromachined impedance spectroscopy flow cytometer for cell analysis and particle sizing," *Lab on a Chip*, vol. 1, no. 1, pp. 76–82, Aug. 2001.
[68] J. Z. Chen, A. A. Darhuber, S. M. Troian, and S. Wagner, "Capacitive sensing of droplets for microfluidic devices based on thermocapillary actuation," *Lab Chip*, vol. 4, no. 5, pp. 473–480, Jun. 2004.
[69] H. Ren, R.B. Fair, and M.G. Pollack, "Automated on-chip droplet dispensing with volume control by electro-wetting actuation and capacitance metering," *Sensors and Actuators B*, vol. 98, no. 2-3, pp. 319–327, Mar. 2004.
[70] N. Srivastava, and M. A. Burns, "Electronic drop sensing in microfluidic devices: automated operation of a nanoliter viscometer," *Lab Chip*, vol. 6, no. 6, pp. 744–751, Mar. 2006.
[71] X. Niu, M. Zhang, S. Peng, W. Wen, and P. Sheng, "Real-time detection, control, and sorting of microfluidic droplets," *Biomicrofluidics*, vol. 1, no. 2, p. 044101, Dec. 2007.
[72] E. Ghafar-Zadeh, M. Sawan, and D. Therriault, "A 0.18-µm CMOS capacitive sensor Lab-on-Chip," *Sensors and Actuators A*, vol. 141, no. 2, pp. 454–462, Feb. 2008.
[73] J. Gong and C.-J. "CJ" Kim, "All-electronic droplet generation on-chip with real-time feedback control for EWOD digital microfluidics," *Lab Chip*, vol. 8, no. 6, pp. 898–906, Jun. 2008.
[74] M. C. Cole, and P. J.A. Kenis, "Multiplexed electrical sensor arrays in microfluidic networks," *Sensors and Actuators B: Chemical*, vol. 136, no. 2, pp. 350–358, Mar. 2009.
[75] A. Banerjee, Y. Liu, J. Heikenfeld, and I. Papautsky, "Deterministic splitting of fluid volumes in electrowetting microfluidics," *Lab Chip*, vol. 12, no. 24, pp. 5138–5141, Sep. 2012.
[76] G. Markx and C. Davey, "The dielectric properties of biological cells at radiofrequencies: Applications in biotechnology," *Enzyme Microbial Technol.*, vol. 25, no. 3–5, pp. 161–171, Aug. 1999.

[77] S. Gawad, K. Cheung, U. Seger, A. Bertsch, and P. Renaud, "Dielectric spectroscopy in a micromachined flow cytometer: theoretical and practical considerations," *Lab Chip*, vol. 4, no. 3, pp. 241-251, Feb. 2004.
[78] A. Denzi, C. Merla, C. Palego, F. Apollonio, J. C. M. Hwang, M. Liberti, "Single cell microdosimetric studies comparing ideal and measured nanosecond pulsed electric fields", in *IEEE MTT-S Int. Microw. Symp. Dig. (IMS)*, Seattle, WA, 2013, pp. 1-4.
[79] A. Vander Vorst, A. Rosen, Y. Kotsuka, "*RF/Microwave Interaction with Biological Tissues*", *IEEE Press, Wiley- Interscience*, 2006.
[80] F. Artis, D. Dubuc, J-J. Fournié, M. Poupot, and K. Grenier, "Microwave dielectric spectroscopy of cell membrane permeabilization with saponin on human B lymphoma cells," in *IEEE MTT-S Int. Microw. Symp. Dig. (IMS)*, Tampa, FL, 2014, pp. 1-4.
[81] S. Seo, T. Stintzing, I. Block, D. Pavlidis, M. Rieke, and P. G. Layer, "High frequency wideband permittivity measurements of biological substances using coplanar waveguides and application to cell suspensions", in *IEEE MTT-S Int. Microw. Symp. Dig. (IMS)*, Atlanta, GA, 2008, pp. 915 – 918.
[82] Y. Chen, H. Wu, Y. Hon, and H. Lee, "40 GHz RF biosensor based on microwave coplanar waveguide transmission line for cancer cells (HepG2) dielectric characterization," *Biosensors and Bioelectronics*, vol. 61, pp. 417–421, Nov. 2014.
[83] C. Palego, C. Merla, Y. Ning, D. Molinero, C. Multari, X. Cheng, G. Ding, and J. C. M. Hwang, "Broadband microchamber for electrical detection of live and dead biological cells," in *IEEE MTT-S Int. Microw. Symp. Dig. (IMS)*, Seattle, WA, 2013, pp. 1 – 3.
[84] K. Grenier, D. Dubuc, M. Poupot, and J.-J. Fournié, "Microwave signatures of alive b-lymphoma cells suspensions," in Proc. IEEE Topic Conf. Biomed. Wireless Technol., Netw., Sens. Syst. (BioWirelessSS), Phoenix, AZ, 2011, pp. 95–98.
[85] T. Chen, F. Artis, D. Dubuc, J-J. Fournié, M. Poupot and K. Grenier, "Microwave biosensor dedicated to the dielectric spectroscopy of a single alive biological cell in its culture medium," in *IEEE MTT-S Int. Microw. Symp. Dig. (IMS)*, Seattle, WA, 2013, pp. 1-4.
[86] W. Chen, D. Dubuc, and K, Grenier, "Microwave dielectric spectroscopy of a single biological cell with improved sensitivity up to 40 GHz," in *IEEE MTT-S Int. Microw. Symp. Dig. (IMS)*, Phoenix, AR, 2015, pp. 1-4.
[87] A. Denzi, F. Apollonio, M. Liberti, M. Caterina, Y. Ning, C. Multari, C. Palego, X. Cheng, and J. C. M. Hwang, "Cell detection and discrimination by a microfluidic-integrated broadband microchamber," in *European Microwave Conference (EuMC)*, Rome, 2009, pp. 695 - 698.
[88] Y. Ning, C. Multari, X. Luo, C. Palego, X. Cheng, J. C. M. Hwang, A. Denzi, C. Merla, F. Apollonio, and M, Liberti, "Broadband electrical detection of individual biological cells," *IEEE Trans.Microw. Theory Techn.*, vol. 62, no. 9, pp. 1905-1911. Sep. 2014.
[89] D. Dubuc, O. Mazouffre, C. Llorens, T. Taris, M. Poupot, J.-J. Fournie´, J.-B. Begueret, and K. Grenier, "Microwave-based biosensor for on-chip biological cell analysis," *Analog Integr Circ Sig Process*, vol. 77, pp. 135–142, Nov. 2013.
[90] K. Grenier, D. Dubuc, T. Chen, F. Artis, T. Chretiennot, M. Poupot, and J.-J. Fournie, "Recent advances in microwave-based dielectric spectroscopy at the cellular level for cancer investigations", *IEEE Trans. Microwave Theory Techniques*, vol. 61, no. 5, pp. 2023-2030, May 2013.

[91] G. R. Facer, D. A. Notterman, L. L. Sohn, "Dielectric spectroscopy for bioanalysis: from 40 Hz to 26.5 GHz in a microfabricated wave guide," *Appl. Phys. Lett.*, vol. 78, no. 7, pp. 996-998, Feb. 2001.
[92] H.-J. Lee, J.-H. Lee, H.-S. Moon, I.-S. Jang, J.-S. Choi, J.-G. Yook, *et al.*, "A planar split-ring resonator-based microwave biosensor for label-free detection of biomolecules," *Sens. Actuators B, Chem.*, vol. 169, pp. 26–31, Jul. 2012.
[93] C. Dalmay, A. Pothier, P. Blond, M. Cheray, F. Lalloue, and M.-O. Jauberteau, "RF Biosensor based on Microwave Filter for Biological Cell Characterisation," in *European Microwave Conference (EuMC)*, Rome, 2009, pp. 41-44.
[94] J. Wessel, K. Schmalz, J. C. Scheytt, B. Cahill, G. Gastrock, "Microwave biosensor for characterization of compartments in teflon capillaries," in *European Microwave Conference (EuMC)*, Amsterdam, 2012, pp. 534 – 537.
[95] C. Dalmay et al., "Ultra Sensitive Biosensor Based on Impedance Spectroscopy at Microwave Frequencies for Cell Scale Analysis", *Sensors and Actuators A: Physical*, vol. 162, no. 2, pp 189-197, Aug. 2010.
[96] N. Haase, A.F. Jacob, "Characterization of biological substances using a substrate integrated microwave near-field sensor," in *Microwave Conference (EuMC), 2012 42nd European*, Amsterdam, Netherlands, 2012, pp. 432 – 435.
[97] C. Dalmay, A. Pothier, P. Blondy, F. Lalloue, M.-O. Jauberteau, "Label free biosensors for human cell characterization using radio and microwave frequencies," in *IEEE MTT-S Int. Microw. Symp. Dig. (IMS)*, Atlanta, GA, 2008, pp. 911 - 914.
[98] C. Dalmay, and al., "Label free bio sensing method using radio frequencies spectroscopy for cell detection and discrimination", *BIODEVICES 2009, International Conference on Biomedical Electronics and Devices*, Porto, 2009.
[99] A. Landoulsi, L. Y. Zhang, C. Dalmay, A. Lacroix, A. Pothier, A. Bessaudou, P. Blondy, S. Battu, F. Lalloué, C. B. MdP, and C. Lautrette, "Tunable Frequency Resonator Biosensors Dedicated to Dielectric Permittivity Analysis of Biological Cell Cytoplasm," in *IEEE MTT-S Int. Microw. Symp. Dig. (IMS)*, Seattle, WA, 2013, pp. 1-4.
[100] Y. Yang, Y. He, H. Zhang, K. Huang, G. Yu, and P. Wang, "Measuring the Microwave Permittivity of Single Particles," *2013 IEEE Topical Conference on Biomedical Wireless Technologies, Networks, and Sensing Systems (BioWireleSS)*, Austin, TX, 2013, pp. 28 – 30.
[101] Y. Yang, H. Zhang, J. Zhu, G. Wang, T-R. Tzeng, X. Xuan, K. Huang, and P. Wang, "Distinguishing the viability of a single yeast cell with an ultra-sensitive radio frequency sensor," *Lab on a Chip*, vol. 10, pp. 553–555, Mar. 2010.
[102] G. A. Ferrier, S. F. Romanuik, D. J. Thomson, G. E. Bridges, and M. R. Freeman, "A microwave interferometric system for simultaneous actuation and detection of single biological cells," *Lab on a Chip*, vol. 9, pp. 3406–3412, Dec. 2009.
[103] L. Y. Zhang, C. Bounaix,M. Du Puch, C. Dalmay, A. Lacroix, A. Landoulisi, J. Leroy, C. Melin, F. Lalloue, S. Battu, C. Lautrette, S. Giraud, A. Bessaudou, P. Blondy,M. O. Jauberteau, and A. Pothier, "Discrimination of colorectal cancer cell lines using microwave biosensor," *Sens. Actuators A, Phys.*, vol. 216, pp. 405–416, Sep. 2014.
[104] L. Y. Zhang, C. Bounaix Morand du Puch, A. Lacroix, C. Dalmay, A. Pothier, C. Lautrette, S. Battu, F. Lalloué, M.-O. Jauberteau, and P. Blondy, "Microwave biosensors for identifying cancer cell aggressiveness grade," in *IEEE MTT-S Int. Microw. Symp. Dig.*, Montréal, QC, Canada, 2012, pp. 1-3.

[105] J. Liu, M. Enzelberger, and S. Quake, "A nanoliter rotary device for polymerase chain reaction," *Electrophoresis*, vol. 23, no. 10, pp. 1531–1536, May 2002.
[106] R.-H. Liu, J. Yang, R. Lenigk, J. Bonanno and P. Grodzinski, "Self contained, fully integrated biochip for sample preparation, Polymerase Chain Reaction Amplification, and DNA Microarray Detection," *Anal. Chem.*, vol. 76, no. 7, pp. 1824–1831, Feb. 2004.
[107] H.-F. Arata, F. Gillot, T. Nojima, T. Fujii and H. Fujita, "Millisecond denaturation dynamics of fluorescent proteins revealed by femtoliter container on micro-thermidevice," *Lab Chip,* vol. 8, no, 9. pp. 1436–1440, Sep. 2008.
[108] A.-J. de Mello, M. Habgood, L. Lancaster, T. Welton and R.-C. Wootton, "Precise temperature control in microfluidic devices using Joule heating of ionic liquids," *Lab Chip*, vol. 4, no. 5, pp. 417–419, Jul. 2004.
[109] A. Kempitiya, D. A. Borca- Tasciuc, H. S. Mohamed, M. M. Hella, "Localized microwave heating in microwells for parallel DNA amplification applications," *Appl. Phys. Lett.*, vol. 94, no. 6, 2009.
[110] J. J. Shah, G. Jon, and G. Michael, "Microwave-induced adjustable nonlinear temperature gradients in microfluidic devices," *J. Micromech. Microeng.*, vol. 20, no. 10, p. 105025, Oct. 2010.
[111] J. J. Shah, S. G. Sundaresan, J. Geist, D. R. Reyes, J. C. Booth, M. V. Rao, and M. Gaitan, "Microwave dielectric heating of fluids in an integrated microfluidic device," *J. Micromech. Microeng*., vol. 17, no. 11, pp. 2224– 2230, Nov. 2007.
[112] I. Chaimov and S. R. Rogers, "Electromagnetic heating apparatus having decoupled excitations," *2013 IEEE International Conference on Microwaves, Communications, Antennas and Electronic Systems (COMCAS 2013)*, Tel Aviv, 2013, pp. 1-4 .
[113] A. Porch, D. Slocombe, J. Beutler, P. Edwards, A. Aldawsari, T. Xiao, V. Kuznetsov, H. Almegren, S. Aldrees, N. Almaqati, "Microwave treatment in oil refining," *Appl. Petrochemical Res.*, vol. 2, no. 1-2, pp. 37-44, Aug. 2012.
[114] K. J. Shaw, P. T. Docker, J. V. Yelland, C. E. Dyer, J. Greenman, G. M. Greenway, and S. J. Haswell, "Rapid PCR amplification using a microfluidic device with integrated microwave heating and air impingement cooling," *Lab on a Chip*, vol. 10, no. 13, pp. 1725-1728, Jul. 2010.
[115] A. J. L. Morgan, et al., "Efficient microwave heating of microfluidic systems," *Sensors and Actuators B*, vol. 181, no. , pp. 904– 909. May 2013.
[116] E. Comer, and M.G. Organ, "A microcapillary system for simultaneous: parallel microwave-assisted synthesis," *Chemistry - A European Journal*, vol. 11, no. 24 pp. 7223–7227, Dec. 2005.
[117] M. Matsuzawa, S. Togashi, S. Hasebe, "A continuous flow microwave-assisted microreactor system," in: *AIChE Annual Meeting, Conference Proceedings*, 2008.
[118] E. Comer, and M. G. Organ, "A microreactor for microwave-assisted capillary (continuous flow) organic synthesis," *journal of the American chemical society*, vol. 127, no. 22, pp. 8160–8167, May 2005.
[119] X. Chen, L. Song, B. Assadsangabi, J. Fang, M. S. M. Ali, and K. Takahata, "Wirelessly addressable heater array for centrifugal microfluidics and *Escherichia Coli* sterilization," *35th Annual International Conference of the IEEE EMBS*, Osaka, Japan, 2013, pp. 5505- 5508.
[120] K D. Issadore, K. J. Humphry, K. A. Brown, L. Sandberg, D. Weitz, and R. M. Westervelt, "Microwave dielectric heating of drops in microfluidic devices," *Lab Chip*, vol. 9, no. 12, pp. 1701–1706, Jun. 2009.

[121] M. Nikolic-Jaric, S. F. Romanuik, G. A. Ferrier, G. E. Bridges, M. Butler, K. Sunley, D. J. Thomson, and M. R. Freeman, "Microwave frequency sensor for detection of biological cells in microfluidic channels," *Biomicrofluidics*, vol. 3, no. 3, 034103, Sep. 2009.
[122] T. Markovic, S. Liu, P. Barmuta, I. Ocket, M. Cauwe, D. Schreurs, and B. Nauwelaers, "Microwave heater at 20 GHz for nanoliter scale digital microfluidics," in *IEEE MTT-S Int. Microw. Symp. Dig. (IMS)*, Phoenix, AR, 2015, pp. 1-4.
[123] F. S. Barnes and B. Greenebaum, *Bioengineering and Biophysical Aspects of Electromagnetic Fields*, 3rd edn. Boca Raton, FL: CRC Press, 2006.
[124] J. G. Webster and H. Eren, *Measurement, Instrumentation, and Sensors Handbook Electromagnetic, Optical, Radiation, Chemical, and Biomedical Measurement*, Second edn. Boca Raton, FL: CRC Press, 2014.
[125] "A Guide to the characterization of dielectric materials at RF and microwave Frequencies", The Institute of Measurement and Control (IMC) and The National Physical Laboratory (NPL), London, ISBN 0 904457 38 9, 2003.
[126] J. C. Anderson, '*Dielectrics*' published by Chapman and Hall, London, Science Paperbacks, Modern Electrical Studies, 1964.
[127] V. Daniel, '*Dielectric Relaxation*' published by Academic Press, London, 1967.
[128] F. Buckley and A. A. Maryott, "Tables of dielectric dispersion data for pure liquids and dilute solutions," *Nat. Bureau Standards Circular*, vol. 589, p. 6, Nov. 1958.
[129] A. P. Gregory and R. N. Clarke, "*Tables of the complex permittivity of dielectric reference liquids at frequencies up to 5 GHz*," National Physical Laboratory ,NPL Report MAT 23, Middlesex, 2012.
[130] U. Kaatze, "Complex permittivity of water as a function of frequency and temperature," *J. Chem. Eng. Data*, vol. *34*, no. 4, pp. 371–374, Oct. 1989.
[131] W. J. Ellison, "Permittivity of pure water, at standard atmospheric pressure, over the frequency range 0–25 THz and the temperature range 0–100 °C," *J. Phys. Chem. Ref. Data*, vol. 36, no. 1, pp.1-18, Feb. 2007.
[132] A. Catenaccio, Y. Daruich, and C. Magallanes, "Temperature dependence of the permittivity of water," *Chemical Physics Letters*, vol. 367, no. 5-6, pp. 669–671, Jan. 2003.
[133] R. Buchner, J. Barthel, and J. Stauber, "The dielectric relaxation of water between 0°C and 35°C," *Chemical Physics Letters*, vol. 306, no. 1-2, pp. 57–63, Jun.1999.
[134] H. J. Liebe, G. A. Hufford, and T. Manabe, "A model for the complex permittivity of water at frequencies below 1 THz," *International Journal of Infrared and Millimeter Waves*, vol. 12, no.7, pp 659-675, Jul. 1991.
[135] V. Komarov, S. Wang, and J. Tang, "*Permittivity and measurements, in: K.Chang (Ed), Encyclopedia of RF and Microwave Engineering*," John Wiley & Sons, Inc, 2005, ISBN 0-471-27053-9.
[136] U. Kaatze, R. Behrends, and R. Pottel, "Hydrogen network fluctuations and dielectric spectrometry of liquids," *Journal of Non-Crystalline Solids*, vol. 305, no. 1-3, pp. 19–28, Jul. 2002.
[137] N. J. English and J. M. D. MacElroy, "Hydrogen bonding and molecular mobility in liquid water in external electromagnetic fields," *JOURNAL OF CHEMICAL PHYSICS*, vol. 119, no. 22, pp. 11806-11813, Dec. 2003.

[138] R. Somaraju and J. Trumpf, “Frequency, temperature and salinity variation of the permittivity of seawater,” IEEE Trans. Antennas Propag., vol. 54, no. 11, pp. 3441–3448, Nov. 2006.
[139] A. Khayari, M. Medrano, E. Verlage, M. C. Vela´zquez-Ahumada, M. J. Freire, and A. Ramos, “Microwave-induced water flow in a microchannel built on a coplanar waveguide,” *Journal of Applied Physics*, vol.110, no. 6, p. 064912, Sep. 2011.
[140] D. M. Pozar, *Microwave Engineering*. Fourth edition, New York, NY, USA: Wiley, 2012.
[141] R. A. Waldron, “Perturbation theory of resonant cavities,” *Proc. Inst. Elect. Eng.*, vol. 107, no. 12, pp. 272–274, Sep. 1960.
[142] R. G. Carter, “Accuracy of microwave cavity perturbation measurements,” *IEEE Trans. Microw. Theory Techn.*, vol. 49, no. 5, pp. 918–923, May 2001.
[143] R. F. Harrington, *Time-Harmonic Electromagnetic Fields*. New York, USA: John Wiley and Sons, 2001.
[144] S.M. Bradshaw, E.J. van Wyk, and J.B. de Swardt, "Microwave heating principles and the application to the regeneration of granular activated carbon," *J. S. Afr. lnst. Min. Metall.*, vol. 98, no. 4, pp. 201-210, 1998.
[145] V. Miralles, A. Huerre, F. Malloggi, and M.-C. Jullien "A Review of Heating and Temperature Control in Microfluidic Systems: Techniques and Applications", *Diagnostics*, Vol. 3, no. 1, pp. 33-67, Jan. 2013.
[146] J. Hong and M. Lancaster, *Microstrip filters for RF/microwave applications*. John Wiley and Sons, 2001.
[147] T. Driscoll, G. O. Andreev, D. N. Basov, S. Palit, S. Y. Cho, N. M. Jokerst, and D. R. Smith, “Tuned permeability in terahertz split-ring resonators for devices and sensors,” *Appl. Phys. Lett.*, vol. 91, no. 6, p. 062511(1-3), Aug. 2007.
[148] J. Naqui, M. Durán-Sindreu, and F. Martín, “Novel sensors based on the symmetry properties of split ring resonators (SRRs),” *Sensors*, vol. 11, no. 8, pp. 7545–7553, Jul. 2011.
[149] K. Chang and L.-H. Hsieh, *Microwave Ring Circuits and Related Structures*. (2nd ed.), New Jersey, USA: Wiley, 2004.
[150] K. Chang, *Microwave Ring Circuits and Antennas*. NewYork,NY, USA: Wiley, 2004.
[151] J. Chen, L. Quyen, and X. Zhu, “Loss compensated high- tunable basspass filter usingmicrostrip ring resonators,” in *Proc. Int.Conf. Adv. Technol. Commun.*, Da Nang, 2011, pp. 191–194.
[152] M. J. Lancaster, *PassiveMicrowave Device Applications of High-Temperature Superconductors*. Cambridge, U.K.: Cambridge Univ., 1997, ch. 4, p. 137.
[153] J. Barthel, K. Bachhuber, R. Buchner, and H. Hetzenauer, “Dielectric spectra of some common solvents in the microwave region. Water and lower alcohols,” *Chem. Phys. Lett.*, vol. 165, no. 4, pp. 369–373, Jan. 1990.
[154] M. Xu, E. Eyring, and S. Petrucci, “Dielectric relaxation of chloroform and chloroform-cyclohexane mixtures at gigahertz and terahertz frequencies. The inertial term,” *J. Mol. Liquids*, vol. 73–74, pp. 41–48, Nov. 1997.
[155] Y. Polevaya, I. Ermolina, M. Schlesinger, B. -Z. Ginzburg, and Y. Feldman, “Time domain dielectric spectroscopy study of human cells II. Normal and malignant white blood cells,” *Biochimica et Biophysica Acta*, vol. 1419, pp. 257 - 271, Jul. 1999.

[156] Q. Hu, R. P. Joshi, and A. Beskok, “Model study of electroporation effects on the dielectrophoretic response of spheroidal cells,” *Journal of Applied Physics*, vol. 106, no. 2, pp. 024701, Jul. 2009.
[157] L. L. Sohn, O. A. Saleh, G. R. Facer, A. J. Beavis, R. S. Allan, and D. A. Notterman, “Capacitance cytometry: Measuring biological cells one by one,” *Proceedings of the National Academy of Sciences of the United States of America (PNAS)*, vol. 97, no. 20, pp. 10687 –10690, Sep. 2000.
[158] K. Asami, “Characterization of biological cells by dielectric spectroscopy,” *Journal of Non -Crystalline Solids*, vol. 305, no. 1 -3, pp. 268 –277, Jul. 2002.
[159] Y. Temiz, R. D. Lovchik, G. V. Kaigala and E. Delamarche, “Lab -on - a - chip devices: How to close and plug the lab?,” *Microelectronic Engineering*, vol. 132, pp. 156 –175, Jan. 2015.
[160] K. Ren, J. Zhou, and H. Wu, “Materials for Microfluidic Chip Fabrication,” *Acc. Chem. Res.*, vol. 46, no. 11, pp. 2396 –2406, Jun. 2013.
[161] S. Gowers , V.F. Curto, C. A. Seneci, C. Wang, S. Anastasova, P. Vadgama, G. Yang, and M. Boutelle, “3D Printed Microfluidic Device with Integrated Biosensors for Online Analysis of Subcutaneous Human Microdialysate”, *Anal. Chem.*, vol. 87, no. 15, pp. 7763 –7770, Aug. 2015.
[162] COMSOL RF Module User’s Guide Version: November 2013 COMSOL 4.4.
[163] S. Abdalla, “Complex permittivity of blood cells and E. coli suspensions,” *Journal of Molecular Liquids*, vol. 160, no. 3, pp. 130 - 135, May 2011.
[164] V. Pohl, D. Fricke, and A. Muhlbauer, “Correction procedures for the measurement of permittivities with the cavity perturbation method,” *The Journal of Microwave Power & Electromagnetic Energy*, vol. 30, no. 1, pp. 10-26, 1995.
[165] T. Ashour, L. Fan, Z. Ding, and K. Chang, “Temperature stability for microstrip delay lines on high permittivity substrates,” *Microwave Symposium Digest, IEEE MTT-S International*, vol. 1, pp. 95-98, San Francisco, CA, 1996.
[166] R. K. Hoffman, *Handbook* of *Microwave Integrated Circuits*, Norwood, MA: Artech House, Inc., 1987.
[167] F. Mernyei and F. Volgyi, “Simple methods for testing the temperature dependence of microstrip antenna array,” *Microwave Conference, 20th European*, vol. 1, pp. 365-370, Budapest, 1990.
[168] W. Su, C. Mariotti, B. S. Cook, S. Lim , L. Roselli, and M. M. Tentzeris, “A metamaterial-inspired temperature stable inkjet-printed microfluidic-tunable bandstop filter,” *44th European Microwave Conference (EuMC)*, Rome, 2014, pp. 9-12.
[169] P. Kabacik, and M. E. Bialkowski, “The temperture dependence of substrate parameters and their effect on microstrip antenna performance,” *IEEE Trans. Antennas Propag.*, vol. 47, no. 6, June 1999.
[170] S. Ramo, J. R. Whinnery, and T. V. Duzer, *Fields and Waves in Communication Electronics*, John Wiley & Sons, Inc, 1994.
[171] G. L. Matthaei, L. Young, and E. M. T. Jones, *Microwave Filters, Impedance-Matching Networks, and Coupling Structures*, Norwood, MA, Artech House, Inc., 1980.
[172] D. Slocombe, A. Porch, E. Bustarret, and O. A. Williams, “Microwave properties of nanodiamond particles,” *Appl. Phys. Lett.*, vol. 102, no. 24, Jun. 2013, Art. ID 244102.
[173] I. C. Hunter, "Design of contiguous RF filterbanks with application in channelised receivers," *IEE Proceedings-Microwaves, Antenna & Propagation*, vol. 138, no 3, pp. 289-292, Jun. 1991.

[174] A. C. Metaxas and R. J. Meredith, *Industrial Microwave Heating*. London, U.K.: Peregrinus, 1983.
[175] S. Lucyszyn and I. D. Robertson, "Analog reflection topology building blocks for adaptive microwave signal processing applications," *IEEE Trans.Microw. Theory Techn.*, vol. 43, no. 3, pp. 601–611, Mar. 1995.
[176] J. Li, J. Chen, P. Chen, and F. Zhu, "Varactor-tuned half mode substrate integrated waveguide reflection-type phase shifter," *in Millim. Wave Wireless Technol. Appl. Microw. Workshop Series*, Nanjing, China, 2012, pp. 1–3.
[177] S. M. Shameli, T. Glawdel, Z. Liu, and C. L. Ren, "Bilinear temperature gradient focusing in a hybrid PDMS/glass microfluidic chip integrated with planar heaters for generating temperature gradients," *Anal. Chem.*, vol. 84, no. 6, pp. 2968–2973, Mar. 2012.
[178] P. K. Ikalainen and G. L. Matthai, "Wide-band, forward-coupling microstrip hybrids with high directivity," *IEEE Trans.Microw. Theory Techn.*, vol. MTT-35, no. 8, pp. 719–725, Aug. 1987.
[179] S. Park, H. Choi, and Y. Jeong, "Microwave group delay time adjuster using parallel resonator," *IEEE Microw. Wireless Compon. Lett.*, vol. 17, no. 2, pp. 109–111, Feb. 2007.
[180] G. A. Dimitrakis et al., "A system for traceable measurement of the microwave complex permittivity of liquids at high pressures and temperatures," *Meas. Sci. Technol.*, vol. 20, no. 4, pp. 1–6, Feb. 2009.